



HAL
open science

Experimental study of the rotor-rotor aerodynamic interaction of a counter-rotating centrifugal compressor

van Thang Nguyen

► **To cite this version:**

van Thang Nguyen. Experimental study of the rotor-rotor aerodynamic interaction of a counter-rotating centrifugal compressor. Fluids mechanics [physics.class-ph]. HESAM Université, 2020. English. NNT : 2020HESAE031 . tel-02967047

HAL Id: tel-02967047

<https://theses.hal.science/tel-02967047v1>

Submitted on 14 Oct 2020

HAL is a multi-disciplinary open access archive for the deposit and dissemination of scientific research documents, whether they are published or not. The documents may come from teaching and research institutions in France or abroad, or from public or private research centers.

L'archive ouverte pluridisciplinaire **HAL**, est destinée au dépôt et à la diffusion de documents scientifiques de niveau recherche, publiés ou non, émanant des établissements d'enseignement et de recherche français ou étrangers, des laboratoires publics ou privés.

ÉCOLE DOCTORALE SCIENCES ET MÉTIERS DE L'INGÉNIEUR

**Laboratoire d'Ingénierie des Fluides et des Systèmes Énergétiques
(LIFSE) - Campus de Paris**

THÈSE

présentée par : **Van-Thang NGUYEN**

soutenue le : **31 Août 2020**

pour obtenir le grade de : **Docteur d'HESAM Université**

préparée à : **École Nationale Supérieure d'Arts et Métiers**

Spécialité : **Mécanique des Fluides**

Étude expérimentale de l'interaction aérodynamique rotor-rotor pour un compresseur centrifuge contrarotatif

THÈSE dirigée par :

Professeur Farid BAKIR

et co-encadrée par :

Docteur Amélie DANLOS

Docteur Richard PARIDAENS

Jury

Xavier CARBONNEAU,	Professeur, ISAE-Toulouse	Président
Pascal CHESSE,	Professeur, Ecole centrale de Nantes	Rapporteur
Miguel ASUAJE,	Professeur, Simon Bolívar University	Rapporteur
Kamel AZZOUZ,	Docteur, VALEO	Examineur
Farid BAKIR,	Professeur, Arts et Métiers	Examineur
Amélie DANLOS,	Maître de conférence, Le Cnam	Examineur
Richard PARIDAENS,	Docteur, Arts et Métiers	Examineur
Didier CHABIRAND,	Responsable R&D, LECTRA	Invité













Table of Contents

Table of Contents	iii
List of figures	vii
List of tables	xvii
1 Introduction	1
1.1 Background	1
1.1.1 History of centrifugal compressors	1
1.1.2 Working principle of a centrifugal compressor	2
1.1.3 Velocity triangles	2
1.1.4 Energy transfer in centrifugal compressors	3
1.2 Performance of centrifugal compressors	5
1.2.1 Slip factor	5
1.2.2 Dimensionless analysis	9
1.2.3 Pressure ratio	10
1.2.4 Efficiency	10
1.2.5 Compressor performance map	10
1.3 Applications of a counter-rotating system and state of art	11
1.3.1 Axial turbomachines	12
1.3.2 Centrifugal turbomachines	14
1.4 Motivation	17
2 Design of counter-rotating rotors	19
2.1 Reference rotor	19
2.2 Counter-rotating rotors design	20
2.2.1 First rotor design	21
2.2.2 Second rotor design	23
2.3 CRCC performance evaluation	26
2.3.1 Rotor performances	27
2.3.2 Compressor performances	31
2.3.3 Effect of speed ratio $\theta = N_1/N_2$	32
2.4 Conclusions	35
3 RAICOR test bench design	37
3.1 Introduction of the existing test bench	37
3.1.1 Description of the test bench operation	37
3.1.2 Performance map of the SRCC	37
3.2 CRCC components design	39
3.2.1 Adaptation with the existing test bench	39

3.2.2	CRCC test bench components design	42
3.3	RAICOR test bench	48
3.3.1	Description of Rotor - rotor Aerodynamic Interaction of a Counter-Rotating centrifugal compressor (RAICOR) test bench	48
3.3.2	Uncertainties and measurement quantities	49
3.3.3	Derived parameters	54
3.4	Conclusions	55
4	Experimental results	57
4.1	Limitation of the experiments	57
4.2	Global performance	57
4.2.1	First rotor rotates freely - second rotor is driven (case 1)	58
4.2.2	First rotor is fixed - second rotor is driven (case 2)	62
4.2.3	Counter-rotating mode (case 3)	64
4.2.4	Conclusions	69
4.3	Influence of rotation speed ratio (θ)	69
4.3.1	Effect of the speed ratio for a fixed speed of $N_2 = 9,000rpm$	70
4.3.2	Effect of the speed ratio for a fixed speed of $N_2 = 10,000rpm$	71
4.3.3	Effect of the speed ratio for a fixed speed of $N_2 = 11,000rpm$	72
4.3.4	Conclusions	73
4.4	Similarity method	78
4.4.1	Similarity method validation	78
4.4.2	CRCC characteristics at the design speed of $16,000rpm$	82
4.4.3	Conclusions	82
4.5	CFD Analysis	83
4.5.1	Meshing	83
4.5.2	Mesh sensitivity analysis	83
4.5.3	Validation of numerical simulation	85
4.5.4	Flow assessment	91
4.5.5	Conclusions	98
5	Instability control and Extension of the operating range	101
5.1	Introduction	101
5.2	Stability and instability control method	104
5.3	Extension of the operating range	113
5.4	CFD analysis in Co-rotating mode	116
5.5	Conclusions	119
6	Conclusions and perspectives	121
6.1	Summary	121
6.2	Design of counter-rotating rotors	121
6.3	Design of RAICOR test bench	121
6.4	Experimental results	122
6.4.1	Global performance	122
6.4.2	Influence of rotation speed ratio (θ)	122
6.4.3	Similarity method	123
6.4.4	CFD analysis	123
6.5	Instability control and extension of the operating range	124
6.6	Recommendations for future work	124

A APPENDIX	I
A.1 Dimensioning method of a centrifugal rotor	I
A.1.1 Inlet velocity triangles	I
A.1.2 Outlet velocity triangles	II
A.1.3 Tracing blades in a meridional view	V
A.1.4 Tracing blades in two views	VIII
A.2 Theory of similarity method	X
A.3 Instability control method	XV
A.3.1 Instability control at the speed of $N_2 = 10,000rpm$	XV
A.3.2 Instability control at the speed of $N_2 = 11,000rpm$	XXII
A.4 Numerical simulation	XXVII
A.4.1 Governing equations	XXVII
A.4.2 Turbulence model	XXIX
A.4.3 Motion	XXIX
A.4.4 Interface	XXX
A.4.5 Boundary condition	XXX
A.4.6 Solving strategies	XXXI
B Résumé de thèse	XXXIII
B.1 Introduction	XXXIV
B.2 Conceptions des rotors contrarotatif	XXXV
B.2.1 Conception du premier rotor	XXXVI
B.2.2 Conception du deuxième rotor	XXXVI
B.2.3 Évaluation des performances	XXXVIII
B.3 Banc d'essai RAICOR	XL
B.3.1 Adaptation avec le banc d'essai du compresseur conventionnel	XL
B.3.2 Banc d'essai RAICOR	XL
B.4 Résultats expérimentaux	XLI
B.4.1 Les limites des expérimentations	XLI
B.4.2 Performances globales du CRCC	XLII
B.4.3 Influence du rapport de vitesses du rotor (θ)	XLV
B.4.4 Étude de la similitude	XLVII
B.4.5 Analyse CFD	XLIX
B.5 Contrôle d'instabilités	LII
B.5.1 Méthode de contrôle d'instabilité	LII
B.5.2 Extension de la plage de fonctionnement	LIII
B.5.3 Analyse CFD en mode corotation	LVI
B.6 Conclusions	LVI
C List of acronyms	LIX
D List of Symbols	LXI

List of figures

1.1	Schematic diagram of a centrifugal compressor	2
1.2	Velocity triangles of the rotor at inlet (a) and outlet (b)	3
1.3	Diagram of a deviation of the flow velocity at the rotor outlet	6
1.4	Logarithmic Spiral Blades where β_b is constants for all radii [1]	7
1.5	Performance map of centrifugal compressors (<i>Source:wikipedia.org</i>)	11
1.6	Application of counter-rotating system on aircraft (a) Antonov AN-70 (Paris Air show 2013) and (b) P51 of North-American (<i>Source:wikipedia.org</i>)	12
1.7	Schematic diagram of Sirocco fan test bench [2]	15
1.8	Comparison of the performances between conventional and counter-rotating sirocco fan [2]	15
1.9	Characteristics of seven best geometries: (a) total to total head rise; (b) total to total efficiency [3]	16
1.10	Comparison between counter-rotating pump (left) and conventional pump (right) with the same working point and tip speed [4]	17
1.11	Comparison of performance between counter-rotating and conventional compressor (a) counter-rotating and conventional configuration; (b) Total pressure rise characteristics (c) Total to total efficiency characteristics [5]	18
2.1	Reference rotor designed by 3D Turbo software: (a) face view and (b) meridional view	20
2.2	Schematic diagram of counter-rotating system	21
2.3	Velocity triangles diagram are used to design the counter-rotating system: (a) face view and (b) meridional view	21
2.4	Four geometries of the first rotors studied for four configurations of CRCC: (a) CF1, (b) CF2, (c) CF3 and (d) CF4	24
2.5	Four geometries of the second rotors studied for four configurations of CRCC: (a) CF1, (b) CF2, (c) CF3, and (d) CF4	26
2.6	Sensitive mesh study for both compressor configurations:  -CRCC and  -SRCC	27
2.7	Different views of SRCC mesh: (a) section mesh, (b) blade leading edge mesh, (c) rotor mesh, and (d) full mesh model	28
2.8	Different view of CRCC mesh:(a) rotor mesh, (b) full mesh model, (c) section mesh, and (d) blade leading and trailing edge mesh	28
2.9	Comparison of pressure ratios at the outlet of the rotors between four CRCC configurations:  -CF1,  -CF2,  -CF3,  -CF4 and  -SRCC	29
2.10	Comparison of polytropic efficiencies at the outlet of the rotors between four CRCC configurations:  -CF1,  -CF2,  -CF3,  -CF4 and  -SRCC	29

2.11	Comparison of relative Mach numbers at the leading edge of the second rotor between four CRCC configurations: \ominus CF1, \boxminus CF2, \diamond CF3, \star CF4	30
2.12	Comparison of power consumptions between four CRCC configurations: \ominus CF1, \boxminus CF2, \diamond CF3, \star CF4 and \oplus SRCC	30
2.13	Comparison of pressure recovery coefficients between four CRCC configurations: \ominus CF1, \boxminus CF2, \diamond CF3, \star CF4 and \oplus SRCC	31
2.14	Comparison of pressure loss coefficients between four CRCC configurations: \ominus CF1, \boxminus CF2, \diamond CF3, \star CF4 and \oplus SRCC	32
2.15	Comparison of stage pressure ratios between four CRCC configurations: \ominus CF1, \boxminus CF2, \diamond CF3, \star CF4 and \oplus SRCC	33
2.16	Comparison of stage polytropic efficiencies between four CRCC configurations: \ominus CF1, \boxminus CF2, \diamond CF3, \star CF4 and \oplus SRCC	33
2.17	The change in pressure ratios of the CF1 with the different speed ratios : $\ominus\theta_1 = -1$, $\boxminus\theta_2 = -1.1$, $\diamond\theta_3 = -1.2$, $\star\theta_4 = -1.3$ compared to the pressure ratio of \oplus SRCC at $16,000rpm$	34
2.18	The change in polytropic efficiencies of the CF1 with the different speed ratios: $\ominus\theta_1 = -1$, $\boxminus\theta_2 = -1.1$, $\diamond\theta_3 = -1.2$, $\star\theta_4 = -1.3$ compared to the efficiency of \oplus SRCC at $16,000rpm$	34
2.19	The configuration 1 selected to build a counter-rotating centrifugal compressor	35
3.1	Centrifugal compressor test bench used to measure the SRCC performances	38
3.2	Performance map of SRCC obtained by experimental measurement	38
3.3	Comparison of performance between straight and bent inlet obtained by CFD simulations	39
3.4	Pressure distribution of (a) straight inlet and (b) bent inlet, at $\dot{m}_{cr} = 0.73kg/s$ and $N_1 = -16,000rpm$, $N_2 = 16,000rpm$ (best efficiency point)	40
3.5	Pressure distribution of (a) straight inlet and (b) bent inlet, at $\dot{m}_{cr} = 0.23kg/s$ and $N_1 = -16,000rpm$, $N_2 = 16,000rpm$ (near surge point)	41
3.6	Velocity field of (a) straight inlet and (b) bent inlet, $\dot{m}_{cr} = 0.73kg/s$ and $N_1 = -16,000rpm$, $N_2 = 16,000rpm$ (best efficiency point)	41
3.7	Velocity field of (a) straight inlet and (b) bent inlet, $\dot{m}_{cr} = 0.23kg/s$ and $N_1 = -16,000rpm$, $N_2 = 16,000rpm$ (near surge point)	42
3.8	Comparison of axial velocity between bent inlet and straight inlet at (a) best efficiency point and (b) near surge point	43
3.9	First rotor analysis of the chosen configuration (CF1) for the experimental test bench	44
3.10	Second rotor analysis of the chosen configuration (CF1) for the experimental test bench	44
3.11	Analysis of the drive shaft of the first rotor used for the CRCC test bench with (a) stress analysis and (b) displacement analysis	45
3.12	Geometry of Shroud block of the CRCC configuration of the test bench: (a) face view and (b) rear view	46
3.13	Geometry of the inlet block of the CRCC configuration used for the test bench (a) front view and (b) rear view	47
3.14	Geometry of the electric motor support of the CRCC configuration used for the test bench: (a) front view and (b) rear view	47

3.15 Counter-rotating centrifugal compressor (CRCC)	48
3.16 Schema of RAICOR test bench	49
3.17 Gaussian distribution (<i>source:www.nde-ed.org</i>)	50
3.18 Error of measurement	51
4.1 Global performance of CRCC (CR- θ_0 : counter-rotating in case 1) in comparison with SRCC at 9,000rpm	59
4.2 Electric power consumption of the CRCC second rotor (CR(P2)) in comparison with SRCC at 9,000rpm	59
4.3 Global performance of CRCC (CR- θ_0 : counter-rotating in case 1) in comparison with SRCC at 10,000rpm	60
4.4 Electric power consumption of the CRCC second rotor (CR(P2)) in comparison with SRCC at 10,000rpm	60
4.5 Global performance of CRCC (CR- θ_0 : Counter-rotating in case 1) in comparison with SRCC at 11,000rpm	61
4.6 Electric power consumption of CRCC (CR(P2)) in comparison with SRCC at 11,000rpm	61
4.7 The first rotor rotation speed (N_1) of CRCC according to the corrected mass flow rate for three rotation speeds of the second rotor: 9,000rpm, 10,000rpm and 11,000rpm	62
4.8 Comparison of global performances between case 1 (CR-free) and case 2 (CR-fix) with three rotation speed of 9,000rpm, 10,000rpm, 11,000rpm of the second rotor	63
4.9 Velocity triangles of CRCC with the first rotor is fixed (case 2)	63
4.10 Pressure fluctuations at the inlet of the first rotor (p_1) and between two rotors (p_{23}) of CRCC with the flow rate of 0.419kg/s and rotation speed of $N_2 = 9,000rpm$	64
4.11 Comparison of global performance of CRCC in counter-rotating mode with $N_1 = -9,000rpm$, $N_2 = 9,000rpm$ (CR - θ_4) and SRCC with $N = 9,000rpm$	65
4.12 Comparison of electric power consumption of CRCC: the first rotor (CR(P1)), the second rotor (CR(P2)), the counter-rotating rotor (CR(P_{total})) and SRCC at 9,000rpm	65
4.13 Comparison of the global performance of CRCC in counter-rotating mode with $N_1 = -10,000rpm$, $N_2 = 10,000rpm$ (CR - θ_4) and SRCC with $N = 10,000rpm$	67
4.14 Comparison of electric power consumption of CRCC: the first rotor (CR(P1)), the second rotor (CR(P2)), the counter-rotating rotor (CR(P_{total})) and SRCC at 10,000rpm	67
4.15 Comparison of global performance of CRCC in counter-rotating mode with $N_1 = -11,000rpm$, $N_2 = 11,000rpm$ (CR - θ_4) and SRCC with $N = 11,000rpm$	68
4.16 Comparison of the electric power consumption of CRCC: the first rotor (CR(P1)), the second rotor (CR(P2)), the counter-rotating rotor (CR(P_{total})) and SRCC at 11,000rpm	68
4.17 Influence of speed ratio on the performances of CRCC (solid lines) with $N_2 = 9,000rpm$ in comparison with the performances of SRCC (dashed lines) at $N = 9,000rpm$ and $N = 11,000rpm$: (a) Pressure ratio and (b) Polytropic efficiency	74

4.18	Influence of speed ratio on the performances of CRCC (solid lines) with $N_2 = 10,000rpm$ in comparison with the performances of SRCC (dashed lines) at $N = 10,000rpm$ and $N = 12,000rpm$: (a) Pressure ratio and (b) Polytropic efficiency	75
4.19	Influence of speed ratio on the performances of CRCC (solid lines) with $N_2 = 11,000rpm$ in comparison with the performances of SRCC (dashed lines) at $N = 11,000rpm$ and $N = 13,000rpm$: (a) Pressure ratio and (b) Polytropic efficiency	76
4.20	Performance map of (a) CRCC and (b) SRCC with the rotation speed changes in range of $[9,000rpm\ 13,000rpm]$	77
4.21	Non-dimensional characteristics of CRCC with different speed ratios are obtained by experiment at the second rotor speed of $10,000rpm$	78
4.22	Comparison between the similarity method and the experimental results for CRCC in case of a second rotor rotating at $9,000rpm$	80
4.23	Comparison between the similarity method and the experimental results for CRCC in case of a second rotor rotating at $11,000rpm$	81
4.24	Characteristics of CRCC calculated by the similarity method at the design speed of $16,000rpm$ with different speed ratios	82
4.25	Different mesh domains used for the numerical simulation of CRCC	84
4.26	Different views of the CRCC mesh model	84
4.27	Distribution of wall $y+$ at the best efficiency point ($\dot{m}_{cor} = 0.531kg/s$, $N_1 = -10,000rpm$, $N_2 = 10,000rpm$)	85
4.28	Diagram of the surfaces measuring pressure (P) and temperature (T) and location of pressure probes used for simulation	86
4.29	Comparison of CRCC performances between numerical results (blue line) and experimental measurements (black points) with $N_2 = 9,000rpm$ and seven speed ratios θ	88
4.30	Comparison of CRCC performances between numerical results (blue line) and experimental measurements (black points) with $N_2 = 10,000rpm$ and seven speed ratios θ	89
4.31	Comparison of CRCC performances between numerical results (blue line) and experimental measurements (black points) with $N_2 = 11,000rpm$ and seven speed ratios θ	90
4.32	Pressure distribution of CRCC at two operating points: BEP and NIP on three equipotential surfaces located at 0.25, 0.5 and 0.75span	92
4.33	Relative Mach number distribution of CRCC at two operating points: BEP and NIP on three equipotential surfaces located at 0.25, 0.5 and 0.75span	92
4.34	Relative velocity streamline of CRCC at two operating points: BEP and NIP on three equipotential surfaces located at 0.25, 0.5 and 0.75span	93
4.35	3D visualization of streamlines on the equipotential surface located at 0.5span with $N_2 = 10,000rpm$ and $\dot{m}_{cr} = 0.543kg/s$ (BEP)	94
4.36	3D visualization of streamlines on the equipotential surface located at 0.5span with $N_2 = 10,000rpm$ and $\dot{m}_{cr} = 0.233kg/s$ (NIP). The vortices are numbered from (1) to (5) in the opposite direction to the second rotor rotation	94
4.37	Meridian velocity distribution for (a) BEP with $N_2 = 10,000rpm$ and $\dot{m}_{cr} = 0.543kg/s$ and (b) NIP with $N_2 = 10,000rpm$ and $\dot{m}_{cr} = 0.233kg/s$	95

4.38	Temperature distribution of CRCC at two operating points: BEP and NIP on three equipotential surfaces located at 0.25, 0.5 and 0.75span	96
4.39	Sequential flow-visualization of the flow velocity for BEP with $N_1 = -10,000rpm$, $N_2 = 10,000rpm$ and $\dot{m}_{cr} = 0.543kg/s$	97
4.40	Sequential streamline flow-visualization for NIP with $N_1 = -10,000rpm$, $N_2 = 10,000rpm$ and $\dot{m}_{cr} = 0.233kg/s$	97
4.41	Wall pressure fluctuation and FFT transform of CFD simulation with $N_1 = -10,000rpm$, $N_2 = 10,000rpm$, and $\dot{m}_{cr} = 0.543kg/s$	98
5.1	Schematic diagrams of (a) mild surge and (b) deep surge [6]	102
5.2	Compressor map with desired instability improvement	103
5.3	Controlling the stability limit points to enlarge the operating range of CRCC with $N_2 = 9,000rpm$ by reducing the first rotor speed (N_1)	105
5.4	The velocity triangles of a Co-rotating mode	106
5.5	Characteristic curves of CRCC at different speed ratios without the unstable working points by reducing the rotation speed of the first rotor while the second rotor speed is fixed $N_2 = 9,000rpm$ compared to the characteristic of SRCC at $9,000rpm$ (REF-9krpm)	107
5.6	The variation of first rotor speed for suppressing the instability phenomenon at $N_2 = 9,000rpm$	108
5.7	The pressure signals (a) and its FFT analysis: (b) at the inlet and (c) between two rotors of the point P8 with $N_1 = -11,700rpm$ and $N_2 = 9,000rpm$	108
5.8	The pressure signals (a) and its FFT analysis at the inlet (b) and between two rotors (c) of the point P9 with $N_1 = -11,700$ and $N_2 = 9,000rpm$	108
5.9	The pressure signals (a) and its FFT analysis at the inlet (b) and between two rotors (c) of the point P10 with $N_1 = -10,500rpm$ and $N_2 = 9,000rpm$	109
5.10	The pressure signals (a) and its FFT analysis at the inlet (b) and between two rotors (c) of the point P11 with $N_1 = -9,540rpm$ and $N_2 = 9,000rpm$	109
5.11	The pressure signals (a) and its FFT analysis at the inlet (b) and between two rotors (c) of the point P12 with $N_1 = -8,880rpm$ and $N_2 = 9,000rpm$	109
5.12	The pressure signals (a) and its FFT analysis at the inlet (b) and between two rotors (c) of the point P13 with $N_1 = -8,880rpm$ and $N_2 = 9,000rpm$	109
5.13	The pressure signals (a) and its FFT analysis at the inlet (b) and between two rotors (c) of the point P14 with $N_1 = -7,740rpm$ and $N_2 = 9,000rpm$	110
5.14	The pressure signals (a) and its FFT analysis at the inlet (b) and between two rotors of the point P15 with $N_1 = -6,240rpm$ and $N_2 = 9,000rpm$	110
5.15	The pressure signals (a) and its FFT analysis at the inlet (b) and between two rotors (c) of the point P16 with $N_1 = -6,240rpm$ and $N_2 = 9,000rpm$	110
5.16	The pressure signals (a) and its FFT analysis at the inlet (b) and between two rotors (c) of the point P17 with $N_1 = -4,920rpm$ and $N_2 = 9,000rpm$	110
5.17	The pressure signals (a) and its FFT analysis at the inlet (b) and between two rotors (c) of the point P18 with $N_1 = -3,900rpm$ and $N_2 = 9,000rpm$	111
5.18	The pressure signals (a) and its FFT analysis at the inlet (b) and between two rotors (c) of the point P19 with $N_1 = -3,900rpm$ and $N_2 = 9,000rpm$	111
5.19	The pressure signals (a) and its FFT analysis at the inlet (b) and between two rotors (c) of the point P20 with $N_1 = 0rpm$ and $N_2 = 9,000rpm$	111

5.20	The pressure signals (a) and its FFT analysis at the inlet (b) and between two rotors (c) of the point P21 with $N_1 = 1200rpm$ and $N_2 = 9,000rpm$	111
5.21	The pressure signals (a) and its FFT analysis at the inlet (b) and between two rotors (c) of the point P22 with $N_1 = 1200rpm$ and $N_2 = 9,000rpm$	112
5.22	The pressure signals (a) and its FFT analysis at the inlet (b) and between two rotors (c) of the point P23 with $N_1 = 2940rpm$ and $N_2 = 9,000rpm$	112
5.23	The pressure signals (a) and its FFT analysis at the inlet (b) and between two rotors (c) of the point P24 with $N_1 = 4140rpm$ and $N_2 = 9,000rpm$	112
5.24	The pressure signals (a) and its FFT analysis at the inlet (b) and between two rotors (c) of the point P25 with $N_1 = 4140rpm$ and $N_2 = 9,000rpm$	112
5.25	The pressure signals (a) and its FFT analysis at the inlet (b) and between two rotors (c) of the point P26 with $N_1 = 5400rpm$ and $N_2 = 9,000rpm$	113
5.26	Three performance curves C_1 (\blacksquare), C_2 (\bullet) and C_3 (\blacktriangle) of CRCC in comparison with those of SRCC at three rotation speeds of $9,000rpm$ (\blacksquare), $10,000rpm$ (\ominus) and $11,000rpm$ (\blacktriangle)	114
5.27	Power consumptions of three characteristic curves C_1 (\blacksquare), C_2 (\bullet) and C_3 (\blacktriangle) of CRCC in comparison with those of SRCC at three rotation speeds of $9,000rpm$ (\blacksquare), $10,000rpm$ (\ominus) and $11,000rpm$ (\blacktriangle)	115
5.28	The relation between coupled rotation speed of two rotors and corrected mass flow rate (black dashed line), pressure ratio (white solid line), polytropic efficiency (colored region) in case of expanding the operating range	116
5.29	Pressure distribution at ESLP with $N_1 = 6,420rpm$, $N_2 = 12,000rpm$ and $\dot{m}_{cr} = 0.08kg/s$ on three equipotential surfaces located at 0.25, 0.5 and 0.75span	117
5.30	Flow structure at ESLP with $N_1 = 6,420rpm$, $N_2 = 12,000rpm$ and $\dot{m}_{cr} = 0.08kg/s$	117
5.31	Temperature distribution at ESLP with $N_1 = 6,420rpm$, $N_2 = 12,000rpm$ and $\dot{m}_{cr} = 0.08kg/s$ on three equipotential surfaces located at 0.25, 0.5 and 0.75span	118
5.32	Relative Mach number distribution at ESLP with $N_1 = 6,420rpm$, $N_2 = 12,000rpm$ and $\dot{m}_{cr} = 0.08kg/s$ on three equipotential surfaces located at 0.25, 0.5 and 0.75span	118
6.1	Three configurations with three value of LR: 0.3, 0.4 and 0.5 need to experimental study in the future	124
6.2	The first rotor with the different outlet blade angles: (a) radial angle and (b) forward angle of the configuration 1	125
A.1	Cordier diagram	III
A.2	Velocity triangles at the outlet of a rotor	IV
A.3	Definition of (a) mean line and (b) correction factor K_m	IV
A.4	Influence of slip factor on the outlet velocity triangles	V
A.5	Evolution and regularity of the meridian surface according to the horizontal curvilinear	VI
A.6	Tracing hub and shroud contours	VII
A.7	Definition of leading and trailing edge for a high specific speed rotor	VII
A.8	Set of geometries elements used to draw the blade: (a) meridian view, (b) mean stream surface, (c) front view and (d) developed blade angle	IX
A.9	Definition of the developed blade angle	X

A.10 Similar velocity triangles of two turbomachines of the same family . . .	XII
A.11 Controlling the stability limit points to enlarge the operating range of CRCC with $N_2 = 10,000rpm$ by varying the first rotor speed (N_1) . . .	XV
A.12 The pressure signals (a) and its FFT analysis at the inlet (b) and between two rotors (c) of the point P10 with $N_1 = -13,000rpm$ and $N_2 = 10,000rpm$	XVI
A.13 The pressure signals (a) and its FFT analysis at the inlet (b) and between two rotors (c) of the point P11 with $N_1 = -13,000rpm$ and $N_2 = 10,000rpm$	XVI
A.14 The pressure signals (a) and its FFT analysis at the inlet (b) and between two rotors (c) of the point P12 with $N_1 = -11,200rpm$ and $N_2 = 10,000rpm$	XVI
A.15 The pressure signals (a) and its FFT analysis at the inlet (b) and between two rotors (c) of the point P13 with $N_1 = -11,200rpm$ and $N_2 = 10,000rpm$	XVI
A.16 The pressure signals (a) and its FFT analysis at the inlet (b) and between two rotors (c) of the point P14 with $N_1 = -10,000rpm$ and $N_2 = 10,000rpm$	XVII
A.17 The pressure signals (a) and its FFT analysis at the inlet (b) and between two rotors (c) of the point P15 with $N_1 = -8,200rpm$ and $N_2 = 10,000rpm$	XVII
A.18 The pressure signals (a) and its FFT analysis at the inlet (b) and between two rotors (c) of the point P16 with $N_1 = -6,400rpm$ and $N_2 = 10,000rpm$	XVII
A.19 The pressure signals (a) and its FFT analysis at the inlet (b) and between two rotors (c) of the point P17 with $N_1 = -4,600rpm$ and $N_2 = 10,000rpm$	XVII
A.20 The pressure signals (a) and its FFT analysis at the inlet (b) and between two rotors (c) of the point P18 with $N_1 = -2,800rpm$ and $N_2 = 10,000rpm$	XVIII
A.21 The pressure signals (a) and its FFT analysis at the inlet (b) and between two rotors (c) of the point P19 with $N_1 = -2,200rpm$ and $N_2 = 10,000rpm$	XVIII
A.22 The pressure signals (a) and its FFT analysis at the inlet (b) and between two rotors (c) of the point P20 with $N_1 = -2,200rpm$ and $N_2 = 10,000rpm$	XVIII
A.23 The pressure signals (a) and its FFT analysis at the inlet (b) and between two rotors (c) of the point P21 with $N_1 = 0rpm$ and $N_2 = 10,000rpm$	XVIII
A.24 The pressure signals (a) and its FFT analysis at the inlet (b) and between two rotors (c) of the point P22 with $N_1 = 1,400rpm$ and $N_2 = 10,000rpm$	XIX
A.25 The pressure signals (a) and its FFT analysis at the inlet (b) and between two rotors (c) of the point P23 with $N_1 = 2,660rpm$ and $N_2 = 10,000rpm$	XIX
A.26 The pressure signals (a) and its FFT analysis at the inlet (b) and between two rotors (c) of the point P24 with $N_1 = 2,660rpm$ and $N_2 = 10,000rpm$	XIX
A.27 The pressure signals (a) and its FFT analysis at the inlet (b) and between two rotors (c) of the point P25 with $N_1 = 4,460rpm$ and $N_2 = 10,000rpm$	XIX
A.28 The pressure signals (a) and its FFT analysis at the inlet (b) and between two rotors (c) of the point P26 with $N_1 = 5,240rpm$ and $N_2 = 10,000rpm$	XX

A.29	The pressure signals (a) and its FFT analysis at the inlet (b) and between two rotors (c) of the point P27 with $N_1 = 5,240rpm$ and $N_2 = 10,000rpm$	XX
A.30	The pressure signals (a) and its FFT analysis at the inlet (b) and between two rotors (c) of the point P28 with $N_1 = 6,260rpm$ and $N_2 = 10,000rpm$	XX
A.31	Characteristic curves of CRCC at different speed ratios without the unstable working points by reducing the rotation speed of the first rotor while the second rotor speed is fixed at $N_2 = 10,000rpm$ compared to the characteristic curve of SRCC at $10,000rpm$ (REF-10krpm)	XXI
A.32	The variation of the first rotor speed for suppressing the instability phenomenon at the speed of $N_2 = 10,000rpm$	XXI
A.33	Controlling the instability limit points to enlarge the operating range of CRCC with $N_2 = 11,000rpm$ by varying the first rotor speed (N_1) . . .	XXII
A.34	The pressure signals (a) and its FFT analysis at the inlet (b) and between two rotors (c) of the point P9 with $N_1 = -14,300rpm$ and $N_2 = 11,000rpm$	XXII
A.35	The pressure signals (a) and its FFT analysis at the inlet (b) and between two rotors (c) of the point P10 with $N_1 = -14,300rpm$ and $N_2 = 11,000rpm$	XXIII
A.36	The pressure signals (a) and its FFT analysis at the inlet (b) and between two rotors (c) of the point P11 with $N_1 = -12,500rpm$ and $N_2 = 11,000rpm$	XXIII
A.37	The pressure signals (a) and its FFT analysis at the inlet (b) and between two rotors (c) of the point P12 with $N_1 = -10,640rpm$ and $N_2 = 11,000rpm$	XXIII
A.38	The pressure signals (a) and its FFT analysis at the inlet (b) and between two rotors (c) of the point P13 with $N_1 = -10,640rpm$ and $N_2 = 11,000rpm$	XXIII
A.39	The pressure signals (a) and its FFT analysis at the inlet (b) and between two rotors (c) of the point P14 with $N_1 = -8,660rpm$ and $N_2 = 11,000rpm$	XXIV
A.40	The pressure signals (a) and its FFT analysis at the inlet (b) and between two rotors (c) of the point P15 with $N_1 = -6,140rpm$ and $N_2 = 11,000rpm$	XXIV
A.41	The pressure signals (a) and its FFT analysis at the inlet (b) and between two rotors (c) of the point P16 with $N_1 = -5,120rpm$ and $N_2 = 11,000rpm$	XXIV
A.42	The pressure signals (a) and its FFT analysis at the inlet (b) and between two rotors (c) of the point P17 with $N_1 = -5,120rpm$ and $N_2 = 11,000rpm$	XXIV
A.43	The pressure signals (a) and its FFT analysis at the inlet (b) and between two rotors (c) of the point P18 with $N_1 = -2,720rpm$ and $N_2 = 11,000rpm$	XXV
A.44	The pressure signals (a) and its FFT analysis at the inlet (b) and between two rotors (c) of the point P19 with $N_1 = 0rpm$ and $N_2 = 11,000rpm$	XXV
A.45	The pressure signals (a) and its FFT analysis at the inlet (b) and between two rotors (c) of the point P20 with $N_1 = 2,700rpm$ and $N_2 = 11,000rpm$	XXV
A.46	The pressure signals (a) and its FFT analysis at the inlet (b) and between two rotors (c) of the point P21 with $N_1 = 2,700rpm$ and $N_2 = 11,000rpm$	XXV

A.47	The pressure signals (a) and its FFT analysis at the inlet (b) and between two rotors (c) of the point P22 with $N_1 = 6,420rpm$ and $N_2 = 11,000rpm$	XXVI
A.48	The pressure signals (a) and its FFT analysis at the inlet (b) and between two rotors (c) of the point P23 with $N_1 = 7,080rpm$ and $N_2 = 11,000rpm$	XXVI
A.49	Characteristic curves of CRCC at different speed ratios without the unstable working points by reducing the rotation speed of the first rotor while the second rotor speed is fixed at $N_2 = 11,000rpm$ compared to the characteristic curve of SRCC at $11,000rpm$ (REF-11krpm)	XXVI
A.50	The variation of the first rotor speed for suppressing the instability phenomenon at the speed of $N_2 = 11,000rpm$	XXVII
B.1	La structure du compresseur centrifuge contrarotatif (CRCC)	XXXV
B.2	Schéma du triangle des vitesses du CRCC: (a) vue de face et (b) vue méridien	XXXVI
B.3	Schéma des quatre géométries de premier rotor étudiés pour les autres configurations de CRCC : (a) CF1,(b) CF2, (c) CF3 et (d) CF4	XXXVII
B.4	Schéma des quatre géométries de deuxième rotor étudiés pour les autres configurations de CRCC : (a) CF1,(b) CF2, (c) CF3 et (d) CF4	XXXVIII
B.5	Comparaison des taux de compression des quatre configurations de CRCC	XXXIX
B.6	Comparaison des rendements polytropiques des quatre configurations de CRCC	XL
B.7	Schéma du banc d'essai RAICOR utilisé pour l'étude des compresseur CRCC	XLI
B.8	Comparaison des performances globales de CRCC dans le cas 1 (premier rotor en rotation libre et deuxième rotor entraîné) et SRCC (en noir et lignes pointillées) aux vitesses de rotation $9\,000\ tr/min$, $10\,000\ tr/min$ et $11\,000\ tr/min$	XLII
B.9	Schéma du triangle des vitesses de CRCC avec le premier rotor fixe (cas 2)	XLIII
B.10	Comparaison des performances entre le premier rotor en rotation libre (CR-free: cas 1, en noir et lignes pointillées) et fixe (CR-Fix: cas 2, en couleur et lignes continues) avec le deuxième rotor tournant aux vitesses de rotation $9\,000\ tr/min$, $10\,000\ tr/min$ et $11\,000\ tr/min$	XLIV
B.11	Comparaison des performances globales de CRCC et SRCC dans le cas 3	XLV
B.12	Comparaison des performances et des plages de fonctionnement entre (a) SRCC avec $9\,000\ tr/min \leq N \leq 13\,000\ tr/min$ et (b) CRCC avec différents rapports de vitesse tandis que $9\,000\ tr/min \leq N_2 \leq 11\,000\ tr/min$	XLVI
B.13	Caractéristiques adimensionnées de CRCC avec différents rapports de vitesses obtenues expérimentalement avec une vitesse de deuxième rotor fixée à $10\,000\ tr/min$	XLVIII
B.14	Caractéristiques de CRCC calculées par la méthode de similitude à la vitesse de $16\,000\ tr/min$ avec différents rapports de vitesses	XLVIII
B.15	Domaines de maillages des différent blocs de CRCC utilisés pour les simulations numériques	XLIX
B.16	Détails des maillages du rotor dans différentes vues	L
B.17	Visualisation 3D des lignes de courant au point BEP du compresseur CRCC avec $N_1=10\,000\ tr/min$, $N_2=10\,000\ tr/min$ et $\dot{m}_{cr}=0.543\ kg/s$	L

B.18	Visualisation 3D des lignes de courant au point NIP du compresseur CRCC avec $N_1=10\ 000\ tr/min$, $N_2=10\ 000\ tr/min$ et $\dot{m}_{cr}=0.27\ kg/s$	LI
B.19	Visualisation séquentielle des lignes de courant au point NIP avec $N_1=10\ 000\ tr/min$, $N_2=10\ 000\ tr/min$ et $\dot{m}_{cr}=0.27\ kg/s$. Les nombres représentent l'ordre des tourbillons dans les passages inter-aubes et ils se déplacent dans le sens de rotation dans le temps.	LI
B.20	Étude du contrôle de la vitesse du premier rotor pour une vitesse du deuxième rotor fixée à $9\ 000\ tr/min$ pour repousser l'apparition du phénomène d'instabilités de CRCC	LII
B.21	Variation de la vitesse du premier rotor pour repousser la limite d'apparition des instabilités à faibles débit de CRCC pour un rapport de vitesse θ_7 et $N_2 = 9\,000rpm$	LIII
B.22	Comparaison des courbes de performances C_1 (■), C_2 (●) et C_3 (▲) de CRCC par rapport aux courbes de performance de SRCC pour les trois vitesses $9\ 000\ tr/min$ (■), $10\ 000\ tr/min$ (●) et $11\ 000\ tr/min$ (▲)	LIV
B.23	Consommation électrique des courbes de performances C_1 (■), C_2 (●) et C_3 (▲) de CRCC et de SRCC pour les vitesses $9\ 000\ tr/min$ (■), $10\ 000\ tr/min$ (●) et $11\ 000\ tr/min$ (▲)	LIV
B.24	Les relations entre les vitesses des deux rotors et le rendement polytropique (la couleur), le débit massique corrigé (la ligne pointillée), et le taux de pression (la ligne continue) en cas d'extension de la plage de fonctionnement	LV
B.25	Structure d'écoulement au point ESLP en mode co-rotatif avec $N_1=6240\ tr/min$, $N_2=12\ 000\ tr/min$ et $\dot{m}_{cr}=0,08\ kg/s$	LVI

List of tables

2.1	Geometric paramters of SRCC	19
2.2	Design parameters for CRCC	20
2.3	Geometric parameters of the first rotor of four CRCC configurations CF1, CF2, CF3, and CF4	24
2.4	Geometric parameters of the second rotor of four configurations CF1, CF2, CF3, and CF4	26
3.1	Modal analysis of the drive shaft	45
3.2	Modal analysis of shroud block	46
3.3	Modal analysis of inlet block	47
3.4	Modal analysis of electric motor support	48
4.1	Global performance of CRCC and SRCC at the best efficiency points with the different speed ratios and $N_2 = 9,000rpm$	71
4.2	Global performance of CRCC and SRCC at the best efficiency points with the different speed ratios and $N_2 = 10,000rpm$	72
4.3	Global performance of CRCC and SRCC at the best efficiency points with the different speed ratios and $N_2 = 11,000rpm$	73
4.4	The study of mesh sensitivity	85
4.5	Simulation parameters	85
4.6	Operating parameters of BEP and NIP	91
A.1	Independent variables	XI
A.2	Dependent variables	XI
B.1	Paramètres géométriques du premier rotor des quatre configurations de CRCC: CF1, CF2, CF3 et CF4	XXXVII
B.2	Paramètres géométriques du deuxième rotor des quatre configurations de CRCC: CF1, CF2, CF3 et CF4	XXXVIII

Remerciements

Je tiens tout d'abord à remercier mon directeur de thèse Professeur Farid BAKIR et mes deux encadrants Docteur Amélie DANLOS et Docteur Richard PARIDAENS pour m'avoir aidé pendant ces quatre années. Mes remerciements s'adressent ensuite aux membres du jury : Professeur Xavier CARBONNEAU pour avoir présidé ma soutenance et examiné mon rapport, Professeur Pascal CHESSE et Professeur Miguel ASUAJE pour avoir accepté de rapporter mon manuscrit de thèse. Enfin, je remercie l'examineur Docteur Kamel AZZOUZ, Directeur métiers thermiques et thermodynamiques chez VALEO et l'invité Monsieur Didier CHABIRAND, Responsable études avancées et recherche chez LECTRA, qui se sont intéressés à mes travaux.

Mes remerciements s'adressent également à Monsieur Moises SOLIS, qui m'a aidé dans la conception du banc d'essai et dans les simulations numériques. Je remercie aussi Monsieur Sébastien PORCHERON, qui m'a aidé dans l'installation du banc d'essai de bonne qualité.

Je pense également à tous ceux avec qui j'ai partagé des moments agréables. Sofiane KHELLADI, Florent RAVELET, Ricardo NOGUERA, Michael DELIGANT, Michael PEREIRA, Carole PETUREAUX qui sont des membres permanents du laboratoire LIFSE. Mes pensées vont également à tous les docteurs : Ivan DOBREV et Pierre PODEVIN ; à tous les techniciens et assistant ingénieur : Emmanuel QUEVEN, Jocelyn MISTIGRES, Marc JOULIN ; à mes collègues doctorants : Birame SY, Cheikh Brahim ABED, Dinh DANG VU, Charles FOULQUIE, Carlos ROMERO CASADO, Killian CROCI, Navideh ABBASNEZHAD, Tchable-Nan DJANAME, Aurélie NICOLAU, Abdenour MENAA, MAGNE Théodor, Jianfei SONG du laboratoire. Je remercie également ma famille pour m'avoir soutenu pendant la thèse.

Résumé

Dans le domaine des turbomachines, les systèmes contrarotatifs sont utilisés depuis le 20^e siècle. L'étude de l'application de ce type de systèmes montre de nombreux avantages : par exemple, l'amélioration des performances, la réduction de l'encombrement et de la masse, l'augmentation de l'efficacité de la poussée, etc. Cependant, ce système n'a pour le moment encore jamais été appliqué pour créer un compresseur centrifuge. Cette thèse présente une configuration de compresseur centrifuge utilisant un système contrarotatif appelé Compresseur Centrifuge Contrarotatif (CRCC pour Counter-Rotating Centrifugal Compressor en anglais). L'objectif de la thèse est d'étudier d'une part l'effet du système contrarotatif sur les performances du compresseur centrifuge, et d'autre part l'influence du système sur la zone de pompage lorsque le débit massique est très faible. Pour concevoir ce CRCC, un compresseur centrifuge conventionnel est sélectionné comme machine de référence. La roue de cette machine est remplacée par un ensemble de deux roues qui tournent en sens inverse, de même taille que la référence. Les autres composants de la machine de référence sont préservés. Ces deux rotors sont conçus sur la base d'un rapport de longueur dans la vue méridienne. L'angle des aubes des rotors est calculé en fonction des relations aérodynamiques. Le banc d'essai RAICOR (Rotor-rotor Aerodynamic Interaction of a COunter-Rotating centrifugal compressor) est développé et conçu à partir du banc d'essai du compresseur centrifuge conventionnel, au LIFSE (Laboratoire d'Ingénierie des Fluides et des Systèmes Energétiques). L'étude expérimentale montre que l'utilisation d'un système contrarotatif améliore non seulement les performances du compresseur à des vitesses de rotation inférieures à la vitesse de conception, mais diminue aussi la zone de pompage. Le compresseur fonctionnant en mode contrarotatif offre un meilleur taux de compression ainsi qu'un meilleur rendement que le compresseur conventionnel. De plus, la machine contrarotative peut fonctionner à une vitesse périphérique inférieure à celle du compresseur de référence tout en ayant les mêmes performances. Pour améliorer la zone de pompage, un mode de co-rotation (les deux rotors tournent dans le même sens de rotation) est adopté pour permettre au compresseur de fonctionner à un débit inférieur à celui du compresseur de référence. La limite du pompage est alors repoussée jusqu'à 24%-28% de la plage de fonctionnement du compresseur, vers les débits plus faibles. Le point limite est atteint lorsque la vitesse de rotation du rotor en amont est comprise entre 48% et 64% de celle du rotor en aval. Les résultats de cette étude jouent un rôle important dans le développement d'une nouvelle génération de compresseur centrifuge pouvant fonctionner sous un très faible débit massique.

Mots-clés : Contrarotatif, co-rotatif, interaction rotor-rotor, compresseur centrifuge, améliorer du pompage.

Abstract

In the field of turbomachinery, counter-rotating systems have been used since the 20th century. Studying the application of this type of system shows many advantages: for example, improving performance, reducing overall dimensions and weight, increasing thrust efficiency, etc. However, this system has never yet been applied until now to create a centrifugal compressor. This thesis presents a configuration of a centrifugal compressor using a counter-rotating system called Counter-Rotating Centrifugal Compressor (CRCC). The objective of this thesis is to study the effect of the counter-rotating system on the performance of the centrifugal compressor, and the ability to extend an operating range to an instability region at a very low mass flow. To design the CRCC configuration, a conventional centrifugal compressor is selected as the reference machine. Its single rotor is replaced by a set of two rotors that rotate in opposite directions, the same size as the reference. The other components of the reference machine are preserved. These two rotors are designed based on a length ratio parameter in the meridian view. The blade angles of the rotors are calculated as a function of the aerodynamic relationships. A RAICOR (Rotor-rotor Aerodynamic Interaction of a COunter-Rotating centrifugal compressor) test bench is developed and designed from a test bench of the conventional centrifugal compressor, at LIFSE (Laboratoire d'Ingénierie des Fluides et des Systèmes Energétiques). Experimental results show that the use of a counter-rotating system not only improves the performance of the compressor at rotational speeds lower than the design speed but also decreases the instability region. The compressor operating in counter-rotating mode gives a better pressure ratio as well as a better efficiency than the conventional compressor. In addition, the counter-rotating machine can operate at a peripheral velocity lower than that of the reference compressor while having the same performance. A co-rotation mode (the two rotors rotate in the same direction) is adopted to allow the compressor to operate at a lower flow rate than that of the reference compressor. The instability limit of the compressor is then pushed back from 24% to 28% of the operating range, towards the lower flow rates. The limit point is reached when the upstream rotor speed is between 48% and 64% of the downstream rotor speed. The results of this study play an important role in the development of a new generation of centrifugal compressor that can operate at a very low mass flow rate.

Keywords : Counter-rotating, co-rotating, centrifugal compressor, rotor-rotor interaction, control instability phenomenon.

Chapter 1

Introduction

Contents

1.1	Background	1
1.2	Performance of centrifugal compressors	5
1.3	Applications of a counter-rotating system and state of art	11
1.4	Motivation	17

1.1 Background

A COMPRESSOR is a device used to pressurize a working fluid and deliver it at a higher pressure than its initial pressure. It is commonly used in industry for various purposes such as: providing air for combustion, compressing air for driving pneumatic tools, circulating fluid through a certain process, etc.

1.1.1 History of centrifugal compressors

The turbomachinery has existed for several centuries, but it is optimized and rapidly developed in the 20th century. The invention of a centrifugal compressor started with the idea of using centrifugal force to lift the liquid by Leonardo Da Vinci(1452-1519)[7]. In 1689, Denis Papin had a major contribution to the concept of creating the free forced vortex within a circular, or spiral casing by means of blades. Following that, in 1754 Euler presented an idealized theoretical application of Newton's law to centrifugal rotor based on a conceptualization of his backward tubular turbine is known as the "Euler equation". A French professor, Auguste Rateau, produced the first centrifugal compressor. His prototype consists of a single-stage which could compress $0.5m^3/s$ of atmospheric air to a discharge pressure of $1.5bar$ at a rotational speed of $20,000rpm$ [8]. After that, to meet the demand of users for compressors with higher pressure, many generations of compressors with one or multi-stage were developed. It led to the rapid development of the design method. Along with this, the evolution of information technology, especially the advancement of programmed computers at the end of 20th century, has helped to design and develop the compressor quickly and accurately with high efficiency.

1.1.2 Working principle of a centrifugal compressor

A centrifugal compressor generally consists of four components named inlet, rotor, diffuser, and collector (or volute). The fluid flows through the compressor by a fast rotating rotor. The velocity of the fluid is converted into pressure, partially in the rotor and partially in the stationary diffuser and the volute. Typically, the centrifugal compressor is designed with a half pressure rise takes place in the rotor and the other one in the diffuser. A structure of a conventional centrifugal compressor is presented in figure 1.1.

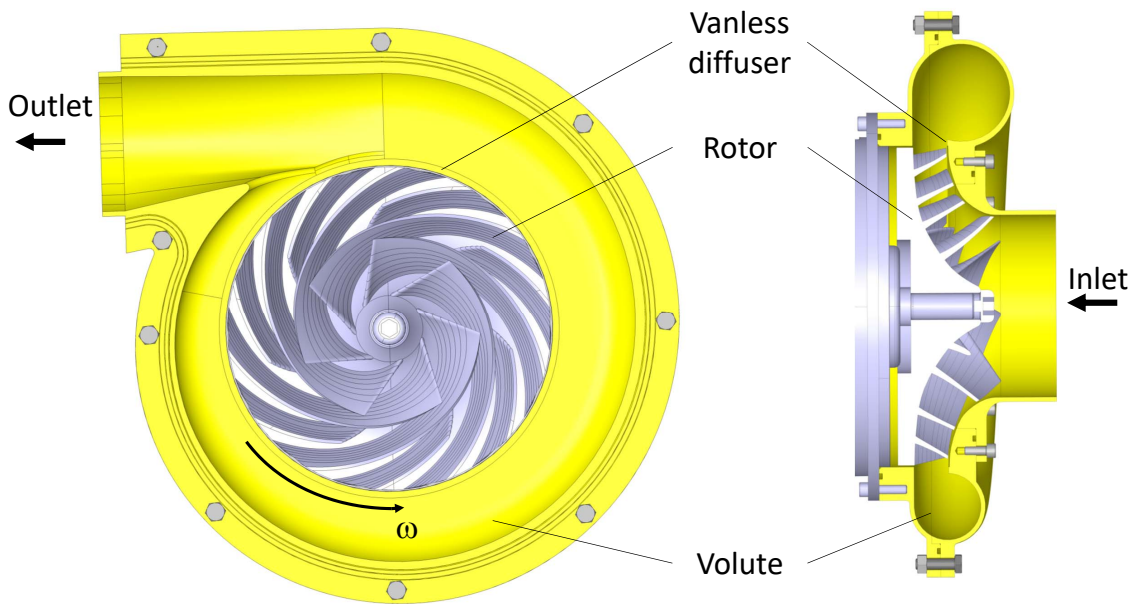


FIGURE 1.1 – Schematic diagram of a centrifugal compressor

The most important component of a centrifugal compressor is a **rotor** which provides energy to the fluid and thereby raises the angular momentum. Through the rotor, the flow direction changes from axial to radial direction with increasing static pressure and velocity. After leaving the rotor, the fluid flows into expanded space called a **diffuser** in which the kinetic energy of the fluid is converted into pressure energy. So, the pressure rises rapidly while the velocity decreases. Finally, the **volute** collects the fluid from the diffuser and delivers it to the outlet pipe. To understand the energy transformation process in a centrifugal compressor, velocity triangles, and a basic Euler equation are shortly presented.

1.1.3 Velocity triangles

The velocity triangles are formed by the vector of gas velocities and the peripheral velocity (tip speed) at the inlet (1) and the outlet (2) of the rotor as shown in figure 1.2. There are three velocity components: absolute velocity C is defined as the velocity of a fluid particle measured in a fixed coordinate system, relative velocity W is tangent to the blade curve in a mobile coordinate system, peripheral velocity U is the blades tip speed depending on the rotation speed and radius of the rotor. The relations of

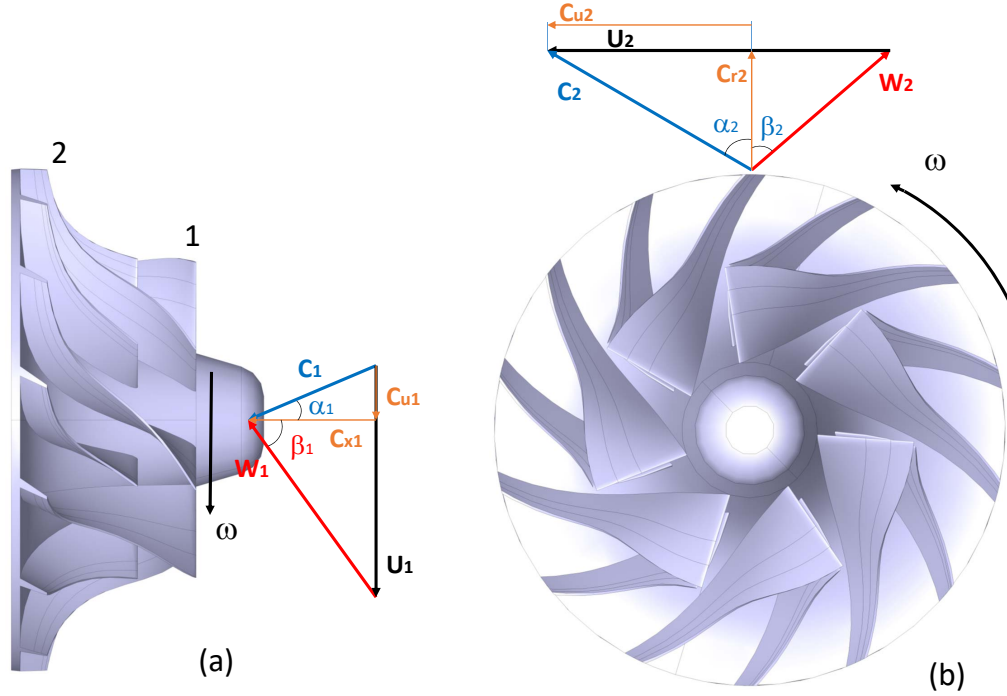


FIGURE 1.2 – Velocity triangles of the rotor at inlet (a) and outlet (b)

these velocity components are described as the following equation:

$$\mathbf{C} = \mathbf{W} + \mathbf{U} \quad (1.1)$$

Inlet triangles

The inlet triangles describe the state of flow infinitesimally upstream of blade leading edge (1). Assuming that the fluid enters the compressor with the velocity C_1 as shown in figure 1.2a. It is split up into two velocity components axial velocity (C_{x1}) and tangential velocity (C_{u1}). If the prewhirl valve does not exist at the inlet ($\alpha = 0^\circ$), the axial velocity component is equal to absolute velocity ($C_{u1}=0$). From the velocity triangles diagram, the relative fluid flow angle at the inlet can calculate by:

$$\operatorname{tg}\beta_1 = \frac{U_1}{C_1} \quad (1.2)$$

Outlet triangles

The exit triangles are valid infinitesimally downstream the blade trailing edge. At the outlet, the fluid is assumed to exit the rotor in the imposed direction of the blade outlet, as presented in figure 1.2b. This hypothesis called Euler's hypothesis is justified only in the case where the number of blades approaching infinity. In fact, the outlet velocity angle is not equal to the blade angle; this phenomenon is depicted in section 1.2.1. From the velocity triangles diagram, the relative flow angle can be computed as follows:

$$\operatorname{tg}\beta_2 = \frac{U_2 - C_{u2}}{C_{r2}} \quad (1.3)$$

The calculation of fluid flow helps to determine the blade angle in method design.

1.1.4 Energy transfer in centrifugal compressors

Energy transfer in centrifugal compressor according to the first law of thermodynamics. The net change in energy of a fluid undergoing any process is equal to the net

energy transfer by work and heat between the fluid and its surroundings. In case of a steady flow, its energy can be considered the sum of internal energy, the work provided by the fluid in the surroundings and the kinetic energy as well as potential energy of the fluid:

$$\dot{Q} - \dot{W} = \dot{m} \left[(h_2 - h_1) + \frac{1}{2} (C_2^2 - C_1^2) + g(z_2 - z_1) \right] \quad (1.4)$$

Where:

- \dot{Q} - Heat transfer rate, [J/s];
- \dot{W} - Euler work rate, [J/s];
- \dot{m} - Mass flow rate, [kg/s];
- h - Specific enthalpy, [J/kg];
- $\frac{1}{2}C^2$ - Kinetic energy per unit mass, [J/kg];
- gz - Potential energy per unit mass, [J/kg];

In addition, most of the centrifugal compressors operate in adiabatic conditions so there are no heat transfer ($\dot{Q} = 0$). The potential energy term $g(z_2 - z_1)$ is small and can be neglected. Total enthalpy is defined as $h_0 = h + \frac{1}{2}C^2$, the equation 1.4 becomes:

$$-\frac{\dot{W}}{\dot{m}} = (h_{02} - h_{01}) \quad (1.5)$$

On the other hand, the fluid passes through a control volume is applied to Newton's second law of motion. The rate change of momentum is equal to the net force applied to the control volume in the flow direction. In an arbitrary direction x , the applied force is calculated as:

$$F_x = \frac{d(mC_x)}{dt} \quad (1.6)$$

In the case of steady flow between the inlet (1) and outlet (2), the applied force can be written as:

$$F_x = \dot{m} (C_{x2} - C_{x1}) \quad (1.7)$$

In the centrifugal compressor, the control volume is considered the rotor. The energy is transferred due to the torque τ at the rotating shaft. By multiplying equation 1.7 with the radius r . The change of fluid angular momentum passes the rotor as:

$$\tau = \dot{m} (r_2 C_{u2} - r_1 C_{u1}) \quad (1.8)$$

where:

- τ - Torque of rotating shaft, [Nm];
- r_1 - Inlet radius, [m];
- r_2 - Outlet radius, [m];
- C_u - Tangential velocity component, [m/s];

Dividing the equation 1.8 by \dot{m} and considering that the peripheral velocity $U = r\omega$ lead to the specific work transfer as given by:

$$\frac{\dot{W}}{\dot{m}} = \frac{\tau\omega}{\dot{m}} = (U_2 C_{u2} - U_1 C_{u1}) \quad (1.9)$$

where:

- U_1 - Blade velocity at inlet, [m/s];
- U_2 - Blade velocity at outlet, [m/s];
- ω - Angular speed of rotor, [rad/s];

From the equations 1.5 and 1.9, equation 1.10 can be obtained:

$$h_{02} - h_{01} = U_2 C_{u2} - U_1 C_{u1} \quad (1.10)$$

Equation (1.10) shows that the exchanged work through the rotor depends on the tangential velocity vector component C_u .

According to the velocity triangles diagram in figure 1.2, the velocity triangles at the outlet can be described by:

$$C_{r2}^2 = C_2^2 - C_{u2}^2 = W_2^2 - W_{u2}^2 = W_2^2 - (U_2 - C_{u2})^2 \quad (1.11)$$

From the equation 1.11 a following relation is obtained:

$$U_2 C_{u2} = \frac{1}{2} (C_2^2 + U_2^2 - W_2^2) \quad (1.12)$$

Similarly, the relation at the inlet is:

$$U_1 C_{u1} = \frac{1}{2} (C_1^2 + U_1^2 - W_1^2) \quad (1.13)$$

By combining the equation 1.10 with the equation 1.12 and the 1.13, the variation of total enthalpy can be obtained by:

$$h_{02} - h_{01} = \frac{1}{2} [(C_2^2 - C_1^2) + (W_1^2 - W_2^2) + (U_2^2 - U_1^2)] \quad (1.14)$$

The equation 1.14 explains why the static enthalpy rises in a centrifugal compressor more than a single-stage axial compressor. It can be noted that there are three terms on the right-hand side of the equation 1.14:

- The first term ($C_2^2 - C_1^2$) represents the kinetic energy supply of the fluid. The increase in kinetic energy leads to the enthalpy rise.
- The second term ($W_1^2 - W_2^2$) shows the contribution from the diffusion of relative velocity.
- The third term ($U_2^2 - U_1^2$) illustrates a centrifugal effect. The increase in the rotor radius leads to an increase of peripheral velocity so that it affects greatly the enthalpy rise. Consequently, the inlet and outlet radius plays an important role in centrifugal compressor design.

1.2 Performance of centrifugal compressors

The energy transfer of a centrifugal compressor happens mainly in a rotor. The fluid enters the rotor at a specific radius with a specific velocity and exits at a different radius with a different velocity direction. The change of momentum of the fluid is derived from the work done by the rotor that is driven by an external torque.

1.2.1 Slip factor

A slip factor is an important factor for finding the value of the energy transfer between the rotor and the fluid. If the rotor could be imagined as being made with an infinite number of infinitesimally thin blades, then the ideal flow would be perfectly guided by the blades. The flow would leave the rotor with the blade angle. Unfortunately, the real physical structure of the rotor has a finite number of blades with a specific thickness. Therefore, the angle of the fluid flow is different from the angle of the blade. It means the fluid flow is deviated, as shown in figure 1.3, which compares the relative flow angle β_2 with the blade angle β_{2b} at the rotor outlet [9].

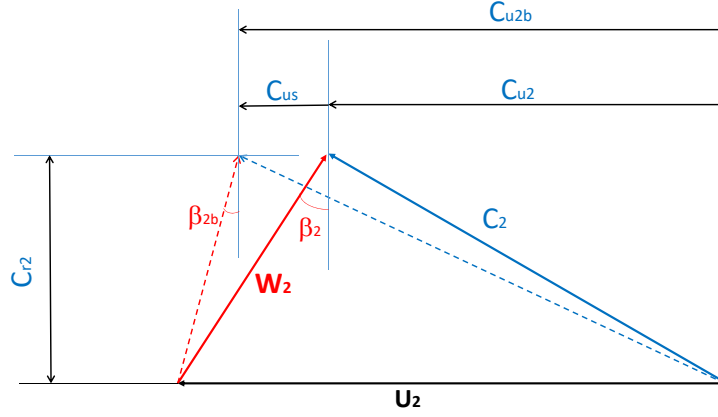


FIGURE 1.3 – Diagram of a deviation of the flow velocity at the rotor outlet

To take into account the deviation of flow, the slip factor is used. It can be defined as the following equation:

$$\sigma = \frac{C_{u2}}{C_{u2b}} \quad (1.15)$$

With C_{u2} is the tangential component of the outlet velocity and is related to the relative flow angle β_2 . The blade tangential velocity component C_{u2b} is related to the relative blade angle β_{2b} . According to the geometric relation presented in figure 1.3, the slip velocity is given by $C_{us} = C_{u2b} - C_{u2}$. So, the slip factor can be calculated as:

$$\sigma = 1 - \frac{C_{us}}{C_{u2b}} \quad (1.16)$$

The C_{u2} component can be obtained from the velocity triangles diagram:

$$C_{u2b} = U_2 - C_{r2} \tan \beta_{2b} \quad (1.17)$$

To determine the exact values of the slip factor, numerous research papers are published. Stodola et al. [10] presented a slip factor based upon the second Helmholtz law. The authors proposed the relative eddy motion of the fluid flow within the rotor and assumed that the slip is due to the relative eddy. Stodola's slip factor is calculated by:

$$\sigma = 1 - \frac{\pi \cos \beta_{2b}}{Z (1 - \phi_2 \tan \beta_{2b})} \quad (1.18)$$

Where Z is the number of blades and $\phi_2 = C_{r2}/U_2$ is the impeller discharge flow coefficient.

Bausemann et al. [1] developed a more accurate theoretical solution and applied it to a special case of two-dimensional blades curved as logarithmic spirals are shown in figure 1.4.

The geometry of the blade can be provided through:

$$\kappa = \tan \beta_b \ln \left(\frac{r_2}{r_1} \right) \quad (1.19)$$

where: β_b - Blade angle, [rad];
 r_1 - Inlet radius, [m];
 r_2 - Outlet radius, [m];

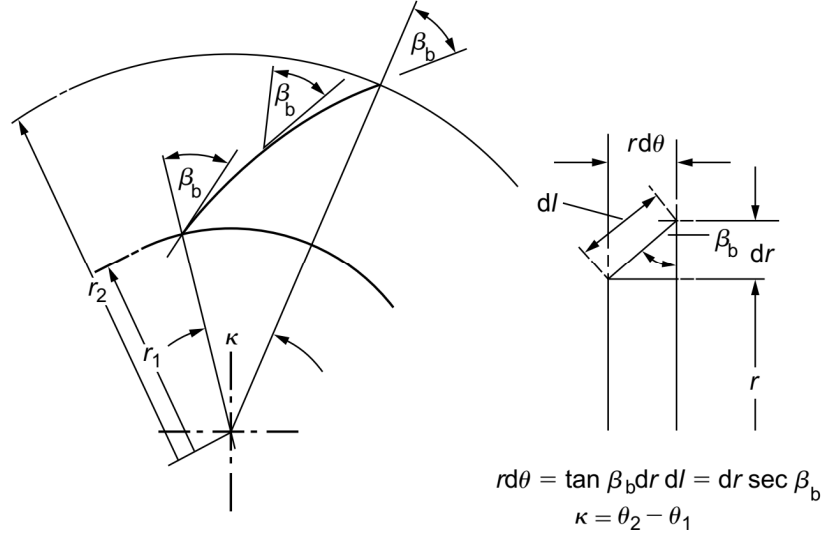


FIGURE 1.4 – Logarithmic Spiral Blades where β_b is constants for all radii [1]

The ratio of blade length to equivalent blade pitch is defined by:

$$\frac{l}{s} = \frac{Z}{2\pi \cos \beta_b} \ln \left(\frac{r_2}{r_1} \right) \quad (1.20)$$

Where the equivalent pitch is calculated by:

$$s = \frac{2\pi (r_2 - r_1)}{Z \ln \left(\frac{r_2}{r_1} \right)} \quad (1.21)$$

The Busemann slip factor could be calculated by the following equation:

$$\sigma = \frac{A - B\phi_2 \tan \beta_{2b}}{1 - \phi_2 \tan \beta_{2b}} \quad (1.22)$$

Where A and B are functions of r_2/r_1 , β_{2b} and Z. However, this slip factor is not accurate when the flow is calculated near the wall.

The study of Dixon et al. [9] showed that Sotdola's slip factor and Busemann slip factor is almost the same if the blade angle is within $50^\circ \leq \beta_{2b} \leq 70^\circ$ and the number of blades exceeds six in zero through-flow condition ($\phi_2 = 0$).

Stanitz et al. [11] presented that the slip velocity C_{us} is independent of the blade angle β_{2b} . It depends only on a number of blades. Likewise, the authors found that the compressibility effects did not affect the slip factor. Therefore, an equation to calculate the slip velocity is given by:

$$C_{us} = \frac{0.63U_2\pi}{Z} \quad (1.23)$$

By combining the equations 1.16 and 1.23, the Stanitz slip factor is calculated as following equation:

$$\sigma = 1 - \frac{0.63\pi}{Z(1 - \phi_2 \tan \beta_{2b})} \quad (1.24)$$

The work of Pfeleiderer et al. [12] considered the contribution from downstream collecting systems. The model can be summarized as:

$$\begin{cases} C_{slip} = pC_{u2} & \text{where } p = \frac{\psi' r_2^2}{\int_1^2 Z r dm} \\ \psi' = a(1 + \sin\beta_2) & \text{with } a = \begin{cases} 0.6 & \text{for vaned diffuser} \\ 0.65 \div 0.85 & \text{for volute} \\ 0.85 \div 1.0 & \text{for vaneless diffuser} \end{cases} \end{cases} \quad (1.25)$$

Where: p - Output coefficient;
 ψ' - Experience number;
 r_2 - Outlet radius, [m];
 $\int_1^2 Z r dm$ - A static moment from leading to the trailing edge;
 Z - Number of blade;

So the slip factor is determined as:

$$\sigma = \frac{C_{slip}}{U_2} = \frac{p_2}{1 + p_2} \left(1 - \frac{1}{C_{Nd}}\right) \quad (1.26)$$

Where: $p_2 = \frac{\psi' r_2^2}{\int_1^2 Z r dm}$; $C_{Nd} = \frac{U_2 \tan\beta_2}{C_{m2d}}$;

Wiesner et al. [13] proposed an empirical well-fitting the Busemann data up to a limiting inlet-to-outlet rotor radius ratio based upon the Busemann's slip factor. An empirical correction factor for conditions beyond this limiting radius factor is presented. The simple empirical expression for slip velocity is:

$$C_{us} = \frac{U_2 \sqrt{\cos\beta_{2b}}}{Z^{0.7}} \quad (1.27)$$

The slip factor is determined by the following relation:

$$\sigma = 1 - \frac{\sqrt{\cos\beta_{2b}}}{Z^{0.7} (1 - \phi_2 \tan\beta_{2b})} \quad (1.28)$$

This formula is applied to calculate the slip factor if the radius ratio is less than the limit value. It is determined by the empirical expression as shown in the following relation:

$$\epsilon_{limit} = \frac{r_1}{r_2} = \exp\left(\frac{-8.16 \cos\beta_{2b}}{Z}\right) \quad (1.29)$$

If the radius ratio excesses of this limit, the following empirical expression is used:

$$\sigma_{limit} = \sigma \left[1 - \left(\frac{\frac{r_1}{r_2} - \epsilon_{limit}}{1 - \epsilon_{limit}}\right)^3\right] \quad (1.30)$$

Qiu et al. [14] suggested a new slip model based on Stodola's and Eck's slip factor. According to this model, the slip factor is mainly affected by the rotor rotation on the radial plane:

$$\sigma = 1 - \frac{F \pi \cos\beta_{2b} \sin\delta_2}{Z_2} - \frac{F s_2 \phi_2}{4 \cos\beta_{2b}} \left(\frac{d\beta}{dm}\right)_2 + \frac{F \phi_2 s_2 \sin\beta_{2b}}{4 \rho_2 b_2} \left(\frac{d\rho b}{dm}\right)_2 \quad (1.31)$$

On the right-hand side of equation 1.31, the second component is a decrement due to the radial rotation effect, the third component is a decrease because of a rotating

blade, and the last component is a decline due to the passage width variation where F is a shape factor and it is calculated by:

$$F = 1 - \sin \frac{\pi}{Z_2} \sin \left(\frac{\pi}{Z_2} + \beta_{2b} \right) \cos \beta_{2b} \sin \delta_2 - \frac{t_2}{s_2 \cos \beta_{2b}} \quad (1.32)$$

Where

- δ_2 - Deviation at the outlet;
- b - Passage width, [m];
- ϕ_2 - Exit flow coefficient, $\phi_2 = C_{m2}/U_2$;
- s - Pitch at the blade exit, $s = 2\pi r_2/Z$;
- ρ - Density, [kg/m^3];
- t_2 - Thickness at trailing edge;

1.2.2 Dimensionless analysis

Dimensionless parameters are often used for the evaluation and the comparison of the performance of turbomachines. Additionally, these parameters help the designers to select the optimized machine and to compare different competing designs. Three dimensionless parameters: flow coefficient ϕ , head coefficient Ψ , and machine Mach number M_a are presented below.

Flow coefficient

The flow coefficient determines the actual achieved flow by a rotor of a given geometry at a given tip speed. This parameter is obtained by the equation:

$$\phi = \frac{\dot{m}}{\rho_1 \omega \pi r_2^3} \quad (1.33)$$

Head coefficient

The head coefficient relates the head increase to the speed kinetic energy $U_2^2/2$. So, it is rather convenient to come up with the head stage of a compressor with a specific speed. The polytropic head coefficient is determined by:

$$\Psi = \frac{y}{U_2^2/2} \quad (1.34)$$

Where y is the head rise of the rotor and it is calculated by the equation:

$$y = \frac{\gamma}{\gamma - 1} RT_1 \left[\left(\frac{P_2}{P_1} \right)^{\left(\frac{\gamma-1}{\gamma} \right)} - 1 \right] \quad (1.35)$$

Machine Mach number

Mach number represents the compressibility of the fluid. The machine Mach number is the ratio of rotor tip speed of the rotor and the local sound speed. It is calculated as the following equation:

$$M_u = \frac{U_2}{a} \quad (1.36)$$

Where speed of sound a is determined by:

$$a = \sqrt{\gamma RT} \quad (1.37)$$

1.2.3 Pressure ratio

The pressure ratio is the ratio of the downstream pressure to upstream pressure. It is a parameter to evaluate the performance of the compressor. According to the thermodynamic analysis, the pressure ratio can be determined by:

$$\Pi = \frac{P_{02}}{P_{01}} = \left(\frac{T_{02-is}}{T_{01}} \right)^{\frac{\gamma}{\gamma-1}} \quad (1.38)$$

1.2.4 Efficiency

The flow enters the compressor with the static temperature T_1 and the total temperature of T_{01} . The difference between these two variables is due to the kinetic energy at the inlet of compressor C_1^2/C_p . At the outlet of the rotor, the static pressure can achieve P_2 with a static temperature of T_2 and a total temperature of T_{02} . An isentropic compression to the same static pressure would have resulted in an outlet static temperature T_{2is} and total temperature T_{02is} .

Considering only the static pressure at the rotor outlet, the ratio of the minimum required energy over the real added one is called total to static efficiency, and it is defined by the following relation:

$$\eta_{ts} = \frac{T_{2is} - T_{01}}{T_{02} - T_{01}} = T_{01} \frac{\left(\frac{P_2}{P_{01}} \right)^{\frac{\gamma-1}{\gamma}} - 1}{T_{02} - T_{01}} \quad (1.39)$$

However, in most cases, this is low values because in this definition the kinetic energy at the rotor outlet is considered as the loss or useless.

The total to total efficiency is defined as:

$$\eta_{tt} = \frac{T_{02is} - T_{01}}{T_{02} - T_{01}} = T_{01} \frac{\left(\frac{P_{02}}{P_{01}} \right)^{\frac{\gamma-1}{\gamma}} - 1}{T_{02} - T_{01}} \quad (1.40)$$

It is clear that the total to total efficiency is much higher than total to static efficiency because the kinetic energy at the rotor exits $C_2^2 = C_p(T_{02is} - T_{2is})$ is considered. Polytropic efficiency is usually used for multistage and high-pressure ratio compressors to correct the divergence of the iso-pressure lines. Polytropic efficiency compares the real enthalpy rise with the hypothetical one. It is calculated by the equation 1.41:

$$\eta_p = \frac{\gamma - 1}{\gamma} \frac{\ln \left(\frac{P_2}{P_1} \right)}{\ln \left(\frac{T_2}{T_1} \right)} \quad (1.41)$$

1.2.5 Compressor performance map

A performance map is important for evaluating the operating range of a compressor. It gives valuable information about the compressor performance under different conditions and it is usually measured on a test bench. On the y-axis, the pressure ratio is presented according to the corrected mass flow or volume flow on the x-axis. At each constant rotation speed of the rotor, the mass flow rate is progressively reduced while the overall pressure ratio simultaneously increases to reach a surge region. Surge is an extremely unstable region where the flow pulsates violently and determines a working limit as a minimum mass flow rate. On the other hand, the maximum mass flow rate is

limited by a phenomenon known as a choke. This occurs when a local velocity becomes equal to the acoustic velocity. The region between surge and choke is called the stable operating range of a compressor and it is very important to predict the response of the compressor for a different situation. In addition, the iso-efficiency lines are also plotted to show the efficiency of the compressor as a function of the mass flow rate. The working condition of the compressor is always controlled within the highest efficiency region. The more details of a compressor performance map are illustrated in figure 1.5.

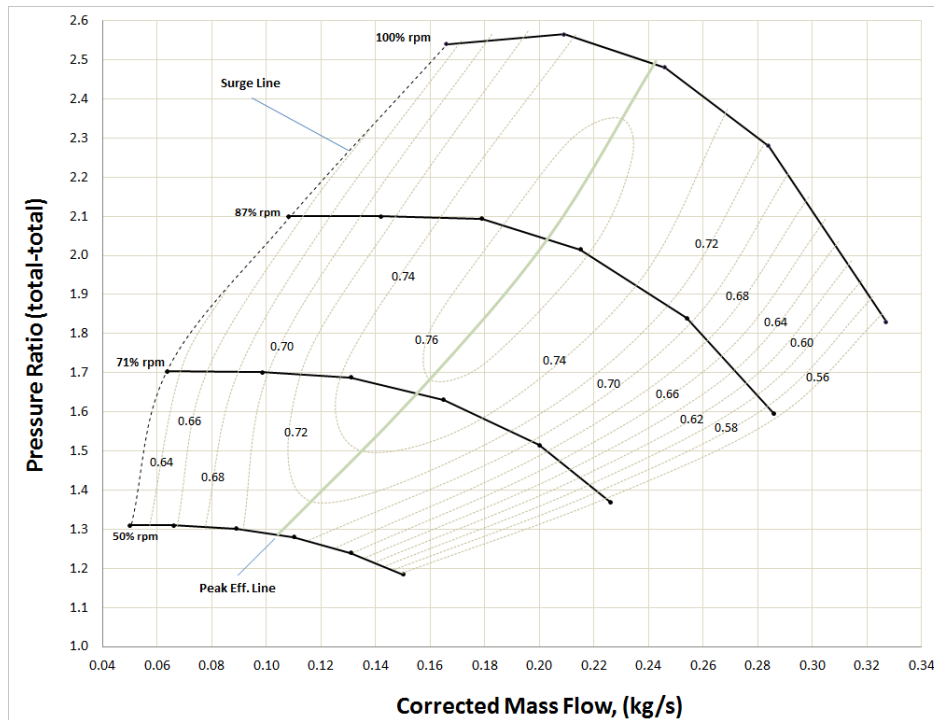


FIGURE 1.5 – Performance map of centrifugal compressors (*Source:wikipedia.org*)

1.3 Applications of a counter-rotating system and state of art

The history of the counter-rotating system started at the beginning of 20th century with the appearance of a counter-rotating gas turbine concept applied to aircraft propeller by Taylor [15] and Bourdon [16]. In this study, a second propeller rotor was added next to the first rotor which rotates the inverse direction. The authors found that using a counter-rotating system improved the through-flow and converted engine energy into thrust more effectively. Similarly, Young [17] and Wilcox [18] reported that a counter-rotating machine with the same speed delivered higher pressure rise and provided high through-flow capacity. Sharma et al. [19, 20] presented that counter-stage performance was significantly affected by numerous parameters such as speed ratio of the two rotors, the axial gap between them, hub-tip ratio, and pitch-chord ratio. Increasing the speed ratio can make better performance but it also decreases aeroacoustics performance progressively. However, a trade-off between aerodynamic and aeroacoustics can be solved by selecting a suitable gap between the two rotors. Recently, some nations have applied a counter-rotating concept in an aircraft and a marine system, for example, a counter-rotating propeller used on the Antonov

AN-70 of Ukraine and P51 aircraft of North-American as shown in figure 1.6. Because of the advantage of a counter-rotating system, many researchers continue to improve the performance of its application in many types of turbomachines.



FIGURE 1.6 – Application of counter-rotating system on aircraft (a) Antonov AN-70 (Paris Air show 2013) and (b) P51 of North-American (*Source:wikipedia.org*)

1.3.1 Axial turbomachines

Furukawa et al. [21] presented an experimental study of an axial counter-rotating pump in comparison with a conventional axial pump (rotor-stator). The results illustrated that using a counter-rotating system could achieve a more compact design and work at a lower rotational speed. In addition, the operating range became wider with higher performance by controlling the rotational speed of the front (N_f) and rear (N_r) rotors individually. Besides, in case the front and rear rotors rotate at the same speed, the relative velocity at the rear rotor inlet became higher, and the rotor blade took a larger stagger angle. However, the cavitation occurred at the rear rotor leading edge due to high relative velocity so that the design under the condition of $N_f > N_r$ is suggested for a better cavitation performance.

Kerrebrock et al. [22] published numerical and experimental results of a vaneless counter-rotating compressor stage. They concluded that using a vaneless counter-rotating compressor provides an adiabatic efficiency of about 87% and offers a light-weight solution for the compression system requirement.

Moroz et al. [23] compared three designs of turbines: the traditional axial turbine and two variations of counter-rotating designs with 4 and 6 stages. Using a counter-rotating turbine with the same number of stages can get the same performance level but reduces the turbine axial length of about 30%. Six stages can be increasing efficiency by 0.7% in comparison with the initial design. The authors concluded that counter-rotating turbine efficiency is higher and wider ranges of rotation speeds. It decreases weight and length simultaneously as well as creates more advanced designs in terms of aerodynamic quality and overall cost-efficiency.

Lee-Sang CHO et al. [24] conducted an experimental study on the three-dimensional unsteady flow of a rotor-rotor interaction of a counter-rotating axial-flow fan at the design point. To measure unsteady flow fields, 45°-inclined hot-wire probes are used and placed at the upstream cross-sectional planes, between and downstream of each

rotor. The stationary hot-wire technique and the phase-locked average method for the 45° inclined hot-wire probe were applied to analyze the unsteady flow. The results showed that the axial velocity highly decreases due to the boundary layer effect by fan casing and the blade vortex at the blade tip region. At the hub region, the axial velocity reduces because of the flow separation at the driving motor. Consequently, it induces the increment of the incidence angle and diffusion factor of the rotors. Therefore, these rotors have required the decline of the stagger at the hub region compared with the free vortex design condition for the increment of the fan efficiency. In addition, the blade passage frequency was affected by the phase-locked average velocity profiles of the front rotor as well as the rear rotor. That means the blockage effect of the front rotor and the suction effect of the rear rotor affected simultaneously between the rotors.

Furukawa et al. [25] studied limiting streamlines on the blade passage walls. It was observed by a multi-colored oil-film method at design and partial flow rates. The velocity distribution in blade-to-blade flow was measured by Laser-Doppler velocimetry and static head distribution on the casing wall by pressure sensors. The results showed that the hydraulic efficiency of the rear rotor, at the design operating point flow rate, was superior to the efficiency of the front rotor. The reason is that the leakage flow between the rear rotor blade tip and the casing, unlike the front rotor. The back-flow in the hub side of the front rotor outlet and the tip side of the rear rotor inlet produces a large head loss. Though the back-flow at blade tip is elongated with a decrease of flow rate and head rise is deteriorated with $dH/dQ > 0$.

Momosaki et al. [26] investigated the internal flow structure of a counter-rotating axial-flow pump and evaluated the pump performance. They found that unsteady simulations for both front and rear rotors are sufficient to predict the pump performance even at the design operating point. However, the drawback of this method is that the pressure performance of the rear rotor does not satisfy the design value in the unsteady simulation due to the flow stagnation near the leading edge on the suction surface rather than the pressure surface. In addition, the tip leakage vortex in the central area of the blade passage near the shroud was also observed at a low flow rate due to the back-flow. Moreover, the combination of leakage vortex and blockage effect of the flow separation decreased the flow turning in main flow across the rear rotor because of reducing Euler's head pressure.

Alexiou et al. [27] presented a modeling contra-rotating system for engine performance simulations. First, the performance characteristics of components are generated by a modified one-dimensional mean line code. The characteristics are then converted to three-dimensional maps and compared to conventional turbomachinery maps. The speed ratio between the two shafts is as an additional map parameter and the torque ratio is as an additional table. To complete the model, the authors used these maps to simulate the design and off-design operating points at the component engine levels. The results showed that new models were more effective in the off-design process. Using a counter-rotating system could reduce about 10% engine weight and more than 0.52% fuel consumption. However, the physics-based performance characteristics for the counter-rotating system need higher fidelity codes or experiments to obtain more accurate results.

Shigemitsu et al. [28] conducted a numerical and experimental study of the influence of blade row distance on the performance and on the flow conditions of counter-rotating small-sized axial fan. Results showed that the fan static pressure is almost constant by the blade row distance $L=30\text{mm}$. The tangential velocity between the front and the rear rotors decreases with the increase of the blade row distance due to the friction

loss of the casing wall. The authors concluded that the blade row distance between the front and rear rotors $L=30\text{mm}$ is an appropriate distance from the point of view of the performance and the pressure interaction.

Nouri et al. [29] carried out an experimental study of aerodynamic characteristics of a subsonic counter-rotating axial-flow fan operating in a ducted configuration. Firstly, the first rotor was designed according to a conventional inverse method. The through-flow was calculated by empirical models of losses under assumptions of axisymmetric and radial equilibrium. The second rotor was designed depending on the tangential velocity. Secondly, the first rotor was modified until the stage meets requirements. The results of this experimental study showed that the efficiency rose strongly contrary to conventional axial fans. The downstream flow angle of the outflow is not completely straightened at the designed operating point. They concluded that the system is highly efficient and is high-pressure rises on a wide range of flow rates so that it is very flexible to use.

Madhur Tiwari et al. [30] presented an axial compressor using a counter-rotation system and variable rotational speed. The purpose of this design is to push compressor performance during the stall by moving the operating point away from the surge line with a higher pressure ratio rise. The flow is modeled by means of Navier-stokes computation using the upstream rotor conditions and outlet static pressure condition with $k - \epsilon$ as the turbulence model. Compressor exit conditions are then changed until the compressor stall. After the compressor stall, the rotational speed of the counter-rotating stage is changed until the compressor recovers from the stall. Results showed that the stall was successfully mitigated, and the overall pressure ratio of the recovered compressor system is higher than the design operating point of the compressor system. However, the counter-rotating system increased the inlet relative Mach number and pushed the compressor design away from design criteria.

1.3.2 Centrifugal turbomachines

Fukutomi et al. [2] studied counter-rotating rotors in Sirocco fan¹ for getting a higher pressure and a structure more compact. An outer rotor was added to a radial position and its rotation speed was equal to the inner rotor speed but in the opposite direction. The authors calculated Euler head of counter-rotating fan by the following equation:

$$H = \frac{U_4 C_{u4} + 2U_2 C_{u2}}{g} \quad (1.42)$$

The equation 1.42 shows that the head of the counter-rotating fan increases two times more than the original fan head. So, high discharge pressure could be considered by using a counter-rotating rotor. An experimental measurement was conducted to compare the performance between the conventional and counter-rotating fan. The schematic diagram of the fan test bench is shown on as figure 1.7.

The authors used two different inner rotors (with different diameters and blade profiles) and the same outer rotor. The static pressure was measured by static pressure holes set at the duct. The torque sensors were used to measure the torque of each rotor shaft. The flow rate was measured by the orifice installed downstream of the rotor. The internal flow measurement at the outlet of the rotor was conducted with a one-hole cylindrical pitot tube with an outer diameter of 3.0mm . It was used as the substitution of a three holes pitot tube by rotating an angle of $\pm 30^\circ$. The flow measurement was

1. Sirocco fan is a centrifugal fan using forward-curved blade

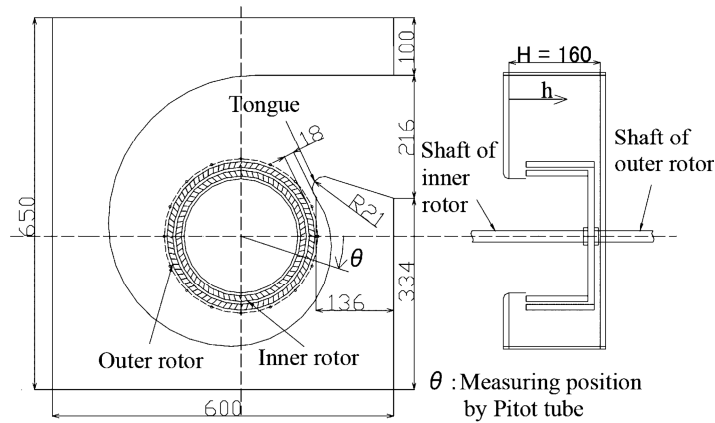


FIGURE 1.7 – Schematic diagram of Sirocco fan test bench [2]

carried out at 16 arbitrary positions on the circumference and a distance of 10mm from outer rotor diameter. Figure 1.8a illustrates that the pressure coefficient of the counter-rotating fan is 2.5 times greater than the conventional fan because of the increase in peripheral velocities at the outlet. However, the maximum efficiency of the counter-rotating fan is 27% lower than that one. Besides that, the influence of inner diameter was conducted. Figure 1.8b shows the comparison of performance between two types of sirocco fan. It is clear that the larger rotor (bc type) gives a higher pressure coefficient than a smaller rotor (ac type). The maximum efficiency of bc type is shifted to a higher flow rate. Therefore, the influence of the wake and pressure interaction between inner and outer rotors on performance caused by decreasing in the blade row distance. The authors concluded that reducing the blade row distance can be effective to increase the discharge pressure using contra-rotating rotors.

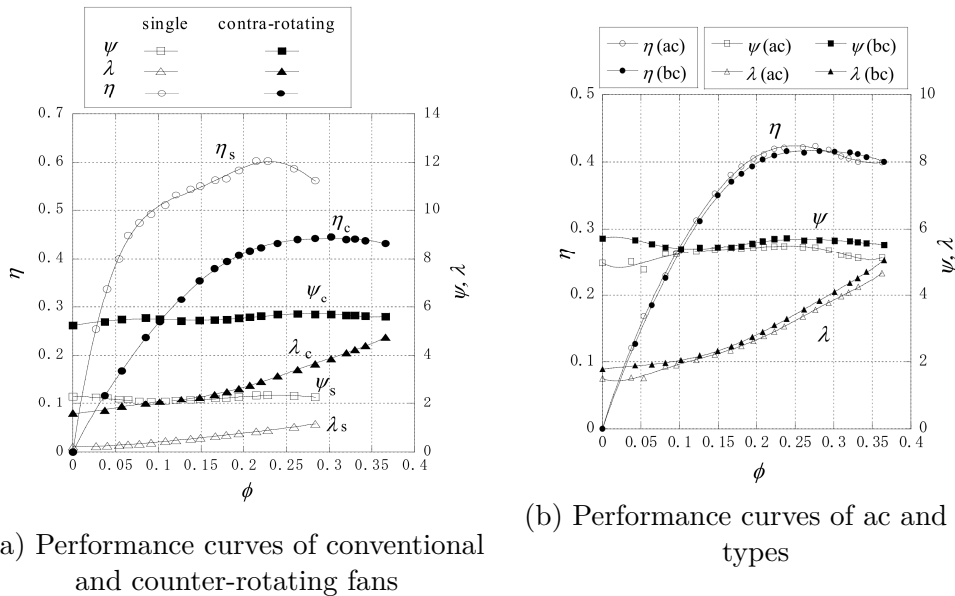


FIGURE 1.8 – Comparison of the performances between conventional and counter-rotating sirocco fan [2]

Tosin et al. [3] presented a preliminary analysis of the applicability of the counter-

rotating impeller concept on mixed-flow and radial-flow pumps. The design concept constituted a mixed-flow first rotor with a radial second rotor that rotates in the opposite direction. Its parameters were selected based on the highest power density coefficient and efficiency. A Response Surface Optimization (RSO) analysis was proposed to choose the best seven machines for investigating. Numerical results were conducted by Ansys-CFX for the design point are presented in figure 1.9. Observing the figure, the vertical black line represents the desired design, while the dashed black line (Prototype 5) shows the best performance in terms of the total to total efficiency. It is also matched the design head of 15m at the desired mass flow rate 36l/s. The basic characteristics of this prototype are a number of blades of the front impeller $Z_{FR} = 11$ and the rear impeller $Z_{RR} = 7$, design speeds values $n_{FR} = +1602rpm$ and $n_{RR} = -1171rpm$, and a load distribution factor $\chi = 0.77$. This prototype was selected for the production process to study an experiment; the transient analysis also confirms the steady-state results. FFT transformation of the pressure pulsations calculated between the rotors defines the blade passing frequency and some secondary harmonics, which can be mathematically previewable.

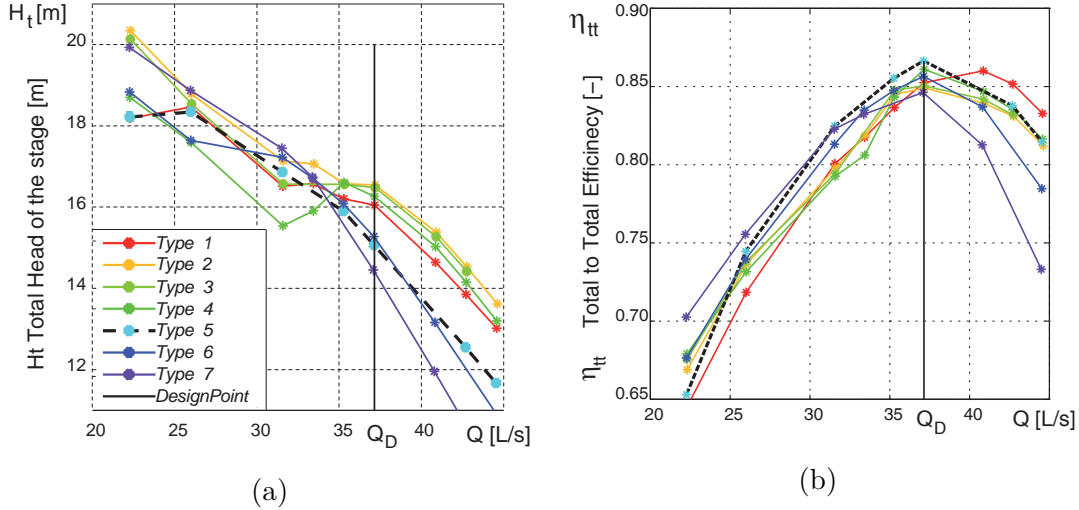


FIGURE 1.9 – Characteristics of seven best geometries: (a) total to total head rise; (b) total to total efficiency [3]

Their experiment study conducted in 2015 [31] showed that the efficiency remained almost constantly over 80% while the head was changed from 12 to 26m. Simultaneously, the head increases if the rear rotor speed is increased and the front rotor speed is reduced. In case of load distribution equal to 77% (rear rotor speed is two times bigger than front rotor), the increased speed of rear rotor leads to higher machine head. At very high discharge 140% of Q_{des} the rear rotor needs a higher speed to minimize the incidence losses. In contrast, at a very low discharge of 60%, the behavior is not clear and needs a result of CFD simulation to identify the sources of losses. In 2016, the extended study on the same type of machine was conducted by the same authors [4]. The comparison between the counter-rotating pump and a conventional pump was carried out as shown in figure 1.10. Two pumps have the same outer diameter, rotation speed, volute casing, and working point. The results showed that the significantly higher static pressure is reached in the counter-rotating layout. However, the efficiency drops due to additional losses are marginal compared to the gain in hydraulic power density.

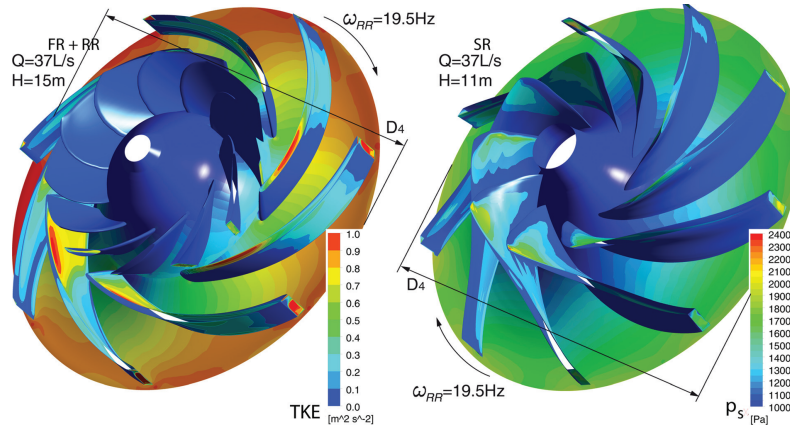


FIGURE 1.10 – Comparison between counter-rotating pump (left) and conventional pump (right) with the same working point and tip speed [4]

Dejour et al [5] presented an assessment of a new non-axial counter-rotating compressor concept as shown in figure 1.11a. This concept consists of replacing the stator of a mixed-flow compressor stage (or diffuser of a centrifugal compressor stage) with a counter-rotating rotor. It turns the flow back to the axial direction with a much lower diffusion factor while providing the equivalent in the work of the upstream mixed-flow rotor. CFD simulations were conducted for a comparative evaluation of the new compressor with the original compressor. The results of the simulation are shown in figure 1.11b and 1.11c. It is clear that the counter-rotating mixed-flow compressor archives more than double the design (peak efficiency) pressure rise with a small advantage in peak-efficiency and higher stall margin as well as having a shorter axial length. However, the lower aspect ratio of the downstream rotor in non-axial counter-rotating compressors means that its tip clearance flow plays an important role in limiting the possible efficiency gain and can cause a large spanwise variation of the exit flow angle.

1.4 Motivation

Nowadays, the tendency of compact design to save materials and space is becoming more and more popular in industrial development. Most of the turbomachines used in the industry need to optimize in size to meet this innovation. Centrifugal compressor is usually used in many types of industrial applications such as aerospace, aviation, automotive, etc. Therefore, developing a new generation of centrifugal compressors with a smaller size but the working characteristics remain stable is a challenge for design engineers. Using counter-rotating systems is one solution to respond to these demands. As concerning in section 1.3, the literature reviews show that applying a counter-rotating system on turbomachines gives more advantages. It not only improves pressure ratio and through-flow but also reduces weight and size. However, its application in a centrifugal compressor has not been considered. The work of Nouri [29], Wang [32] in our laboratory show many advantages of a counter-rotating system used on the axial turbomachine. Furthermore, these results show the outstanding feature of this type of turbomachine with the ability to independently change rotor speeds to modify its characteristics. Using the counter-rotating system on a centrifugal compressor is a new idea to develop a new generation of compressors. However, how does it affect the performance of the centrifugal compressor? How does the characteristic change when

changing the rotor speed? What are the advantages and disadvantages when using the counter-rotating system on a centrifugal compressor? etc. To answer these questions, studies on a numerical method and experimental method are performed. Therefore, the effects of a counter-rotating system on the performance of a centrifugal compressor under different operating conditions have a better understanding. Furthermore, the method of optimizing the advantage and minimizing the disadvantage of the counter-rotating system used in a centrifugal compressor will be explored in this study.

Besides, the numerical method provides a qualitative analysis of a flow field to recognize the flow structure inside the compressor and the reason for the instability phenomenon. The experimental method provides a real performance of the compressor to validate with the numerical results. In addition, the experiment shows a better observation of the improvement of the instability region when changing the rotor speed simultaneously. These results are valuable information for engineers to design the counter-rotating turbomachines in the future for many applications.

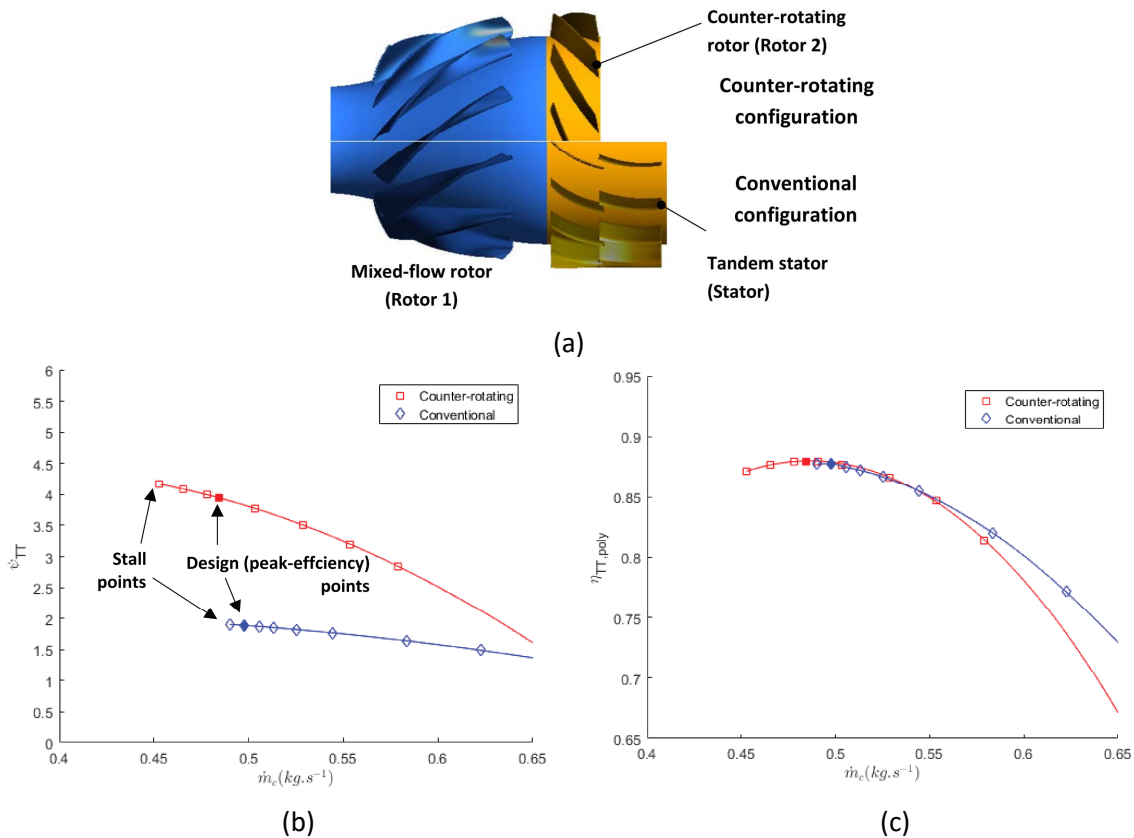


FIGURE 1.11 – Comparison of performance between counter-rotating and conventional compressor (a) counter-rotating and conventional configuration; (b) Total pressure rise characteristics (c) Total to total efficiency characteristics [5]

Chapter 2

Design of counter-rotating rotors

Contents

2.1 Reference rotor	19
2.2 Counter-rotating rotors design	20
2.3 CRCC performance evaluation	26
2.4 Conclusions	35

2.1 Reference rotor

The dimensioning method of a centrifugal rotor has been developed by laboratory of fluid engineering and energy system ([Laboratoire d'Ingénierie des Fluides et des Systèmes Énergétiques \(LIFSE\)](#)) as a part of the research work on the dimension and analysis of the performance of turbomachinery. The details of this method are presented in Appendix [A.1](#). This method has been integrated into 3D-Turbo software which helps to design new turbomachinery based on given parameters. A [Single Rotor Centrifugal Compressor \(SRCC\)](#) used in a suction application was designed by 3D-Turbo software and selected as a reference compressor for this thesis. Figure [2.1](#) presents two views of the reference rotor designed by 3D-Turbo software. A designed point of the compressor is defined as the pressure ratio of $\Pi = 1.31$ at the designed volume flow rate of $\dot{m} = 0.73kg/s$ and the rotor speed of $16,000rpm$. The rotor geometry taken from this method is then optimized to meet the real structure by the [CFD](#) simulation. The single rotor geometry is obtained and summarized in table [2.1](#).

TABLE 2.1 – Geometric paramters of [SRCC](#)

Parameter	Value	Parameter	Value
d_{1h}	$59.5mm$	β_{1h}	45.25°
d_{1sh}	$161mm$	β_{1sh}	69.8°
d_2	$286mm$	β_2	64°
b_2	$29.7mm$	ϕ	2.2°
N	$16,000rpm$	\dot{m}	$0.73kg/s$
Z	$7 + 7$	η_p	73%
Π	1.31	Power consumption	$28kW$

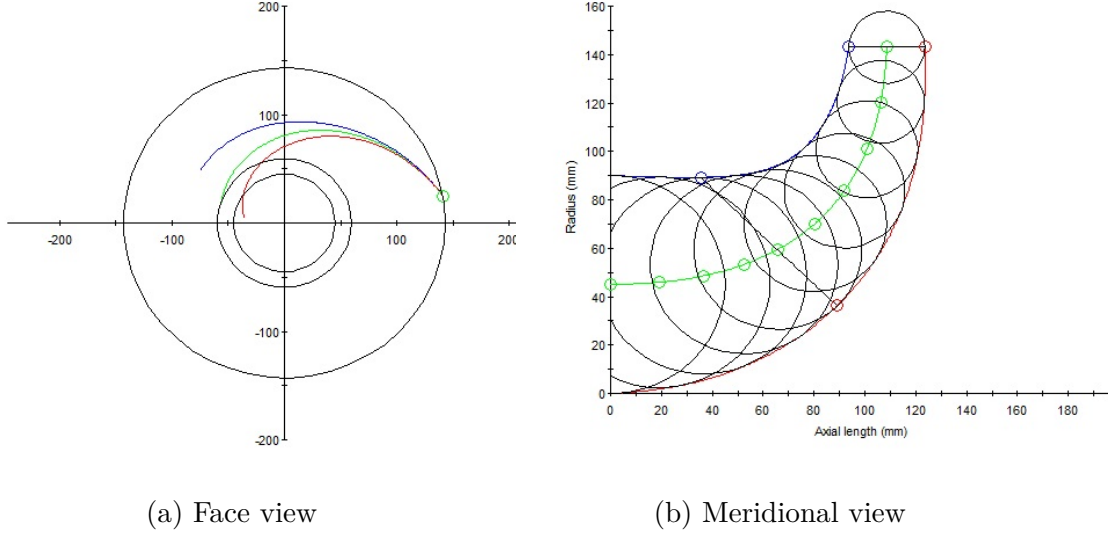


FIGURE 2.1 – Reference rotor designed by 3D Turbo software: (a) face view and (b) meridional view

2.2 Counter-rotating rotors design

The objective of this section is to design two successive rotors that maintain the same size as the single rotor of **SRCC**. These rotors rotate in two opposite directions called a counter-rotating system, as shown in figure 2.2. The first rotor places upstream and rotates with an angular velocity of ω_1 . The second one locates downstream and rotates with an angular velocity of ω_2 in the inverse direction. In this configuration, the second rotor receives the fluid flow from the first rotor and provides additional energy to compress the fluid in order to obtain more pressure rise. To simply design, all parameters of the **SRCC** rotor in the meridian view are preserved and rotate with the same rotation speed. In addition, to minimize the loss between the second rotor and the volute, the blade angle at the outlet of the second rotor remains the same as the **SRCC** rotor. A centrifugal compressor uses a counter-rotating system to build a new compressor generation called a **Counter-Rotating Centrifugal Compressor (CRCC)**.

The counter-rotating rotor design is conducted as the following steps: Firstly, the dimension of the first rotor is determined. The pressure ratio of the first rotor is calculated by the conventional method. The total pressure ratio of two rotors is imposed to calculate the pressure at the inlet and outlet of each rotor. Secondly, the geometric parameters of the rotors are determined by calculating the blade angle according to the aerodynamic relations. The design parameters of the counter-rotating centrifugal compressor are proposed and summarized in table 2.2.

TABLE 2.2 – Design parameters for CRCC

Parameter	Value	Unit
Π_{total}	1.36	-
\dot{m}	0.73	<i>kg/s</i>
η_{is}	80	%
N_1	-16,000	<i>rpm</i>
N_2	16,000	<i>rpm</i>

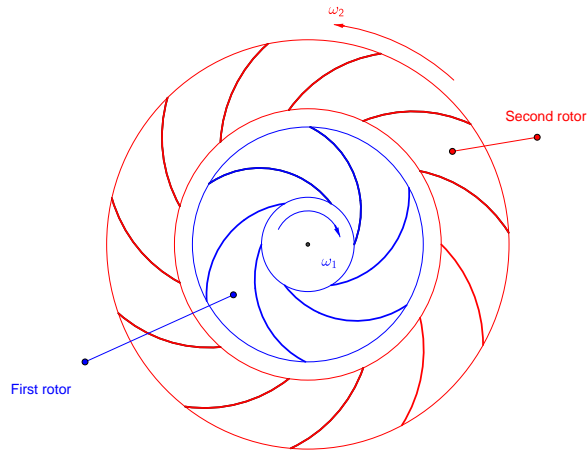


FIGURE 2.2 – Schematic diagram of counter-rotating system

2.2.1 First rotor design

The first rotor is established by finding out the outlet diameter which can be determined by the **Length Ratio (LR)** parameter. It is defined as the ratio of the first rotor contour length at the hub (or shroud) (L_{1st}) to the total contour length of the reference rotor in the meridional view (L_m), as shown in figure 2.3b. The LR can be specified by the following equation:

$$LR = \frac{L_{1st}}{L_m} \quad (2.1)$$

This is a free parameter and chosen by an arbitrary value. In this study, four values of 0.3, 0.4, 0.5 and 0.6 are respectively selected to build four counter-rotating configurations **CF1**, **CF2**, **CF3**, and **CF4**. For each configuration, the blade parameters such as inlet and outlet blade angles are calculated according to the aerodynamic equations. The velocity components at the inlet/outlet are identified by the velocity triangles, as shown in figure 2.3a.

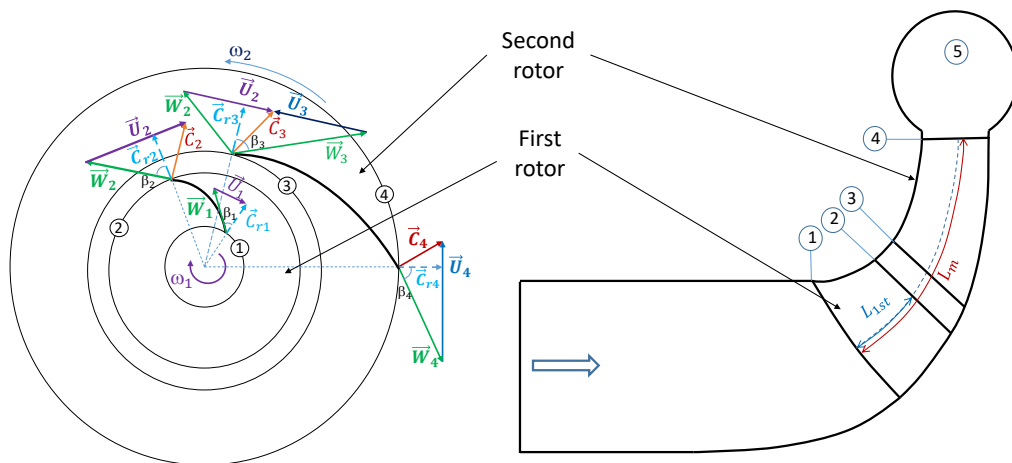


FIGURE 2.3 – Velocity triangles diagram are used to design the counter-rotating system: (a) face view and (b) meridional view

Inlet calculation

+ The inlet pressure of the first rotor is calculated by:

$$P_1 = \frac{P_4}{\Pi_{total}} \quad (2.2)$$

+ Inlet gas density:

$$\rho_1 = \frac{P_1}{RT_1} \quad (2.3)$$

+ Absolute velocity:

$$C_1 = \frac{\dot{m}}{\rho_1 \pi (r_{1h}^2 - r_{1s}^2)} \quad (2.4)$$

+ Inlet relative velocity:

$$W_1 = \sqrt{(C_1^2 + U_1^2)} \quad (2.5)$$

+ Blade inlet angle:

$$\tan \beta_{1b} = \frac{U_1}{C_1} \quad (2.6)$$

Outlet calculation

+ The outlet pressure of the first rotor:

$$P_2 = P_1 \Pi_1 \quad (2.7)$$

+ Outlet temperature:

$$T_2 = T_1 \left[\frac{\Pi_1^{\frac{\gamma-1}{\gamma}} - 1}{\eta_{is}} + 1 \right] \quad (2.8)$$

+ Outlet gas density:

$$\rho_2 = \frac{P_2}{RT_2} \quad (2.9)$$

According to the velocity triangle in figure 2.3a, the other velocity components can be determined by the following relations:

+ Meridional velocity component which is determined by:

$$C_{m2} = \frac{\dot{m}}{\rho S_2} \quad (2.10)$$

Where S_2 - is determined by:

$$S_2 = \pi (r_{2h} + r_{2sh}) b_2 - Z_1 t_b b_2 \quad (2.11)$$

+ Radial velocity component C_{r2} :

$$C_{r2} = C_{m2} \sin \delta \quad (2.12)$$

+ Axial velocity component C_{a2} :

$$C_{a2} = C_{m2} \cos \delta \quad (2.13)$$

+ Absolute velocity component C_2 :

$$C_2 = \sqrt{C_{u2}^2 + C_{m2}^2} \quad (2.14)$$

+ Relative tangential velocity component:

$$W_{u2} = U_2 - C_{u2} \quad (2.15)$$

+ Slip factor is calculated according to Wiesner [13] equation:

$$\sigma = \frac{\sqrt{\cos \beta_b}}{Z^{0.7}} \quad (2.16)$$

+ The enthalpy rise of the first rotor is calculated by:

$$\Delta h_1 = C_p T_1 \left(\Pi_1^{\frac{\gamma-1}{\gamma}} - 1 \right) \quad (2.17)$$

On the other hand, it is also calculated by:

$$\Delta h_1 = U_2 C_{u2} \quad (2.18)$$

From the equation 2.17 and 2.18, the outlet tangential velocity component C_{u2} is determined by the following relation:

$$C_{u2} = \frac{\Delta h_1}{U_2} \quad (2.19)$$

+ The fluid flow angle is estimated as:

$$\tan \beta_2 = \frac{W_u}{C_{r2}} \quad (2.20)$$

+ The blade angle is defined as:

$$\tan \beta_{2b} = \tan \beta_2 - (1 - \sigma) \frac{U_2}{C_{r2}} \quad (2.21)$$

+ Absolute Mach number:

$$M_2 = \frac{C_2}{\sqrt{\gamma R T_{02}}} \quad (2.22)$$

The first rotor is then designed in ANSYS BladeGen based on the meridional view of the reference rotor and LR parameters as well as the blade angles calculated above. Four geometries of the first rotor are made, as shown in figure 2.4, and its specifications are summarized in table 2.3.

2.2.2 Second rotor design

The aerodynamic conditions at the first rotor outlet are used as the input condition at the second rotor inlet. To simplify the calculation, some assumptions are made:

+ The pressure at the first rotor outlet is the same at the second rotor inlet, $P_3 = P_2$;

+ The direction of the fluid flow is constant from the first rotor outlet to the second rotor inlet, $\alpha_2 = \alpha_3$;

+ The temperature between the first outlet is equal to the second rotor inlet, $T_2 = T_3$;

+ The velocity is preserved from the outlet of the first rotor to the inlet of the second rotor, $C_2 = C_3$.

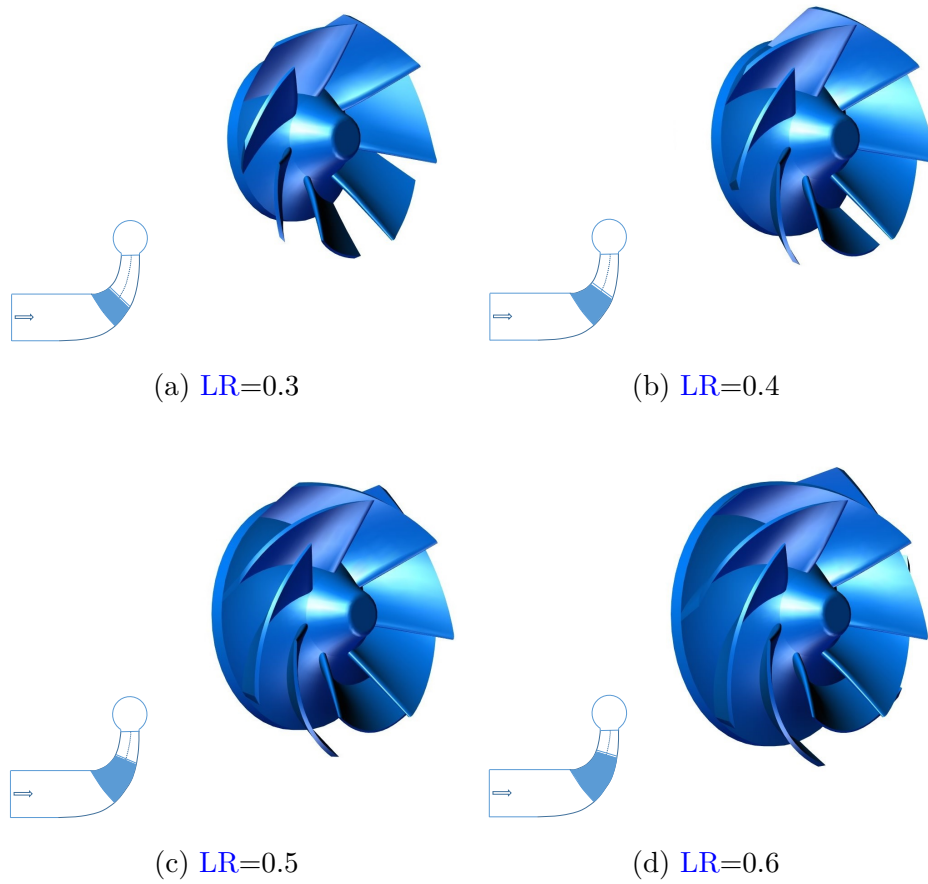


FIGURE 2.4 – Four geometries of the first rotors studied for four configurations of CRCC: (a) CF1, (b) CF2, (c) CF3 and (d) CF4

TABLE 2.3 – Geometric parameters of the first rotor of four CRCC configurations CF1, CF2, CF3, and CF4

Parameters	CF1	CF2	CF3	CF4
LR	0.3	0.4	0.5	0.6
d_{1h}	59.5mm	59.5mm	59.5mm	59.5mm
d_{1sh}	161mm	161mm	161mm	161mm
d_{2h}	118mm	140mm	163mm	186mm
d_{2sh}	176mm	186mm	200.8mm	216mm
Π_1	1.03	1.05	1.08	1.11
η_{1i}	90	90	90	90
β_{1h}	46°	46°	46°	46°
β_{1sh}	70.4°	70.4°	70.4°	70.4°
β_{2h}	51°	57.4°	56°	60°
β_{2sh}	68°	69.4°	68°	66.4°
N_1	-16000rpm	-16000rpm	-16000rpm	-16000rpm
Z_1	7	7	7	7

Inlet calculation

The blade inlet parameters of the second rotor are determined based on the velocity triangles, as shown in figure 2.3a:

$$\tan\beta_{3b} = \frac{U_3 + C_{u2}}{C_{r2}} \quad (2.23)$$

+ Inlet relative velocity:

$$W_3 = \sqrt{(U_3 + C_{u2})^2 + C_{r2}^2} \quad (2.24)$$

Outlet calculation

+ Outlet pressure is atmosphere pressure: $P_4 = P_{atm}$

+ Outlet temperature:

$$T_4 = T_3 \left[\frac{\Pi_2^{\frac{\gamma-1}{\gamma}} - 1}{\eta_{is}} + 1 \right] \quad (2.25)$$

+ Outlet gas density:

$$\rho_4 = \frac{P_4}{RT_4} \quad (2.26)$$

+ Meridional velocity component is determined by:

$$C_{m4} = \frac{\dot{m}}{\rho S_4} \quad (2.27)$$

Where S_4 is outlet area of the first rotor and determines by:

$$S_4 = 2\pi r_4 b_4 - Z_2 t_b b_4 \quad (2.28)$$

Because the fluid flows out in a radial direction at the second rotor outlet, the radial velocity component is equal to the meridional velocity component ($C_{r4} = C_{m4}$).

+ Total enthalpy rise is determined by:

$$\Delta h_2 = C_p T_3 \left(\Pi_2^{\frac{\gamma-1}{\gamma}} - 1 \right) \quad (2.29)$$

$$\Delta h_2 = U_4 C_{u4} + U_3 C_{u3} \quad (2.30)$$

+ Absolute tangential velocity component is calculated by:

$$C_{u4} = \frac{\Delta h_2 - U_3 C_{u3}}{U_4} \quad (2.31)$$

+ Relative tangential velocity component is obtained by the following equation:

$$W_{u4} = U_4 - C_{u4} \quad (2.32)$$

+ The outlet flow angle:

$$\tan \beta_4 = \frac{W_{u4}}{C_{r4}} \quad (2.33)$$

+ The outlet blade angle:

$$\tan \beta_{4b} = \tan \beta_4 - (1 - \sigma) \frac{U_4}{C_{r4}} \quad (2.34)$$

The second rotor parameters obtained are used to design the rotor geometry in ANSYS BladeGen. Four geometries of the second rotor are attained based on the previous design of the first rotor, as shown in figure 2.5. The summary of the geometric parameters of the second rotor is also presented in table 2.4.

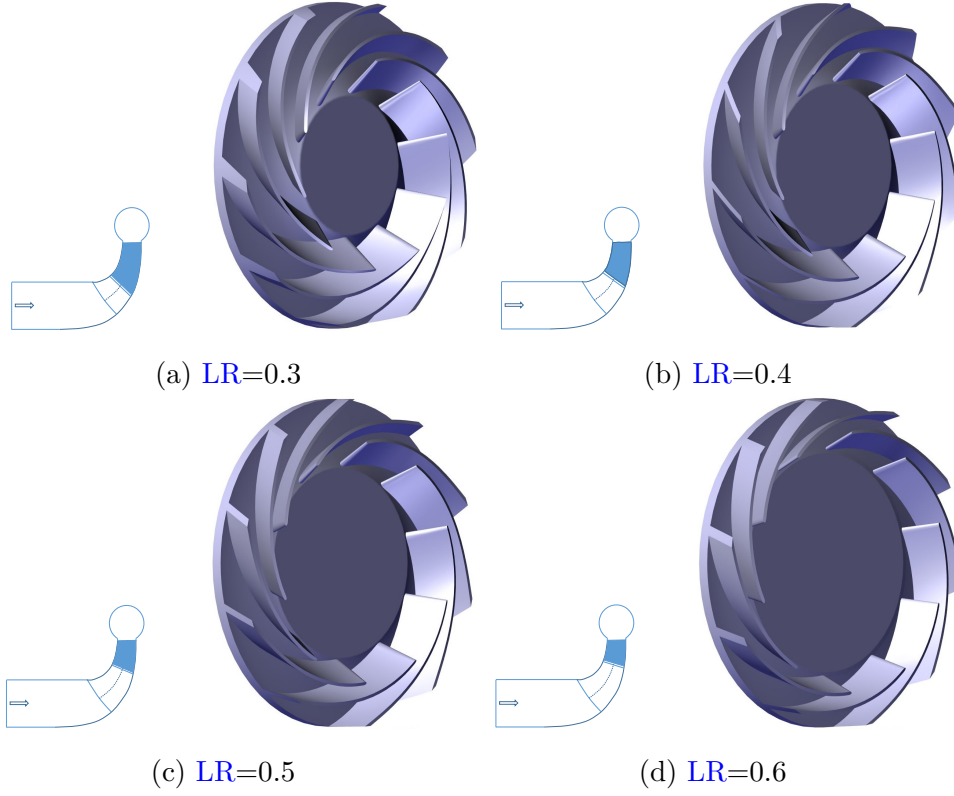


FIGURE 2.5 – Four geometries of the second rotors studied for four configurations of CRCC: (a) CF1, (b) CF2, (c) CF3, and (d) CF4

TABLE 2.4 – Geometric parameters of the second rotor of four configurations CF1, CF2, CF3, and CF4

Parameters	CF1	CF2	CF3	CF4
LR	0.3	0.4	0.5	0.6
d_{3h}	128.5mm	150mm	172mm	198mm
d_{3sh}	183mm	198mm	210mm	228mm
d_4	286mm	286mm	286mm	286mm
Π_2	1.27	1.25	1.22	1.20
η_{2i}	90	90	90	90
β_{3h}	73.9°	76.4°	79.6°	81.3°
β_{3sh}	77.7°	79°	80.9°	82.1°
β_4	64°	64°	64°	64°
N_2	16000rpm	16000rpm	16000rpm	16000rpm
Z_2	10	10	10	10

2.3 CRCC performance evaluation

An investigation is conducted to evaluate the effect of the LR parameter on the performance of the compressor. The results of this investigation allow us to choose the best configuration for CRCC in order to build a test bench for the experimental study. Computational Fluid Dynamic (CFD) simulation is a useful tool to predict the aerodynamic performances of a compressor. The simulation uses a three-dimensional, steady-state, compressible model with the commercial software STAR CCM+. The turbulence model is realizable k- ϵ two-layers and the second-order discretization method

is selected. The gap between the rotor and the casing does not consider in this study. More details of the numerical simulation are discussed in section 4.5.

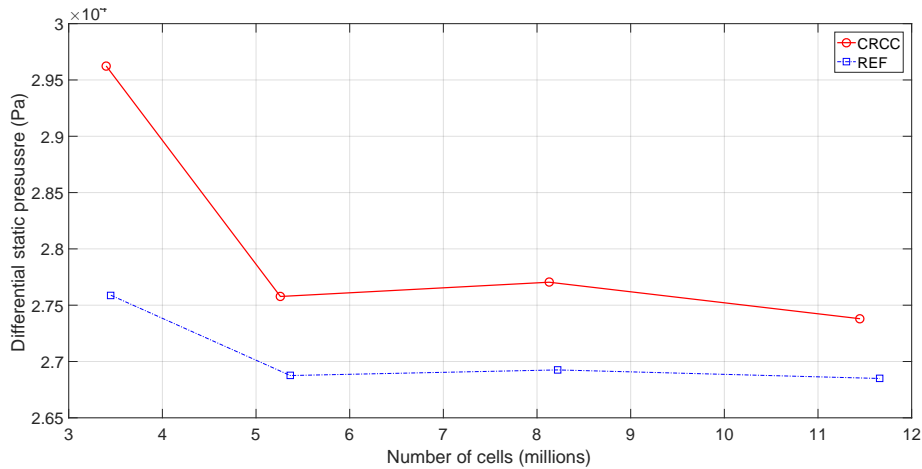


FIGURE 2.6 – Sensitive mesh study for both compressor configurations: \ominus -CRCC and \square -SRCC

The mass flow rate of 0.73kg/s is given as a boundary condition of the inlet domain. The pressure outlet is imposed at the outlet domain as the atmospheric pressure of $101,325\text{ Pa}$. In CRCC configuration, the first rotor rotates with a speed of $-16,000\text{rpm}$ and the second one as well as the rotor rotation speed of SRCC is fixed at $16,000\text{rpm}$. The frozen rotor interface is used between the stationary and rotating domain, while mixing-plane is used for the rotating domains interface [3]. The pressure and temperature values are taken from a constant grid surface as mass-average values at the inlet domain and the outlet domain. The mesh convergence is checked to find out the best mesh type of the model in order to reduce computational resources. For meshing in STAR CMM+, the polyhedral and prism layer mesher are used with refined mesh at the blade surfaces, interfaces, and boundary layers. The size of the mesh needs to respect the value of y^+ at the wall boundary near to 1. Four types of meshes are generated by adjusting the value of the relative size of the local refined mesh. The number of cells of these models are respectively 3.4, 5.26, 8.13, and 11.45 million.

Figure 2.6 shows the convergence of mesh of CRCC and SRCC. It can be seen from the figure that the static differential pressure between the inlet and outlet compressor seems to be stable when the number of cells is higher than 5.26 million. Therefore, it can be concluded that 5.26 million cells are sufficient to produce grid independent results. The details of mesh model are respectively presented in figure 2.7 and figure 2.8 for the SRCC and CRCC configurations.

2.3.1 Rotor performances

The rotor performance analysis is conducted to evaluate the impact of the counter-rotating system. Figure 2.9 illustrates the variation of the pressure ratio of the counter-rotating system and the reference rotor with the change of mass flow rate. This parameter is calculated between the inlet and outlet pressure of rotors. It is clear that the counter-rotating system gives a higher pressure ratio than the reference one at the flow rate lower than the Design Point (DP). There are three types of tendency: the first type shows the pressure ratio increases when the mass flow rate reduces. After attaining a peak, it drops sharply in CF3 and CF4 configurations. In the second type,

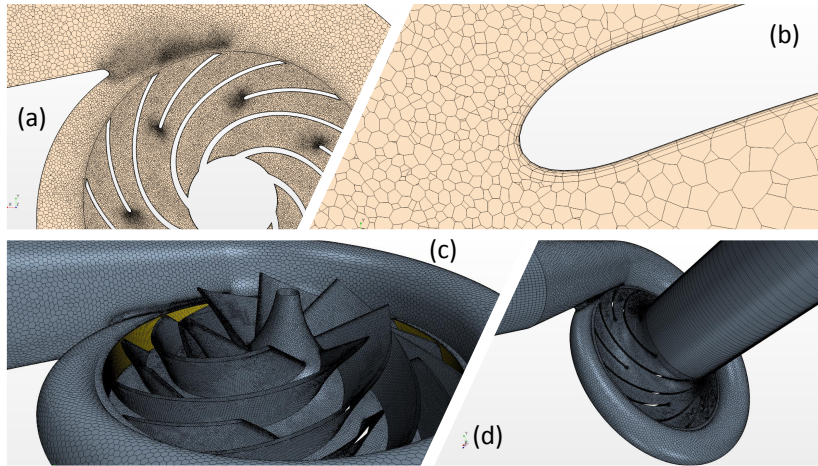


FIGURE 2.7 – Different views of **SRCC** mesh: (a) section mesh, (b) blade leading edge mesh, (c) rotor mesh, and (d) full mesh model

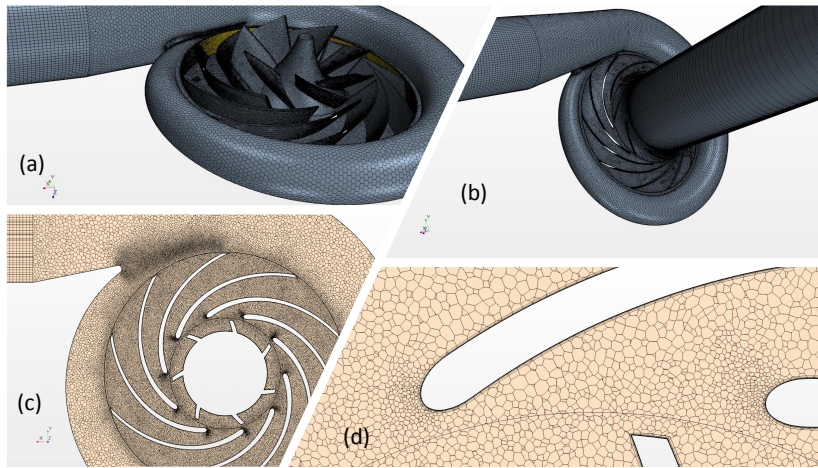


FIGURE 2.8 – Different view of **CRCC** mesh:(a) rotor mesh, (b) full mesh model, (c) section mesh, and (d) blade leading and trailing edge mesh

the pressure rises rapidly, after reaching the highest value, it becomes almost stable in **CF1**. The third one is stable and diminishes at 0.43kg/s in **CF2**. Looking at **DP** ($\dot{m} = 0.73\text{kg/s}$), the pressure ratio increases when **LR** rises. The highest pressure ratio can be achieved in **CF3** and **CF4** because the first rotor outlet has a larger diameter. As a matter of fact, it produces a higher kinetic energy flow into the second rotor. The maximum value of pressure ratio is 1.44 at the mass flow rate of 0.43kg/s while it is 1.29 for the **SRCC** configuration. **CF1** gives a quite stable pressure ratio at a low flow rate and the maximum pressure ratio reaches 1.34 which increases about 5% in comparison with the pressure ratio of **SRCC**. In contrast, at the higher mass flow rate, the pressure ratio of **CF1** decreases rapidly because of a smaller inlet surface area of the second rotor.

Figure 2.10 presents a variation of the polytropic efficiency of the rotors at different mass flow rates. This figure shows that the efficiency of the counter-rotating system is always lower than that of **SRCC** because of the extra loss at the inlet of the second rotor. Obviously, the efficiency of **CF1** is always higher than the other ones. The highest efficiency can reach 78% at **DP**. However, at high flow rates, it drops dramatically because of the appearance of the choked region. The lower efficiency of the counter-rotating system can be explained by the high relative Mach number at the leading edge

of the second rotor.

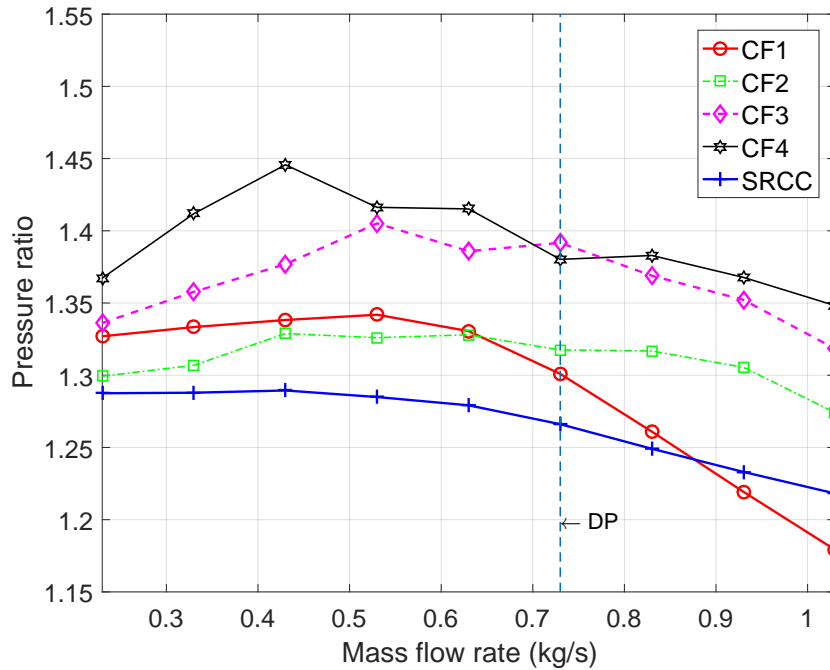


FIGURE 2.9 – Comparison of pressure ratios at the outlet of the rotors between four CRCC configurations: \circ CF1, \square CF2, \diamond CF3, \star CF4 and $+$ SRCC

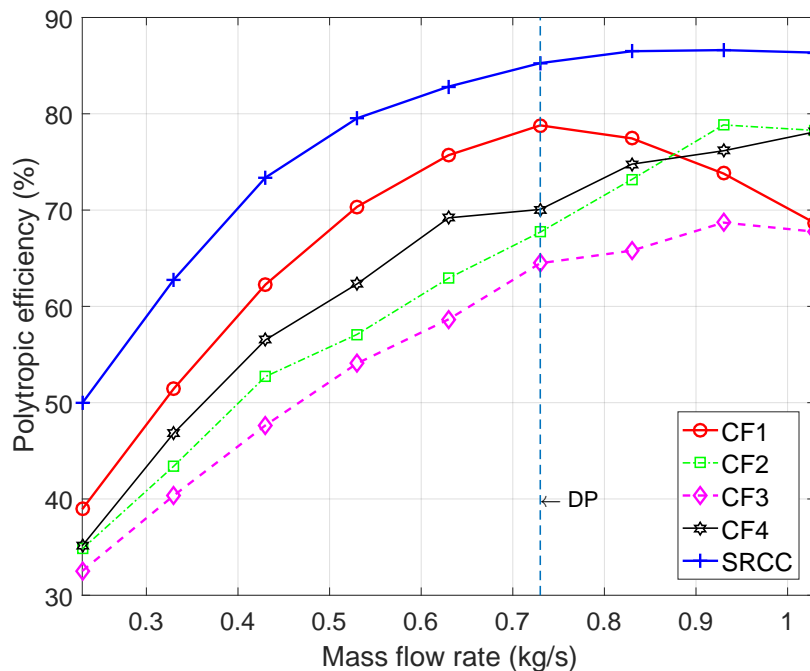


FIGURE 2.10 – Comparison of polytropic efficiencies at the outlet of the rotors between four CRCC configurations: \circ CF1, \square CF2, \diamond CF3, \star CF4 and $+$ SRCC

Figure 2.11 demonstrates the change of the relative Mach number at the leading edge of the second rotor. It can be observed that the relative Mach number increases monotonically with the increase of first rotor outlet diameter because of the counter-rotating effect. High relative Mach number leads to the shock waves and blockage at the inlet so that it reduces the performances of the rotor.

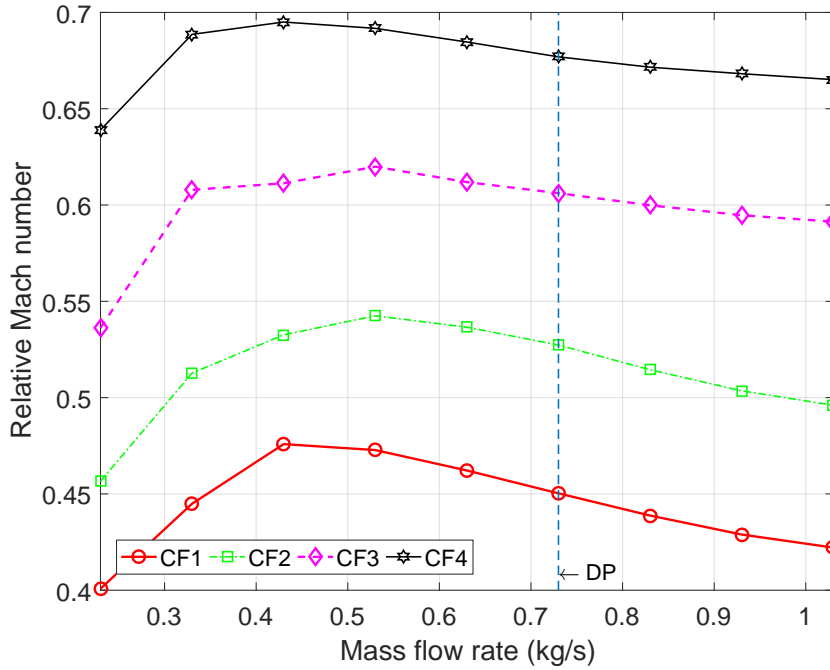


FIGURE 2.11 – Comparison of relative Mach numbers at the leading edge of the second rotor between four CRCC configurations: \circ CF1, \square CF2, \diamond CF3, \star CF4

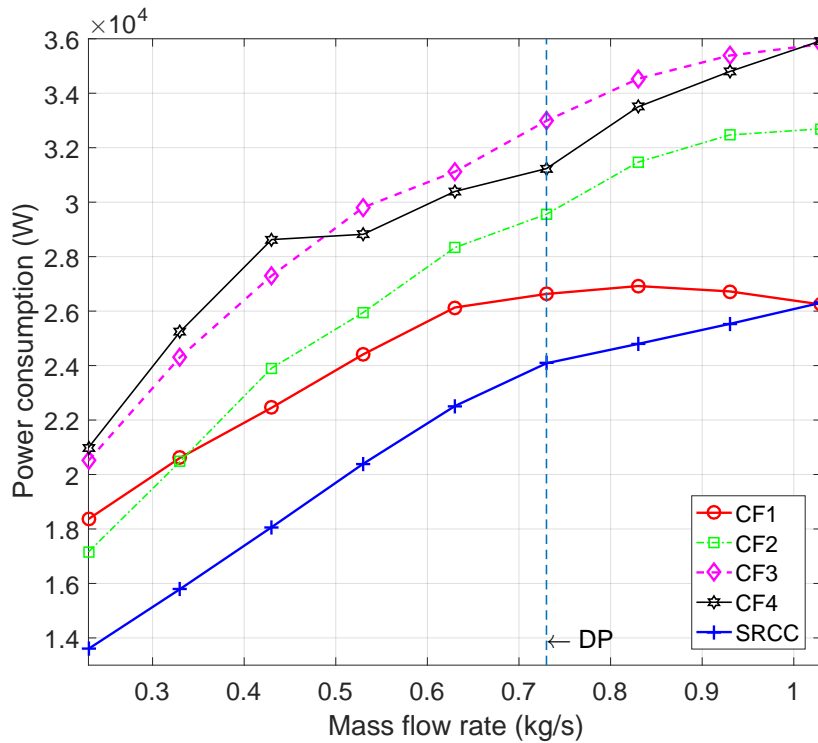


FIGURE 2.12 – Comparison of power consumptions between four CRCC configurations: \circ CF1, \square CF2, \diamond CF3, \star CF4 and $+$ SRCC

Concerning the power consumption, figure 2.12 shows that the counter-rotating system needs more energy than SRCC because of the higher pressure ratio and the extra loss at the inlet of the second rotor. CF3 and CF4 have a quite similar power consumption while there is a slight difference between CF1 and CF2. Looking at the

mass flow rate of 0.63kg/s in figure 2.9, *CF1* and *CF2* have the same pressure ratio but *CF2* consumes more energy than the first one. It means that *CF2* configuration generates more loss.

2.3.2 Compressor performances

Before analyzing the performances of the compressor, the volute performances are tested to estimate the ability of the adaptation between rotors and volute. The volute of the compressor transforms the kinetic energy of the fluid flow from the vanless diffuser or rotor into pressure, with minimum losses. To assess the adaptation of the volute with the counter-rotating system, the pressure recovery coefficient, and the pressure loss coefficient are used. According to Pitkanen et al. [33] the pressure recovery coefficient (C_{pr}) and the pressure loss coefficient (ω_{loss}) are respectively determined by:

$$C_{pr} = \frac{P_5 - P_4}{P_{04} - P_4} \quad (2.35)$$

$$\omega_{loss} = \frac{P_{04} - P_{05}}{P_{04} - P_4} \quad (2.36)$$

Figure 2.13 shows the change of the pressure recovery coefficient of the volute with the variation of mass flow rate. It is obvious that *CF1* and *CF2* have a value of C_{pr} close to the loss pressure coefficient of *SRCC* while this value for *CF3* and *CF4* decreases sharply when the mass flow rate increases. At near surge region, C_{pr} is positive with all configurations. At *DP*, the C_{pr} value of *CF4* is approximately zero while *CF1*, *CF2* and *CF3* remain positive in the range from 0.5 to 0.7. At very high flow rate, C_{pr} of *CF3* and *CF4* decreases rapidly and reaches the negative value of -0.6 and -1.5 , respectively. Consequently, *CF1*, *CF2* and *CF3* can recover pressure better than *CF4*.

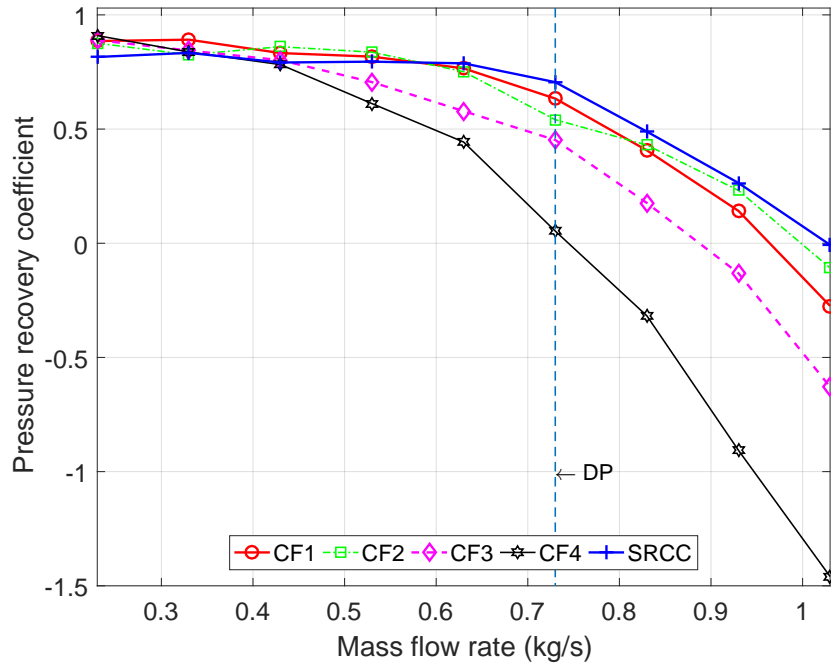


FIGURE 2.13 – Comparison of pressure recovery coefficients between four CRCC configurations: \circ CF1, \square CF2, \diamond CF3, \star CF4 and $+$ SRCC

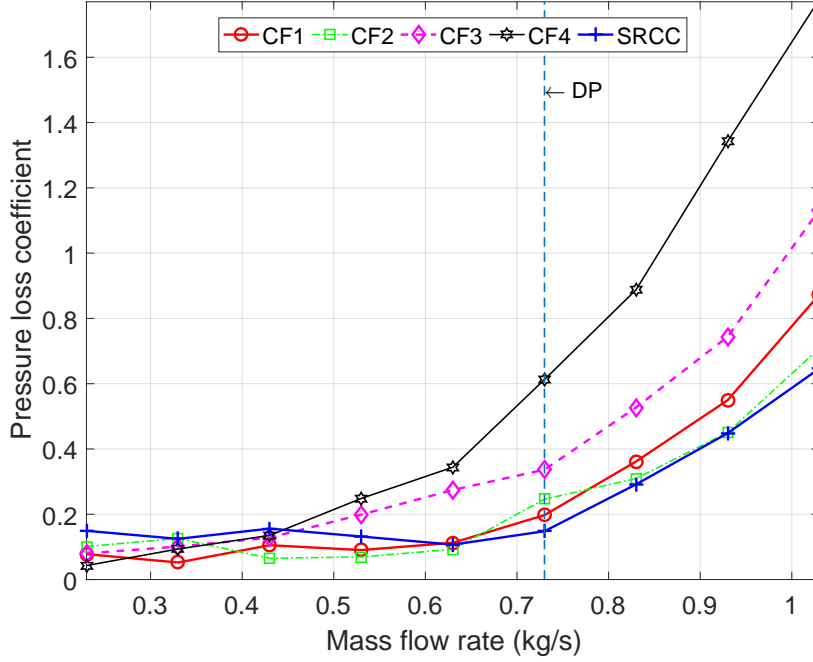


FIGURE 2.14 – Comparison of pressure loss coefficients between four CRCC configurations: \ominus CF1, \square CF2, \diamond CF3, \star CF4 and \oplus SRCC

Figure 2.14 illustrates the variation of the loss coefficient with the mass flow rate. The value of ω_{loss} remains stable in CF1 and CF2 and it is approximately equal to the loss coefficient of SRCC. It slightly increases in CF3 and rapidly rises in CF4 when the mass flow rate increases. In general, CF1 and CF2 are well adapted to the volute, while CF3 and CF4 configurations present higher pressure loss.

Figure 2.15 presents static pressure ratio of CRCC according to the mass flow rate variation. It is evident that, the pressure ratio of CRCC is indeed improved at a flow rate lower than DP. CF1, CF3 and CF4 configurations obtain a significant improvement in pressure ratio, while the pressure ratio of CF2 quite close to that of SRCC. At near surge region, the pressure ratio of CF1, CF3, CF4 maintain a similar values. Besides, CF2 pressure ratio has a values similar to the SRCC's one. Consequently, CF1 allows obtaining a pressure ratio more stable than other configurations.

Figure 2.16 shows the comparison of the polytropic efficiency of the compressor with the change of mass flow rate. It is clear that CF1 gives the best efficiency of 80% at DP. It reduces about 5% in comparison with the SRCC configuration. Therefore, CF1 is selected to build a CRCC test bench for experiment study.

2.3.3 Effect of speed ratio $\theta = N_1/N_2$

The advantage of CRCC is an independency of the rotation speed of each rotor. Changing the speed of the first rotor or the second rotor allows to obtain the different characteristics of the compressor. In this study, the speed of the first rotor is adjusted to increase of 110%, 120% and 130% of the design speed. The speed of the second rotor is fixed at 16,000rpm. The rotation speed ratio is defined as $\theta = N_1/N_2$, so that four values of θ are determined: $\theta_1 = -16,000rpm/16,000rpm$ (design speed), $\theta_2 = -17,600rpm/16,000rpm$, $\theta_3 = -19,200rpm/16,000rpm$ and $\theta_4 = -20,800rpm/16,000rpm$.

Figure 2.17 shows the variation of the pressure ratio of CF1 when the mass flow rate

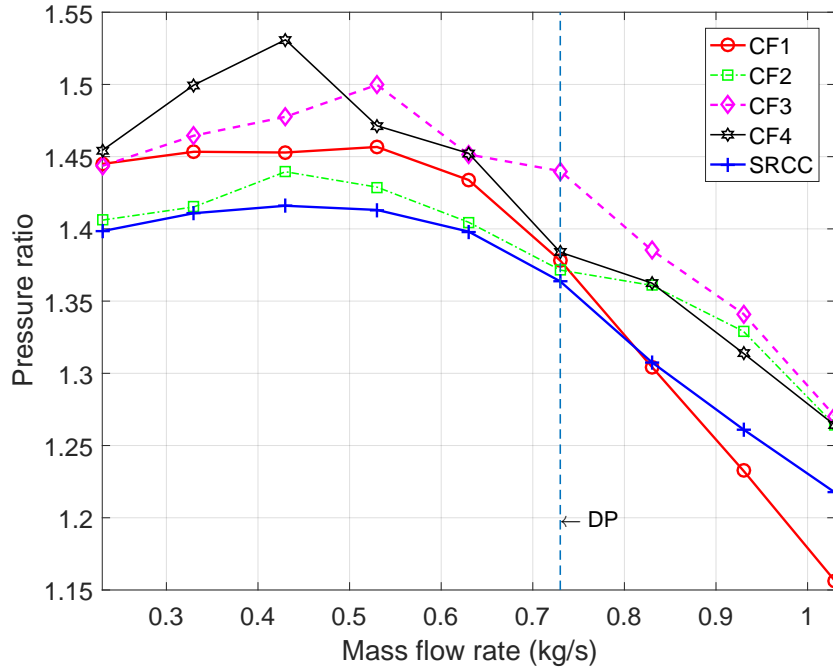


FIGURE 2.15 – Comparison of stage pressure ratios between four CRCC configurations: \ominus CF1, \square CF2, \diamond CF3, \star CF4 and $+$ SRCC

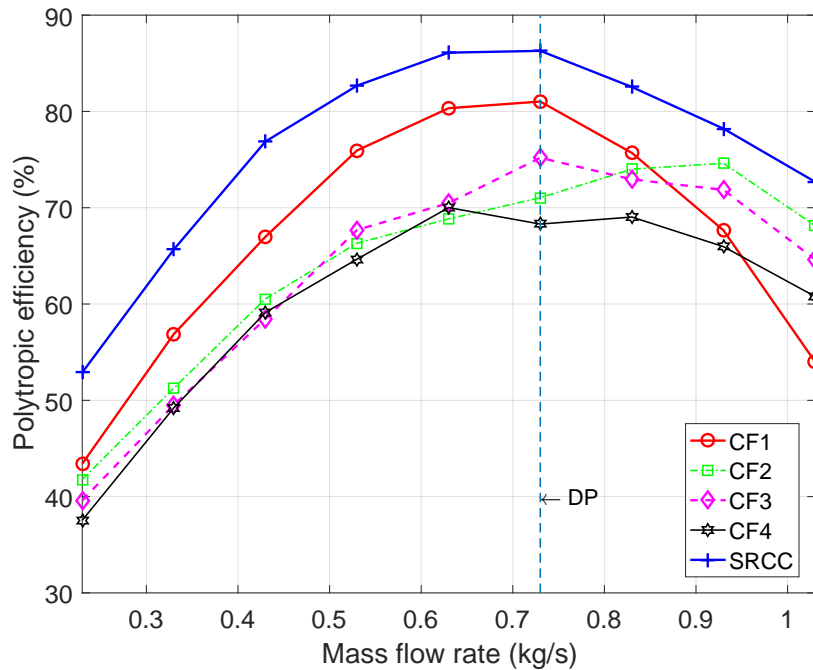


FIGURE 2.16 – Comparison of stage polytropic efficiencies between four CRCC configurations: \ominus CF1, \square CF2, \diamond CF3, \star CF4 and $+$ SRCC

changes with the different speed ratios of θ . It is obvious that the pressure ratio rises significantly with a higher rotation speed of the first rotor. At DP, the pressure ratio rises about 3% when the speed ratio increases by 10% of design speed (θ_2). Continuing to increase the speed ratio up to 130% of design speed (θ_4), the pressure ratio rises by about 8.78% in comparison with the pressure ratio of SRCC. The maximum pressure ratio of CRCC configuration can reach 1.53 at $\theta_3 = -1.3$, while the pressure ratio of

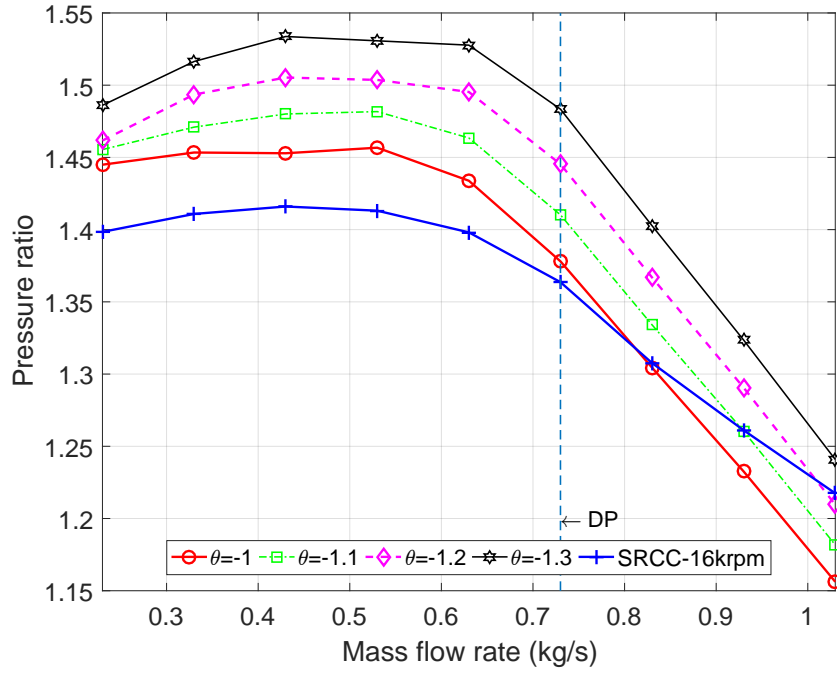


FIGURE 2.17 – The change in pressure ratios of the CF1 with the different speed ratios : $\ominus \theta_1 = -1$, $\square \theta_2 = -1.1$, $\diamond \theta_3 = -1.2$, $\star \theta_4 = -1.3$ compared to the pressure ratio of \oplus SRCC at 16,000rpm

SRCC is 1.41 at a flow rate of 0.73kg/s.

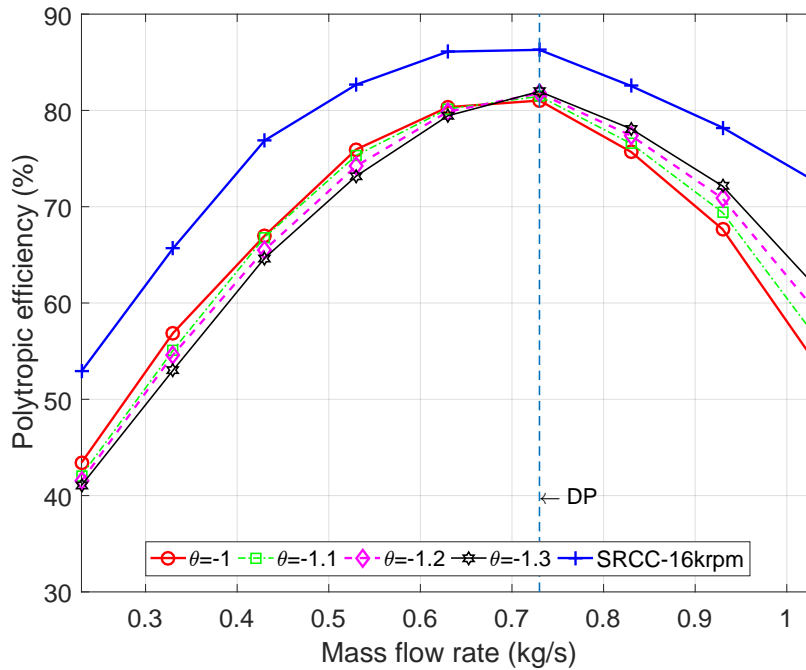


FIGURE 2.18 – The change in polytropic efficiencies of the CF1 with the different speed ratios: $\ominus \theta_1 = -1$, $\square \theta_2 = -1.1$, $\diamond \theta_3 = -1.2$, $\star \theta_4 = -1.3$ compared to the efficiency of \oplus SRCC at 16,000rpm

Figure 2.18 presents the efficiency of CRCC at different speed ratios in comparison with that of SRCC. It becomes clear that the polytropic efficiency reaches a maximum value of 80% at DP. It seems to be constant when the rotation speed increases.

2.4 Conclusions

In this chapter, the **CRCC** rotors are designed based on the geometric dimensions of the **SRCC** rotor. Four **CRCC** configurations are made based on the **LR** parameter to evaluate its effect on the global performance of the compressor. Four configurations **CF1**, **CF2**, **CF3** and **CF4** are respectively chosen based on four **LR** values of 0.3, 0.4, 0.5 and 0.6. Numerical simulations are conducted by using STAR CCM+ software to find the best **CRCC** configuration. The results of simulation show that:

- The counter-rotating system can improve the pressure ratio of the compressor. The pressure ratio rise depends on the **LR** parameter. The configuration with a higher length ratio gives more pressure ratio rise, however, the efficiency decreases rapidly.
- **CF1** and **CF2** are well adapted with the volute of the compressor because of higher pressure recovery coefficient and lower pressure loss coefficient. In addition, the efficiency of **CF1** reaches the highest value of 80% at the design point so that this configuration is selected to build **CRCC** configuration for a further experimental study (developed in chapter 4).
- The investigation of the variation of the first rotor rotation speed shows that it can be improved by about 8.7% pressure ratio at **DP** with the speed increase of 130% of design speed while the efficiency remains constant.

Configuration 1 selected to construct a counter-rotating centrifugal compressor for the experimental study is shown in figure 2.19. In chapter 4, the experimental study in this configuration is conducted on a test bench to analyze the performances. In addition, a study of the rotor speed on the **CRCC** operating range, especially, in the instability region is presented in chapter 5.

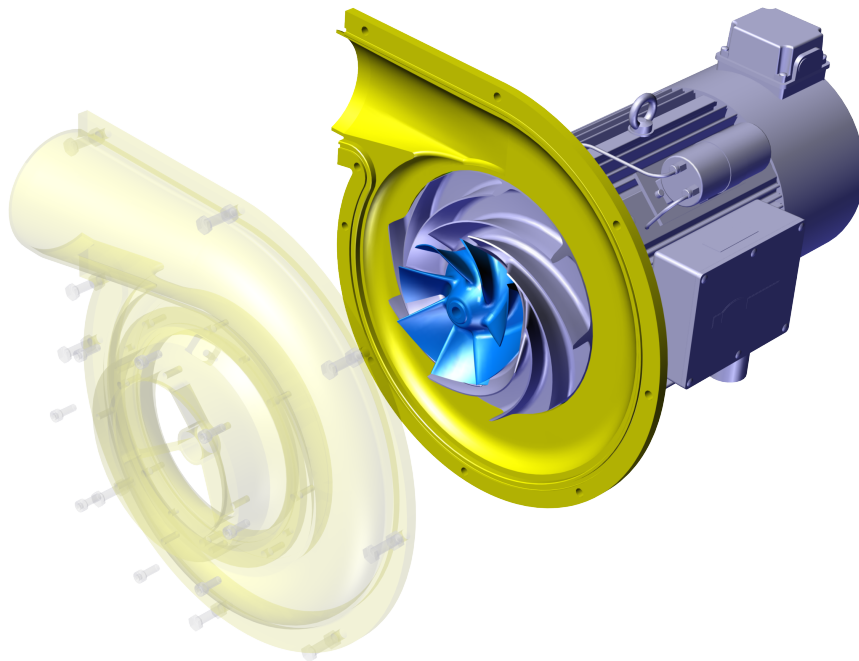


FIGURE 2.19 – The configuration 1 selected to build a counter-rotating centrifugal compressor

Chapter 3

RAICOR test bench design

Contents

3.1	Introduction of the existing test bench	37
3.2	CRCC components design	39
3.3	RAICOR test bench	48
3.4	Conclusions	55

A Rotor - rotor Aerodynamic Interaction of a COunter-Rotating centrifugal compressor (RAICOR) test bench is developed from an existing test bench of a conventional centrifugal compressor at the Laboratoire d'Ingénierie des Fluides et des Systèmes Énergétiques (LIFSE). A Single Rotor Centrifugal Compressor (SRCC) is selected as the reference compressor in this study. Because of using two independent rotors, Counter-Rotating Centrifugal Compressor (CRCC) is designed with some modifications at the inlet to be compatible with the existing test bench. SRCC is then replaced by CRCC while the other components of the test bench are preserved in order to evaluate influences of the counter-rotating system.

3.1 Introduction of the existing test bench

3.1.1 Description of the test bench operation

The centrifugal compressor test bench has been designed at LIFSE since 2016. It consists of a centrifugal compressor connected to an open-loop pipe. The compressor aspirates air at room temperature through a long pipe. The amount of air is regulated by a control valve. Then, the air enters the compressor where it is compressed before being blown out the atmospheric via a muffler. The test bench is illustrated as the figure 3.1. The sensor system is installed at the inlet and outlet of the compressor to determine the working parameters. The characteristics of SRCC is obtained by changing the mass flow rate at a constant speed. The combination of the characteristics at several constant speeds constitutes the performance map.

3.1.2 Performance map of the SRCC

The compressor characteristic map depicts the change of pressure ratio, efficiency according to the variation of mass flow rate with the different rotor speeds, as shown in figure 3.2. The x-axis represents the mass flow rate of the compressor, while the y-axis describes the static pressure ratio. The polytropic efficiency is then displayed

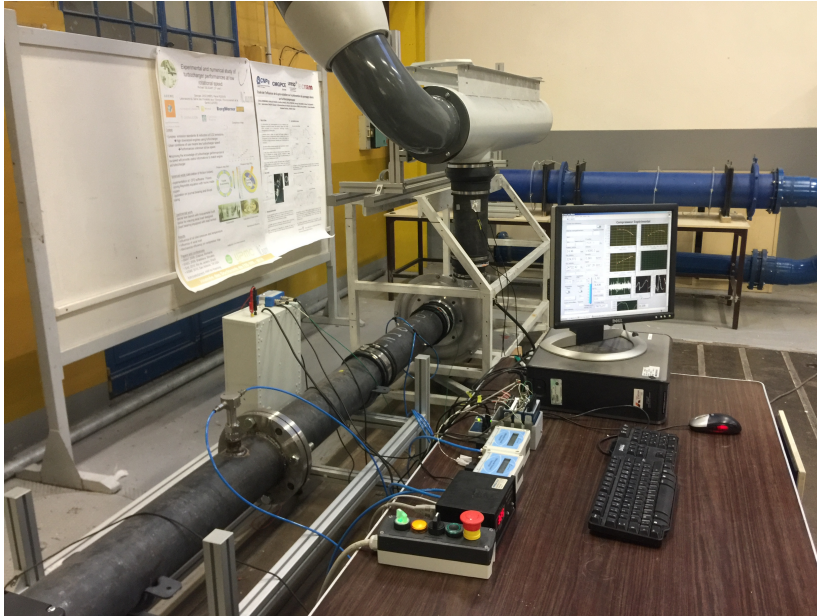


FIGURE 3.1 – Centrifugal compressor test bench used to measure the **SRCC** performances

as the coloring region. At each rotor speed, a characteristic curve of the compressor is obtained by changing the mass flow rate. A set of characteristic curves at the different rotor speeds produces a compressor map that allows us to know a working ability of compressor under different working conditions. In this study, eight rotor speeds are selected to measure the working parameters in order to build the compressor maps. At the design point, the compressor can achieve a pressure ratio of 1.31 and a maximum efficiency of 73% with the rotation speed of 16,000rpm and corrected mass flow rate of $\dot{m}_{cr} = 0.966\text{kg/s}$. At the lowest rotation speed of 9,000rpm, the pressure ratio attains 1.1 and the peak efficiency decreases to 64% with the mass flow rate of $\dot{m}_{cr} = 0.458\text{kg/s}$.

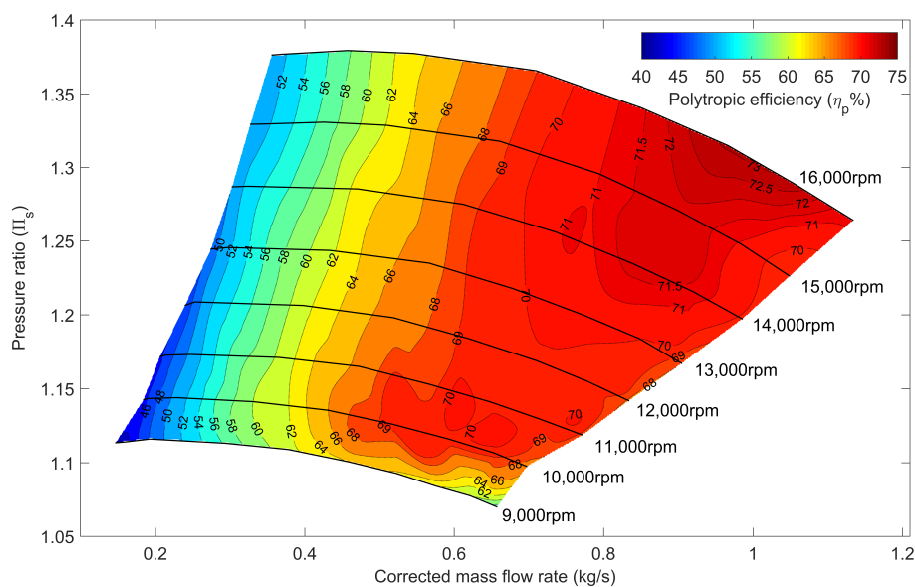


FIGURE 3.2 – Performance map of **SRCC** obtained by experimental measurement

3.2 CRCC components design

3.2.1 Adaptation with the existing test bench

The difference between CRCC and SRCC is in the structure of the counter-rotating system. CRCC has two independent rotors so that it needs two drive motors. These motors are arranged on both sides of the compressor and are controlled by two inverters. For that reason, CRCC needs to modify the drive system of the upstream rotor in order to be compatible with the test bench, especially the inlet form. Because the two motors are located on both sides of the compressor, it is impossible to make a straight inlet as the reference compressor. Therefore, the direction of the fluid flow must be changed before entering the compressor. There are many ways to direct the fluid flow into the compressor such as spiral inlet, bent inlet, etc. A bent inlet is suitable in this circumstance because it is easy to produce and cheaper than the others. In addition, the distance between the upstream rotor and the drive motor should be minimal to respect the critical speed of the drive shaft at high speed. A bent pipe with an angle of 90° can meet these requirements so it is used to design an inlet component. However, the use of the 90° bent pipe changes the flow structure at the inlet of the compressor so a study of the bent pipe effect the performance of CRCC is performed.

Comparison of the performance between straight inlet and bent inlet

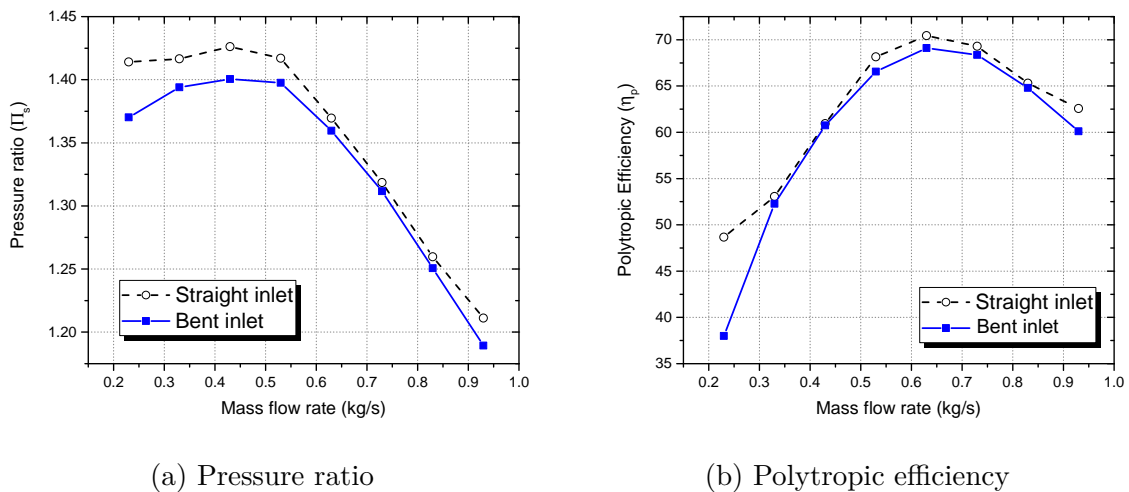


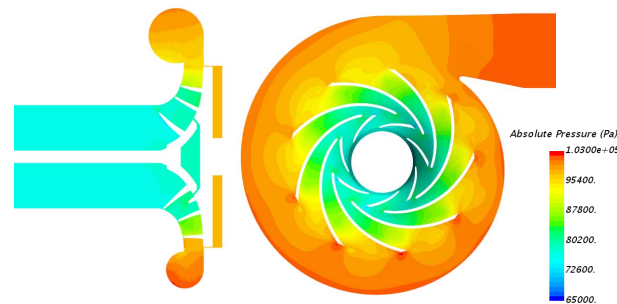
FIGURE 3.3 – Comparison of performance between straight and bent inlet obtained by CFD simulations

In the industry, there is not always enough space to install straight inlet pipes so that a bent inlet pipe is used as an alternative solution. However, using the bent inlet makes an inlet distortion and causes the variation in the incidence angle. Consequently, it affects the performance and the surge margin of a compressor [34]. Wright et al. [35] attempted to quantify the inlet flow distortion effects on the performance of a centrifugal fan. Results showed that the inflow distortion of the fan reduces the efficiency and pressure rise. Each level of distortion from 10 – 15% of velocity variations can reduce 5% of the efficiency and pressure rise. Kim et al. [36] used a 90° bent pipe in front of a centrifugal compressor and found that the inlet environment has a significant impact on the performance of the compressor. The work of Yan et al. [37] compared

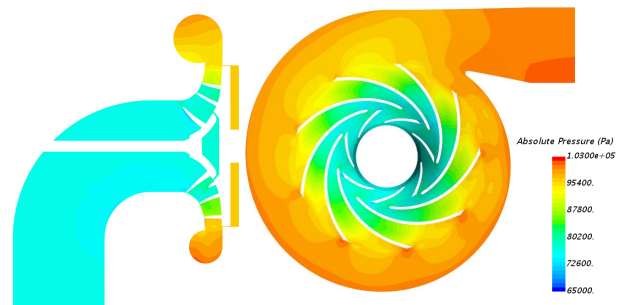
also 90° duct to a straight duct. They concluded that the distortion of an inlet flow has a negative impact on the performance of the centrifugal fan. Li et al. [38] studied the effect of two types of 90° bent inlet on the performance of a high-speed centrifugal compressor. They presented the inlet distortion decreases the choke limit to a lower mass flow rate. In addition, the performance near the choke is reduced as the rotation speed increases. The authors concluded that the bent inlet with longer axial distance makes larger radial range distortion on the impeller inlet. The results also showed that the use of a curved inlet influences the performance of the compressor, especially near the choke with a high flow rate. In this study, it is necessary to evaluate the impact of a bent inlet on compressor performance because of the input structure change. To do that, two numerical models of the straight and bent inlet are modeled. A numerical study is conducted with the STAR CCM+ software to figure the difference between two configurations. The more detail of the numerical models presents in section 4.5.

Figure 3.3 compares the performances between the straight inlet and bent inlet at different flow rates. In general, the performance of the two cases is almost the same. The most significant difference occurs in the near surge region, where the efficiency value and pressure ratio of the bent inlet decrease. In order to have a better understanding of this phenomenon, the flow field analysis is shown to see what is going on at the low mass flow rates.

Figure 3.4 and figure 3.5 show the pressure distribution of both straight and bent inlet at the highest efficiency and near surge point. At the highest efficiency, the pressure distribution is overall the same for two cases. At near surge point, however, it can be seen that the flow is facing an adverse pressure gradient at the outlet of the second rotor and the volute - the inertial forces cannot overcome the pressure forces [39]. The iso-pressure is formed from the volute tongue inside the volute.

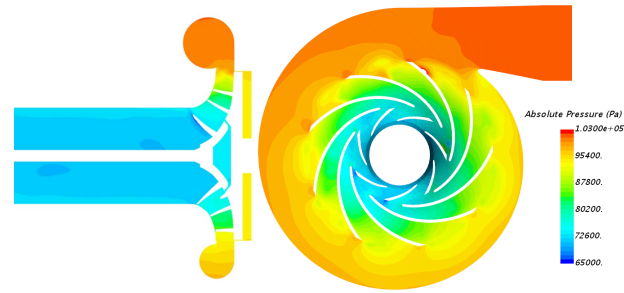


(a) Straight inlet

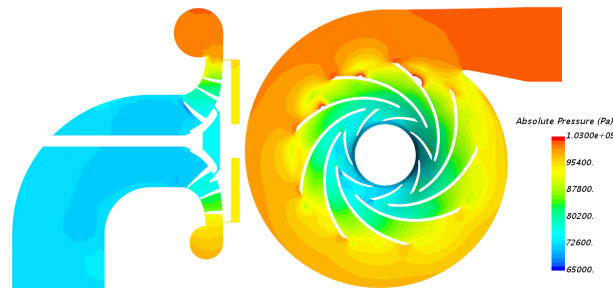


(b) Bent inlet

FIGURE 3.4 – Pressure distribution of (a) straight inlet and (b) bent inlet, at $\dot{m}_{cr} = 0.73\text{kg/s}$ and $N_1 = -16,000\text{rpm}$, $N_2 = 16,000\text{rpm}$ (best efficiency point)

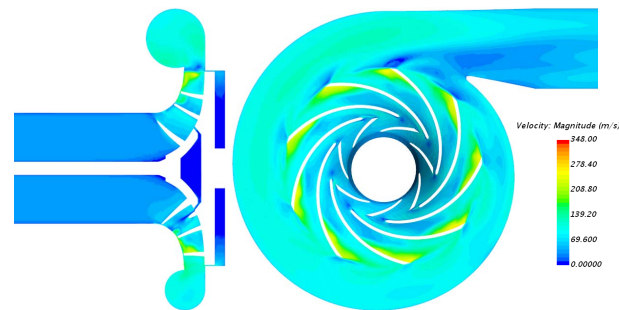


(a) Straight inlet

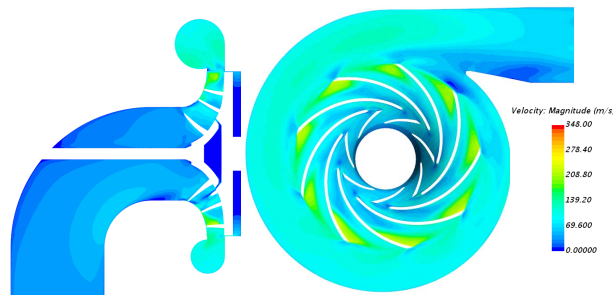


(b) bent inlet

FIGURE 3.5 – Pressure distribution of (a) straight inlet and (b) bent inlet, at $\dot{m}_{cr} = 0.23\text{kg/s}$ and $N_1 = -16,000\text{rpm}$, $N_2 = 16,000\text{rpm}$ (near surge point)



(a) Straight inlet



(b) bent inlet

FIGURE 3.6 – Velocity field of (a) straight inlet and (b) bent inlet, $\dot{m}_{cr} = 0.73\text{kg/s}$ and $N_1 = -16,000\text{rpm}$, $N_2 = 16,000\text{rpm}$ (best efficiency point)

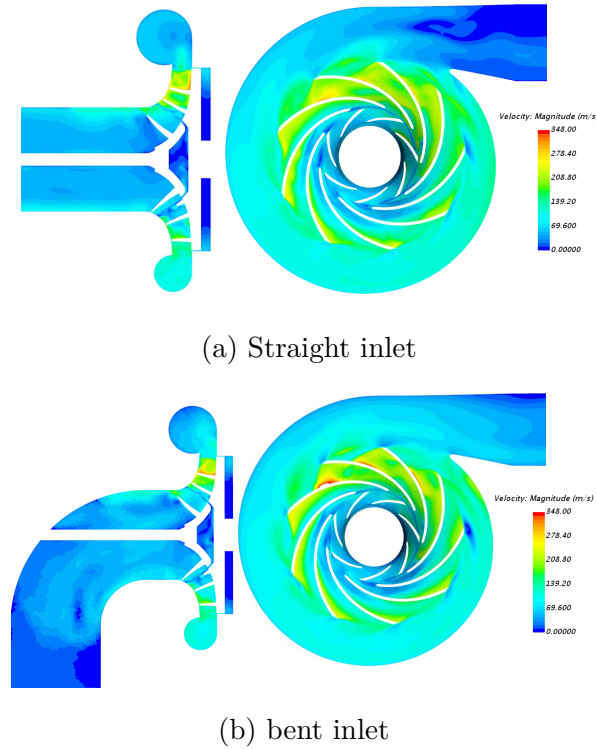


FIGURE 3.7 – Velocity field of (a) straight inlet and (b) bent inlet, $\dot{m}_{cr} = 0.23\text{kg/s}$ and $N_1 = -16,000\text{rpm}$, $N_2 = 16,000\text{rpm}$ (near surge point)

The velocity distribution in both cases is shown in figure 3.6 and figure 3.7. Some differences are found in the inlet region. It is clear that the straight inlet has an asymmetric flow field, while the bent inlet creates a non-symmetric flow before the first rotor, especially near the surge region. This phenomenon generates more inlet losses so that the performance of the compressor decrease.

The imbalance of axial velocity distribution of bent inlet can be clearly seen if it is analyzed in the direction perpendicular to the axis of rotation as shown in figure 3.8. At the best efficiency point, the axial velocity is properly balanced in the straight inlet but it does not balanced for the bent inlet. The velocity of distribution on the small radius side is greater than the other side. In contrast, at near surge region, the velocity on the larger radius side is higher, and the backflow is observed in this case (negative velocity). In such a way, the use of bent inlet has an effect on the performance of the machine, but it can be seen that the bent inlet has a slight impact on the performance of the compressor near the point design. It is only a major influence that occurs near the surge region. Fortunately, this region can be improved by adjusting the rotation speed of each rotor. Therefore, using a bent inlet is possible before obtaining an optimal mechanical solution for this case.

3.2.2 CRCC test bench components design

The CRCC components of the test bench need to design include: two counter-rotating rotors, driveshaft, shroud block, bent inlet block, support blocks, etc. Because CRCC is a high-speed compressor so that all rotating components need to analyze the strength and the natural frequency to ensure the durability and to avoid the resonance phenomenon. This section presents a method for analyzing constraints and determining the natural frequency of test bench components.

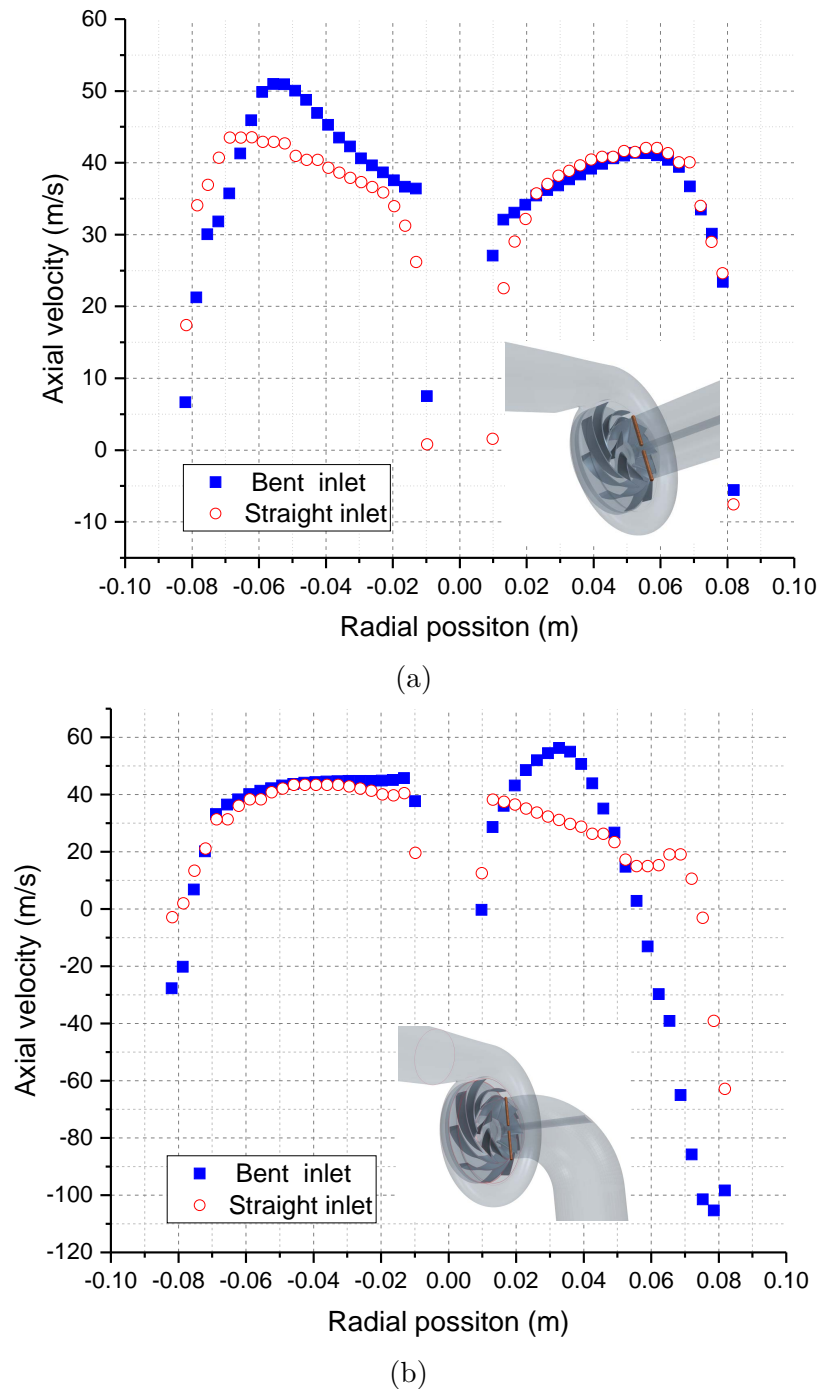


FIGURE 3.8 – Comparison of axial velocity between bent inlet and straight inlet at (a) best efficiency point and (b) near surge point

The first rotor

The first rotor geometry is designed by CATIA with the parameters presented in chapter 2. The geometry is optimized with the space inside the compressor, as shown in figure 3.9a. This rotor works at high rotation speeds so that it is necessary to conduct mechanical analysis to check the working ability. There are two types of mechanical analysis include stress analysis and displacement analysis are performed. Stress analysis is conducted to check the stress to avoid rotor damage. The result of stress analysis is presented in figure 3.9b. It is easy to see that the stress is concentrated at the foot of the blades with a value of 271MPa . The material is Aluminum 7075 with a shear

stress of 331MPa so that the first rotor meets durability requirements. Displacement analysis is also carried out as shown in figure 3.9c. The largest displacement occurs at the tip of the blade with a maximum value of 0.71mm . This value is smaller than the gap between the rotor and shroud of 1.5mm . So this design meets the working requirements of the first rotor.

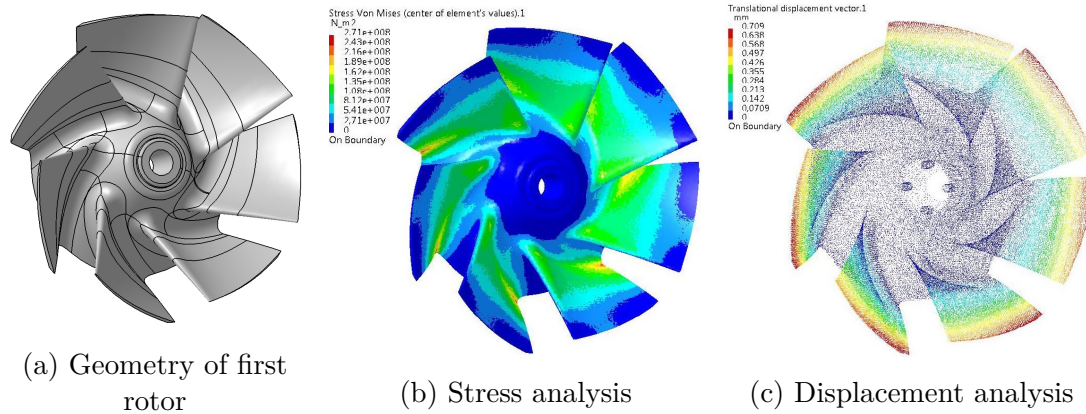


FIGURE 3.9 – First rotor analysis of the chosen configuration (CF1) for the experimental test bench

The second rotor

The second rotor is also designed and tested for durability and displacement by CATIA software. The stress analysis shows that results do not match with the stress of the material so we need to reduce the blade number from ten blades to nine blades. The geometry and stress analysis of the second rotor are shown in figure 3.10a and figure 3.10b. The analysis depicts that the maximum stress occurs at the foot of the blade. It is less than the allowable stress value of the Aluminum 7075 material. In addition, the displacement analysis in figure 3.10c illustrates the maximum displacement on the tip of blade about 0.4mm . It is always smaller than the gap between the rotor and shroud. Therefore, the design of the second rotor meets the requirements, too.

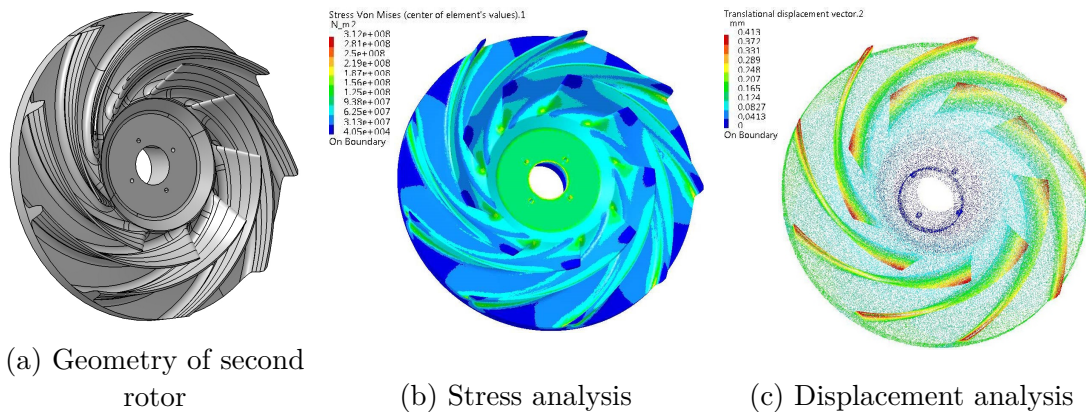


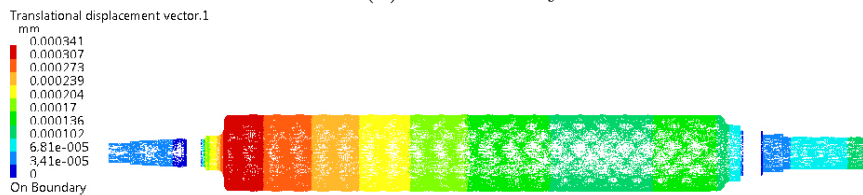
FIGURE 3.10 – Second rotor analysis of the chosen configuration (CF1) for the experimental test bench

Drive shaft of the first rotor

The first rotor is driven by an electric motor through an extra shaft. The length of the shaft is determined after selecting the geometry of the bent inlet. The shaft diameter is then calculated by optimizing the geometry to respect the critical speed. The static analysis and displacement analysis are shown in figure 3.11.



(a) Stress analysis



(b) Displacement analysis

FIGURE 3.11 – Analysis of the drive shaft of the first rotor used for the CRCC test bench with (a) stress analysis and (b) displacement analysis

The stress analysis shows that the greatest stress is concentrated at the shoulder fillet of the step, as shown in figure 3.11a. The maximum stress value of 22MPa is much smaller than the strength limit of 350MPa . Therefore, the shaft meets durable conditions. The maximum displacement takes place at the largest diameter of the shaft as shown in figure 3.11b. This displacement is very small, so it can be ignored. Besides, the modal analysis is also conducted, and the results are shown in table 3.1. It displays the first natural frequency value of 1147.1Hz corresponds to $68,826\text{rpm}$. This speed is much higher than the nominal rotation speed of the shaft. So the design shape of the shaft is reasonable.

TABLE 3.1 – Modal analysis of the drive shaft

Mode	Frequency (Hz)	Stability	Mode	Frequency (Hz)	Stability
1	1,147.1	$9.6242e-14$	6	3,514.6	$4.5219e-10$
2	1,147.5	$2.7806e-14$	7	3,515.9	$2.7096e-9$
3	3,100.3	$1.0596e-10$	8	6,401.7	$7.5957e-6$
4	3,210.5	$4.1614e-10$	9	6,406	$4.2726e-5$
5	3,213.8	$3.5387e-9$	10	6,406.9	$9.8198e-5$

Shroud block

The shroud block consists of a half shroud contour of the compressor. In the CRCC configuration, the first rotor is driven by an electric motor through a long shaft. In order

to ensure the stability of the drive system in relation to the critical speed of the shaft, a support bridge is made. The geometry of the shroud block is depicted in figure 3.12. A shape of support bridge is determined and verified by a modal analysis to find out its natural frequency. This step is necessary to avoid a resonance phenomenon. Table 3.2 shows the results of natural frequency analysis by CATIA. The natural frequency is $415Hz$, corresponding to the rotation speed of $24,900rpm$. It is larger than the nominal speed of the drive shaft so that this component meets the requirements.

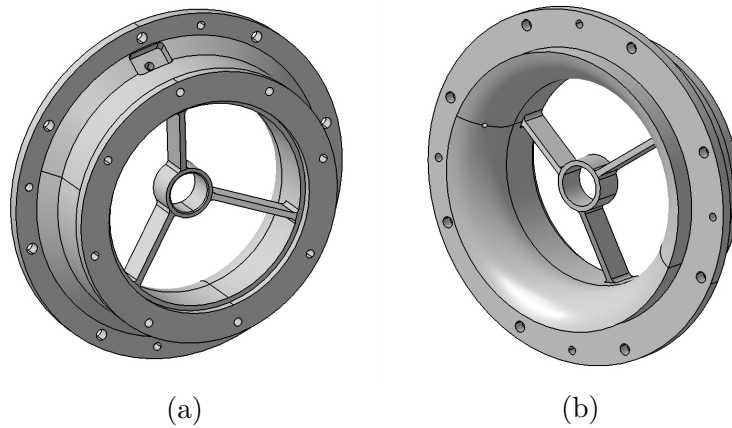


FIGURE 3.12 – Geometry of Shroud block of the CRCC configuration of the test bench: (a) face view and (b) rear view

TABLE 3.2 – Modal analysis of shroud block

Mode	Frequency (Hz)	Stability	Mode	Frequency (Hz)	Stability
1	415.03	$6.8452e-11$	6	702.30	$1.9831e-7$
2	471.75	$2.3556e-10$	7	161.33	$6.4904e-5$
3	474.38	$6.0429e-10$	8	161.39	$4.7703e-5$
4	560.73	$2.3638e-10$	9	215.05	$4.2646e-4$
5	702.14	$4.1553e-8$	10	236.67	$9.0831e-4$

Inlet block

The inlet block consists of a 90° bent pipe and a housing of a bearing. This block is responsible for directing flow into the compressor. The inlet block geometry is shown in figure 3.13. The modal analysis results are shown in table 3.3. It illustrates that the natural frequency reaches $1,410Hz$ which corresponds to the rotation speed of $84,684rpm$. This speed is much larger than the design speed of the drive shaft so that this component ensures no resonance during the operation.

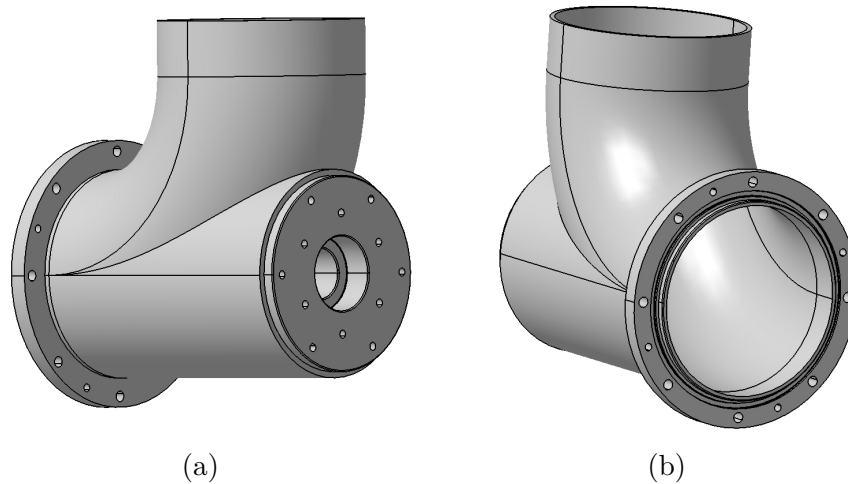


FIGURE 3.13 – Geometry of the inlet block of the CRCC configuration used for the test bench (a) front view and (b) rear view

TABLE 3.3 – Modal analysis of inlet block

Mode	Frequency (Hz)	Stability	Mode	Frequency (Hz)	Stability
1	1,411.4	$9.3339e-9$	6	2,520.7	$1.5208e-6$
2	1,437.4	$3.5050e-9$	7	2,549	$3.8400e-5$
3	1,730.6	$1.7101e-8$	8	2,610.9	$8.2048e-6$
4	1,760.6	$2.4277e-8$	9	2,887.8	$6.5777e-5$
5	2,420.6	$1.2072e-5$	10	3,117.4	$5.9586e-4$

Support of electric motor

A support block of the electric motor is designed to ensure the concentricity of rotational parts because of high-speed rotation. This block links the drive motor and the inlet block. The structure and geometry of the block are shown in figure 3.14. The modal analysis is shown in table 3.4. The first frequency is $4884.9Hz$, which means the resonance speed of the system reaches $293,094rpm$. Consequently, this component meets safety requirements.

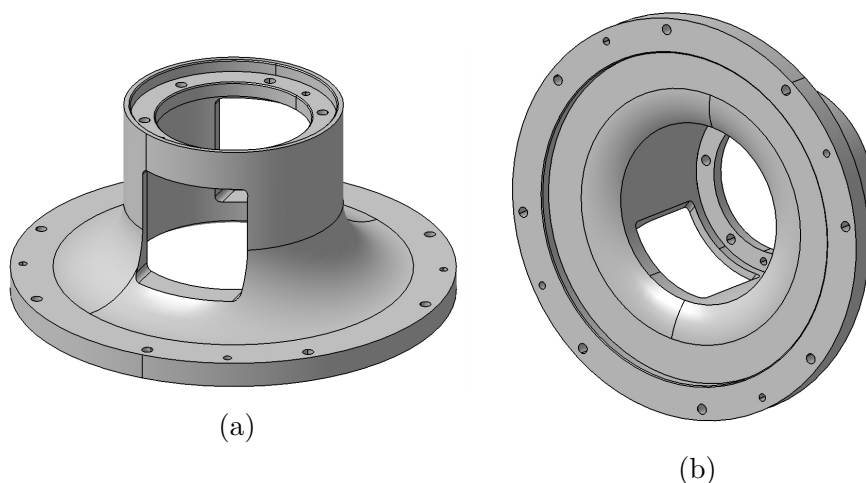


FIGURE 3.14 – Geometry of the electric motor support of the CRCC configuration used for the test bench: (a) front view and (b) rear view

TABLE 3.4 – Modal analysis of electric motor support

Mode	Frequency (Hz)	Stability	Mode	Frequency (Hz)	Stability
1	4,884.9	$1.9554e-8$	6	5,847.8	$4.4559e-7$
2	5,035.9	$2.4754e-8$	7	6,319.6	$1.2921e-5$
3	5,372.5	$4.3348e-7$	8	6,923.9	$2.9898e-5$
4	5,542.7	$7.1500e-7$	9	6,940.8	$2.0430e-4$
5	5,678.3	$3.8406e-6$	10	7,245.2	$5.2465e-5$

Counter-rotating centrifugal compressor assembly

After designing all components of the compressor, they are manufactured and assembled to form the counter-rotating centrifugal compressor. The structure of the counter-rotating centrifugal compressor is illustrated in figure 3.15.

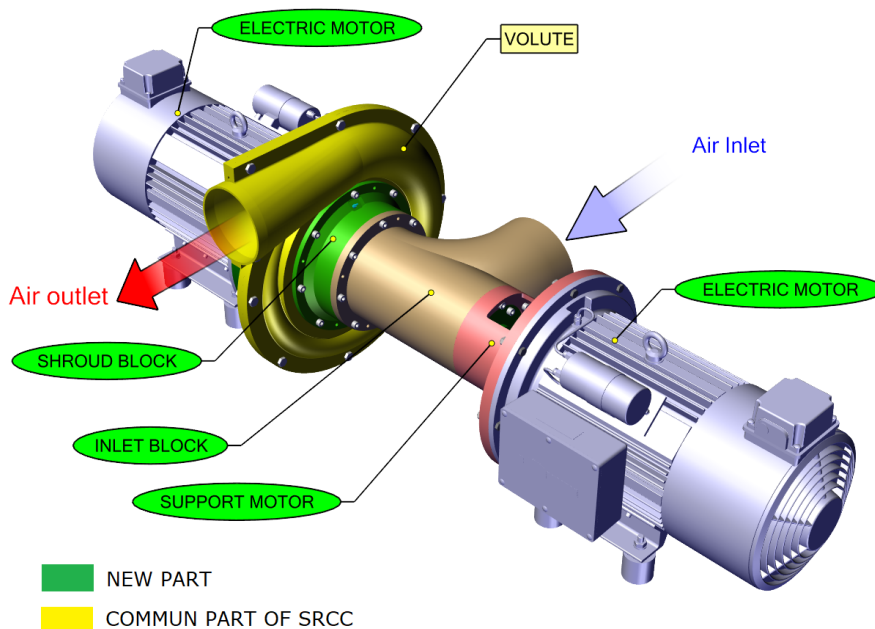


FIGURE 3.15 – Counter-rotating centrifugal compressor (CRCC)

3.3 RAICOR test bench

3.3.1 Description of Rotor - rotor Aerodynamic Interaction of a COunter-Rotating centrifugal compressor (RAICOR) test bench

As described in the preceding section, Counter-Rotating Centrifugal Compressor (CRCC) components are redesigned to adapt to the existing test bench. SRCC is then replaced by CRCC to form a new test bench called the Rotor - rotor Aerodynamic Interaction of a COunter-Rotating centrifugal compressor (RAICOR). Figure 3.16 shows the schema of the RAICOR test bench used in this study.

The working of the test bench is described here: Firstly, the air at room temperature is aspirated into the tank (1) through a plate that has 120 holes with a diameter of

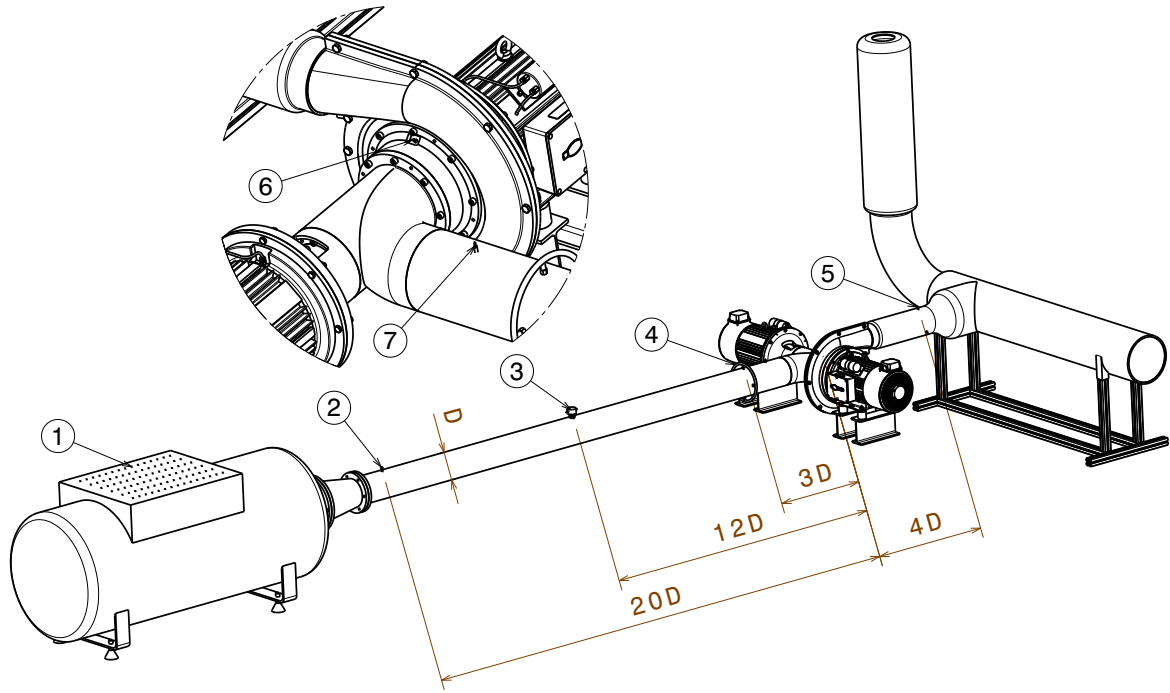


FIGURE 3.16 – Schema of RAICOR test bench

8mm. These holes permit to adjust the inlet flow rate into the compressor. Then, the air passes through a long pipe diameter of $D = 158,5\text{mm}$. A honeycomb is placed upstream of the pipe to ensure that the inlet flow is laminar. Next, the air enters the compressor where it is transmitted energy by the rotors. The differential pressure between the inlet and outlet of compressor increases. Finally, the air passes via a muffler and is blown out into the atmosphere. Two rotors of CRCC are driven by two electric motors with a maximum speed of $17,000\text{rpm}$. Two inverters are used to control the speed of the rotors and to measure the power consumption of the electric motors. The sensor system is arranged as shown in figure 3.16. A thermocouple Pt100 (2) is used to measure the inlet temperature and located upstream at a distance of $20D$ from the compressor. The Platon pitot tube (3) places upstream at a distance of $12D$ from the compressor. It is connected to the FCO16 manometer to measure the differential pressure of the fluid flow through the pitot tube. The mass flow rate is calculated by this differential pressure according to equation 3.24. Four pressure taps (4) on the circumference of the inlet pipe at a distance of $3D$ use to collect the average pressure at the inlet of the compressor. It is connected to the FC332 manometer to measure the differential pressure between the inlet pressure and atmospheric pressure. Three thermocouples Pt100 (5) are located downstream on the outlet pipe at a distance of $4D$ from the compressor to measure the outlet temperature. Two Kistler dynamic pressure sensors (6), (7) are mounted on the inlet and between two rotors to measure instantaneous pressure and identify the frequency of instability phenomenon.

3.3.2 Uncertainties and measurement quantities

Measuring a quantity is not simply looking for the value of this quantity, but also associating it with uncertainty in order to be able to qualify the quality of the measurement. This uncertainty is associated with measurement errors which may be due to the measuring instrument, the operator, or the variability of the measured quantity.

Measurement uncertainty is the value characterizes the dispersion of values that can be attributed to the measured quantity. There are two types of measurement errors:

Random measurement error

When the same operator repeats several times, under the same conditions and the measurement of the same quantity, the measured values may be different. This is called a random error of measurement. The associated uncertainty is a repeatability uncertainty, called type-A. Type A uncertainty is evaluated by statistical methods that involve the mean and the standard deviation. It comes from the exploitation of a large number of measured values. If we consider the value x_i can be measured directly from the measurement i , \bar{x} is the mean value of K repeated measurements, uncertainty value can be calculated by the following equation:

$$\bar{x} = \frac{\sum_{i=1}^K x_i}{K} \quad (3.1)$$

Standard deviation σ refers to the amount of an individual reading which is expected to vary from the mean. In other words, any single value has an uncertainty equal to the standard deviation. Therefore, if another measurement is acquired for the same measuring points, there is a 68% chance the measurement falls within one standard deviation of the mean and a 95% chance to fall within two standard deviations of the mean, as shown in figure 3.17 [40].

$$\sigma = \sqrt{\frac{\sum_{i=1}^K (x_i - \bar{x})^2}{K - 1}} \quad (3.2)$$

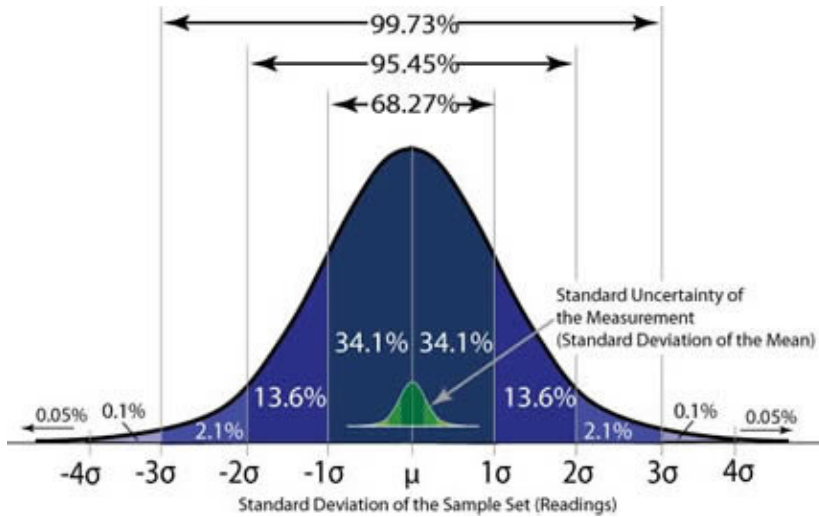


FIGURE 3.17 – Gaussian distribution (*source:www.nde-ed.org*)

The random measurement error is calculated by:

$$u_A = \frac{\sigma}{\sqrt{K}} \quad (3.3)$$

In practice, only a limited number of measurements can be performed. To take into account this limited number, the standard uncertainty is multiplied by a factor k called expansion factor:

$$U_A = k \frac{\sigma}{\sqrt{K}} \quad (3.4)$$

For a 95% confidence interval, k is about 2 when K is about 20.

The systematic error

In a single measurement, it must be taken into account the accuracy of the measuring device, the measurement method, and the quality of measurement. They correspond to a systematic error called uncertainty type B, as shown in figure 3.18. It is necessary to look for all sources of errors and to assess the uncertainty associated with each source for evaluating results. For type B uncertainties, the measurement uncertainty to be taken into account is the expanded uncertainty $U_B = 2u_B$, for a 95% confidence level. Some of the uncertainties depend on the devices are listed below:

Reading on a graduated scale:

$$u_{\text{reading}} = \frac{1 \text{ graduation}}{\sqrt{12}} \quad (3.5)$$

Double reading:

$$U_{\text{double reading}} = u_{\text{reading}} \sqrt{2} \quad (3.6)$$

A given tolerance instrument (instructions):

$$u_{\text{tolerance}} = \frac{t}{\sqrt{3}} \quad (3.7)$$

where: t is tolerance of instrument (x% of the value read).

Digital device (see device instructions):

$$u_{\text{tolerance}} = \frac{t + n \text{ digit}}{\sqrt{3}} \quad (3.8)$$

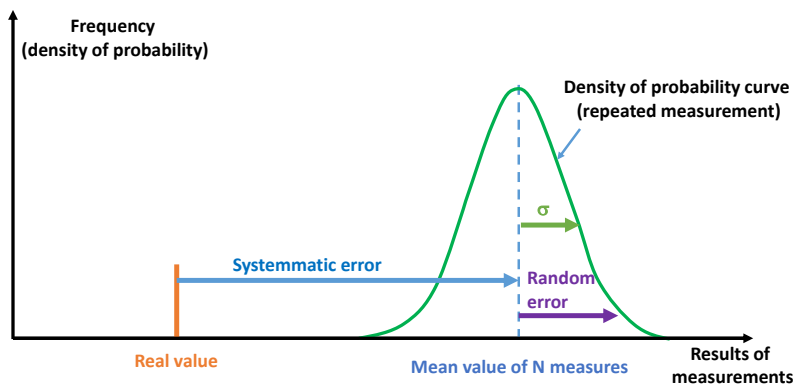


FIGURE 3.18 – Error of measurement

In addition, the relative uncertainty, defined by the uncertainty value divide by the mean value of the measurement, is used to estimate the percent of the deviation from the true value ε :

$$\varepsilon = \frac{u}{\bar{x}} \quad (3.9)$$

Composition of type A and type B uncertainties

If a series of measurements are available and each of them has a type B uncertainty, the standard uncertainty is obtained:

$$u = \sqrt{u_A^2 + u_B^2}; U = 2u; M = \bar{x} \pm U \quad (3.10)$$

Propagation of uncertainties

For processing results of measurement, measured values used to calculate the desired quantity, are called derived quantities. The uncertainty of the derived quantities is combined by the uncertainty of each measured value by the propagation functions:

+ Addition or Subtraction function: If function F is a combination of variable x and y : $F = x \pm y$. The uncertainty of F is determined by:

$$u_F = \sqrt{u_x^2 + u_y^2}; \quad (3.11)$$

+ Multiplication or Division function:

If function F is a combination of variables x and y : $F = xy$ or $F = \frac{x}{y}$. The uncertainty of F can be obtained by:

$$\frac{u_F}{|F|} = \sqrt{\left(\frac{u_x}{x}\right)^2 + \left(\frac{u_y}{y}\right)^2}; \quad (3.12)$$

+ Power function:

If F function is defined by: $F = x^n$. The uncertainty of F is calculated by:

$$\frac{u_F}{|F|} = |n| \frac{u_x}{x}; \quad (3.13)$$

+ Logarithm function:

if function F is defined by: $F = \ln x$, the uncertainty of F is given by:

$$\ln(F \pm u_x) = \ln F \pm \frac{u_F}{F}; \quad (3.14)$$

Measurement quantities

Two types of measurements are conducted in this test bench: global performance and fluctuation of the pressure. The global performances of the compressor are measured with the static pressure ratio II , the polytropic efficiency η_p as a function of the volume flow rate Q_v or mass flow rate \dot{m} . Static pressure fluctuation at the inlet of the compressor determines the surge point and finds out the surge frequency of the compressor.

Atmospheric pressure P_{atm}

The value of P_{atm} is given by the pressure atmospheric from the site of France government [41]. Because the measurements are taken in a long time, the atmospheric pressure is updated each hour of experimental tests. The uncertainty of the atmospheric pressure is estimates about $u_{P_{out}} = \pm 100 Pa$.

Pitot probe

The mass flow rate is measured by a robust averaged pitot tube. This device gives the differential pressure to calculate the volume flow rate. A manometer FCO16 is used to transmit the differential pressure of the pitot to the digital signal. The scales of the transmitter are 1999 Pa with accuracy $< \pm 1\%$ of reading. The total uncertainty of the differential pressure is determined by the uncertainty of the transmitter and DAQ card. It can be calculated by the following equation:

$$u_{pitot} = \sqrt{u_{FCO16}^2 + u_{DAQ}^2} \quad (3.15)$$

Inlet pressure measurement

The inlet pressure is determined by measuring the static differential pressure between the static pressure upstream of the compressor and the atmospheric pressure P_a . This parameter is measured by manometer FC322 with a scale of $\pm 30kPa$ and an accuracy of $< 0.5\%$ of reading. The total uncertainty of inlet pressure can be determined by the following relation:

$$u_{P_1} = \sqrt{u_{FC322}^2 + u_{DAQ}^2 + u_{P_{out}}^2} \quad (3.16)$$

Temperature measurement

The temperature is measured by thermocouple Pt100. It is also called RTD (Resistance Temperature Detector) which is made of platinum. The Pt100 element has a resistance of 100 ohms at 0° . Normally, these sensors are equipped with a protective or mounting sheath to form a temperature probe, and these are commonly referred to as PRTs (Platinum Resistance Thermometers) or Pt100 probes. Pt100 probe are much more linear than thermocouples. In cases of limited ranges and accuracy, it can be considered linear. The temperature is calculated by the linear equation of resistance function:

$$R_t = R_0 (1 + \alpha T) \quad (3.17)$$

$$T = \frac{\frac{R_t}{R_0} - 1}{\alpha} \quad (3.18)$$

With:

R_t - Resistance at $t^\circ C$;

R_0 - Resistance at $0^\circ C$ (100 Ω);

α - Temperature coefficient of the probe (0.00385 $\Omega / \Omega / ^\circ C$);

T - Temperature in $^\circ C$.

In addition, the relation between the resistance value of RTD and temperature is also calculated by the equation Callendar-Van Dusen (CVD).

$$R_t = R_0 + R_0 \alpha \left[t - \delta \left(\frac{t}{100} - 1 \right) \left(\frac{t}{100} \right) - \beta \left(\frac{t}{100} - 1 \right) \left(\frac{t}{100} \right)^3 \right] \quad (3.19)$$

where:

R_t - Resistance at $t^\circ C$;

R_0 - Resistance at $0^\circ C$ (100 Ω);

α - Temperature coefficient at $0^\circ C$ ($\Omega / \Omega / ^\circ C$);

δ - Linearization coefficient;

β - Second coefficient of linearization for the negative value of temperature ($\beta = 0$ for $t > 0^\circ C$).

This equation gives accuracy about $\pm 0.01^\circ C$ for the temperature range $-100^\circ C$ and $+ 100^\circ C$. However, the error increases rapidly at high temperatures until about 0.1%. Moreover, this equation calculates the resistance as a function of temperature. That is the opposite of the most common use: temperature depending on the resistance. So, in this thesis, all temperatures are calculated according to the CVD equations.

The uncertainty of the inlet temperature is obtained by:

$$u_{T_1} = \sqrt{u_{pt100}^2 + u_{DAQ}^2} \quad (3.20)$$

The outlet temperature is an average measured value of three Pt100 sensors. The uncertainty of the outlet temperature can be calculated by:

$$u_{T_{outlet}} = \sqrt{3} \sqrt{u_{pt100}^2 + u_{DAQ}^2} \quad (3.21)$$

3.3.3 Derived parameters

Inlet density

The inlet density is determined by the temperature and the pressure at the inlet of the compressor according to the equation:

$$\rho = \frac{P_1}{RT_1} \quad (3.22)$$

The uncertainty of the inlet density can be calculated according to the propagation law (section 3.3.2) as the following equation:

$$u_\rho = \rho \sqrt{\left(\frac{u_{P_1}}{P_1}\right)^2 + \left(\frac{u_{T_1}}{T_1}\right)^2} \quad (3.23)$$

Mass flow rate

The mass flow rate can be calculated by:

$$\dot{m} = \frac{\pi D^2}{4} k \sqrt{2\rho \Delta P} \quad (3.24)$$

Where:

- D - Diameter of the pipe, $D = 158.5mm$;
- k - coefficient of the sensor, $k = 0.72$;
- ΔP - Differential pressure of the Flow pitot, Pa ;
- ρ - Gas density kg/m^3 ;

The uncertainty of the mass flow rate can be obtained by the following equation:

$$u_{\dot{m}} = \frac{\dot{m}}{2} \sqrt{\left(\frac{u_{\Delta P}}{\Delta P}\right)^2 + \left(\frac{u_\rho}{\rho}\right)^2} \quad (3.25)$$

Pressure ratio

The pressure ratio of the compressor is determined by the ratio of the outlet pressure to the inlet pressure according to the formula:

$$\Pi_s = \frac{P_{out}}{P_1} \quad (3.26)$$

According to the equation 3.12, the uncertainty of pressure ratio is given by:

$$u_{\Pi_s} = \Pi_s \sqrt{\left(\frac{u_{P_{out}}}{P_{out}}\right)^2 + \left(\frac{u_{P_1}}{P_1}\right)^2} \quad (3.27)$$

Polytropic efficiency

The polytropic efficiency compares the real enthalpy rise with the hypothetical one of a multistage and high pressure compressor. It is determined by the equation:

$$\eta_p = \frac{\gamma - 1}{\gamma} \frac{\ln\left(\frac{P_{out}}{P_{in}}\right)}{\ln\left(\frac{T_{out}}{T_{in}}\right)} \quad (3.28)$$

The uncertainty is calculated by the following formula:

$$u_{\eta_p} = \eta_p \sqrt{\left[\frac{(\ln(\Pi_s + u_{\Pi_s}) - \ln \Pi_s) \Pi_s}{\ln \Pi_s} \right]^2 + \left[\frac{(\ln(\Pi_T + u_{\Pi_T}) - \ln \Pi_T) \Pi_T}{\ln \Pi_T} \right]^2} \quad (3.29)$$

Where:

- Π_s - Static pressure ratio;
 - Π_T - Static temperature ratio;
 - u_{Π_s} - Uncertainty of static pressure ratio, is calculated by equation 3.27;
 - u_{Π_T} - Uncertainty of static pressure ratio, is calculated by equation 3.27;
- $$u_{\Pi_T} = \Pi_T \sqrt{\left(\frac{u_{T_{out}}}{T_{out}}\right)^2 + \left(\frac{u_{T_1}}{T_1}\right)^2};$$

3.4 Conclusions

The **RAICOR** test bench has been developed from the existing test bench at **LIFSE**. Due to the use of two independent rotors, **CRCC** is equipped with two electric motors on both sides of the compressor. It is impossible to make the straight inlet as the **SRCC** configuration. Therefore, the components of the compressor need to redesign in order to accommodate the existing test bench, especially, at the compressor inlet. A bent pipe with an angle of 90° is used to direct the fluid flow into the compressor. An investigation of the bent inlet effects on global performance is performed at the design rotation speed by **CFD** method. The analysis results showed that these change slightly affects the performance, mainly near the surge region due to the distortion of fluid flow at the inlet. Compressor parts are also designed and are analyzed for stress, displacement, and natural frequency to ensure that these parts meet the durability and avoid resonance. In addition, the measurement devices and methods of calculating uncertainty of the working parameters are presented and applied in the experiments, which is presented in chapter 4 and chapter 5.

Chapter 4

Experimental results

Contents

4.1	Limitation of the experiments	57
4.2	Global performance	57
4.3	Influence of rotation speed ratio (θ)	69
4.4	Similarity method	78
4.5	CFD Analysis	83

4.1 Limitation of the experiments

The second rotor always plays a major role in the operation of the [Counter-Rotating Centrifugal Compressor \(CRCC\)](#). So all rotation speed limits mentioned in this section are those of the second rotor. The test bench is designed to operate at a maximum speed of $16,000rpm$. For safety reasons, the compressor should operate up to a maximum speed of 75% design speed. So the maximum rotation speed of the second rotor used for this study is $12,000rpm$.

The experimental measurements are performed at three main speeds of $9,000rpm$, $10,000rpm$, and $11,000rpm$ in the counter-rotating mode. The design rotation speed is then calculated based on the similarity method which is described in section [4.4](#).

4.2 Global performance

Global performance is an important parameter to evaluate the performance of the compressor. It is determined through the input and output parameters of the compressor during operation. In this section, the experimental results are compared with the measured results of the [Single Rotor Centrifugal Compressor \(SRCC\)](#) to evaluate the effectiveness of a centrifugal compressor using the counter-rotating system. Therefore, the advantages and disadvantages of this compressor generation are analyzed by the experimental study. As mentioned in the section [2.2](#), the first rotor of [CRCC](#) is responsible for accelerating the flow and determining the input conditions of the second rotor. The second rotor is the main part of the compressor, which is responsible for creating pressure rise during the work. In addition, two rotors are driven independently by the electric motors, which can vary from 0 to $17,000rpm$. The speed of each rotor can be adjusted smoothly and met different working conditions. In this study, the evaluation of global performance is conducted in three cases of the operating mode:

- Case 1: The first rotor rotates freely - the second rotor is driven;
- Case 2: The first rotor is fixed - the second rotor is driven;
- Case 3: Counter-rotating mode (both rotors are driven).

Because the measurement process is carried out for a long time. The variation of ambient temperature and atmospheric pressure lead to the change in mass flow rate value. To facilitate the comparison of the experimental results at different measurements, the calculated values of the mass flow rate are referred to the same condition at $T_{ref} = 288.15^\circ K$ and $P_{ref} = 101,325 Pa$, called corrected mass flow rate. This value is determined by the following formula:

$$\dot{m}_{cr} = \frac{\dot{m} \sqrt{T_{inlet}/T_{ref}}}{P_{inlet}/P_{ref}} \quad (4.1)$$

4.2.1 First rotor rotates freely - second rotor is driven (case 1)

In this case, the second rotor is driven by an electric motor while the first rotor rotates freely (it is not driven). The pressure rise of the compressor is generated by the work of the second rotor. The comparison of a global performance between **CRCC** and **SRCC** at the rotation speed of $9,000rpm$ is shown in figure 4.1. The black solid line presents for the global performance of **CRCC**, while the blue dash line represents for that of **SRCC**.

Generally, the pressure ratio of **CRCC** is quite smaller than that of **SRCC**, however, its polytropic efficiency is higher. The best efficiency points of **CRCC** and **SRCC** take place at the mass flow rate of $0.42kg/s$ and $0.458kg/s$, respectively. Obviously, this point of **CRCC** is shifted to the lower mass flow rate. Comparing the pressure ratio of two best efficiency points of **CRCC** and **SRCC** shows that two configurations have almost the same pressure ratio of 1.097 ± 0.002 for **CRCC** and 1.100 ± 0.002 for **SRCC**. Beside that, the polytropic efficiency of **CRCC** is always higher than that of **SRCC**, the peak efficiency increase from $64\% \pm 2\%$ for **SRCC** to $72\% \pm 2\%$ for **CRCC**. It can be said that using counter-rotating system can enhance the efficiency by about 8%. Additionally, the power consumption of **CRCC** (green solid line) is always less than the power consumption of **SRCC** (blue dash line) about $0.5kW$ due to the higher efficiency, as shown in figure 4.2.

At rotation speed of $10,000rpm$, **CRCC** gives a lower pressure ratio but its efficiency is slightly higher at the low mass flow rate region, as illustrated in figure 4.3. So, the best efficiency point of **CRCC** is moved to a lower mass flow rate. The pressure ratio and the maximum efficiency of **CRCC** are respectively 1.120 ± 0.002 and $72.6 \pm 2\%$ at mass flow rate of $0.504kg/s$. Meanwhile, the pressure ratio value of **SRCC** is 1.116 ± 0.002 and the efficiency is $69.6 \pm 2\%$ at $0.592kg/s$. The comparison between best efficiency points of **CRCC** and **SRCC** shows that the pressure ratio of the **CRCC** increases slightly about 0.3% and polytropic efficiency is improved by about 3%. Consequently, the power consumption of **CRCC** is $1.5kW$ lower than that of **SRCC**, as shown in figure 4.4.

Figure 4.5 presents a performance comparison between **CRCC** and **SRCC** at rotation speed of $11,000rpm$. Obviously, the **CRCC** performance has the same tendency as the other speeds in comparison with the performance of **SRCC**. At the best efficiency point, the **CRCC** pressure ratio can reach 1.152 ± 0.002 and its polytropic efficiency is $73 \pm 2\%$, while **SRCC** attains $1,141 \pm 0.002$ for the pressure ratio and $70 \pm 2\%$ for

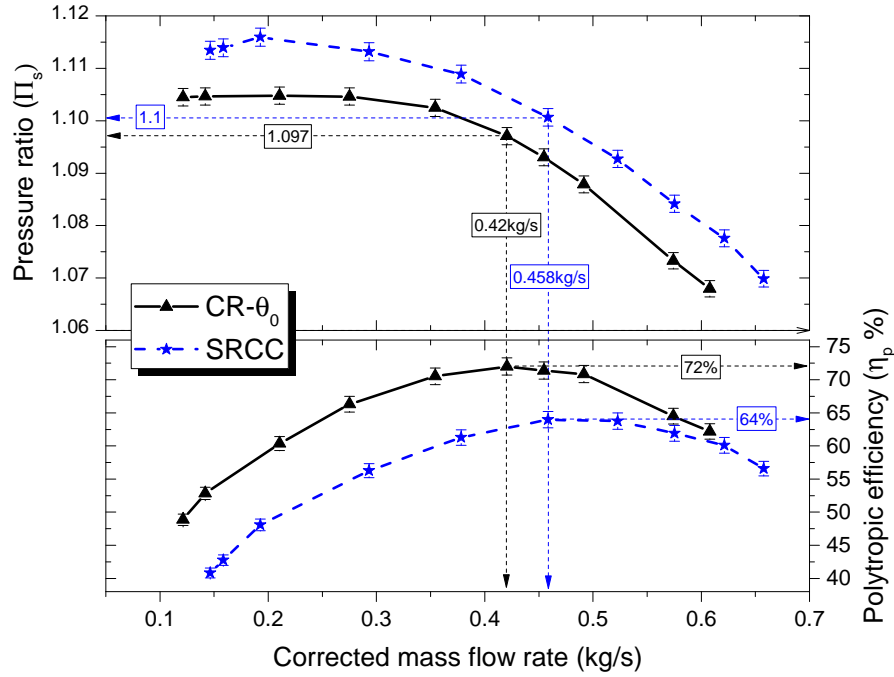


FIGURE 4.1 – Global performance of CRCC (CR- θ_0 : counter-rotating in case 1) in comparison with SRCC at 9,000rpm

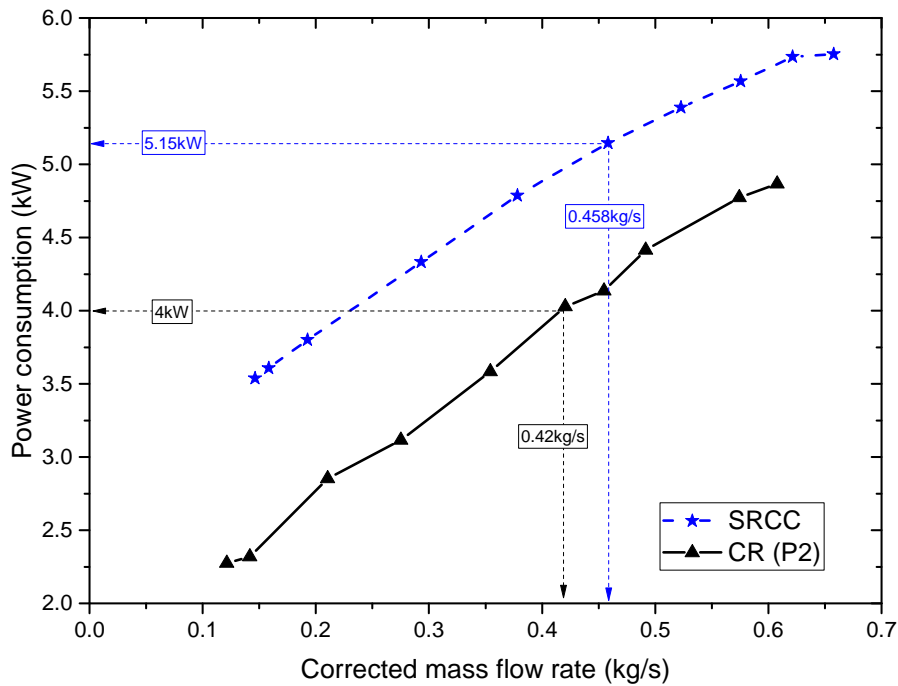


FIGURE 4.2 – Electric power consumption of the CRCC second rotor (CR(P2)) in comparison with SRCC at 9,000rpm

the polytropic efficiency. It means that the pressure ratio increases slightly by about 1% and the polytropic efficiency rises by about 3%. The enhanced efficiency can be seen clearly in the reduction of power consumption. Figure 4.6 shows that the electric power of CRCC is always lower than that of SRCC of about 1.5kW.

Figure 4.7 shows a variation of first rotor speed according to the mass flow rate.

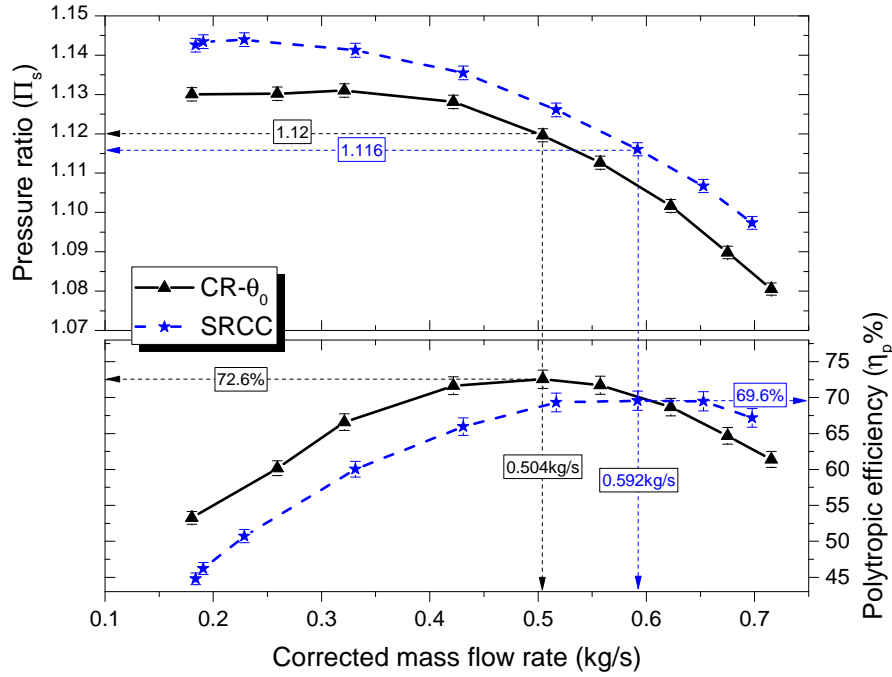


FIGURE 4.3 – Global performance of CRCC (CR- θ_0 : counter-rotating in case 1) in comparison with SRCC at 10,000rpm

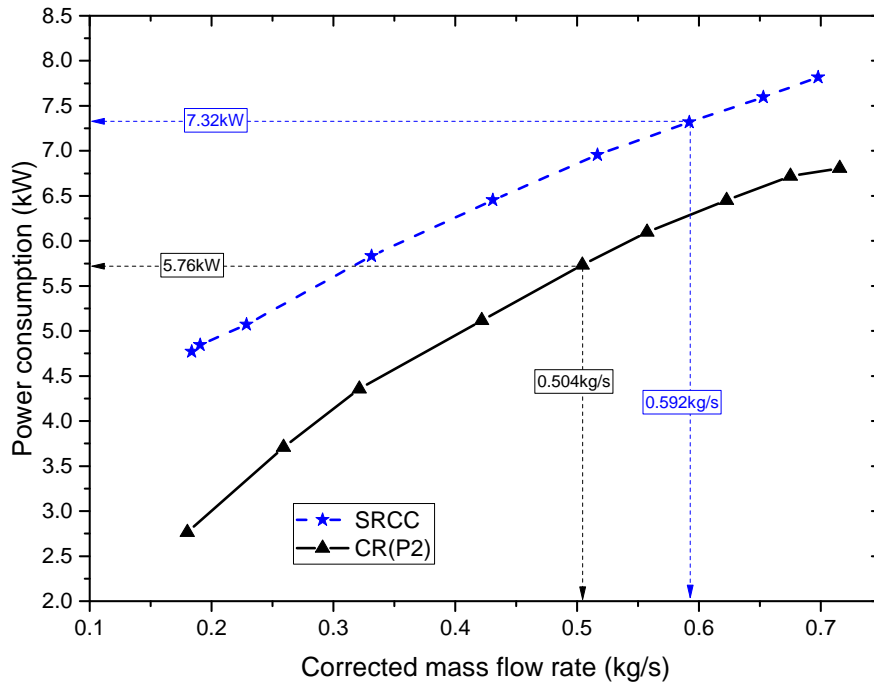


FIGURE 4.4 – Electric power consumption of the CRCC second rotor (CR(P2)) in comparison with SRCC at 10,000rpm

When the fluid flows through the compressor, its impact on the first rotor blade generates a drive torque. In this case, the first rotor acts as a turbine and its rotation speed depends on the mass flow rate of the compressor. It is easy to see that the maximum speed of the first rotor increases when the speed of the second rotor rises. At the speed of $N_2 = 9,000rpm$, the maximum speed of the first rotor reaches $-5,472rpm$ (a minus

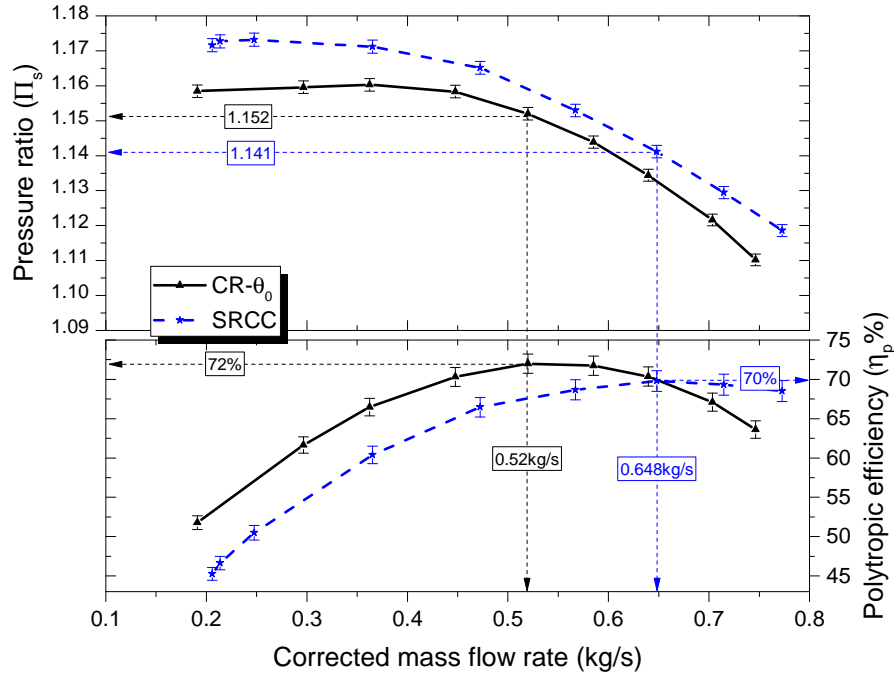


FIGURE 4.5 – Global performance of CRCC (CR- θ_0 : Counter-rotating in case 1) in comparison with SRCC at 11,000rpm

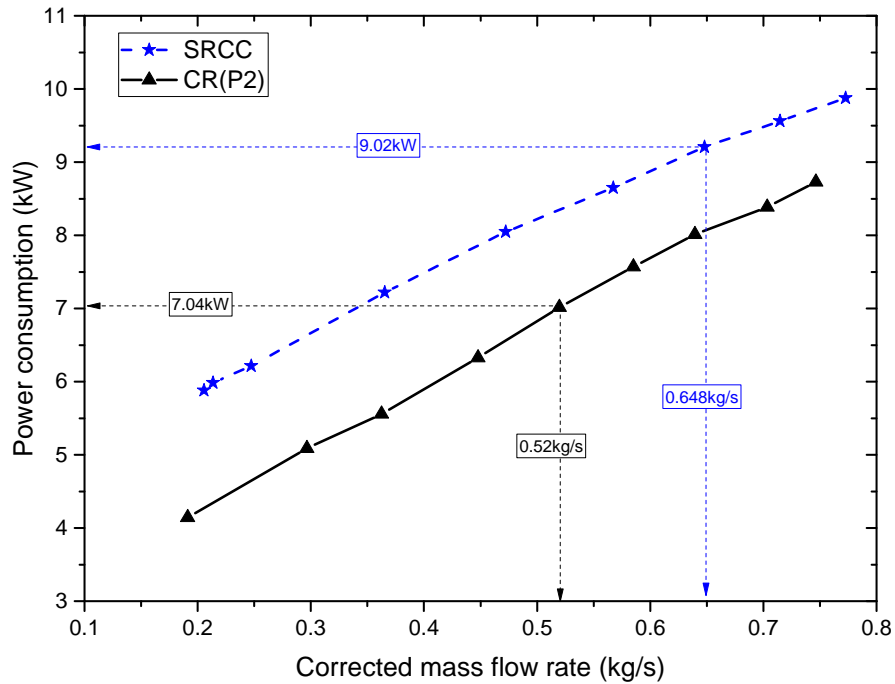


FIGURE 4.6 – Electric power consumption of CRCC (CR(P2)) in comparison with SRCC at 11,000rpm

sign indicates that the rotor rotates in the opposite direction to the second rotor) at the largest flow rate of 0.629kg/s . The first rotor speed reduces as the flow rate decreases according to the linear relationship. When the flow rate drops to 0.21kg/s , the torque does not overcome the mechanical resistance of the drive system, the rotor no longer rotates.

At the speed of $N_2 = 10,000rpm$, the flow through the compressor is greater because the second rotor rotates at a higher speed. It makes an increase in the rotation speed of the first rotor. The maximum rotation speed that can be achieved in this case is $-6,540rpm$ at a flow of $0.716kg/s$. The first rotor stops the rotation when the mass flow rate decreases to $0.18kg/s$. Similarly, it can easily see at the speed of $11,000rpm$ that the maximum speed of the first rotor achieves $-7,023rpm$ at a flow of $0.746kg/s$ and the first rotor stops its rotation for the mass flow rate of $0.191kg/s$.

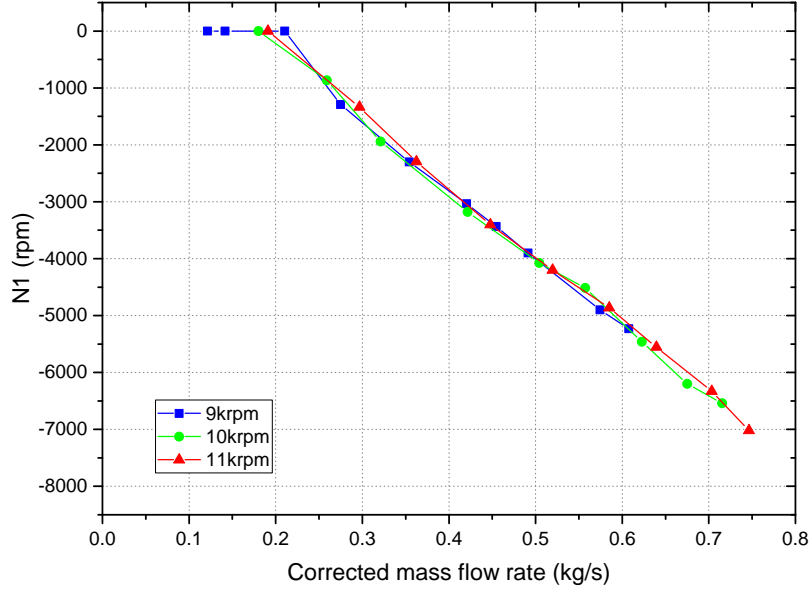


FIGURE 4.7 – The first rotor rotation speed (N_1) of CRCC according to the corrected mass flow rate for three rotation speeds of the second rotor: $9,000rpm$, $10,000rpm$ and $11,000rpm$

4.2.2 First rotor is fixed - second rotor is driven (case 2)

The first rotor is fixed by the electric inverter (stationary rotor) and the second one is driven at a constant speed. There is no doubt that the first rotor acts as an inlet positive prewhirl valve, so it decreases the relative Mach number at the inlet of the second rotor [42]. The velocity triangles of CRCC are formed, as shown in figure 4.9. The Euler work of the second rotor is then calculated by the equation 4.2. Obviously, this work decreases because the velocity component C_{u3} has a positive value due to the effect of the prewhirl valve.

$$\Delta h_2 = U_4 C_{u4} - U_3 C_{u3} \quad (4.2)$$

Figure 4.8 shows the comparison of global performance between case 1 and case 2 with three rotation speeds of the second rotor. The solid lines introduce the performances in case 2 and the dashed lines represent for case 1. It is clear that for each rotation speed of the second rotor, the performance of CRCC is significantly reduced, especially at a high flow rate. At rotation speed of $9,000rpm$ (blue line), the pressure ratio of case 2 is much lower than that of case 1 at large flow rates. Then, it increases gradually as the flow rate decreases. Then, the characteristic curve of case 2 coincides

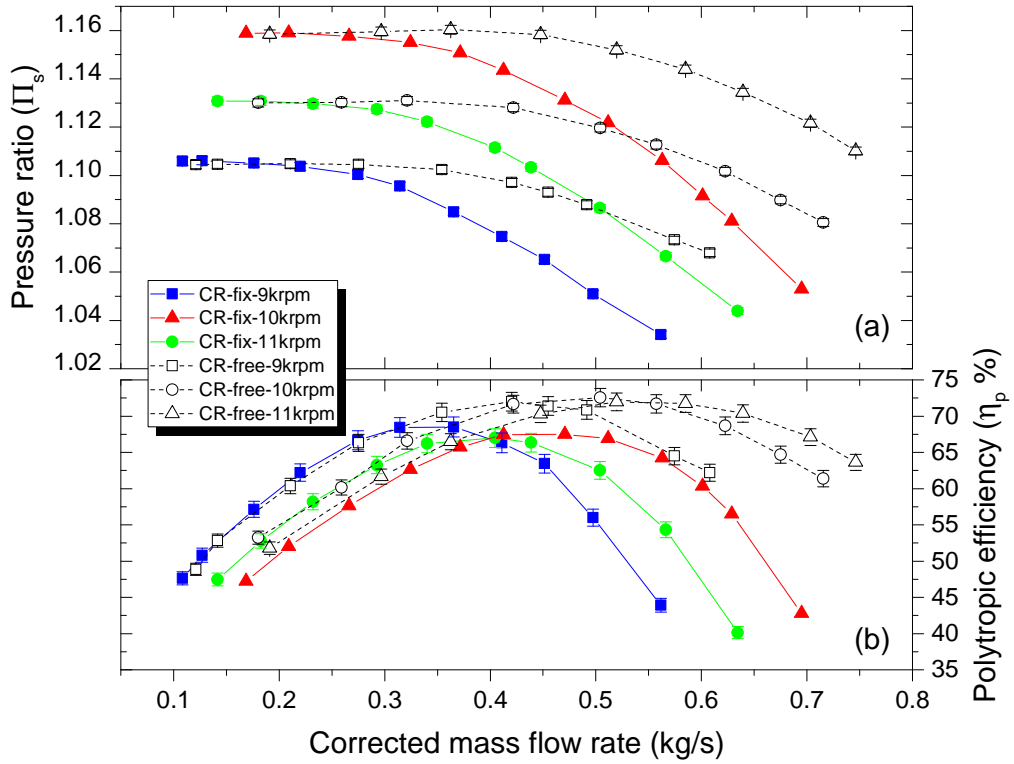


FIGURE 4.8 – Comparison of global performances between case 1 (CR-free) and case 2 (CR-fix) with three rotation speed of 9,000rpm, 10,000rpm, 11,000rpm of the second rotor

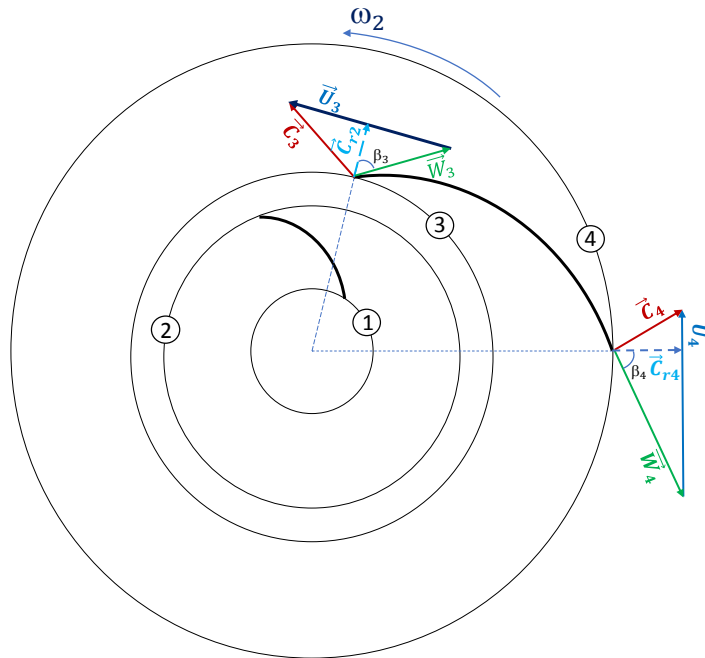


FIGURE 4.9 – Velocity triangles of CRCC with the first rotor is fixed (case 2)

with the curve of case 1 when the first rotor is stationary in both cases. The decrease of the pressure ratio at large flow rates can be explained by the compatibility of the

second rotor with the fluid flow of the first rotor. The blade angle of the second rotor is designed to be adapted to fluid flow coming out from the first rotor, which rotates at the same speed as the other one. When the first rotor is fixed, the incidence angle at the inlet of the second rotor raises. It leads to an increase in the losses and a decrease in performance. In addition, the incompatibility with the fluid flow of the second rotor causes a pressure fluctuation at the second rotor inlet, while the pressure at the first rotor inlet remains stable. This fluctuation can be seen in pressure signals which are obtained by two instantaneous pressure sensors shown in figure 4.10. As a result, the maximum polytropic efficiency also decreases significantly from $73 \pm 2\%$ in case 1 to $69 \pm 2\%$ in case 2.

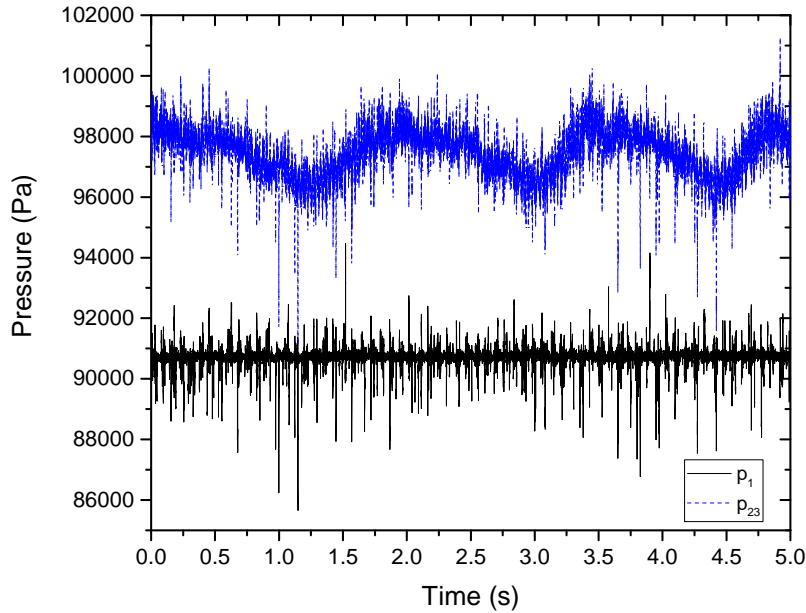


FIGURE 4.10 – Pressure fluctuations at the inlet of the first rotor (p_1) and between two rotors (p_{23}) of CRCC with the flow rate of 0.419kg/s and rotation speed of $N_2 = 9,000\text{rpm}$

The same trends are found at the speed of $N_2 = 10,000\text{rpm}$ (green line) and $N_2 = 11,000\text{rpm}$ (red line). The comparison between the two cases can conclude that the operation of CRCC in case 1 gives higher performance due to the reduction of losses between rotors. Therefore, to maintain the compressor stability with the highest performance and to avoid losses caused by the incompatibility of fluid flow, it needs to keep the rotors working at an optimal coupled rotation speed according to the fluid flow rate.

4.2.3 Counter-rotating mode (case 3)

In counter-rotating mode (two rotors rotate in the opposite direction with same speed), both rotors are driven simultaneously by the electric motors. Figure 4.11 shows comparison of the global performance between CRCC and SRCC at the rotation speed of $9,000\text{rpm}$. It can be seen that the pressure ratio of CRCC is always higher than the pressure ratio of SRCC. At the best efficiency point, the pressure ratio of CRCC and SRCC are respectively 1.128 ± 0.002 and 1.100 ± 0.002 . That means CRCC pressure

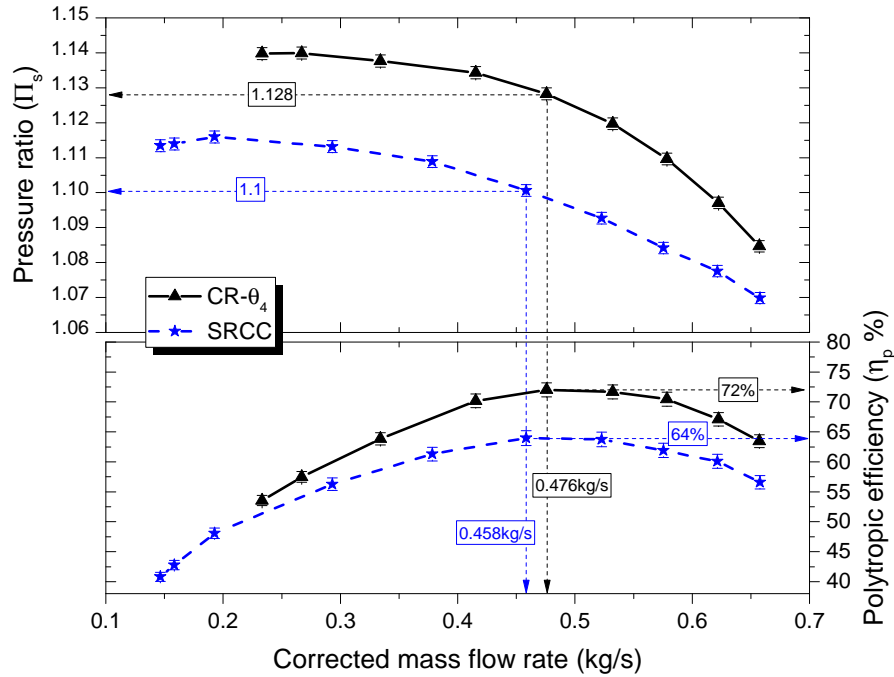


FIGURE 4.11 – Comparison of global performance of CRCC in counter-rotating mode with $N_1 = -9,000rpm$, $N_2 = 9,000rpm$ ($CR - \theta_4$) and SRCC with $N = 9,000rpm$

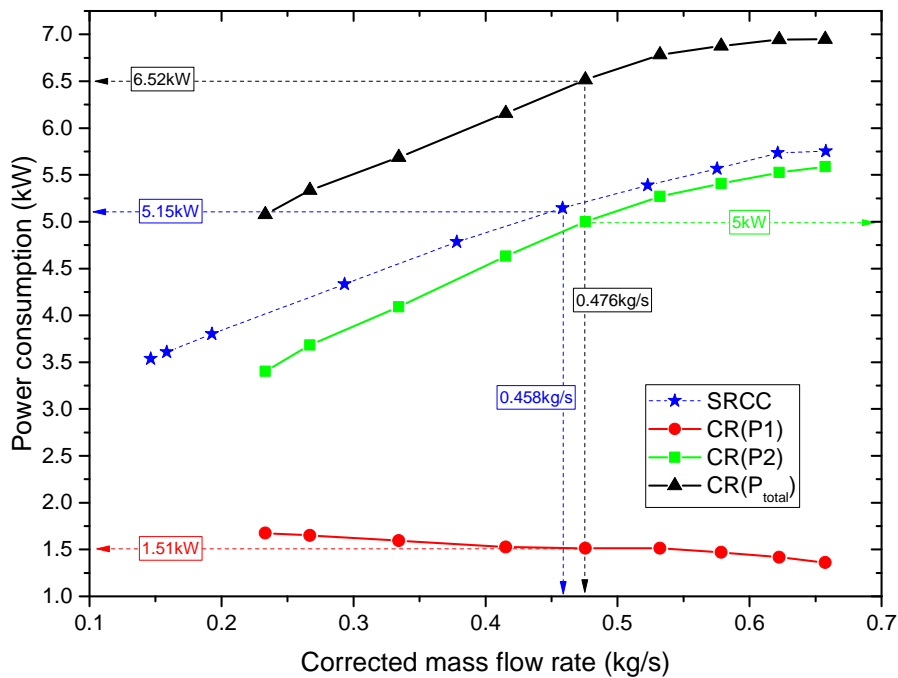


FIGURE 4.12 – Comparison of electric power consumption of CRCC: the first rotor ($CR(P1)$), the second rotor ($CR(P2)$), the counter-rotating rotor ($CR(P_{total})$) and SRCC at $9,000rpm$

ratio increases by about 2.5%. Besides, CRCC polytropic efficiency is significantly improved. It attains the maximum value of $72 \pm 2\%$, which is increased by about 8% in comparison with that of SRCC at the same rotor speed. It is easy to see that the maximum efficiency of CRCC seems to be constants compared to the case 1 (figure

4.1). However, the mass flow rate of the CRCC instability limit is changed to a larger flow rate. The limit flow rate of CRCC is 0.233kg/s which is larger than the limit flow rate of 0.146kg/s for SRCC. This could be explained by the increase of pressure ratio and the adaptation between two rotors. Increasing the speed ratio leads to the change in the inlet condition. The incidence angles at the inlet of two rotors increase. When the mass flow rate diminishes, these angles increase rapidly due to the counter-rotating effect, especially at the second rotor inlet. Consequently, the separation region appears in the blade passage of the rotors leads to form a stall cells. The instability appears when the stall cells are developed in the entire rotor. If the speed ratio does not change during the work, of course, the limit instability of CRCC is shifted to larger mass flow rate.

Figure 4.12 shows the comparison of total power consumption between CRCC and SRCC in counter-rotating mode at the speed of $N_2 = 9,000\text{rpm}$. In this figure, the red solid line and the green solid line represent the power consumption of the first rotor (*Counter – Rotating mode*(CR)(P1)) and the second rotor (CR(P2)), respectively. The black solid line and blue dashed line are respectively the total power consumption of CRCC (CR – (P_{total})) and SRCC. It is easy to see that the power consumption of the second rotor is approximately equal to the power consumption of SRCC. The consumption of the first rotor is quite small and increases slightly as the flow decreases. It can be interpreted that the first rotor work almost as axial turbomachinery and the second rotor works completely as a radial compressor. Consequently, the CRCC configuration gives a higher pressure ratio so it needs more power to compress the fluid than the SRCC's one. At a best efficiency point, the power consumption of the first and second rotors is respectively 1.51kW and 5kW , while the power consumption of SRCC is 5.15kW . This shows that the compression mainly occurs in the second rotor because it has a large variable diameter from the inlet to the outlet. The explanation can be seen from equation 1.14 in section 1.1.4, a large variety of diameter leads to a higher impact of the centrifugal effect. Meanwhile, the pressure ratio rise of the first rotor is small because of the smaller diameter variation. Therefore, the first rotor mainly accelerates the fluid flow to the second rotor.

At the rotation speed of $10,000\text{rpm}$, the pressure ratio of CRCC increases significantly compared with the pressure ratio of SRCC at the same rotor speed, as shown in figure 4.13. The CRCC pressure ratio is 1.158 ± 0.002 at the best efficiency point, which is increased by about 3.76% compared to the SRCC's one. The maximum efficiency of CRCC and SRCC are respectively $73.1 \pm 2\%$ and $69.6 \pm 2\%$. So, the polytropic efficiency of CRCC increases slightly by about 3% in comparison with that of SRCC. It can be noticed that the best efficiency point of CRCC is moved towards a lower flow rate than that of SRCC. Likewise, the instability limit appearance, similar to the rotation speed of $9,000\text{rpm}$, is shifted to the flow rate of 0.269kg/s , which is larger than the instability limit of SRCC at the mass flow rate of 0.183kg/s .

Figure 4.14 shows the power consumption comparison between CRCC and SRCC at rotation speed of $10,000\text{rpm}$. It is clear that the CRCC consumes more energy than SRCC due to the higher pressure ratio. At the best efficiency point, the total power consumption of CRCC and SRCC are 8.57kW and 7.32kW , respectively. It can be seen that CRCC consumes 1.25kW more than SRCC to increase the pressure ratio by about 3.76% and the efficiency by about 3%.

When the rotors speed up to $11,000\text{rpm}$, the same tendency is found. The pressure ratio generated by CRCC is always higher and its efficiency is also bigger, as shown in figure 4.15. At the best efficiency point, the pressure ratio increase by about 4.65%, and

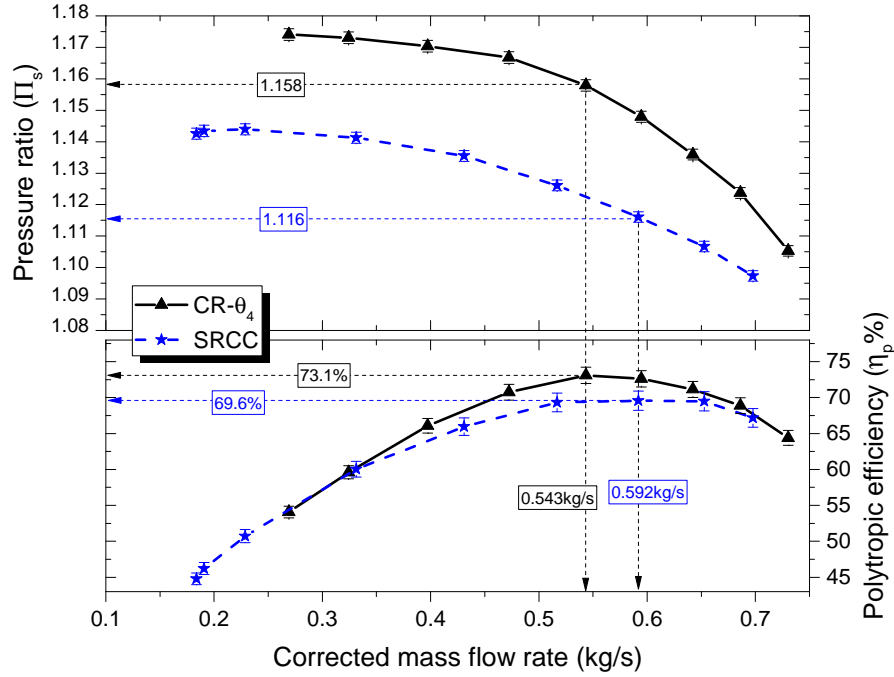


FIGURE 4.13 – Comparison of the global performance of CRCC in counter-rotating mode with $N_1 = -10,000rpm$, $N_2 = 10,000rpm$ ($CR - \theta_4$) and SRCC with $N = 10,000rpm$

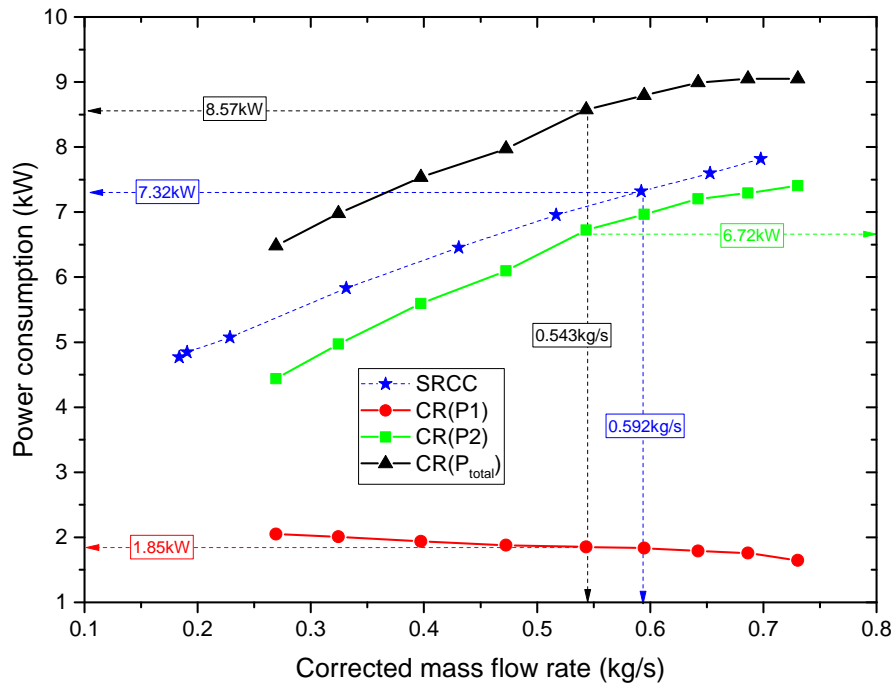


FIGURE 4.14 – Comparison of electric power consumption of CRCC: the first rotor ($CR(P1)$), the second rotor ($CR(P2)$), the counter-rotating rotor ($CR(P_{total})$) and SRCC at 10,000rpm

the efficiency enhanced by about 4%. Similar to the other cases, the power consumption of CRCC is always greater than that of SRCC, as shown in figure 4.16. It is easy to see that the power consumption of the second rotor is close to the SRCC's rotor consumption. Besides, the consumption of the first rotor increases gradually as the

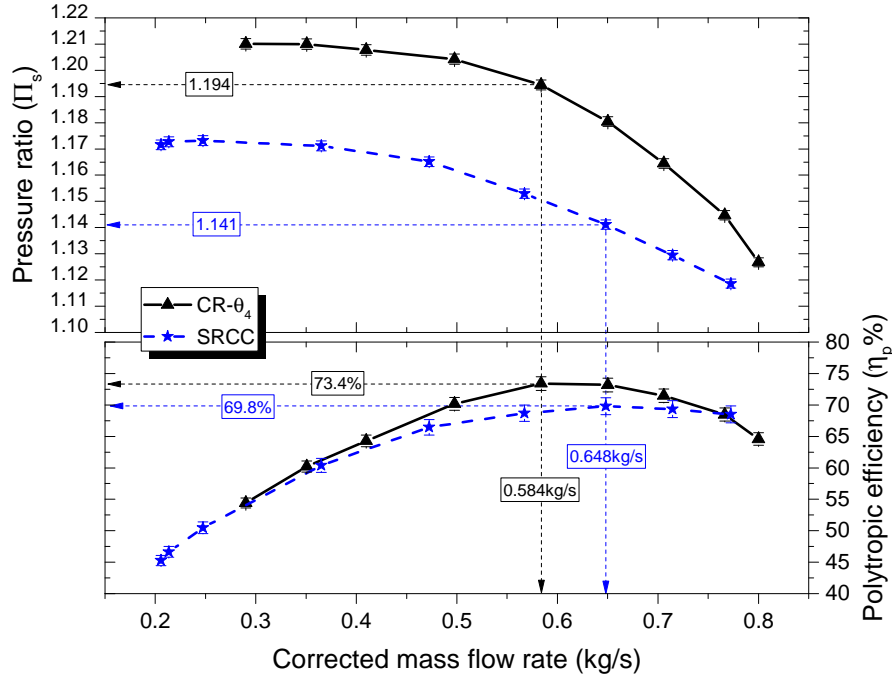


FIGURE 4.15 – Comparison of global performance of **CRCC** in counter-rotating mode with $N_1 = -11,000rpm$, $N_2 = 11,000rpm$ ($CR - \theta_4$) and **SRCC** with $N = 11,000rpm$

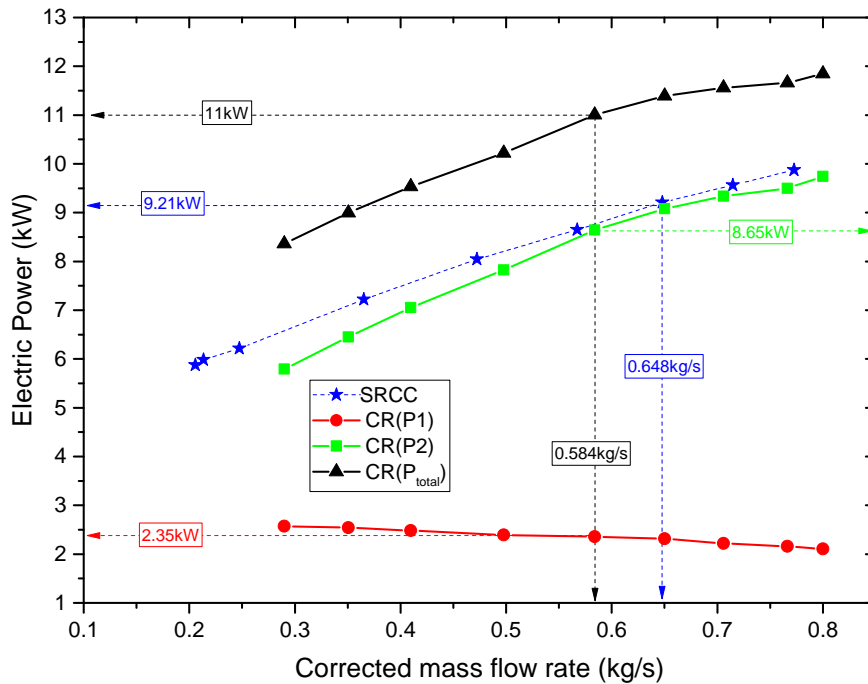


FIGURE 4.16 – Comparison of the electric power consumption of **CRCC**: the first rotor ($CR(P1)$), the second rotor ($CR(P2)$), the counter-rotating rotor ($CR(P_{total})$) and **SRCC** at $11,000rpm$

mass flow rate decreases. As a result, the total power consumption of **CRCC** represents a sum of two rotors consumption so it is always greater than **SRCC**.

4.2.4 Conclusions

Global performance in three operating cases of **CRCC** is analyzed and compared to the global performance of **SRCC** at the same speed to assess the effect of a counter-rotating system. Experimental results indicate that:

- Case 1: **CRCC** produces lower pressure ratio and higher efficiency than **SRCC**. At $9,000rpm$, the efficiency is increased by about 8%, however, it is improved by about 3% when the rotation speed increases to $10,000rpm$ and $11,000rpm$. Consequently, **CRCC** consumes less energy than **SRCC** and the operating range is a little bit expanded to lower flow rate.
- Case 2: The global performance of **CRCC** is significantly reduced due to the incompatibility of the fluid flow at the second rotor inlet and a great inlet loss is generated. As a result, this case is not interesting because it is inefficient, so it is not further studied in this work.
- Case 3: The pressure ratio of **CRCC** is slightly improved from 2.5% to 4.65% compared to that **SRCC** at the same speed. Moreover, the polytropic efficiency remains constant compared to case 1. However, the **CRCC** consumes more power due to the higher pressure ratio rise and its instability limit appears earlier.

4.3 Influence of rotation speed ratio (θ)

As shown in section 4.2.3, **CRCC** gives higher pressure ratio and higher efficiency than **SRCC**. This result shows the advantages of the counter-rotating effect applied to a centrifugal compressor. However, how the compressor performance change when the rotation speed ratio between the first rotor and second rotor changes? Studying the effect of speed ratio $\theta = \frac{N_1}{N_2}$ on the performance finds out the adaptation of **CRCC** to the change of working conditions. Many authors studied the effect of speed ratios on the performance of counter-rotating turbomachines. Sharma et al. [43] studied many parameters that affect the performance of counter-rotating axial compressors, including speed ratios. Their results showed that if the second rotor rotates 50% faster than the first rotor, the rotation stall on the first rotor is suppressed. In 2007, Furukawa et al. [44] conducted an experimental study of counter-rotating axial pumps. They found that the maximum efficiency can be obtained at different mass flow rates when the speed ratio is changed, while the speed of the first rotor is constant. They concluded that using the counter-rotating component can give a wider operating range and a higher efficiency according to the speed ratio. To emphasize the effect of the speed ratio on the efficiency of the axial counter-rotating compressor, the work of Chen et al. [45] pointed out that with a speed ratio of 1.143, the compressor can achieve the highest efficiency with a slight reduction of the total pressure ratio and of the working margin. The authors concluded that if the speed ratio is inferior to one, a stable range of the compressor becomes smaller and decreases when the speed ratio decreases. In 2012, the study of Limin et al. [46] presented that with a speed ratio (that is defined as $\nu = \frac{N_2}{N_1}$) higher than 0.9, the first stall stage appears in the second rotor with a reduction of mass flow rate. In contrast, when the second rotor rotates slower than the first rotor, the tip leakage flow of the second rotor decreases significantly with the decrease of the speed ratio. Moreover, the stall phenomenon firstly occurs in the first rotor. The study of Mistry et al. [47] on an axial counter-rotating fan showed that the speed ratio plays an important role in terms of overall pressure rise. When the second rotor rotates

faster than the first one, the suction effect is generated stronger. This improves the fan performance. Similarly, the study conducted by Nouri et al. [29] on the speed ratio (in this study, the speed of the first rotor is fixed at $200rpm$ and the speed ratio is defined by $\nu = \frac{N_2}{N_1}$) between two rotors of an axial counter-rotating fan. Their results showed that the low-speed ratios $\nu = 0$ and $\nu = 0.5$ gives lower performances. Nevertheless, increasing the speed ratio within the range of $[0.8 - 1.2]$ results in a slight increase in performance. They concluded that the efficiency can reach a maximum value if ν is in a range of $[1.05 - 1.15]$. The work of Subbarao et al. [48] on the speed ratio of a counter-rotating turbine indicates that the overall efficiency is improved with a speed ratio greater than one (the first rotor rotates at a higher speed than the second one). In addition, they identified that the losses vary with the speed ratio and the performance can be improved by adjusting the rotation speed of the rotors. In 2015, the experimental study of the counter-rotating mixed-flow pump conducted by Tosin et al. [31] showed that the speed ratio has a strong effect on the modification of entire pump characteristics. Their study focuses on the improvement of the head and on the optimization of the efficiency by changing the speed ratio. Experimental results showed that the head is changed from $12m$ to $26m$ when the rotor has a higher rotation speed. The efficiency of the pump is almost constant at 80%. They also emphasized that the head rise is significantly improved by increasing the speed of the second rotor while reducing the speed of the first rotor.

The results of previous studies are paid attention to the importance of speed ratio in a counter-rotating turbomachinery. Determining the effect of speed ratio on the characteristics of the compressor plays an essential role in improving performance as well as controlling the counter-rotating compressor to meet different working conditions. In this study, the experimental study is conducted to study the effect of the speed ratio on the characteristics of CRCC within the working limits. The measurements are carried out with three main rotation speeds (N_2) of $9,000rpm$, $10,000rpm$, and $11,000rpm$. At each speed of the second rotor, the rotation speed of the first rotor (N_1) is determined to get a speed ratio of $\theta = N_1/N_2$ in the range of $[-0.7 - 1.3]$ (the minus sign represents two rotors rotating in opposite direction). Seven speed-ratios $\theta_1 = -0.7$, $\theta_2 = -0.8$, $\theta_3 = -0.9$, $\theta_4 = -1$, $\theta_5 = -1.1$, $\theta_6 = -1.2$ and $\theta_7 = -1.3$ are chosen for experimental study.

4.3.1 Effect of the speed ratio for a fixed speed of $N_2 = 9,000rpm$

The speed of the first rotor is calculated by the speed of the second rotor and the speed ratio θ . At rotation speed of $N_2 = 9,000rpm$, seven speeds (N_1): $-6,300rpm$, $-7,200rpm$, $-8,100rpm$, $-9,000rpm$, $-9,900rpm$, $-10,800rpm$ and $-11,700rpm$ are determined.

Figure 4.17 shows variation of the CRCC global performances with the different speed ratios in comparison with the SRCC's ones at the speed of $N_2 = 9,000rpm$ and $N_2 = 11,000rpm$. At each speed ratio, the best efficiency point of CRCC is shifted to the higher mass flow rate. It can be seen that this point of CRCC changes from the mass flow rate of $0.480kg/s$ to $0.557kg/s$ when speed ratio changes from $\theta_1 = -0.7$ to $\theta_7 = -1.3$, while the mass flow rate of SRCC is fixed at $0.458kg/s$ (BEP1). Additionally, the pressure ratio rises significantly when the speed ratio increases (figure 4.17a). The pressure ratio reaches 1.107 ± 0.002 with $\theta_1 = -0.7$ and increases up to 1.145 ± 0.002 with $\theta_7 = -1.3$. Comparing with the pressure ratio of SRCC, the pressure ratio of CRCC is improved up to 4.1% with the first rotor increases. It can be noticed that

the pressure ratio curve of **CRCC** with the θ_7 is close to the pressure ratio curve of **SRCC** at the rotation speed of 11,000rpm. This means that **CRCC** can achieve the same performance but the peripheral speed is lower than that of **SRCC**. Besides, the polytropic efficiency is almost unchanged at 72%, as shown in figure 4.17b. It is always higher than the efficiency of **SRCC** at 64%. A set of best efficiency points gives an effective operating area of **CRCC**. This region is determined by the change in mass flow rate from 0.48kg/s (with $\theta_1 = -0.7$) to 0.557kg/s (with $\theta_7 = -1.3$). Nonetheless, the instability limit shifts to the larger flow rate when the speed ratio increases, as shown in figure 4.17.

TABLE 4.1 – Global performance of **CRCC** and **SRCC** at the best efficiency points with the different speed ratios and $N_2 = 9,000rpm$

θ	N_1 rpm	N_2 rpm	\dot{m}_{cor} (kg/s)	Π_s	η_p (%)
-0.7	-6,300	9,000	0.480	1.107±0.002	72±2
-0.8	-7,200	9,000	0.490	1.112±0.002	72±2
-0.9	-8,100	9,000	0.503	1.117±0.002	73±2
-1	-9,000	9,000	0.476	1.128±0.002	72±2
-1.1	-9,900	9,000	0.524	1.133±0.002	72±2
-1.2	-10,800	9,000	0.526	1.140±0.002	72±2
-1.3	-11,700	9,000	0.557	1.145±0.002	72±2
SRCC		9,000	0.458	1.100±0.002	64±2

Table 4.1 summarizes the performance of **CRCC** at the best efficiency points with different speed ratios. It can be considered that **CRCC** configuration provides a wider effective operating range than **SRCC** by changing the speed ratio. It works flexibly to accommodate changes in working conditions.

4.3.2 Effect of the speed ratio for a fixed speed of $N_2 = 10,000rpm$

The second rotor rotates at a speed of $N_2 = 10,000rpm$, the speed of the first rotor corresponding to the seven studied speed ratios are $-7,000rpm$, $-8,000rpm$, $-9,000rpm$, $-10,000rpm$, $-11,000rpm$, $-12,000rpm$ and $-13,000rpm$. A Comparison of global performance between **CRCC** with the different speed ratios and **SRCC** with the rotation speed of $N = 10,000rpm$ and $11,000rpm$ are shown in figure 4.18. It is easy to see that the speed ratio also greatly influences the pressure ratio and the best efficiency point of the compressor. The pressure ratio of **CRCC** increases significantly according to an increase of speed ratio, as shown in figure 4.18a. Indeed, the pressure ratio rises from 1.134 ± 0.002 to 1.181 ± 0.002 when the speed ratio changes from $\theta_1 = -0.7$ to $\theta_7 = -1.3$ at the best efficiency points. That means the pressure ratio of **CRCC** increases up to 5.8% in comparison with that of **SRCC** (BEP2) at the same rotation speed. Furthermore, it can be considered that the pressure ratio curve of θ_7 is close to the curve of **SRCC** at 12,000rpm. That means **CRCC** configuration can operate at a lower speed of 2000rpm in comparison with **SRCC** while the pressure ratio remains the same. In addition, figure 4.18b reveals the efficiency comparison between **CRCC** with different speed ratios and **SRCC** at the speed of 10,000rpm and 12,000rpm. Obviously, the maximum polytropic efficiency of **CRCC** is almost stable for all speed ratios at about $74 \pm 2\%$ and it is improved by about 4% in comparison with **SRCC** efficiency. Moreover, the maximum efficiency takes place at the different

mass flow rate in line with the speed ratios and moves around the point of **SRCC** at the mass flow rate of 0.592kg/s . This characteristic permits **CRCC** configuration to work more flexibly to meet various working conditions. The summary results at the best efficiency points are presented in table 4.2.

TABLE 4.2 – Global performance of **CRCC** and **SRCC** at the best efficiency points with the different speed ratios and $N_2 = 10,000\text{rpm}$

θ	N_1 rpm	N_2 rpm	\dot{m}_{cor} kg/s	Π_s	η_p %
-0.7	-7,000	10,000	0.534	1.134 ± 0.002	74 ± 2
-0.8	-8,000	10,000	0.546	1.138 ± 0.002	73 ± 2
-0.9	-9,000	10,000	0.542	1.147 ± 0.002	73 ± 2
-1	-10,000	10,000	0.543	1.158 ± 0.002	74 ± 2
-1.1	-11,000	10,000	0.577	1.163 ± 0.002	74 ± 2
-1.2	-12,000	10,000	0.603	1.169 ± 0.002	74 ± 2
-1.3	-13,000	10,000	0.610	1.181 ± 0.002	74 ± 2
SRCC		10,000	0.592	1.116 ± 0.002	70 ± 2

4.3.3 Effect of the speed ratio for a fixed speed of $N_2 = 11,000\text{rpm}$

At the second rotor speed of $N_2 = 11,000\text{rpm}$, seven first rotor speeds $-7,700\text{rpm}$, $-8,800\text{rpm}$, $-9,900\text{rpm}$, $-11,000\text{rpm}$, $-12,100\text{rpm}$, $-13,200\text{rpm}$ and $-14,300\text{rpm}$ are determined. Figure 4.19a shows the variation of the global performance of **CRCC** according to the change of speed ratio. It is clear that the pressure ratio increases rapidly when the speed ratio rises. At the best efficiency points, the pressure ratio attains 1.163 ± 0.002 with $\theta_1 = -0.7$ and it increases up to 1.217 ± 0.002 with the speed ratio of $\theta_7 = -1.3$. It can be said that the **CRCC** pressure ratio improved by up to 6.66% compared to the **SRCC**'s one. Similar to the other speeds, the characteristic curve of **CRCC** with θ_7 is close to that of **SRCC** at the speed of $13,000\text{rpm}$. However, the speed ratio does not seem to affect the efficiency of **CRCC**. Figure 4.19b presents that the peak efficiency is almost constant and equal to about $74 \pm 2\%$ when speed ratio changes. This value is always higher than the efficiency of **SRCC** at $70 \pm 2\%$. Consequently, the **CRCC** configuration enhances slightly the efficiency by about 4% compared to the **SRCC**'s one. Table 4.3 summarizes the values of pressure ratio and polytropic efficiency according to the speed ratios. The effective operating range is obtained by combining the best efficiency points of **CRCC** with different speed ratios. This region has a range from mass flow rate of 0.585kg/s to 0.704kg/s . Obviously, it always includes the best efficiency point of **SRCC** (BEP3), as shown in figure 4.19. However, the instability limit shifts to the larger mass flow side as the speed ratio increases. It means that the instability phenomenon occurs earlier at high speed ratios as it is explained in the section 4.3.1. Fortunately, this limit can be improved and can extend the operating range by controlling the rotation speed of the rotors. This content is introduced in chapter 5.

Figure 4.20 show the performance map of **CRCC** with different speed ratios and **SRCC** with three rotation speeds of $9,000\text{rpm}$, $10,000\text{rpm}$ and $11,000\text{rpm}$. Obviously, **CRCC** gives a better performance than **SRCC** and the effective range is wider in case of the same peripheral velocity. The pressure ratio of **CRCC** varies from $\Pi_s = 1.08$ to $\Pi_s = 1.25$ (figure 4.20b), it is higher than the range of **SRCC** from $\Pi_s = 1.06$ to

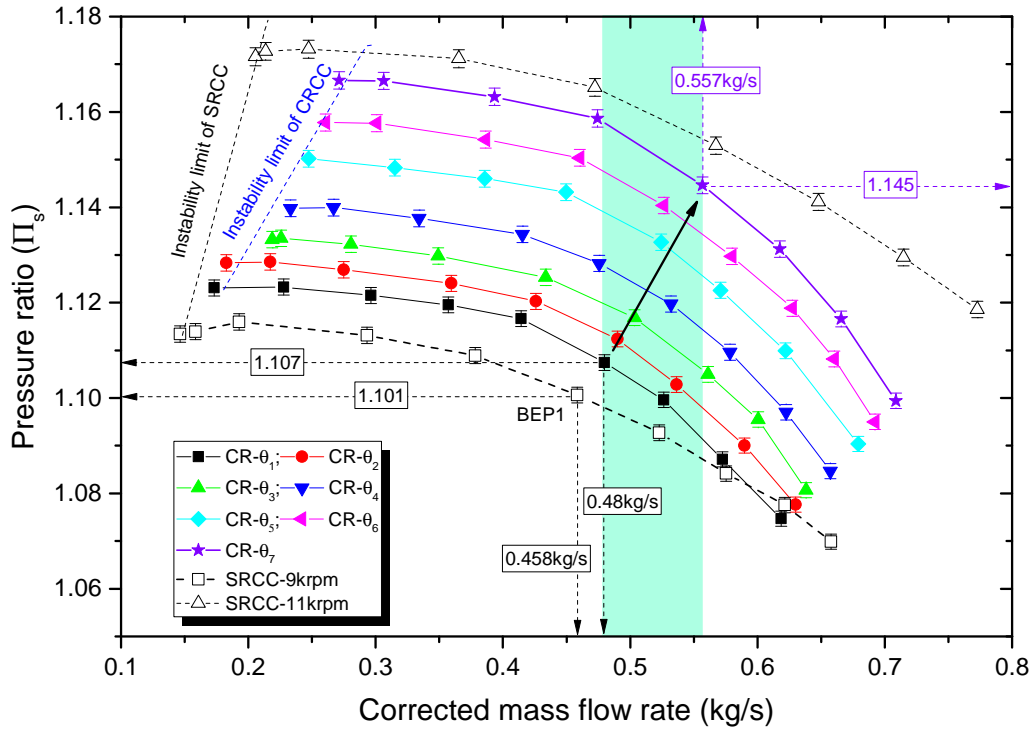
TABLE 4.3 – Global performance of **CRCC** and **SRCC** at the best efficiency points with the different speed ratios and $N_2 = 11,000rpm$

θ	N_1 rpm	N_2 rpm	\dot{m}_{cor} kg/s	Π_s	η_p %
-0.7	-7,700	11,000	0.585	1.163±0.002	74±2
-0.8	-8,800	11,000	0.59	1.172±0.002	74±2
-0.9	-9,900	11,000	0.587	1.184±0.002	74±2
-1	-11,000	11,000	0.584	1.194±0.002	74±2
-1.1	-12,100	11,000	0.624	1.201±0.002	73±2
-1.2	-13,200	11,000	0.676	1.22±0.002	74±2
-1.3	-14,300	11,000	0.704	1.217±0.002	74±2
SRCC		11,000	0.648	1.141±0.002	70±2

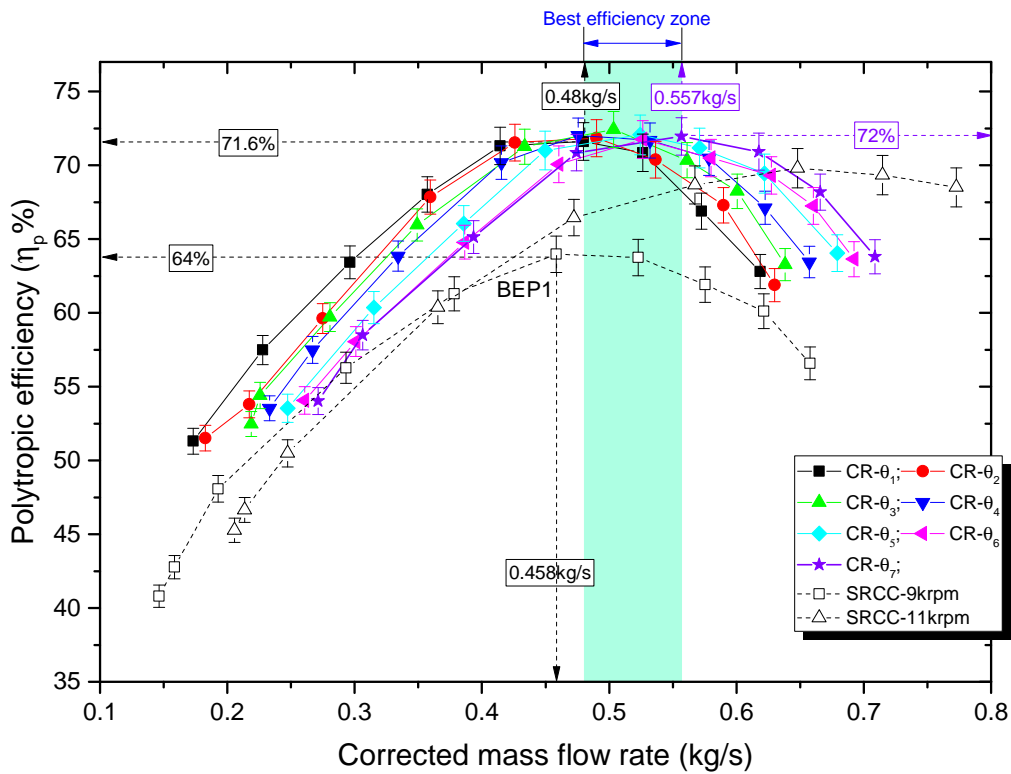
$\Pi_s = 1.17$ (figure 4.20a). Furthermore, the maximum efficiency zone of **CRCC** is bigger than that of **SRCC**. This region is formed by changing the speed of two rotors lead to a change in mass flow rate and pressure ratio. It is worth noting that the maximum polytropic efficiency value of **CRCC** reaches 74%, which is higher than the **SRCC**'s one is 70%. In addition, the **CRCC** operating range is equal to the operating range of **SRCC**, which rotates at maximum speed of 13,000rpm. This means that **CRCC** can operate at the lower peripheral velocity than **SRCC** to obtain the same performance.

4.3.4 Conclusions

The experimental results show that the rotation speed ratio has a great influence on the performance of **CRCC**. The pressure ratio increases linearly with the rotation speed ratio while the maximum of polytropic efficiency seems to be stable. The pressure ratio can be increased by 6.6% for a speed ratio equal to -1.3 . The polytropic efficiency is enhanced by about 4%. It is worth noting that **CRCC** can operate at a lower speed than 2,000rpm in comparison with the speed of **SRCC** to obtain the same performance. Moreover, the best efficiency point of **CRCC** changes according to the variation of speed ratio. The set of maximum efficiency points at different rotation speed ratios indicates the effective working area of **CRCC**. This area expands around the operating point of **SRCC** with the same peripheral velocity. It can be concluded that **CRCC** gives a more flexible operating range to meet the various working conditions in comparison with **SRCC**. However, the instability limit of **CRCC** in counter-rotating mode appears earlier. This phenomenon can be solved by changing the speed of two rotors simultaneously, this content is presented in chapter 5.

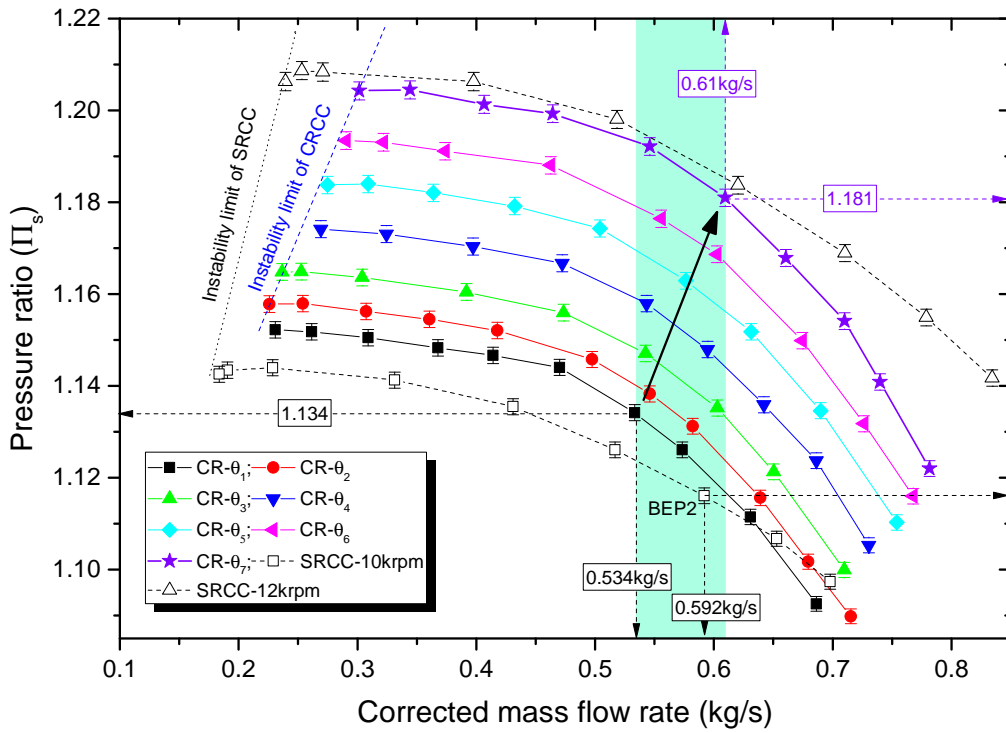


(a) Pressure ratio

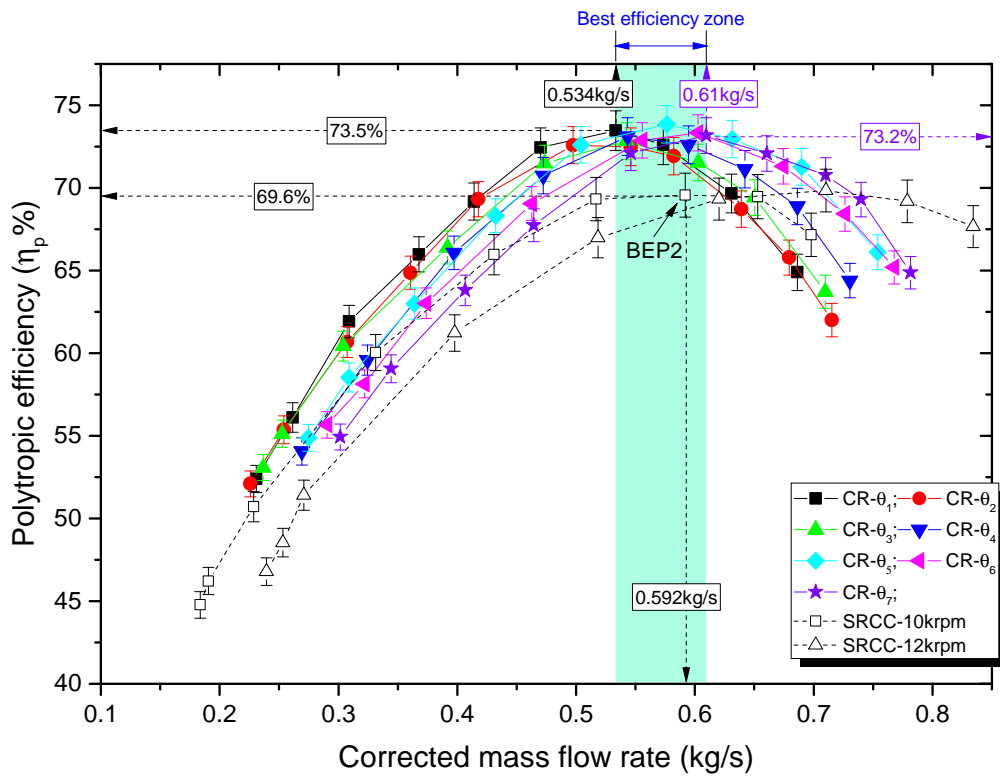


(b) Polytopic efficiency

FIGURE 4.17 – Influence of speed ratio on the performances of CRCC (solid lines) with $N_2 = 9,000rpm$ in comparison with the performances of SRCC (dashed lines) at $N = 9,000rpm$ and $N = 11,000rpm$: (a) Pressure ratio and (b) Polytopic efficiency

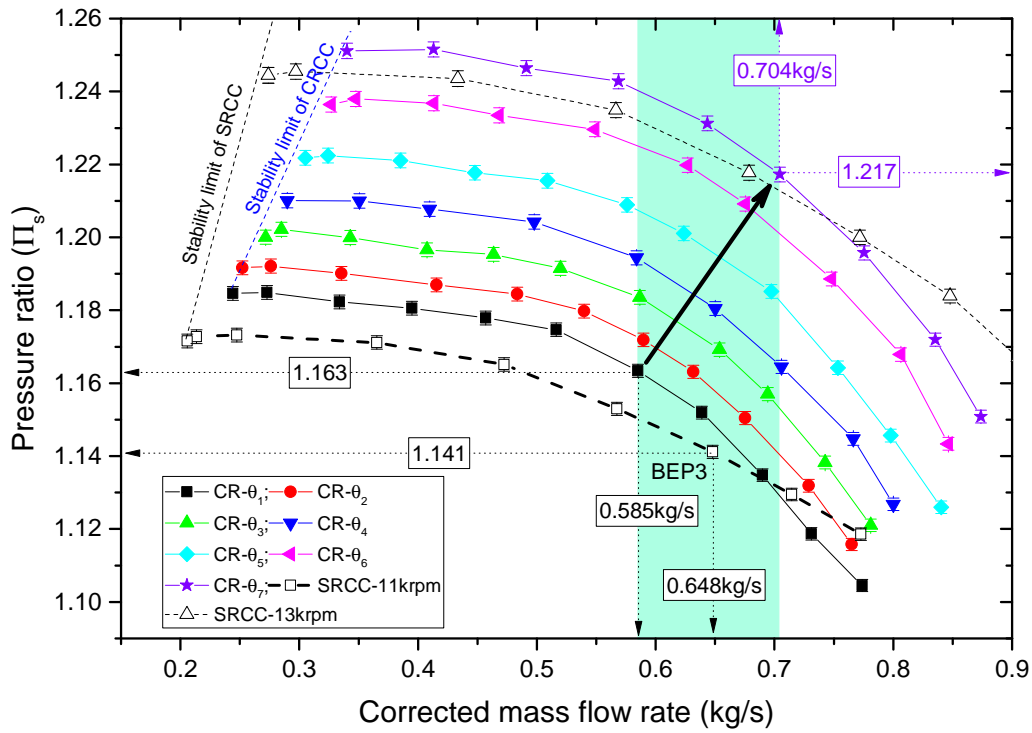


(a) Pressure ratio

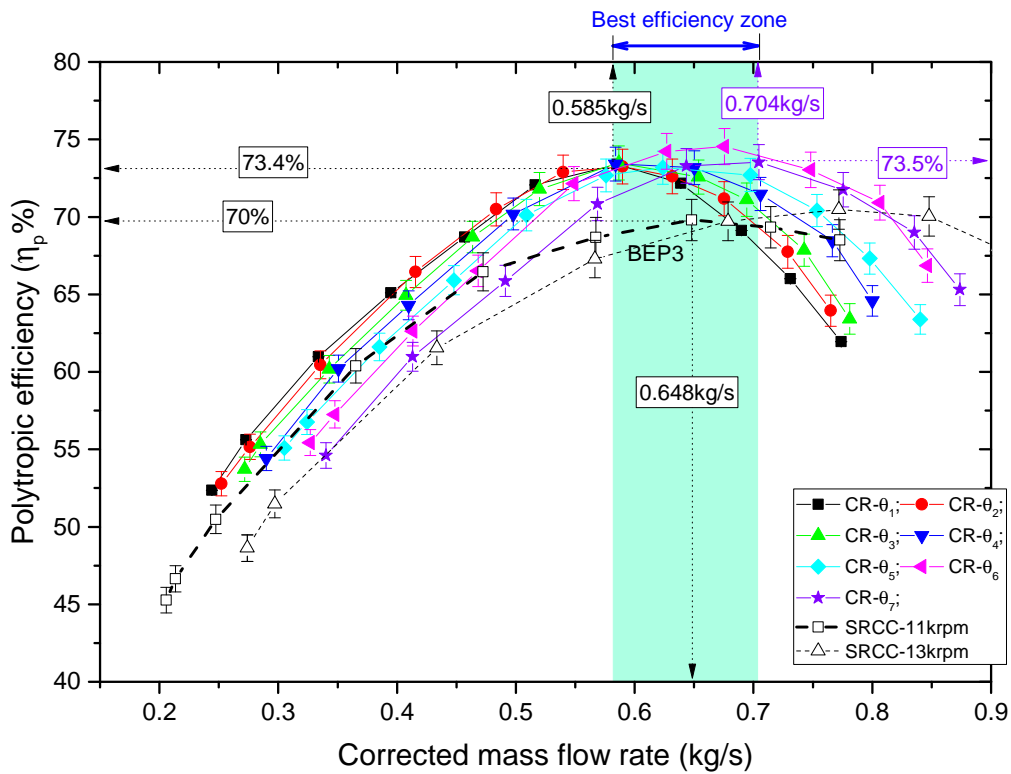


(b) Polytopic efficiency

FIGURE 4.18 – Influence of speed ratio on the performances of CRCC (solid lines) with $N_2 = 10,000rpm$ in comparison with the performances of SRCC (dashed lines) at $N = 10,000rpm$ and $N = 12,000rpm$: (a) Pressure ratio and (b) Polytopic efficiency

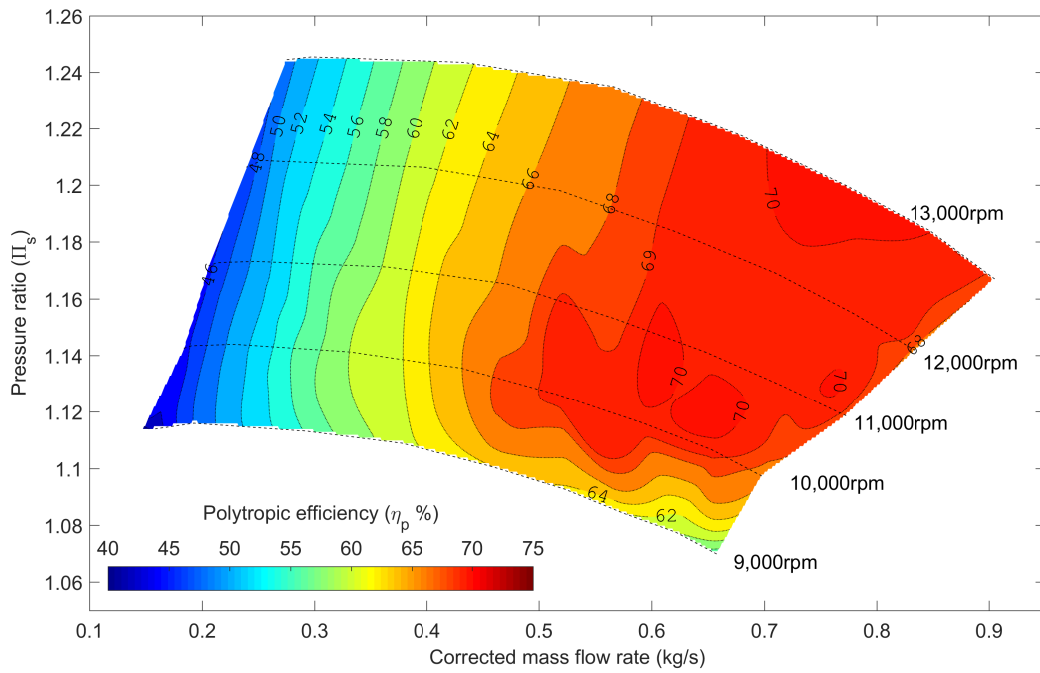


(a) Pressure ratio

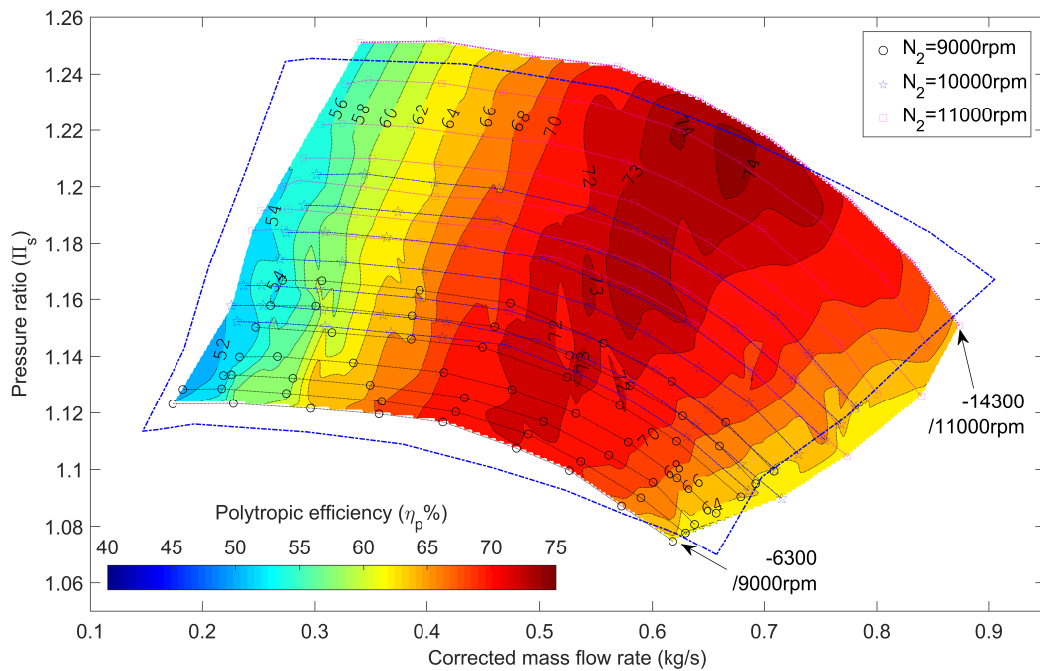


(b) Polytypic efficiency

FIGURE 4.19 – Influence of speed ratio on the performances of CRCC (solid lines) with $N_2 = 11,000rpm$ in comparison with the performances of SRCC (dashed lines) at $N = 11,000rpm$ and $N = 13,000rpm$: (a) Pressure ratio and (b) Polytypic efficiency



(a) Performance map of SRCC with $9,000rpm \leq N \leq 13,000rpm$



(b) Performance map of CRCC with $9,000rpm \leq N_2 \leq 11,000rpm$

FIGURE 4.20 – Performance map of (a) CRCC and (b) SRCC with the rotation speed changes in range of $[9,000rpm \ 13,000rpm]$

4.4 Similarity method

The performance of turbomachinery can be defined by the pressure curves plotted as a function of the volume flow for the different rotation speeds. An attempt to study the variations of all the involved quantities would require an excessive number of experiments. On the other hand, it would be impossible to make a concise presentation of the results. Most of these complications can be overcome by using, for example, dimensional analysis, which allows combining the variables to form a smaller and more manageable number of dimensionless groupings. The head-flow characteristics can then be represented reasonably by a single curve. The non-dimensional curve is then used to build the characteristic curves of the compressor at different speeds by similarity method. More details of the similarity method theory are presented in Appendix A.2.

4.4.1 Similarity method validation

The non-dimensional parameters describe the performance of the compressor by combining two main non-dimensional variables, including flow coefficient and head coefficient. From this relationship, the other non-dimensional variables of the compressor at different rotation speeds can be interpolated by the similarity. The flow coefficient ϕ and head coefficient Ψ are determined by [49]:

$$\phi = \frac{4\dot{m}}{\rho_1 U_2 \pi d_2^2} \quad (4.3)$$

$$\Psi = \frac{2\Delta h}{U_2^2} \quad (4.4)$$

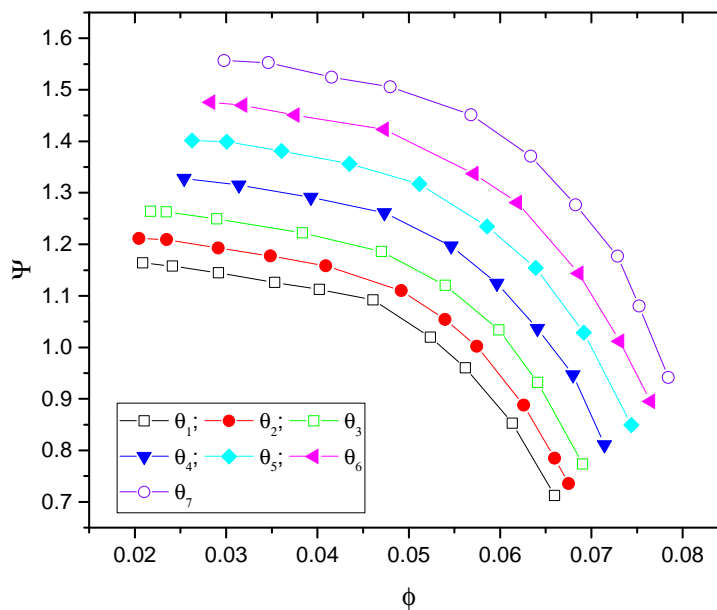


FIGURE 4.21 – Non-dimensional characteristics of CRCC with different speed ratios are obtained by experiment at the second rotor speed of $10,000rpm$

Because the experimental conditions do not allow CRCC to operate at the designed speed of $16,000rpm$ (as described in section 4.1), these characteristic curves of CRCC at the design speed are built based upon the given empirical non-dimensional curves. These curves must be obtained by the experimental measurement on the same machine. The non-dimensional curves at $10,000rpm$ are chosen for the similarity method, as shown in figure 4.21. From that, the characteristic curves of the compressor at the design speed can be obtained by interpolation calculation of the similarity method. To ensure the reliability of the method, the compressor characteristics are calculated by using the similarity method and are compared with experimental results for a second rotor speed of $9,000rpm$ and $11,000rpm$.

Figure 4.22 shows a comparison of calculation and experiment at seven speed ratios with the second rotor speed of $9,000rpm$. It is clear that the calculation results coincide with the experimental data. Besides, a comparison between calculations and measurements at the speed of $11,000rpm$ shows that the similarity method gives quite good results, as shown in figure 4.23. However, there is a slight deviations at a high mass flow rate with the speed ratios of $\theta_6 = -1.2$ and $\theta_7 = -1.3$. The maximum deviation between calculation and experiment is about 0.8% for pressure ratio and 3% for polytropic efficiency. Thus, the results of validation show that the similarity method allows predicting characteristics at different speeds quite accurately and reliably.

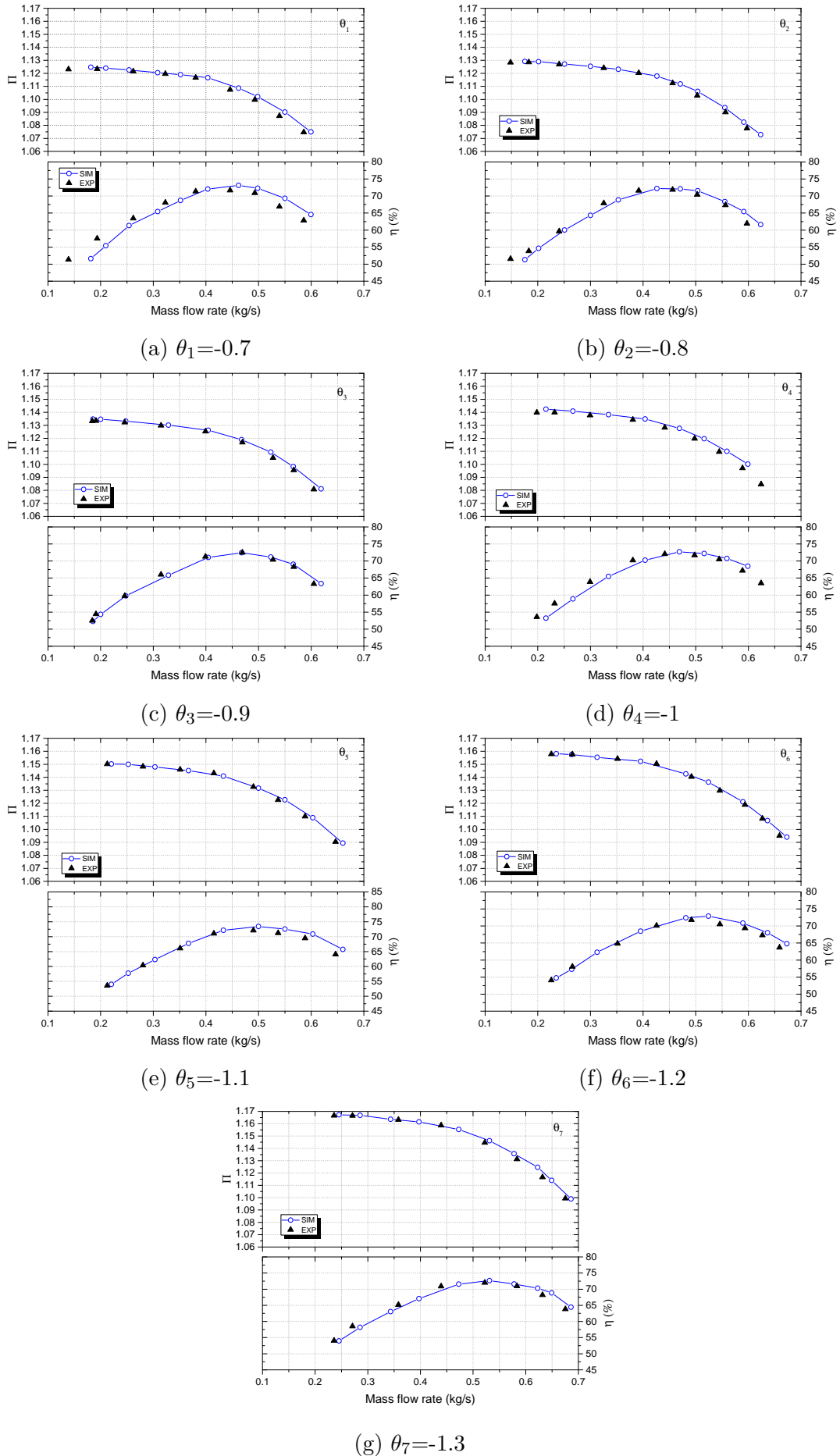


FIGURE 4.22 – Comparison between the similarity method and the experimental results for CRCC in case of a second rotor rotating at $9,000rpm$

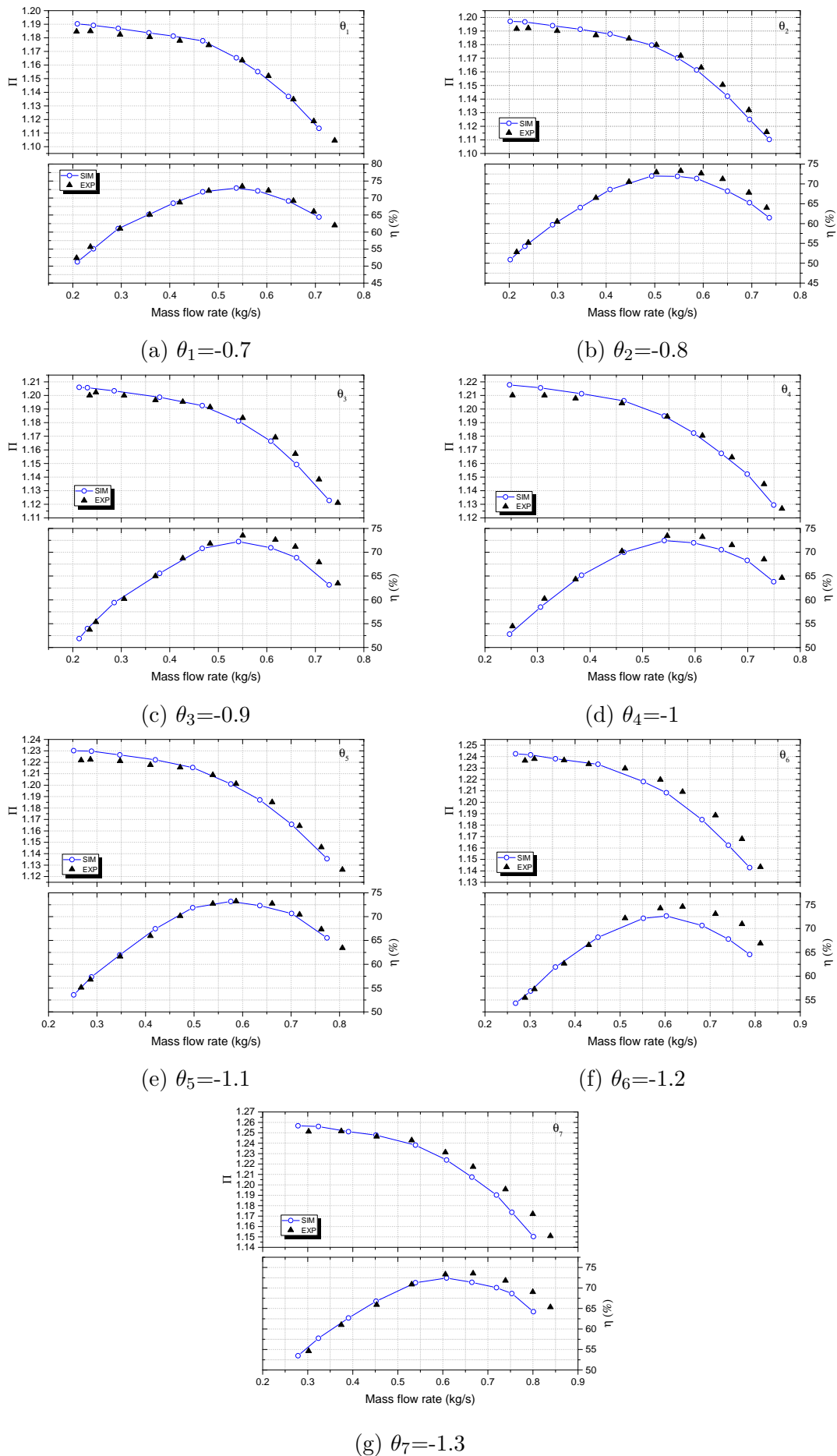


FIGURE 4.23 – Comparison between the similarity method and the experimental results for CRCC in case of a second rotor rotating at 11,000rpm

4.4.2 CRCC characteristics at the design speed of 16,000rpm

Calculation results of the similarity method at the design speed of 16,000rpm are shown in figure 4.24. The pressure ratio curves show that CRCC always produces a higher pressure ratio than SRCC. This raise is proportional to the increase in the speed ratio. The pressure ratio of CRCC reaches 1.37 at θ_1 and goes up to 1.514 at θ_7 at the best efficiency points. That means the pressure ration is improved by about from 4.5% to 15.13% in comparison with the pressure ratio of SRCC at the rotation speed of 16,000rpm. At the speed ratio $\theta_4 = -1$, the pressure ratio of CRCC can reach 1.442, which improves by about 10.3%. However, the polytropic efficiency of CRCC remains stable at about 72% and slightly reduces by about 1% in comparison with the peak efficiency of SRCC. It can be noticed that the best efficiency points of CRCC achieve at the different mass flow rates and depend on the rotation speed ratio. The peak efficiency takes place at the mass flow rate of 0.869kg/s with the θ_1 and increases up to the mass flow rate of 1,117kg/s with the θ_7 . Consequently, a wider effective region is generated by changing speed ratio.

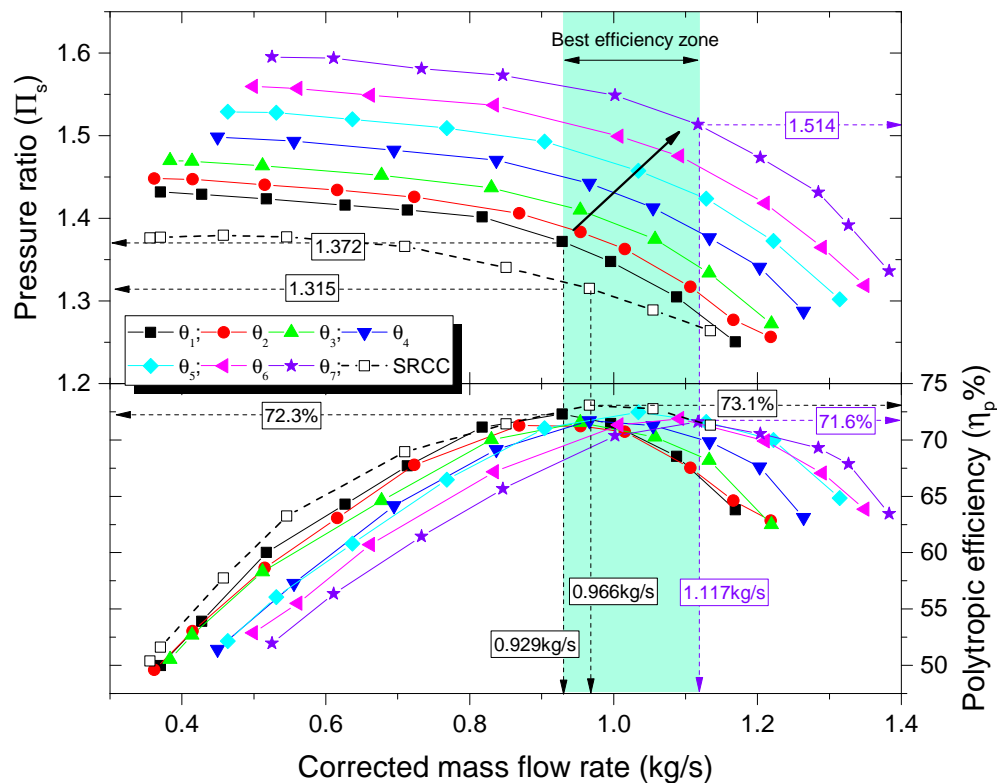


FIGURE 4.24 – Characteristics of CRCC calculated by the similarity method at the design speed of 16,000rpm with different speed ratios

4.4.3 Conclusions

The similarity method allows calculating and constructing the performance curve of a compressor's family based on known operating parameters at a specific speed. The results of the similarity calculation are compared with the experimental results at the second rotor speed of 9,000rpm and 11,000rpm. The results show that the similarity method correctly predicts the working parameters of the compressor at those rotation speeds. Therefore, it is used to build the CRCC characteristic curves at the design

speed of $16,000rpm$. These curves show that the **CRCC** pressure ratio is always higher than **SRCC**'s one. It is increased up to 15.3% for the $\theta_7 = -1.3$ in comparing to the pressure ratio of **SRCC** at $16,000rpm$. Moreover, **CRCC** efficiency remains stable at about 72% and it slightly reduced by about 1% compared to the peak efficiency of **SRCC**. These peak efficiency of **CRCC** are obtained at different mass flow rates when changing the speed ratio. A wider effective region is formed that means **CRCC** is more flexible.

4.5 CFD Analysis

Computational Fluid Dynamic (CFD) is a useful tool for analyzing fluid flow during the design process. The principle of this method is to solve the governing equations of continuity, momentum, and energy together across the complete domain to predict the flow field. The detail of the equations, the turbulence models as well as the boundary conditions used in this thesis are presented in the appendix [A.4](#). The following section presents the **CRCC** model used for numerical study.

4.5.1 Meshing

Before calculating the numerical simulation of the governing equations, it is necessary to discretize the surfaces of all boundaries and to generate a volume grid inside the flow domain. In this thesis, the grid is generated automatically by Star CCM+. Although the automated mesh generator has some disadvantages such as some loss of flexibility, it is a much faster technique when dealing with complex geometries such as centrifugal rotor. The meshing model is done with the Surface Remesher, Polyhedral, and Prism Layer Mesher. The base size of the mesh is chosen equal to $30mm$, and the local refinements are done in the blade surfaces, shrouds, and interfaces. An extrusion at both inlet and outlet boundary conditions in order to keep the flow with a uniform behavior and to have better control over the boundary condition. A general view of the mesh is present in figure [4.25](#). Seven mesh domains are generated for the inlet, bend inlet, first rotor, second rotor, casing, volute, and outlet domains.

In order to refine the mesh of both two main rotors domains, the mesh size of the blades and the shroud is controlled by the maximum and the minimum sizes of cells are $1.5mm$ and $0.3mm$, respectively. In addition, to ensure the conformity of two adjacent domains during the unsteady simulation, the cell size in the interfaces between the domains is imposed equal to $0.9mm$. The total thickness of prism layer is fixed to $0.3mm$ with six layers to ensure the boundary layer resolution value of y^+ close to 1, as shown in figure [4.27](#). The first rotor with seven blades is meshed with $1.3e6$ cells and with $2.1e6$ cells for the second rotor with nine blades. The entire model of **CRCC** consists of about $5.2e6$ cells. More details of the mesh are illustrated in figure [4.26](#).

4.5.2 Mesh sensitivity analysis

As it is known to all, in numerical simulations, grid quality always plays a very important role and greatly affects the results. If the quality of the mesh is poor quality leads to inaccurate results, besides the good quality gives more accurate predictions that can be used to study the properties of the fluid flow inside the compressor. However, mesh quality often goes hand in hand with the number of cells: if the mesh has too many cells, the calculation takes a long time and more resources. Therefore, the

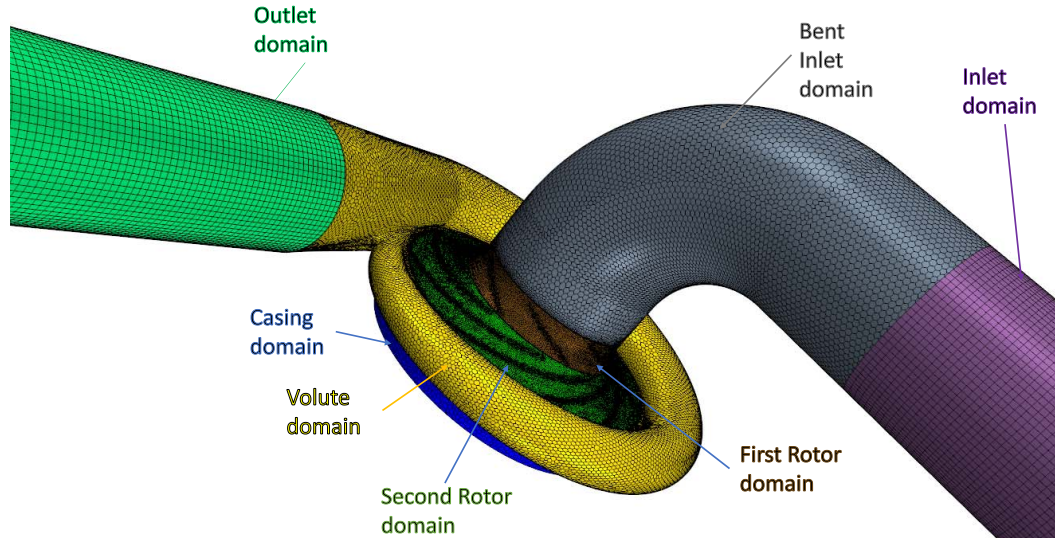


FIGURE 4.25 – Different mesh domains used for the numerical simulation of CRCC

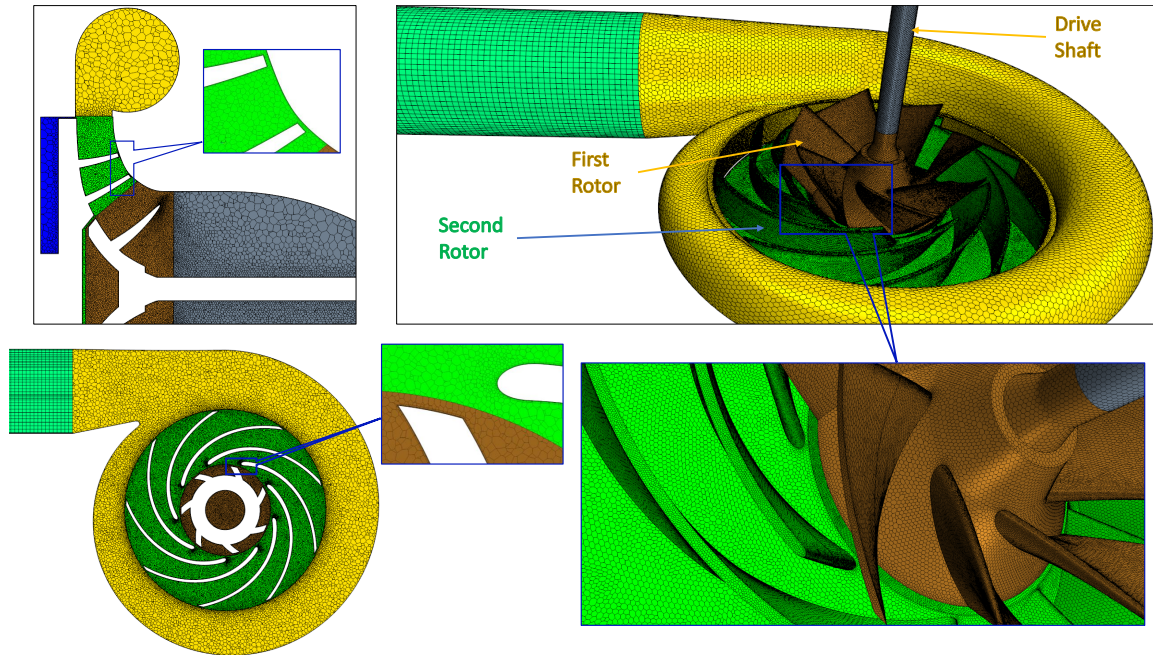


FIGURE 4.26 – Different views of the CRCC mesh model

selection of reasonable parameters for meshing to get good results as well as saving the calculation time is necessary. The study of mesh sensitivity is conducted in this thesis. This study is performed at the best efficiency point of the compressor at the speed of $N_1 = -10,000rpm$ and $N_2 = 10,000rpm$ with four different mesh types of $3e6$, $5.3e6$, $10e6$, $20e6$ and $50e6$ cells. The results of the grid sensitivity study are presented in table 4.4. It is easy to see that the difference in simulation results between models is not large. In other words, when the mesh number is greater than $5.3e6$ cells, the increase of cells has little influence on the numerical results of the compressor performance. In addition, the result of the first mesh configuration gives the highest accuracy with the tolerance of pressure ratio and efficiency are 2.19% and 0.03%, respectively. Consequently, the mesh of $5.3e6$ cells is chosen for the numerical study in

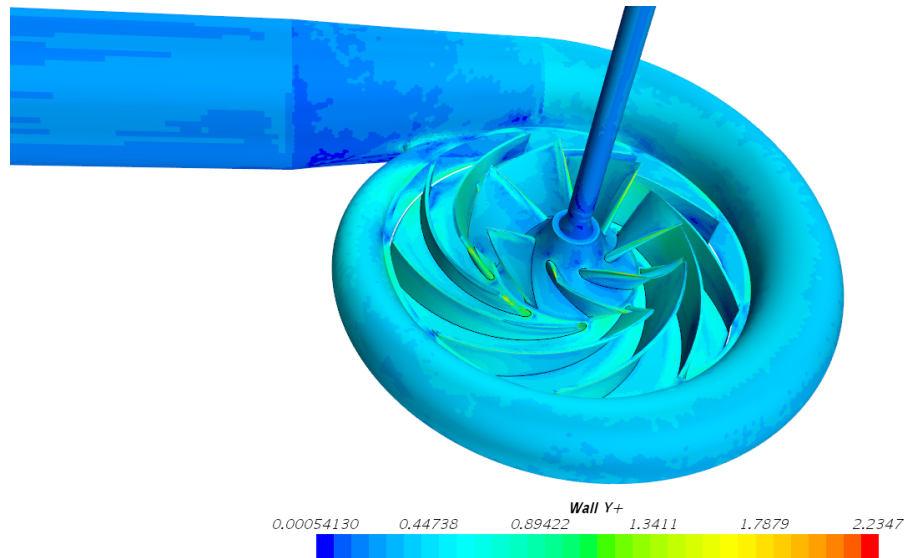


FIGURE 4.27 – Distribution of wall y^+ at the best efficiency point ($\dot{m}_{cor} = 0.531\text{kg/s}$, $N_1 = -10,000\text{rpm}$, $N_2 = 10,000\text{rpm}$)

TABLE 4.4 – The study of mesh sensitivity

Number of cells (million)	\dot{m}_{cr} (kg/s)	Π_s	η_p (%)	$Error_{\Pi_s-EXP}$ (%)	$Error_{\eta_p-EXP}$ (%)
5.3	0.531	1.137	72	1.8	2
10	0.530	1.136	72	1.9	2
20	0.530	1.052	72	9.2	2
50	0.532	1.052	73	9.2	1

order to save the resources and calculation time. The simulation parameters and the boundary conditions are summarized in the table 4.5.

TABLE 4.5 – Simulation parameters

Mesh model (number of cells)	5.3e6
N_1	-10,000rpm
N_2	10,000rpm
Inlet temperature	300°K
Outlet pressure	101,325Pa
Mass flow rate	0.53kg/s
Turbulence model	k- ω SST
Interface	Direct (frozen rotor)
Time step (for unsteady simulation)	2.143e - 5s

4.5.3 Validation of numerical simulation

All simulations are carried out at three main speeds of the second rotor and seven speed ratios as presented in chapter 4. The air assumed as an ideal gas with standard properties is used as the working fluid in the compressor. The inlet static pressure and temperature are collected as a mass average at a constant surface located upstream at

a distance of $4D$. The static temperature of the outlet is taken at a constant surface located downstream at a distance of $3D$. The outlet static pressure is imposed as the atmospheric pressure of $101,325Pa$ at the outlet pipe. A pressure probe is placed at the shroud of two rotors interface to collect the wall pressure fluctuation. Figure 4.28 depicts the position of the sensor as well as the surface of measurement at inlet and outlet.

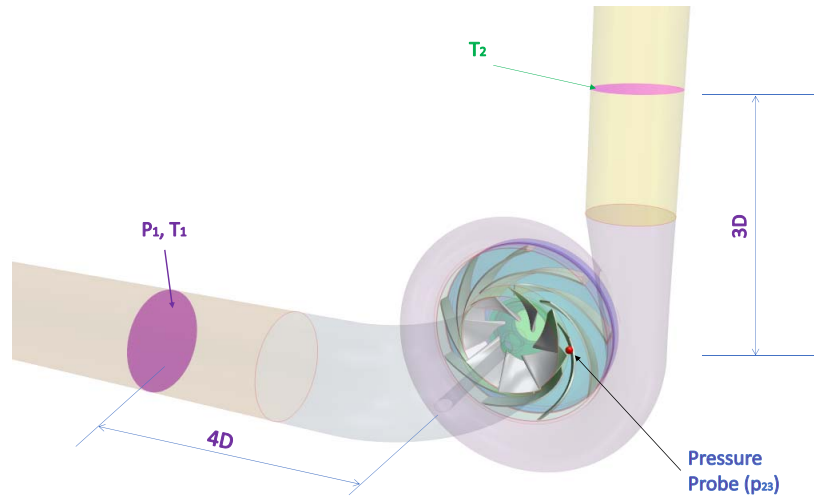


FIGURE 4.28 – Diagram of the surfaces measuring pressure (P) and temperature (T) and location of pressure probes used for simulation

Figure 4.29, 4.30, and 4.31 show the experimental and predicted performance of CRCC at three speeds of the second rotor in term of variation of pressure ratio and polytropic efficiency with the corrected mass flow rate. The simulation results are slightly underestimated compared to the experimental measurement, but the divergence is not large. Referring to figure 4.29, the predicted and tested pressure ratio presents a fairly good agreement at a low mass flow rate with a minimum divergence of about 0.7% for $\theta_1 = -0.7$. However, as the flow rate increases, the gap between the predicted and the experimental results becomes larger. This deviation reaches a maximum value of about 4.05% for $\theta_5 = -1.1$ at the largest flow rate. In the same way, concerning polytropic efficiency, the predicted results are quite good compared to the experimental measurement. The divergence between simulation and experiment reaches a minimum value of about 0.15% at best efficiency point with $\theta_5 = -1.1$ and it is broadened as the mass flow rate increases. The maximum deviation value can reach about 8.7% at the $\dot{m}_{cor} = 0.7kg/s$ with $\theta_6 = -1.2$. At 10,000rpm, as shown in figure 4.30, the maximum deviation between the predicted and experimental results is 4.98% for pressure ratio and 9.3% for efficiency at $\dot{m}_{cor} = 0.75kg/s$ and $\theta_5 = -1.1$. The smallest deviation is 0.9% for pressure ratio at $\dot{m}_{cor} = 0.23kg/s$, $\theta_1 = -0.7$ and 0.56% for efficiency at $\dot{m}_{cor} = 0.33kg/s$, $\theta_4 = -1$. At the best efficiency point, the maximum and minimum deviation of pressure ratio are respectively 2.7% and 1.01% while that of the efficiency are 0.4 % and 4.24 %, respectively. At 11,000rpm, figure 4.31 presents the maximum divergence between simulation and experimental results does not exceed the value of 5.7% for pressure ratio and 10% for polytropic efficiency at $\dot{m}_{cor} = 0.88kg/s$ and $\theta_7 = -1.3$. The minimum gap obtained for pressure ratio and efficiency are respectively 1.13% at $\dot{m}_{cor} = 0.29kg/s$, $\theta_4 = -1$ and 0.26% at $\dot{m}_{cor} = 0.38kg/s$, $\theta_7 = -1.3$. Otherwise, at the best efficiency point, the largest gap does not exceed 2.42% for pressure ratio and

4.66% for polytropic efficiency while the smallest one is 1.25% and 0.37%, respectively. The significant deviation between prediction and experimental measurement at a high mass flow rate can be interpreted by the increase of losses between two rotors. This also explains why when the speed ratio increases, the divergence between simulation and measurement broadens. On the other hand, it can be easy to see that these models produce good results when the flow rate changes from the maximum efficiency point toward a lower mass flow rate. The deviation in this region does not exceed 2.8% for pressure ratio and 4.66% for efficiency. These values are not large (below 5%) and acceptable. In addition, the purpose of this thesis deals with the region of low flow rate so that these results can be manipulated to study further the flow analysis.

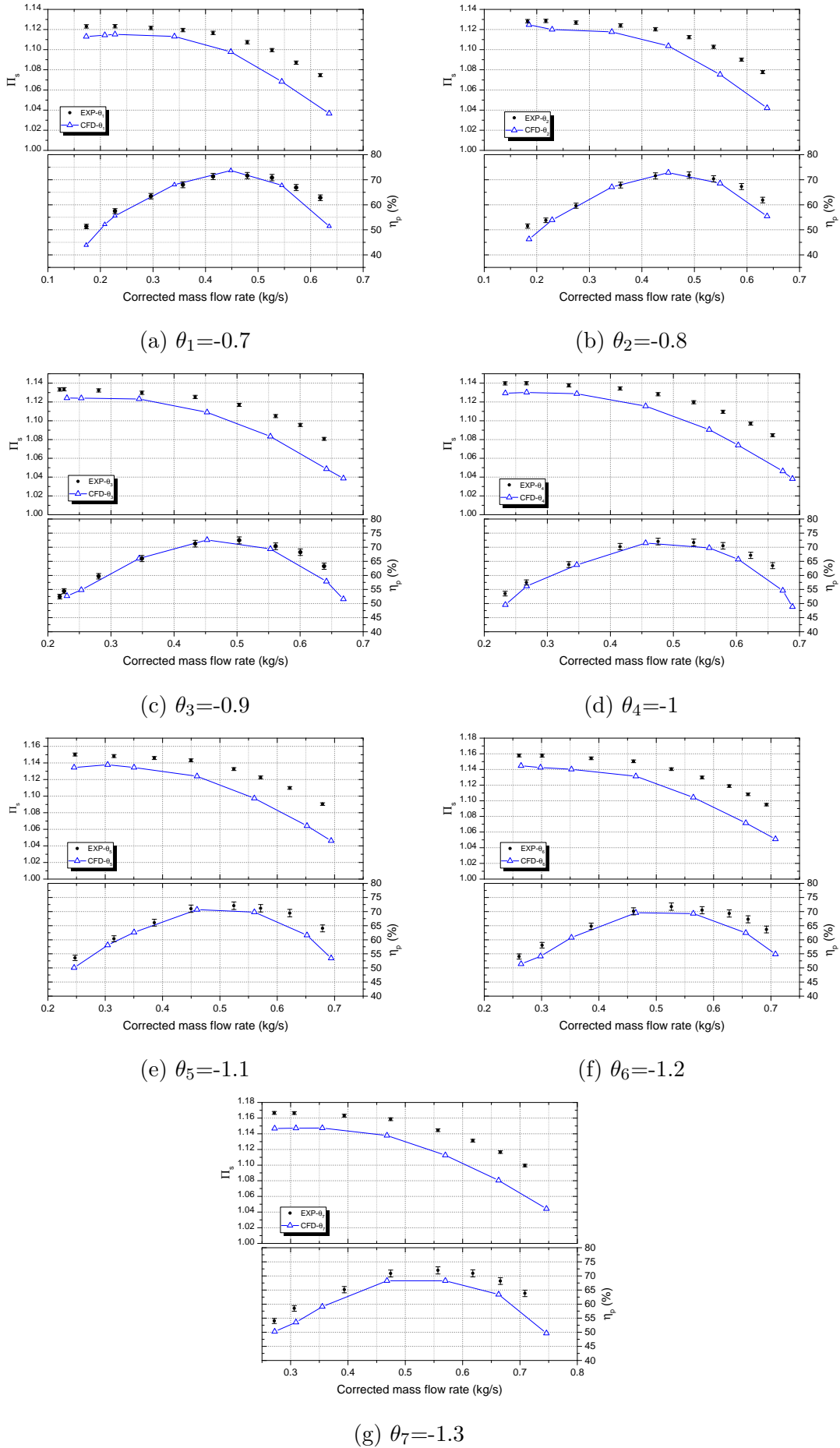


FIGURE 4.29 – Comparison of CRCC performances between numerical results (blue line) and experimental measurements (black points) with $N_2 = 9,000rpm$ and seven speed ratios

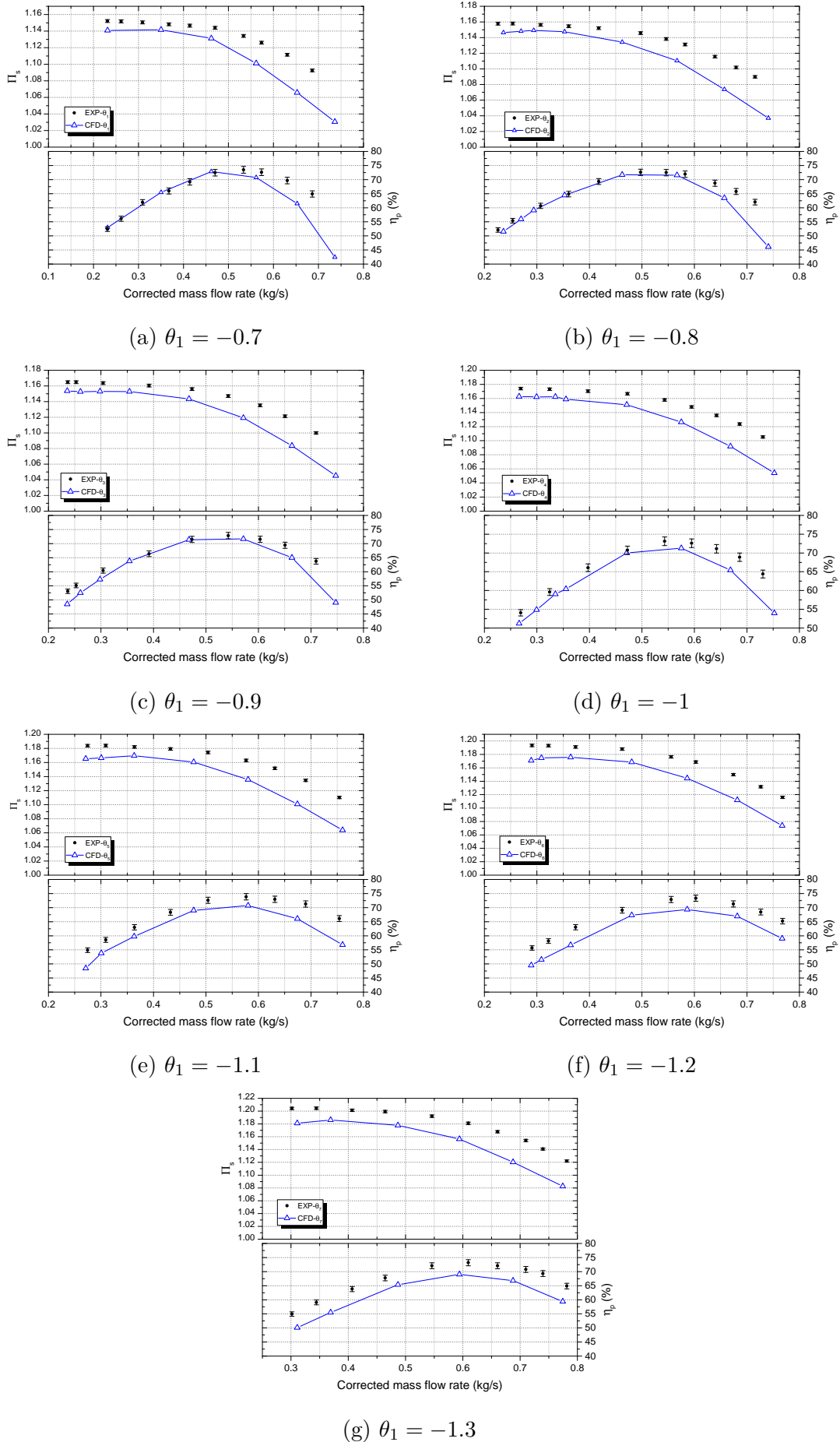


FIGURE 4.30 – Comparison of CRCC performances between numerical results (blue line) and experimental measurements (black points) with $N_2 = 10,000rpm$ and seven speed ratios θ

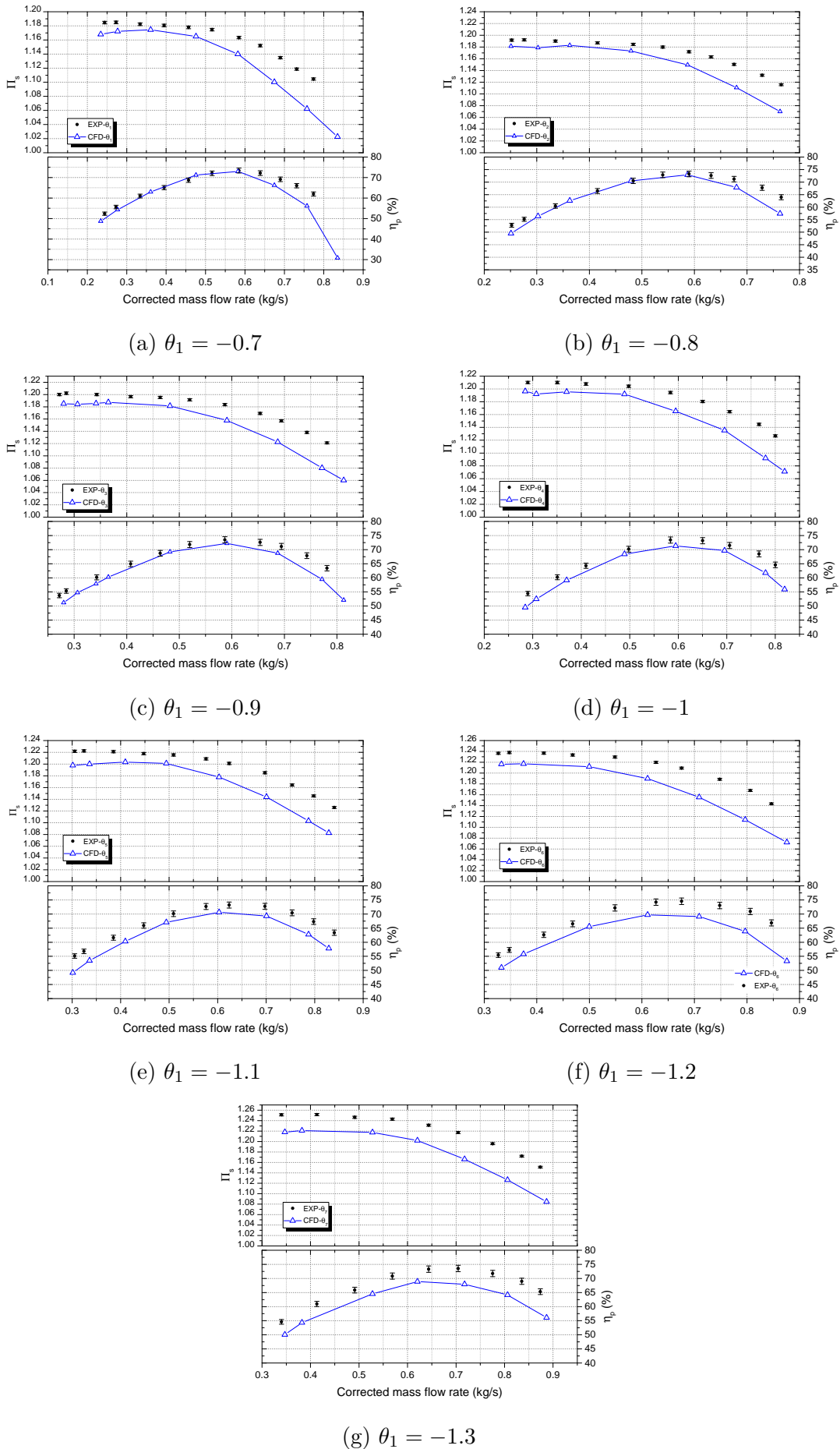


FIGURE 4.31 – Comparison of CRCC performances between numerical results (blue line) and experimental measurements (black points) with $N_2 = 11,000rpm$ and seven speed ratios θ

4.5.4 Flow assessment

The steady and unsteady computations are performed to study the flow field inside the compressor. Firstly, the steady simulation is conducted to analyze the global aerodynamic parameters as well as flow structure inside the compressor. Secondly, the unsteady computation is used to study the interaction between two rotors and the fluctuations of wall pressure in time-step. There are two points to be analyzed in this thesis are **Best Efficiency Point (BEP)**, **Near Instability Point (NIP)**. The first rotor speed of $N_1 = -10,000rpm$ and the second rotor speed of $N_2 = 10,000rpm$ are chosen because it represents the design operating point of the **CRCC** in the contra-rotating mode. Furthermore, the deviation between simulations and experimental results is equal to 2.7% for pressure ratio and 1.83% for efficiency at **BEP**. At **NIP**, it represents about 1% for pressure ratio and 0.5% for efficiency, respectively.

TABLE 4.6 – Operating parameters of BEP and NIP

Parameters	BEP	NIP
$\dot{m}_{cr}(kg/s)$	0.543	0.233
$N_1(rpm)$	-10,000	-10,000
$N_2(rpm)$	10,000	10,000

Steady simulation analysis

In a steady-state analysis, **BEP** and **NIP** are computed to evaluate the fluid flow inside the compressor. The pressure, Mach number, velocity, and temperature field are studied in three equipotential surfaces located at 0.25, 0.5, and 0.75 span.

- Pressure field

Figure 4.32 shows the pressure field in different equipotential surfaces of **CRCC** at **BEP** and **NIP**. The three images on the top represent pressure distributions at **BEP** while the other ones on the bottom display the pressure field at **NIP**. In general, the pressure distribution at **BEP** is quite similar for all positions. The pressure increases gradually from the rotor inlet to the rotor outlet and from the tongue of the volute to the outlet of the compressor.

At **NIP**, it is easy to see that the pressure rises rapidly inside the volute from the tongue¹ to the outlet of the compressor. Moreover, it is easy to realize that an adverse high-pressure gradient is developed progressively towards inside the volute and close to the outlet the second rotor. It prevents the air circulation in the passages next to the tongue of the volute. As a result, the turbulence appears to block these passages completely or partially, while gas circulates normally in the other passages (figure 4.34).

1. the joint of the volute smallest, largest volume area and the exit cone

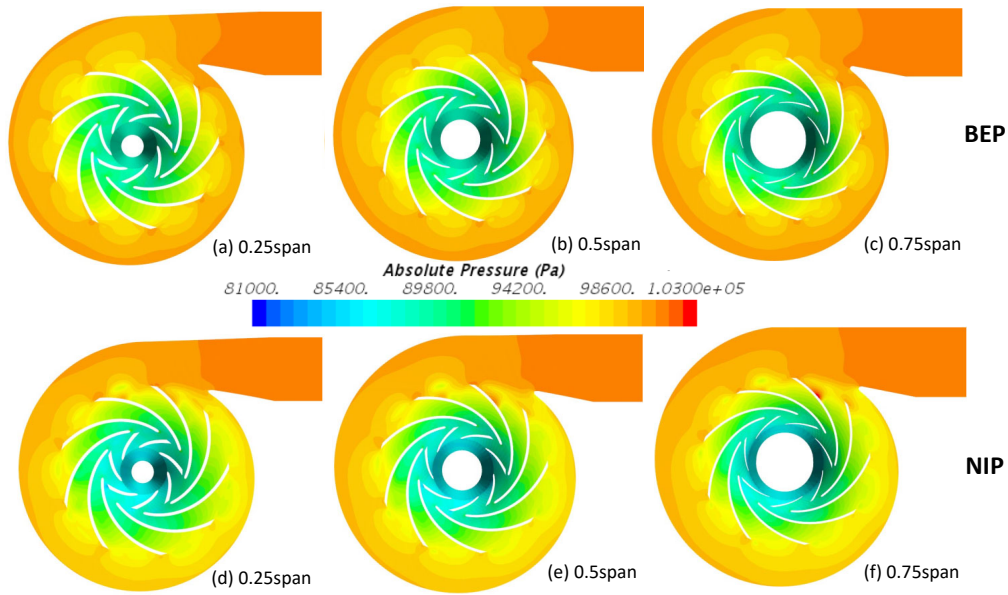


FIGURE 4.32 – Pressure distribution of CRCC at two operating points: BEP and NIP on three equipotential surfaces located at 0.25, 0.5 and 0.75span

- Relative Mach number field

The distribution of the relative Mach number is shown in figure 4.33. It is clear that the relative Mach number increases significantly at the leading edge of the second rotor caused by the relative velocity combines itself with the new local peripheral velocity to produce a relatively higher velocity [3], called the contra-rotating effect. The Mach number distribution is quite similar in most blade passages of the second rotor at BEP, as shown in figure 4.33a, 4.33b and 4.33c. However, this field occurs unevenly at NIP because some blade passages are blocked by eddy flows - especially near the tongue region of the volute, as presented in figure 4.33d, 4.33e and 4.33f.

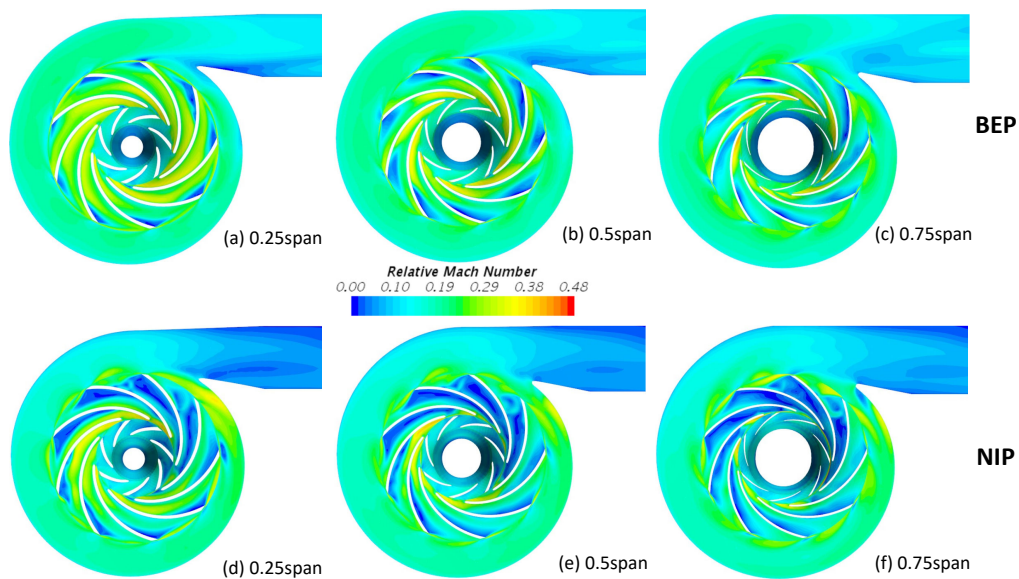


FIGURE 4.33 – Relative Mach number distribution of CRCC at two operating points: BEP and NIP on three equipotential surfaces located at 0.25, 0.5 and 0.75span

- Velocity streamline

Figure 4.34 show the velocity streamline on three equipotential surfaces located at 0.25, 0.5, and 0.75span. It is easy to see that the streamline is quite laminar in both rotors as well as in the volute for **BEP** (figure 4.34a, figure 4.34b and figure 4.34c). Nonetheless, there is several blade passages with local vortex region for **NIP** as shown in figure 4.34d - figure 4.34f. Depending on the position of the blade passage compared to the volute tongue, the size of the vortexes is different. If its position is close to the volute tongue in the direction of the rotor rotation, the size of the vortexes will become larger due to the fluid flow encountering the high-pressure gradient from the output side. It affects the fluid flow and changes the incidence angle of the blade passage. Consequently, the separation of the fluid flow occurs in the blade passage and forms the vortex cells. These vortex cells grow in the opposite direction to the rotor rotation, which explains why in the successive blade passages of the rotor also has vortex cells, but its size decreases gradually.

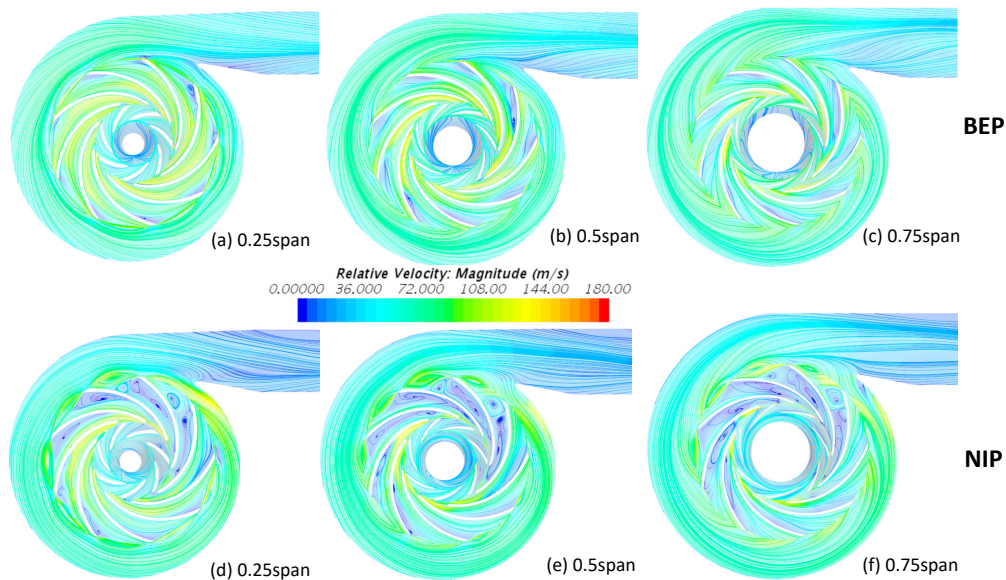


FIGURE 4.34 – Relative velocity streamline of **CRCC** at two operating points: **BEP** and **NIP** on three equipotential surfaces located at 0.25, 0.5 and 0.75span

Figure 4.35 shows a 3D visualization of streamlines at 0.5 span for **BEP**. Obviously, the fluid flow in the first rotor and the second rotor is homogeneous because the incidence angle of the fluid flow matches the blade inlet angle. The exit flow is quite uniform, so the performance of the compressor can reach a high value of efficiency. However, it is easy to see that some blade passages of the second rotor are blocked for **NIP** due to the appearance of vortices within it, as shown in figure 4.36. These vortices appear usually near the volute tongue. In this region, the fluid flow encounters a dividing plane, above which the flow exits the compressor, below which the flow re-enters the volute [50]. It is clear that there are two blade passages completely blocked by the vortices and they decrease in size in the adjacent blade passages and in the opposite to the rotational direction of the second rotor. The fluid flow can pass through this passage and it is increased in the next passages. The size of the vortices inside the blade passage decreases according to blade passages numbered from (1) to (5). The vortices (1)

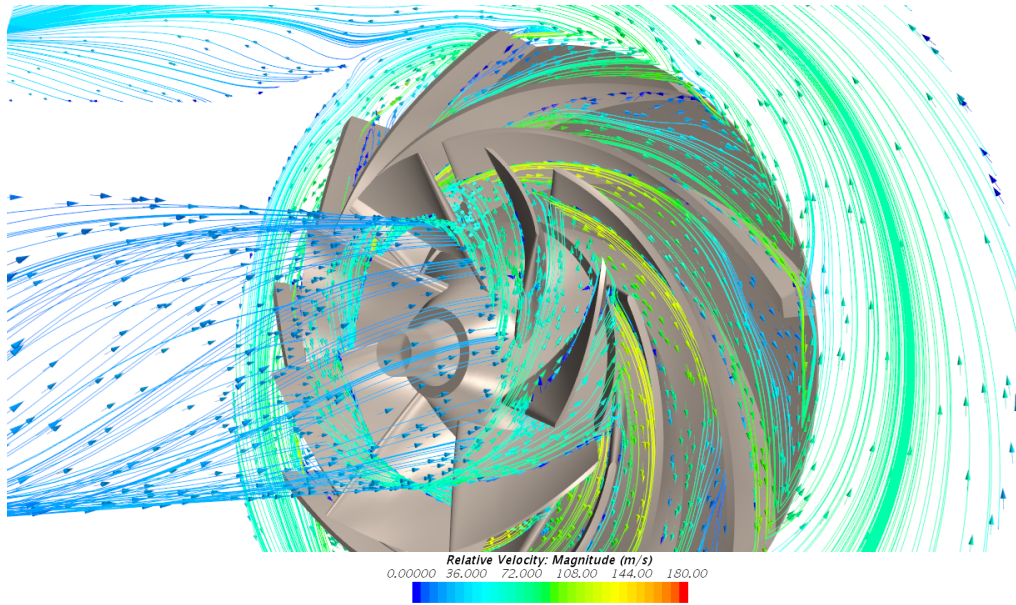


FIGURE 4.35 – 3D visualization of streamlines on the equipotential surface located at 0.5span with $N_2 = 10,000rpm$ and $\dot{m}_{cr} = 0.543kg/s$ (BEP)

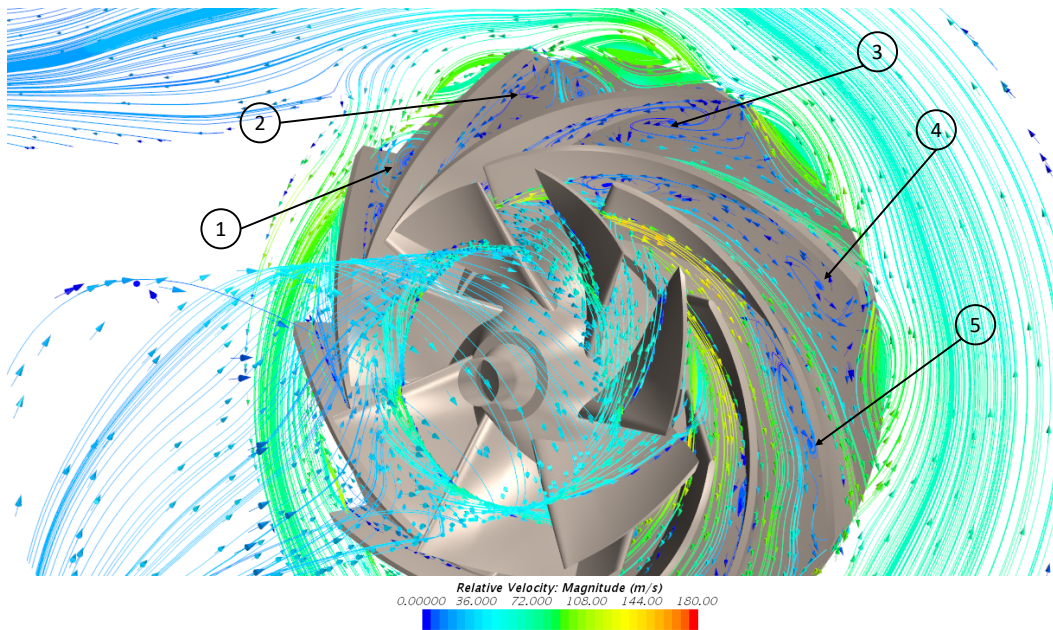


FIGURE 4.36 – 3D visualization of streamlines on the equipotential surface located at 0.5span with $N_2 = 10,000rpm$ and $\dot{m}_{cr} = 0.233kg/s$ (NIP). The vortices are numbered from (1) to (5) in the opposite direction to the second rotor rotation

and (2) are completely blocked the passages, however, the vortex (3) in the adjacent passage is blocked by about 80% and is gradually increased in the inverse direction of the rotor rotation. This can be interpreted by the development of the stall cell inside the blade passage as mentioned in [51, 52, 53].

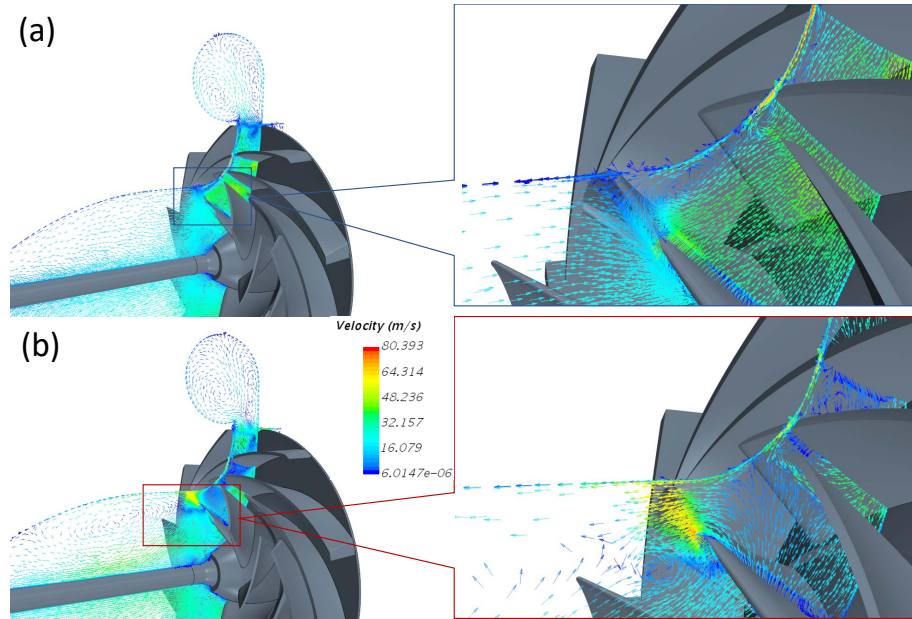


FIGURE 4.37 – Meridian velocity distribution for (a) **BEP** with $N_2 = 10,000rpm$ and $\dot{m}_{cr} = 0.543kg/s$ and (b) **NIP** with $N_2 = 10,000rpm$ and $\dot{m}_{cr} = 0.233kg/s$

Furthermore, the inlet tip re-circulation is clearly shown on the meridian section as demonstrated in figure 4.37. For **BEP** (figure 4.37a), it happens near the shroud side but it is not large. The cause of this phenomenon is the distortion inlet because of using the bent inlet part [36] and the secondary flow due to the gap between the rotor and the casing. Another cause of this phenomenon is the incidence angle at the leading edge of the first rotor, and it depends on the certain flow conditions. This phenomenon is more clearly observed for **NIP**, as indicated in figure 4.37b. A larger re-circulation area due to the significant increase of the incidence angle and the enlargement of the downstream pressure gradient causes a strong secondary flow on the shroud side to fill up the deficit of the flow regime due to the continuity of fluid. As a result, the performance of the device decreases.

- Temperature field

Figure 4.38 shows the internal temperature distribution of **CRCC** at **BEP** and **NIP** on three equipotential surfaces. Figure 4.38a-4.38c show the temperature field is quite similar inside the rotors as well as in the volute for all studied surfaces at **BEP**. Nevertheless, this uniformity is broken at **NIP**, as presented in figure 4.38d-figure 4.38f. It is obvious that for this point the temperature of the compressor increases significantly and occurs unevenly distribution. The temperature increases near the tongue region of the volute - in some blade passages and some trailing edge of the second rotor. This can be easily explained by the secondary flow caused by the downstream pressure gradient, which occurs due to the continuity of the fluid to compensate for the deficit of flow. The combination of secondary flow and fluid flow creates a vortex region. As a result, an increase in turbulence inside the compressor leads to an increase in temperature and a decrease in polytropic efficiency.

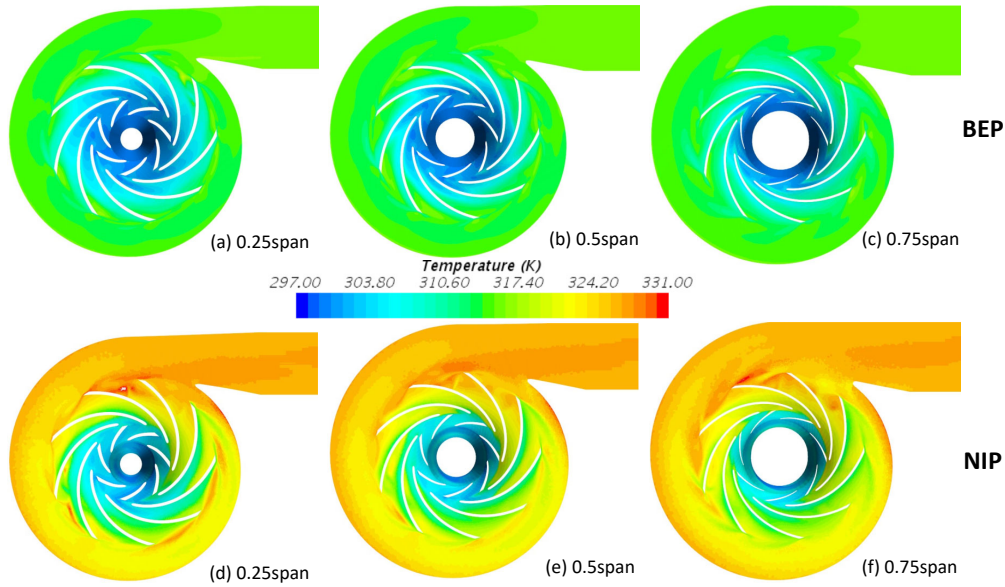


FIGURE 4.38 – Temperature distribution of CRCC at two operating points: BEP and NIP on three equipotential surfaces located at 0.25, 0.5 and 0.75span

Unsteady simulation analysis

The difference in the number of blades as well as the change of rotation speed of each rotor leads to a variation in blade pitch between adjacent blade rows. Therefore, the flow conditions at any given instant in adjacent blade rows are also changed. To understand the unsteady flow phenomenon in the compressor stage, a time-accurate CFD simulation is carried out. The temporal evolution of pressure field, temperature, and velocity inside the compressor are also observed in this simulation. The time-step of $2.143e - 5s$ is selected for each operating condition causing a rotor rotation of 1.29° per time-step. Each blade passage is captured 40 times. So, with a rotation at $10,000rpm$ and seven-blade passages, it needs 280 captures. Figure 4.39 depicts the velocity of fluid flow according to the relative position of the blade row according to time the section located in 0.5span. The velocity field shows the direction of the fluid flow in relative coordinates while the color scale represents the magnitude of velocity. Each field shows the relative position of the blade row with a time period of $4.29e - 5s$. It can be seen that the low-speed region appears at the trailing edge of the first rotor and the leading edge of the second rotor indicates a stagnation area. The size of this area depends on the relative position of the blade row. It is minimized when the two blades are aligned.

The relative positions of two rotors over time are shown in figure 4.40 at NIP. Each image of the figure 4.40 presents a constant time period of 10-time-steps. It is easy to see that the fluid flow inside the blade passages of the first rotor is homogeneous, however, there are many vortices in blade passages of the second rotor. For ease of analysis, these blade passages are numbered from one to nine. Note that the large vortices (from (1) to (4)) occupy most of the blade passage area and gradually decrease its size in the next blade passage. When the relative position changes, the size of these vortices is also changed. The vortices (1), (2) and (3) gradually decrease in size when moving away from the volute tongue region while the remaining vortex areas increase in size as they move close to the volute tongue. This suggests that the vortex is formed mainly near the tongue region of the volute as explained in section 4.5.4, and the vortex is developed

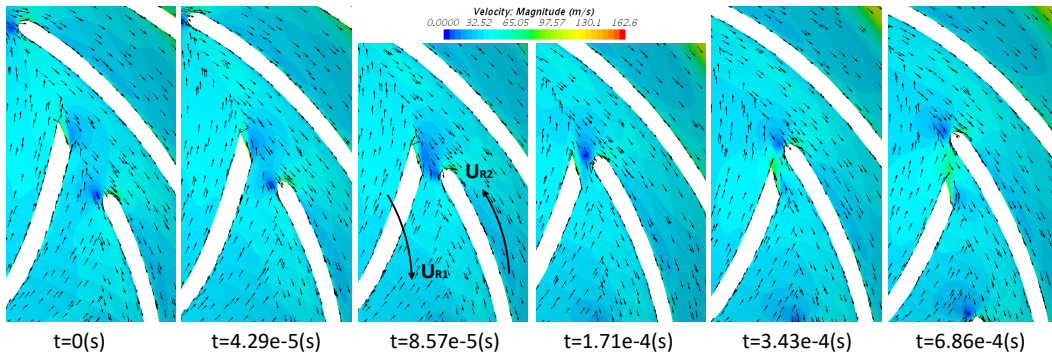


FIGURE 4.39 – Sequential flow-visualization of the flow velocity for BEP with $N_1 = -10,000rpm$, $N_2 = 10,000rpm$ and $\dot{m}_{cr} = 0.543kg/s$

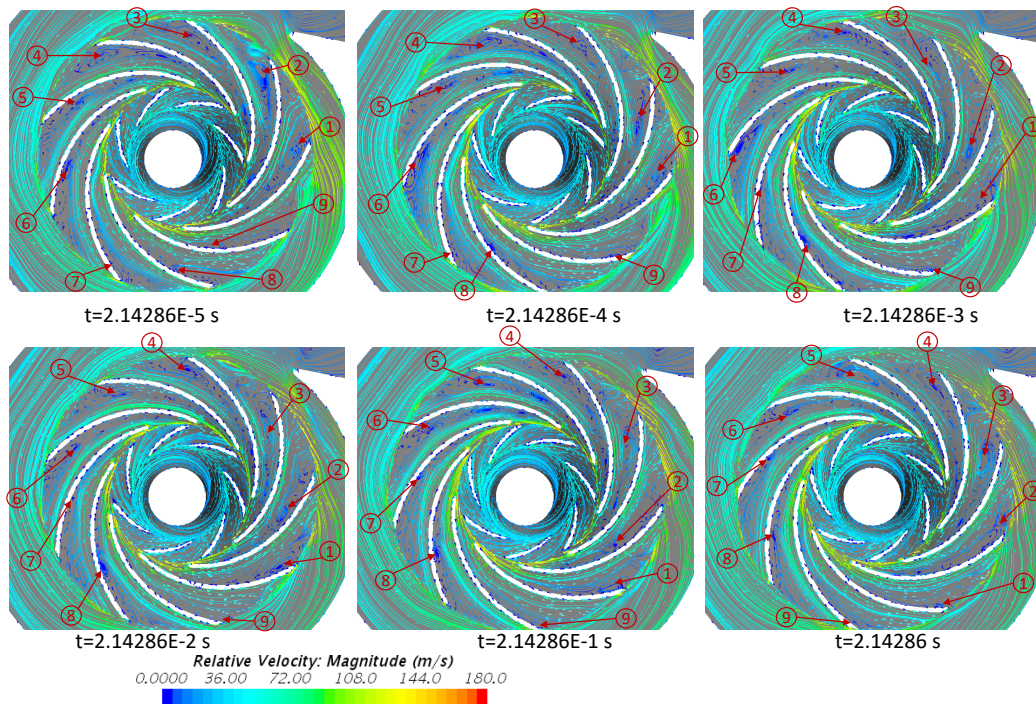


FIGURE 4.40 – Sequential streamline flow-visualization for NIP with $N_1 = -10,000rpm$, $N_2 = 10,000rpm$ and $\dot{m}_{cr} = 0.233kg/s$

in the blade passage in the opposite direction to the rotation of the rotor. If continued to reduce the flow, these vortex areas gradually develop in the blade passage and block the flow in it. In addition, they broaden in the entire rotor causing the rotating stall and surge phenomenon.

The pressure signal is taken from the pressure probe located between the trailing edge of the first rotor and the leading edge of the second rotor as shown in figure 4.28. The Fast Fourier Transform (FFT) is applied to pressure signals to observe blade passing and blade interactions. The pressure signal and FFT transform of CFD simulation in one rotation (360°) are shown in figure 4.41. It can be clearly seen that there are seven pressure positions drop on the pressure signal due to the passing of seven trailing edges of the first rotor. The first strong peak frequency shows exactly the frequency value of $f_b = \frac{(N_2 Z_2)}{60} = 1500Hz$, which is generated by the periodicity of subsequent passing of the leading edge of the second rotor. Besides that the frequency value $f_a = \frac{(N_1 Z_1)}{60} = 1166.67Hz$ is observed. It is also clearly shown the blade

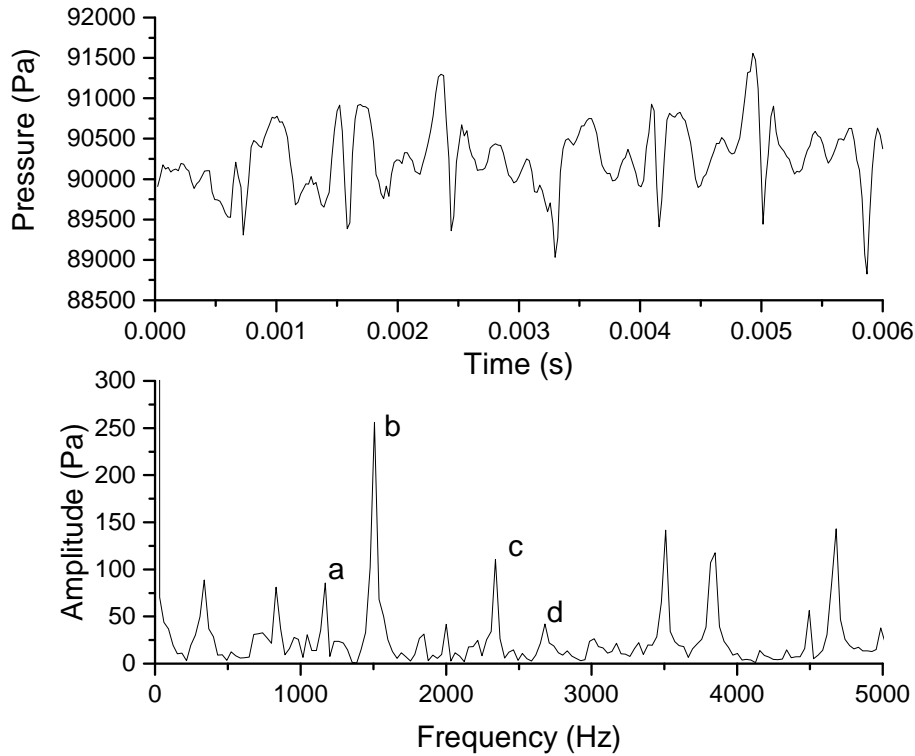


FIGURE 4.41 – Wall pressure fluctuation and FFT transform of CFD simulation with $N_1 = -10,000rpm$, $N_2 = 10,000rpm$, and $\dot{m}_{cr} = 0.543kg/s$

passing frequency of the first rotor trailing edge and its second following harmonic frequency $f_c = 2f_a$. It can be noted that the peak frequency f_d is also monitored, it is an accumulated frequency of both rotors frequencies $f_d = \frac{(N_1 Z_1 + N_2 Z_2)}{60} = 2666.67Hz$.

4.5.5 Conclusions

Numerical simulation studies are conducted to further investigate the fluid flow characteristics inside the CRCC. A comparison with experimental results shows that the numerical model is quite close to the experimental measurement, especially at a low flow rate. The smallest deviation value of pressure ratio is about 0.7% at a low flow rate and gradually increases to about 4% at high flow value. Besides, the polytropic performance is quite close to the experimental results at a low flow rate. The smallest deviation at the maximum efficiency point is about 0.15%. Two special points, BEP, and NIP, are observed in steady and unsteady simulations to study the characteristics of the internal fluid flow with $N_1 = -10,000rpm$ and $N_2 = 10,000rpm$. The distribution of pressure, velocity, and temperature are quite uniform in the rotor as well as in the volute at BEP. The fluid flow inside the rotor does not show eddy zones so the fluid flow is quite compatible with the rotor during operation. However, some blade passages present a large vortex that represents the stall cell at NIP. These vortices block all or a part of the blade passage due to secondary back-flow generated by the downstream pressure gradient and fluid continuity to compensate for the flow deficit. Although stall cells appear inside the second rotor, it only occurs in a few blade passages and it is not spread in the entire rotor so that the compressor remains stable. If the flow rate continues to decrease, these stall cells continue to grow and spread

in the entire rotor causing the instability of the compressor. In addition, unsteady simulation is also conducted to study the relative position between blade rows of the rotors and the changes of stall cells inside blade passages. The results indicate that stall cells appear near the volute tongue and grow gradually in the blade passages in the inverse direction of the rotation. When blade passage passes through the volute tongue region, its stall cells gradually decrease in size and disappear. The fluid flow normally circulates. Furthermore, wall pressure fluctuations are also observed in this simulation. The FFT analysis results show that the frequency of blade passing and its harmonic frequencies can be observed.

Chapter 5

Instability control and Extension of the operating range

Contents

5.1	Introduction	101
5.2	Stability and instability control method	104
5.3	Extension of the operating range	113
5.4	CFD analysis in Co-rotating mode	116
5.5	Conclusions	119

5.1 Introduction

Each compressor has an operating point corresponding to the minimum value of a flow rate that the compressor can still work stably. If this value is exceeded, the compressor falls into instability state. This limit is determined when the pressure generated by the compressor cannot overcome the downstream pressure so that a back and forth flow motion occurs until the downstream pressure is equalized with the fluid flow leaving the rotor. The boundary layer then reforms. The pressure builds up until it rises high to cause a breakdown of the boundary layer. The rapid breakdown and the subsequent reforming boundary layer generate a violent pressure pulsation [54]. The instability state of a compressor system known as surge phenomenon and rotating stall is the natural limit of the performance of all compressors. There are two different types of dynamic behavior related to the instability of the compressor system. The first, known as surge, is an overall oscillation of the annulus-averaged flow in the compressor. Basically, surge can be considered as one-dimensional system instability. It is not only dependent on the local fluid dynamics of the compressor but also on the properties of the system (Inlet and outlet plenum, volumes and throttle resistance valve...). Surge typically progresses into a large-amplitude limit-cycle oscillation, with the reversal of flow during some parts of the cycle. Frequency and amplitude are the two basic characteristics of the surge. The surge frequency and amplitude are determined by the size and volume of the installation components before and after the compressor as well as the flow characteristics and compressor rotation speed. Jadger et al.[55] classify surge into four main types based on the amplitude and the frequency, correspond to the oscillation: mild surge, classic surge, deep surge, and modified surge. Figure 5.1 illustrates the difference between mild and deep surge [56]. Obviously, the mild surge is no flow

reversal and its frequency is often close to the natural frequency of the compression system [57]. The deep surge is the most severe form of the surge. It is associated with low frequency, large amplitude oscillations, and negative flow rate during a part of the surge limit cycle [52]. The second type is the rotating stall. It is identified by a distortion of the circumferential flow pattern. One or more regions of stagnant flow, so-called stall cells, travel around the circumference of the compressor at $10\div 90\%$ of the shaft speed. The stall cells reduce or completely block the flow. It results in large vibratory stresses and thermal loads on the compressor blades [52]. In the linear stage of instability, surge can be regarded as the zeroth-order instability mode. The rotating stall can be considered as the higher-order modes. In many compressors, rotating stall precedes surge [58]. Prolonged operation in instability state may cause damage to the mechanical parts of the compressor. Therefore, to avoid the above endangerment, reducing the instability region to expand the working range of the compressor is extremely urgent. As mentioned above, the working limit of the compressor stability is the set of points where the compressor can work stably at the minimum flow rate and different speeds, called the stability limit line. Reducing instability region means that the working range is extended towards the smaller flow rate, as shown in figure 5.2. However, working in this region may costs efficiency.

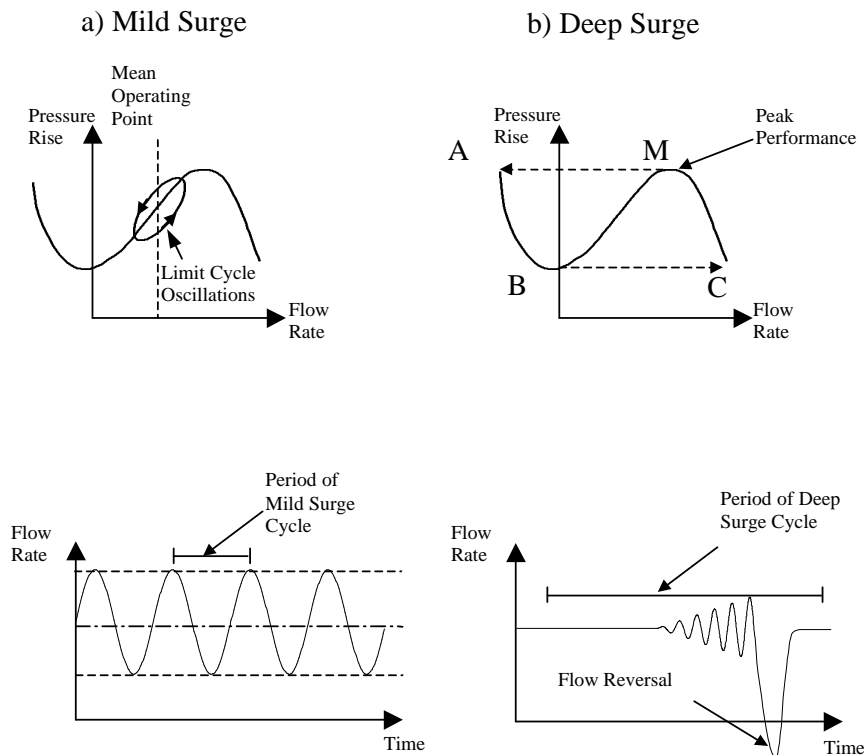


FIGURE 5.1 – Schematic diagrams of (a) mild surge and (b) deep surge [6]

Numerous studies are conducted to enhance the instability region of the compressor, especially surge phenomenon, to enlarge the operating range of the compressor at a higher pressure ratio. These studies focus on solutions to avoid unstable operating points and to enlarge the operating range of the compressor in the surge region. One of the most popular methods is used the safety margin by selecting a control path away from the actual surge line of the compressor [59, 60]. The aim of this method is to increase the flow rate, to reduce the downstream pressure or to change the rotor speed

to prevent the development of rotating stall. In addition, some techniques are used to suppress surge such as using a variable inlet guide valve to enable adjustment of the relevant flow angles [53, 61] or using a variable vaned diffuser to improve efficiency, the choke margin and the operating range [62]. Moreover, the casing treatment methods including grooves, slots, or even holes cut in the compressor casing are effective, too. Koyyalamudi et al. [63] present a casing treatment applied to a high speed, 4:1 pressure ratio centrifugal compressor. This method improves stall margin up to 18% and choke mass flow by 9.5%, while the peak of efficiency drops by 0.8÷1%. Furthermore, some studies propose replacing grooves and slots of casing treatment by holes. The advantage of this method is that these holes can be closed and opened to make variable geometry. Eynon et al. [64] propose an inducer bleed slot, which is described as a Map Width Enhancement (MWE). The subsequent study shows that the MWE pipe length is optimized to get a 15% improvement of the surge margin [65]. More recently, an active surge controller uses a plenum bleed valve and a hybrid one-way control strategy to minimize bleed losses is introduced by Willem et al. [66]. Other techniques using air injection with valves to damp out perturbations of the compressor can improve about 4% in the stall margin. In addition, to remove emerging stall cells, the air is injected directly in their vicinity. The stall margin can be improved by 6% [67].

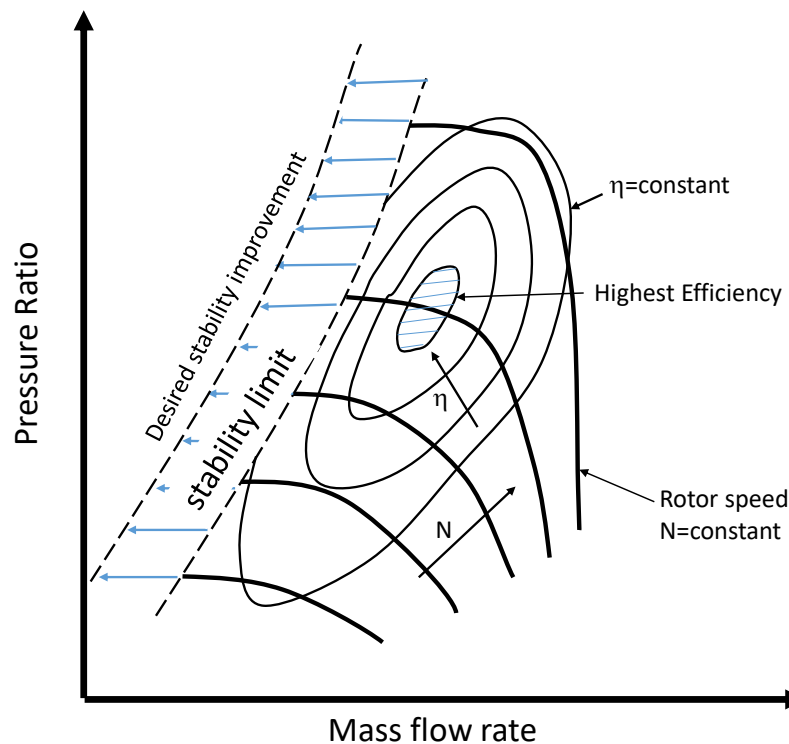


FIGURE 5.2 – Compressor map with desired instability improvement

In this study, a solution to enlarge the operating range of the centrifugal compressor towards the instability region is proposed by controlling the speed of two rotors of CRCC. The general principle of this method is to reduce the speed of the first rotor to diminish the incidence angle between the fluid flow and the blade angle. The incidence angle increases with the flow rate decrease. If this angle is large enough, there is a separation of flow in the blade passages. The stall cell is then formed, and it can grow up to a fully developed cell covering half the flow annulus or more under suitable conditions [51]. Reducing the speed of the first rotor not only reduces its inlet

incidence angle but also diminishes the inlet incidence of the second rotor to suspend the instability phenomenon. The speed ratio of $\theta_7 = -1.3$ is chosen to control the instability phenomenon. This characteristic curve gives the highest pressure ratio and the instability phenomenon appears earlier than the other studied speed ratio during the operation. In addition, the second rotor speed is kept constant to maintain the incidence angle at the inlet and is easily compared to **SRCC** at the same speed. To suspend the instability phenomenon, the speed of the first rotor is adjusted to reduce. The instability phenomenon generates pressure fluctuations in the system so it can be detected by two dynamic pressure sensors located at the inlet (p_1) and between rotors (p_{23}). The rotation speed of the second rotor is fixed at $N_2 = 9,000rpm$ in this case. The other speeds of $N_2 = 10,000 rpm$ and $N_2 = 11,000rpm$ are presented in Appendix A.3.

5.2 Stability and instability control method

Figure 5.3 shows the characteristic curves of **CRCC** for $N_2 = 9,000rpm$ with a speed ratio of $\theta_7 = -1.3$. In this figure, the blue points indicate that the compressor works stably, while the red points represent instability state. The maximum pressure ratio can reach 1.167, which corresponds to the lowest flow rate of $0.271kg/s$ (point **P8**). This point is considered as a stability limit point of **CRCC** with $\theta_7 = -1.3$. It is clearly shown in figure 5.7a that the pressure signals is stable. Its FFT transform at the inlet (figure 5.7b) and the between two rotors (figure 5.7c) show that there is no instability frequency detected. When the mass flow rate is reduced by the control valve, the compressor falls into an instability state (point **P9**). The pressure in the system fluctuates, as shown in figure 5.8a. These fluctuations are detected by two instant pressure sensors. Return on the figure 5.3, it can be seen that the flow rate seems to be greater than the flow rate of the stable working point **P8**. However, the pressure ratio falls down sharply. This may explain by introducing hysteresis into the system in rotating stall mode, which means that the flow rate has to be increased to bring the system out of its unstable working mode [52]. Looking at the FFT transforms of the inlet pressure signal (p_1) in figure 5.8b, the first and strong peak shows a frequency of $f_a = 2Hz$, which is the frequency of the instability phenomenon of the system¹. Following frequencies $f_b = 2f_a, f_c = 3f_a, f_d = 4f_a$ are respectively the second, third and fourth-order harmonic frequencies of the main frequency f_a . Likewise, the FFT transform of the pressure signal between the two rotors (p_{23}) gives also the peak frequency of $f_a = 2Hz$, as shown in figure 5.8c. The second harmonic $f_b = 2f_a$ and third harmonic $f_c = 3f_a$ frequencies are also obtained.

It is obvious that the frequency of this signal is equal to the frequency obtained from the inlet pressure signal. Therefore, the pressure fluctuation occurs in the whole system and according to the classification of Jager [55], the compressor falls into a mild surge state. Nonetheless, comparing the amplitude of the pressure fluctuations of two pressure signals show that the pressure signal between the two rotors gives a bigger amplitude than the other one. It could be explained that this sensor is located at the interface of the two rotors and is close to the source of the surge phenomenon. The signal obtains by this sensor is stronger and clearer. In order to bring the compressor to a stable state, the speed of the first rotor is controlled to reduce. The points **P10** and

1. The measurement of the **SRCC** configuration showed that the frequency of instability phenomenon was also fixed at 2Hz.

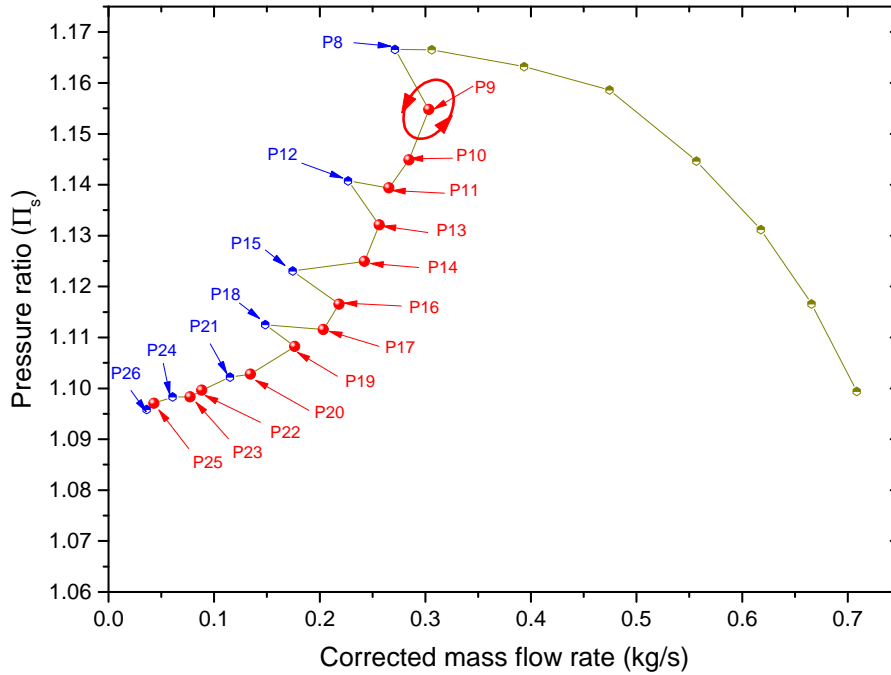


FIGURE 5.3 – Controlling the stability limit points to enlarge the operating range of CRCC with $N_2 = 9,000rpm$ by reducing the first rotor speed (N_1)

P11 correspond to the two points where the first rotor speed is respectively reduced to $-10,500rpm$ and $-9,540rpm$. Looking at the pressure signal and its FFT transform, it can be seen that the pressure fluctuations still occur in the system but the amplitude of oscillation is greatly reduced, as shown in figure 5.9a - figure 5.10c. At point **P9**, the amplitude of the oscillation achieves about $1300Pa$ with four harmonic frequencies of the inlet signal (p_1) (figure 5.8b). It is decreased to $700Pa$ and there is no more harmonic signal at point **P11** (figure 5.10b). The same phenomenon can be seen in pressure signal p_{23} : the amplitude value is reduced from $1800Pa$ to $1200Pa$. Figure 5.11a shows the pressure signal with the first rotor rotation speed of $-8880rpm$ (point **P12**). Obviously, the pressure signal is no longer fluctuating and its FFT transforms show that the compressor returns to a stable state, as shown in figure 5.11b and 5.11c. This point is close to the limit point of the counter-rotating mode with $\theta_4 = -1$ at the flow value of $0.227kg/s$. It means that the surge line can be pushed back toward the lower flow rate by reducing the first rotor speed, while the rotation speed of the second rotor is fixed.

If the mass flow rate decreases continuously, the stability phenomenon is suspended. The compressor continues to enter the unstable state at the point **P13**, the pressure fluctuations are shown in figure 5.12a. Its FFT transforms show that the amplitude of the fluctuation is smaller than the previous point because of the lower pressure ratio. The frequency of these fluctuations are always $2Hz$, as shown in figure 5.12b and figure 5.12c. When the first rotor rotation speed drops to $-7,740rpm$ at point **P14**. The phenomenon of instability still exists in the system (figure 5.13a). Although the amplitude of oscillation is significantly decreased, as shown in figure 5.13b and figure 5.13c. To restore the compressor to the stable state at this flow rate, the first rotor speed is further reduced to $-6,240rpm$, the pressure oscillation in the system completely disappears. The pressure signals are stable, as shown in figure 5.14a. Its FFT transform does not show any frequency of instability phenomenon shown in figure 5.14b

and figure 5.14c. At this time, the compressor work at the stable point **P15**. This point is close to the limit point of the speed ratio $\theta_1 = -0.7$ ($\theta_1 = N_1/N_2 = -6,300rpm/9,000rpm$) at the mass flow rate of $0.174kg/s$. Using the same method at lower flow rates, it can get a stable working point at a flow of $0.148kg/s$ at the point **P18** corresponding to $N_1 = -3,900rpm$ (figure 5.17a-figure 5.17c). However, further reducing the flow rate, although the speed of the first rotor is reduced to zero (stationary), the compressor still operates in an unstable state at the point **P20** (figure 5.19a-figure 5.19c). It means that the incidence angle is still higher than the allowed value. In order to further reduce it, the first rotor needs to reverse the rotation. That means it needs to rotate in the same direction as the second rotor. In other words, the compressor operates in co-rotating mode².

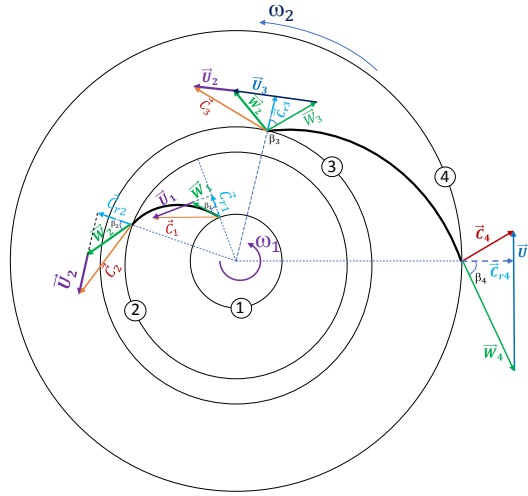


FIGURE 5.4 – The velocity triangles of a Co-rotating mode

Figure 5.4 shows the velocity triangle in the case of the compressor operates in co-rotating mode. From that, the Euler work is calculated as follows:

$$\Delta h_{total} = U_4 C_{u4} - U_3 C_{u3} + U_2 C_{u2} - U_1 C_{u1} \quad (5.1)$$

Because the change in diameter of the first rotor is small, the Euler work of the first rotor is also small. On the other hand, because of rotating in the same direction with the second rotor, the relative velocity component W_3 at the inlet of the second rotor is also smaller than the counter-rotating mode. In addition, the Euler work of the second rotor is small because the peripheral velocity component C_{u3} is positive as shown in equation (5.1). This explains why the pressure ratio in co-rotating mode is lower than in other modes, but it can improve the ability of the compressor to work in low flow rates. It is obvious that when the speed of the first rotor changes, the change of the velocity components U_2 , W_2 , C_2 leads to a modification of W_3 . So, the incidence angle is determined by the difference between β_3 and β_{3b} at the inlet of the second rotor is changed. The compatibility of the fluid flow with the rotor blade angle at the inlet causes the reduction or suppression of the instability of the compressor.

Returning to the figure 5.3, the compressor works in co-rotating mode at the point **P21** (figure 5.20a). It indicates that the compressor achieves a stable state. At this

2. In co-rotating mode, two rotors rotate in the same direction.

point, the rotation speed of the first rotor is $1200rpm$ while the rotation speed of the second rotor remains at $9,000rpm$. It is clear that the pressure ratio of the compressor is smaller than case 2 due to the co-rotating effect as explained above. Continuing to reduce the flow rate, the compressor enters in an unstable working state at point **P22**, which can be seen by the pressure fluctuation in figure 5.21a. Increasing the speed of the first rotor until the compressor achieves a stable state at the point **P24** (figure 5.23a), where the first rotor speed is $4,140rpm$ and the flow of the compressor is $0.06kg/s$. When the mass flow rate reduces to $0.036kg/s$, the compressor achieves a steady state when the first rotor reaches a speed of $5,400rpm$ at the point **P26**, as shown in figure 5.25a. This is the stability limit point of **CRCC** configuration at this speed. The variable speed of the first rotor in this section is shown in figure 5.6. It is obvious that the rotation speed of the first rotor change from $-11,700rpm$ to $5,400rpm$ leads to the stability limit appears then at $0.036kg/s$ instead of $0.271kg/s$ with constant second rotor speed. That means the operating range of **CRCC** is extended. Nonetheless, the pressure ratio drops to 1.096 and is much smaller than the value of 1.167 at the point **P8**. This problem can be resolved by changing the rotation speed of the second rotor (this content is presented in section 5.3). Figure 5.5 shows the performance of **CRCC** in the working range with eliminating instability points at different rotation speed ratios. There can be no doubt that if the second rotor speed is constant, the surge margin always exists and the instability region can only be improved when the first rotor changes the speed and/or the rotation direction.

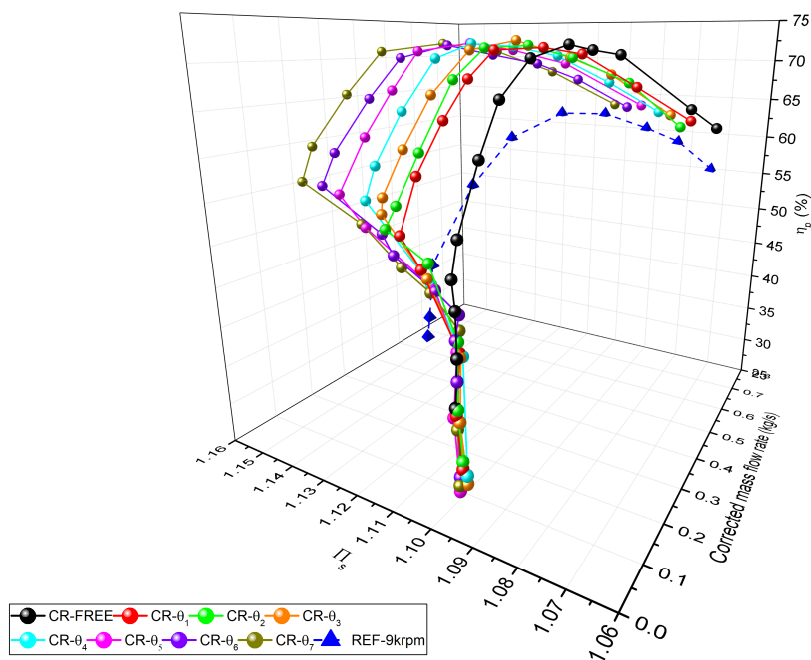


FIGURE 5.5 – Characteristic curves of **CRCC** at different speed ratios without the unstable working points by reducing the rotation speed of the first rotor while the second rotor speed is fixed $N_2 = 9,000rpm$ compared to the characteristic of **SRCC** at $9,000rpm$ (REF-9krpm)

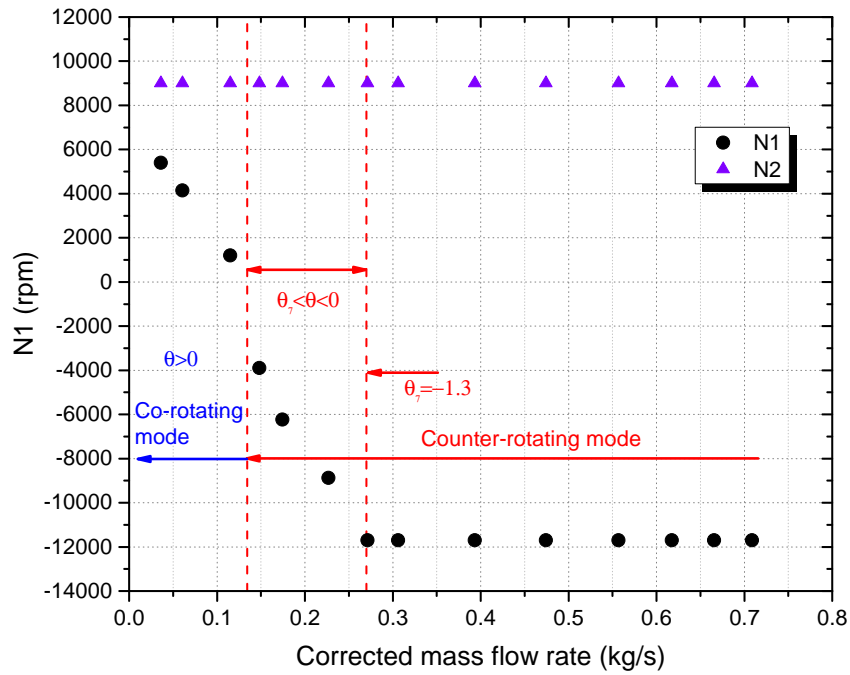


FIGURE 5.6 – The variation of first rotor speed for suppressing the instability phenomenon at $N_2 = 9,000rpm$

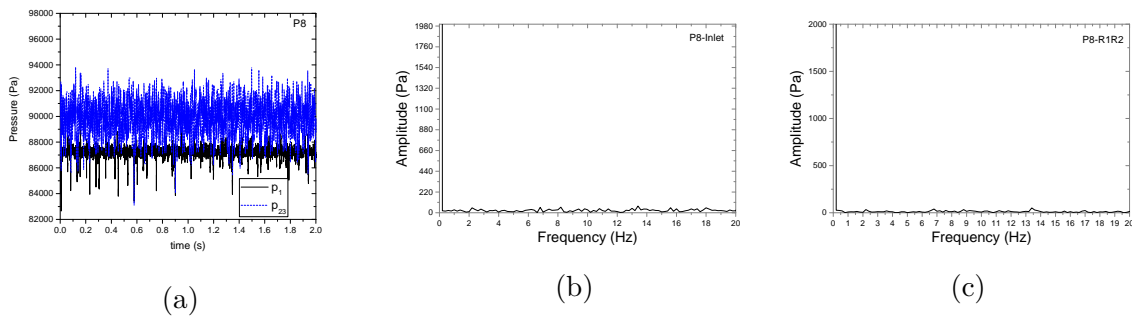


FIGURE 5.7 – The pressure signals (a) and its FFT analysis: (b) at the inlet and (c) between two rotors of the point **P8** with $N_1 = -11,700rpm$ and $N_2 = 9,000rpm$

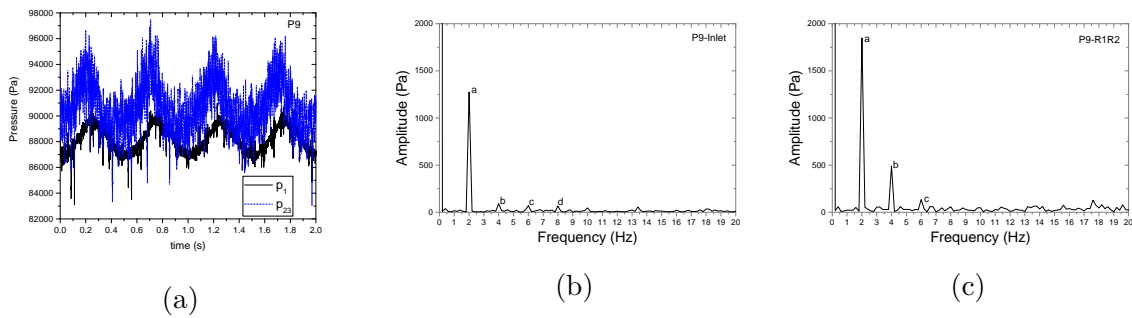


FIGURE 5.8 – The pressure signals (a) and its FFT analysis at the inlet (b) and between two rotors (c) of the point **P9** with $N_1 = -11,700$ and $N_2 = 9,000rpm$

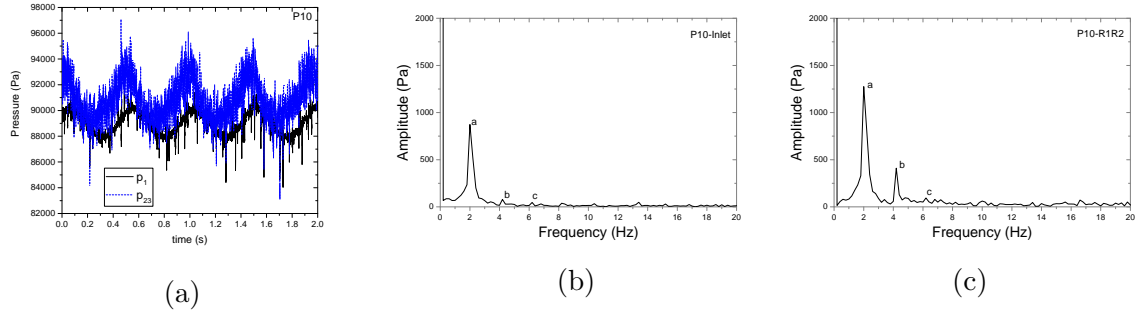


FIGURE 5.9 – The pressure signals (a) and its FFT analysis at the inlet (b) and between two rotors (c) of the point **P10** with $N_1 = -10,500rpm$ and $N_2 = 9,000rpm$

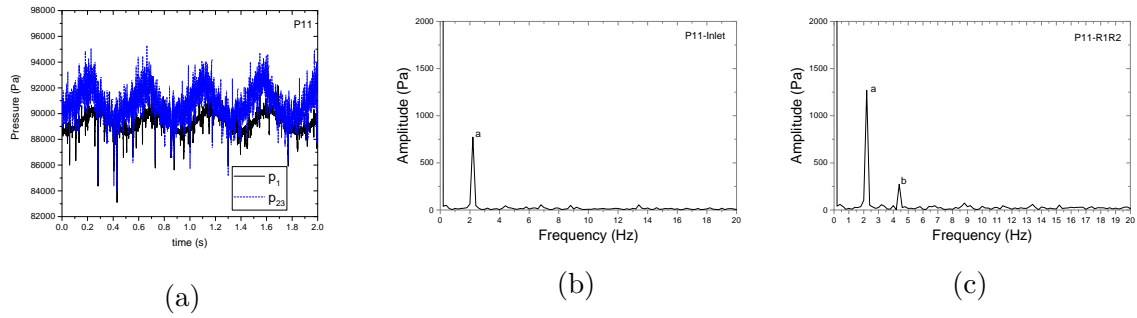


FIGURE 5.10 – The pressure signals (a) and its FFT analysis at the inlet (b) and between two rotors (c) of the point **P11** with $N_1 = -9,540rpm$ and $N_2 = 9,000rpm$

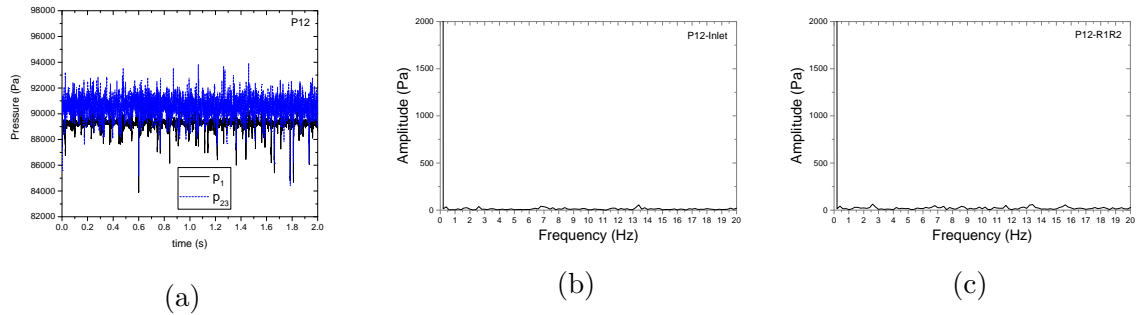


FIGURE 5.11 – The pressure signals (a) and its FFT analysis at the inlet (b) and between two rotors (c) of the point **P12** with $N_1 = -8,880rpm$ and $N_2 = 9,000rpm$

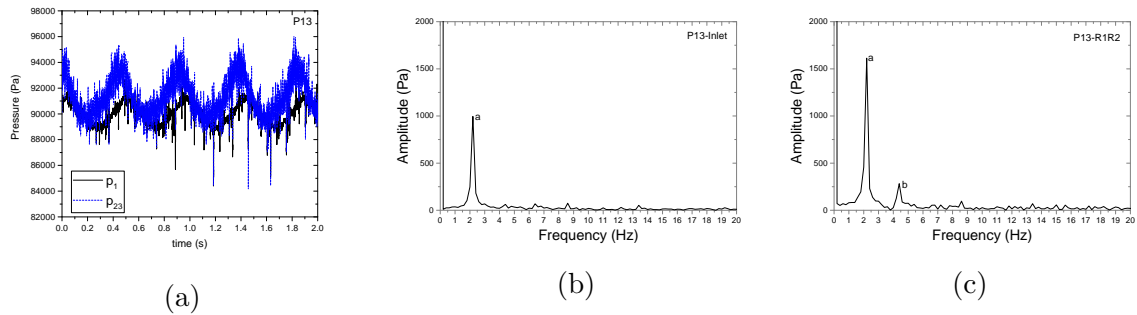


FIGURE 5.12 – The pressure signals (a) and its FFT analysis at the inlet (b) and between two rotors (c) of the point **P13** with $N_1 = -8,880rpm$ and $N_2 = 9,000rpm$

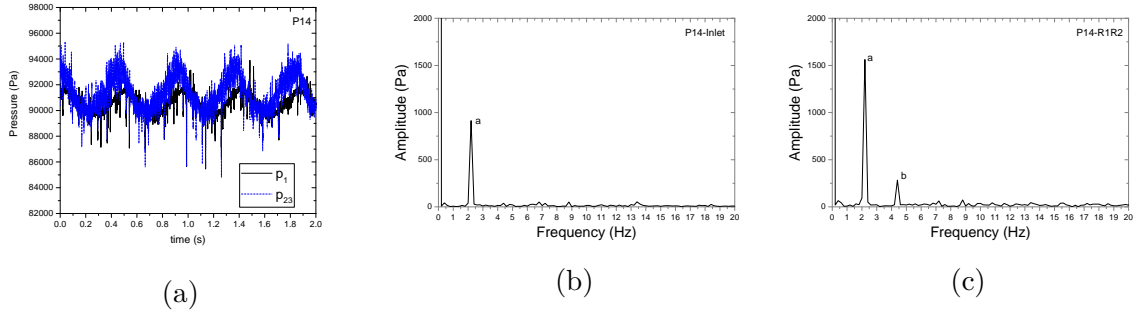


FIGURE 5.13 – The pressure signals (a) and its FFT analysis at the inlet (b) and between two rotors (c) of the point **P14** with $N_1 = -7,740rpm$ and $N_2 = 9,000rpm$

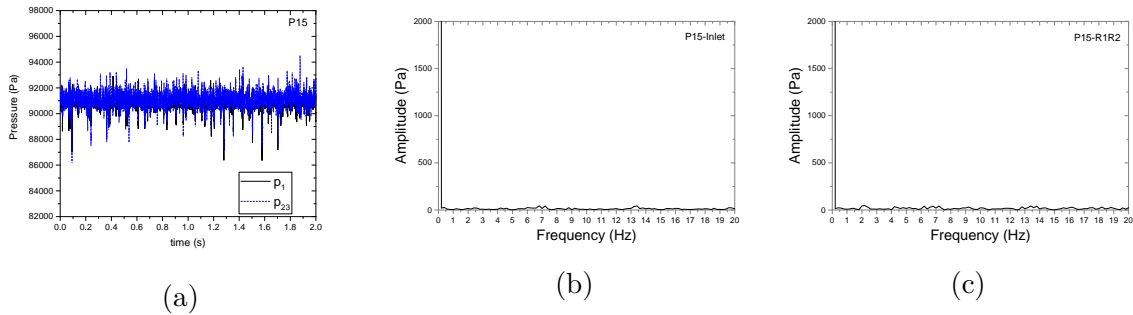


FIGURE 5.14 – The pressure signals (a) and its FFT analysis at the inlet (b) and between two rotors of the point **P15** with $N_1 = -6,240rpm$ and $N_2 = 9,000rpm$

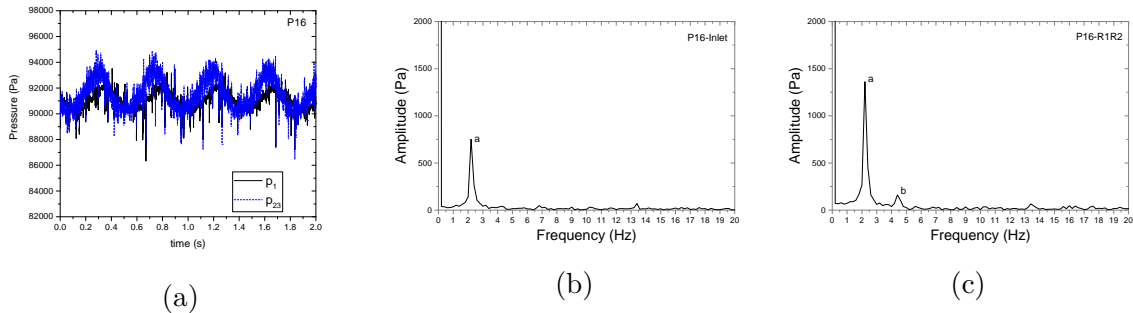


FIGURE 5.15 – The pressure signals (a) and its FFT analysis at the inlet (b) and between two rotors (c) of the point **P16** with $N_1 = -6,240rpm$ and $N_2 = 9,000rpm$

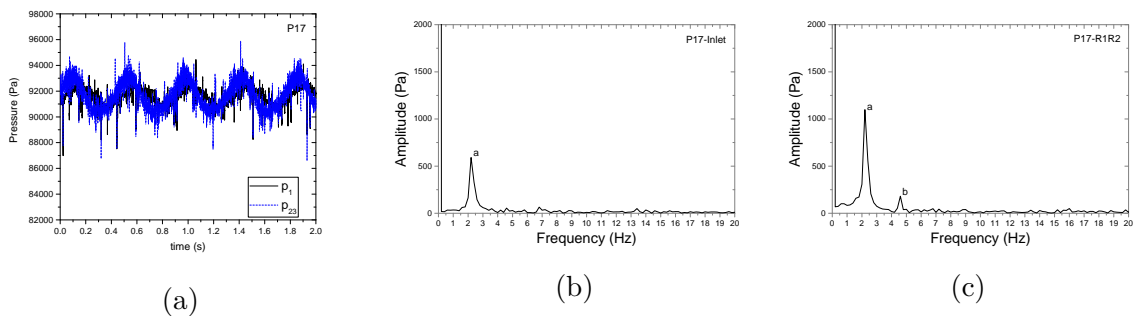


FIGURE 5.16 – The pressure signals (a) and its FFT analysis at the inlet (b) and between two rotors (c) of the point **P17** with $N_1 = -4,920rpm$ and $N_2 = 9,000rpm$

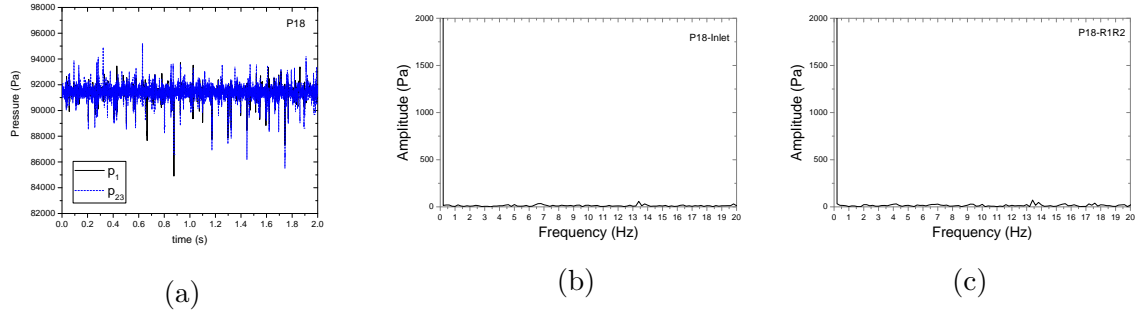


FIGURE 5.17 – The pressure signals (a) and its FFT analysis at the inlet (b) and between two rotors (c) of the point **P18** with $N_1 = -3,900rpm$ and $N_2 = 9,000rpm$

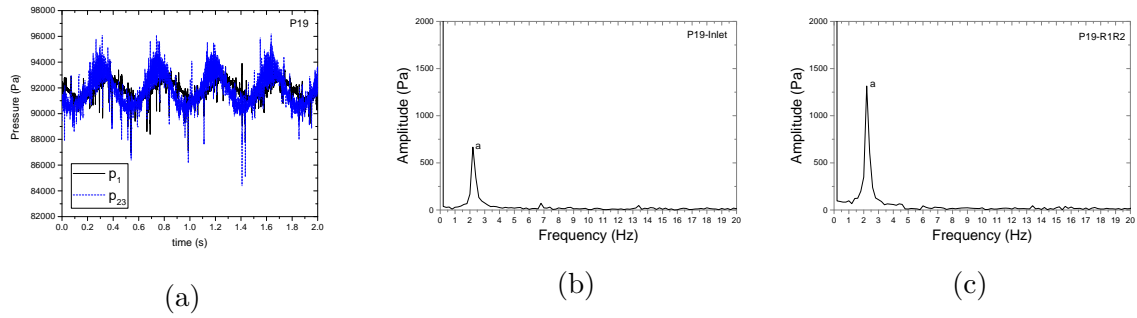


FIGURE 5.18 – The pressure signals (a) and its FFT analysis at the inlet (b) and between two rotors (c) of the point **P19** with $N_1 = -3,900rpm$ and $N_2 = 9,000rpm$

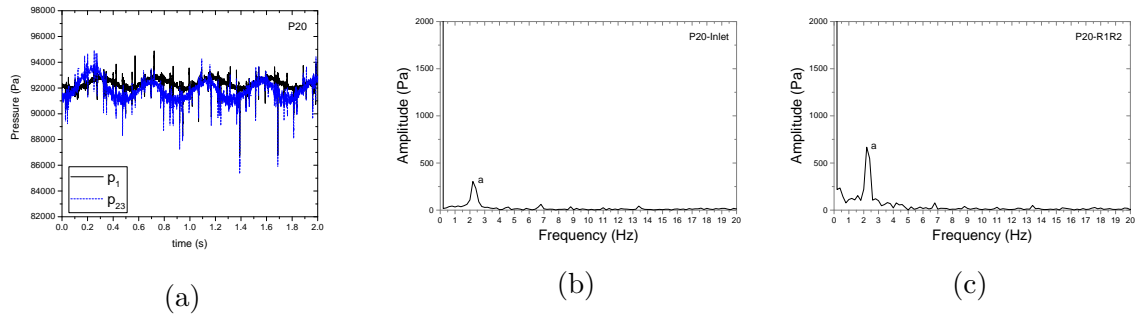


FIGURE 5.19 – The pressure signals (a) and its FFT analysis at the inlet (b) and between two rotors (c) of the point **P20** with $N_1 = 0rpm$ and $N_2 = 9,000rpm$

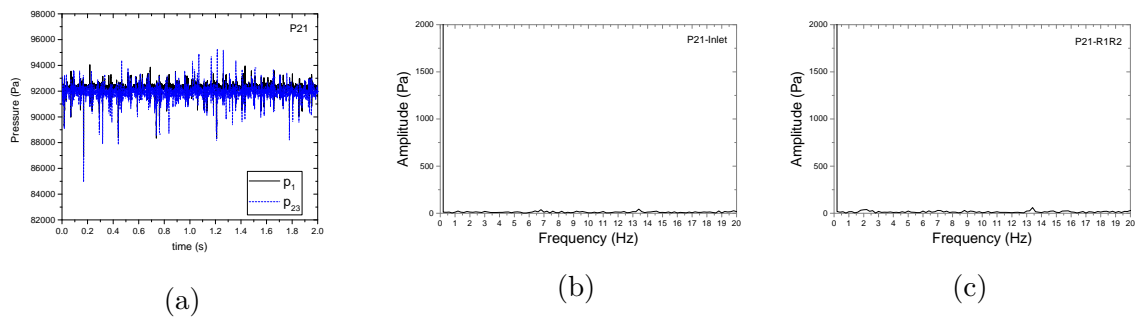


FIGURE 5.20 – The pressure signals (a) and its FFT analysis at the inlet (b) and between two rotors (c) of the point **P21** with $N_1 = 1200rpm$ and $N_2 = 9,000rpm$

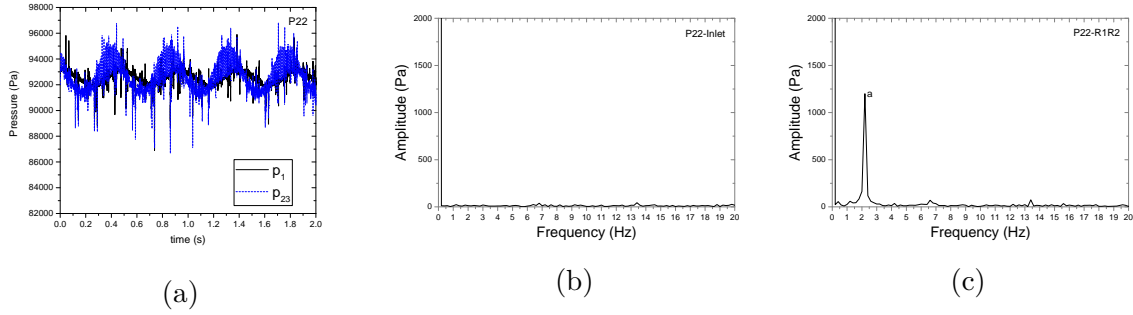


FIGURE 5.21 – The pressure signals (a) and its FFT analysis at the inlet (b) and between two rotors (c) of the point **P22** with $N_1 = 1200rpm$ and $N_2 = 9,000rpm$

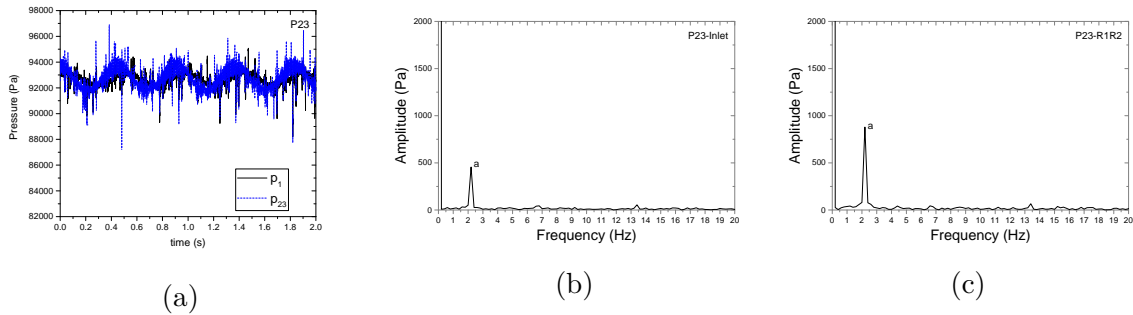


FIGURE 5.22 – The pressure signals (a) and its FFT analysis at the inlet (b) and between two rotors (c) of the point **P23** with $N_1 = 2940rpm$ and $N_2 = 9,000rpm$

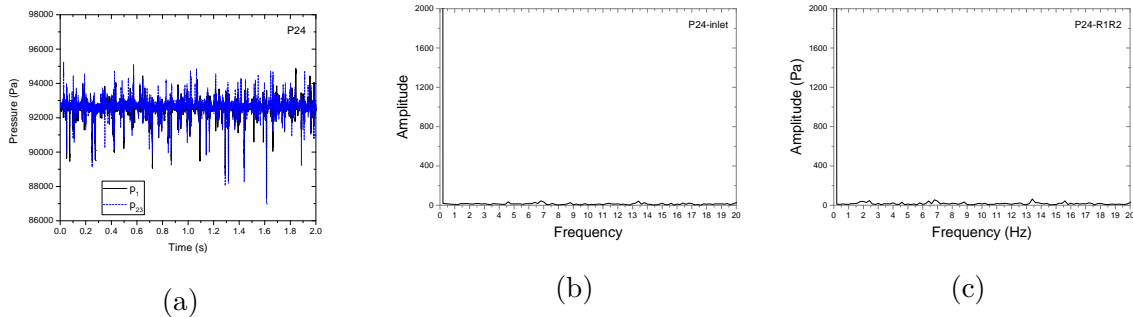


FIGURE 5.23 – The pressure signals (a) and its FFT analysis at the inlet (b) and between two rotors (c) of the point **P24** with $N_1 = 4140rpm$ and $N_2 = 9,000rpm$

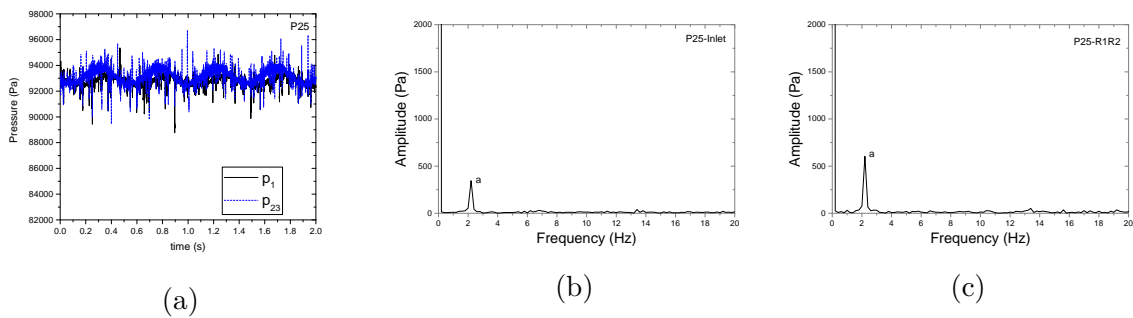


FIGURE 5.24 – The pressure signals (a) and its FFT analysis at the inlet (b) and between two rotors (c) of the point **P25** with $N_1 = 4140rpm$ and $N_2 = 9,000rpm$

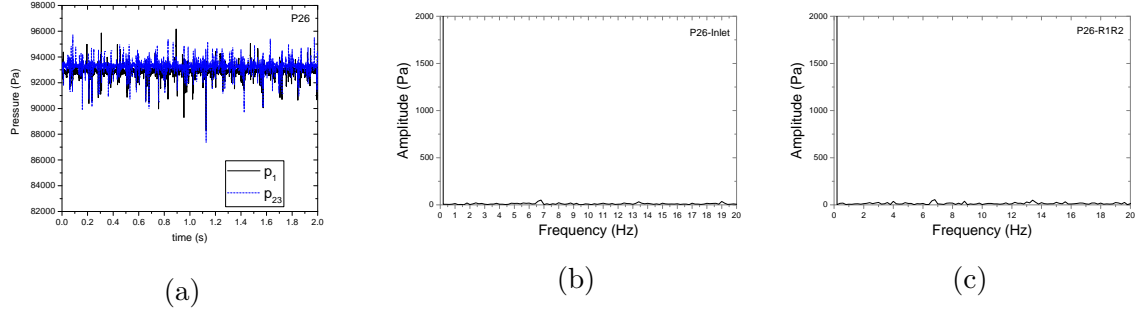


FIGURE 5.25 – The pressure signals (a) and its FFT analysis at the inlet (b) and between two rotors (c) of the point **P26** with $N_1 = 5400rpm$ and $N_2 = 9,000rpm$

5.3 Extension of the operating range

In order to assess the extension of the operating range of **CRCC** in the instability region, three experimental characteristic curves³ of **CRCC** are built and compared to those of **SRCC** at three rotation speeds $9,000rpm$, $10,000rpm$ and $11,000rpm$. The extension is more evident when the pressure ratio is maintained constant at the low flow rate region. A constant pressure ratio can be obtained in various ways, such as increasing or decreasing the rotation speed of each **CRCC** rotor independently, changing the rotation speed of both rotors simultaneously, when the mass flow rate reduces. The characteristic curve C_1 of the **CRCC** is obtained by fixing the initial rotation speed of the second rotor $N_2 = 9,000rpm$. The speed of the first rotor N_1 is then changed in counter-rotating mode to achieve a pressure ratio close to the value of **SRCC** at the same mass flow rate. So this characteristic curve is controlled close to the **SRCC**'s one at the speed of $9,000rpm$. When the pressure ratio reaches $\Pi_s = 1.112$, this value is close to the pressure ratio of **SRCC** at the limited instability point with the mass flow rate is equal to $0.146kg/s$, the compressor is controlled to produce the constant pressure ratio by simultaneously changing the speed of both rotors. At a low mass flow rate less than the limit value of **SRCC** (the instability region of **SRCC**), the co-rotating mode is active to push back the instability phenomenon. This method allows a clear observation of expanding the operation range. The curves C_2 and C_3 are respectively close to the curves of **SRCC** with rotation speed $10,000rpm$ and $11,000rpm$. They are also formed by the same method of C_1 . These performance curves are compared to **SRCC** and are shown in figure 5.26.

Look at the pressure ratio curve C_1 in figure 5.26a. The pressure ratio of **CRCC** increases rapidly when the mass flow rate decreases because of counter-rotating effect. At a flow rate of $0.413kg/s$, the pressure ratio reaches $\Pi_s = 1.112$ with a speed ratio of $\theta = \frac{-6,000rpm}{9,000rpm} = -0.667$. This pressure ratio value is then maintained when the mass flow diminishes by reducing the speed of the first rotor and fixing the speed of the second rotor. At a flow rate of $0.108kg/s$, the pressure ratio of **CRCC** is constant with the speed ratio of $\theta = \frac{-2340rpm}{9000rpm} = -0.26$. It is clear that the limited point is moved to lower mass flow rate by reducing the speed of the first rotor. Although the co-rotating mode is not active, the operating range of **CRCC** is expanded. To continue maintaining the compressor operating at a smaller flow rate, the co-rotating mode is activated. Obviously, **CRCC** can work stably at a very flow rate of $0.011kg/s$ with a speed ratio of $\theta = \frac{4500rpm}{9420rpm} = 0.48$. Similarly, for the pressure ratio curve C_2 , the minimum flow

3. These characteristic are obtained by changing the rotation speed of both rotors simultaneously.

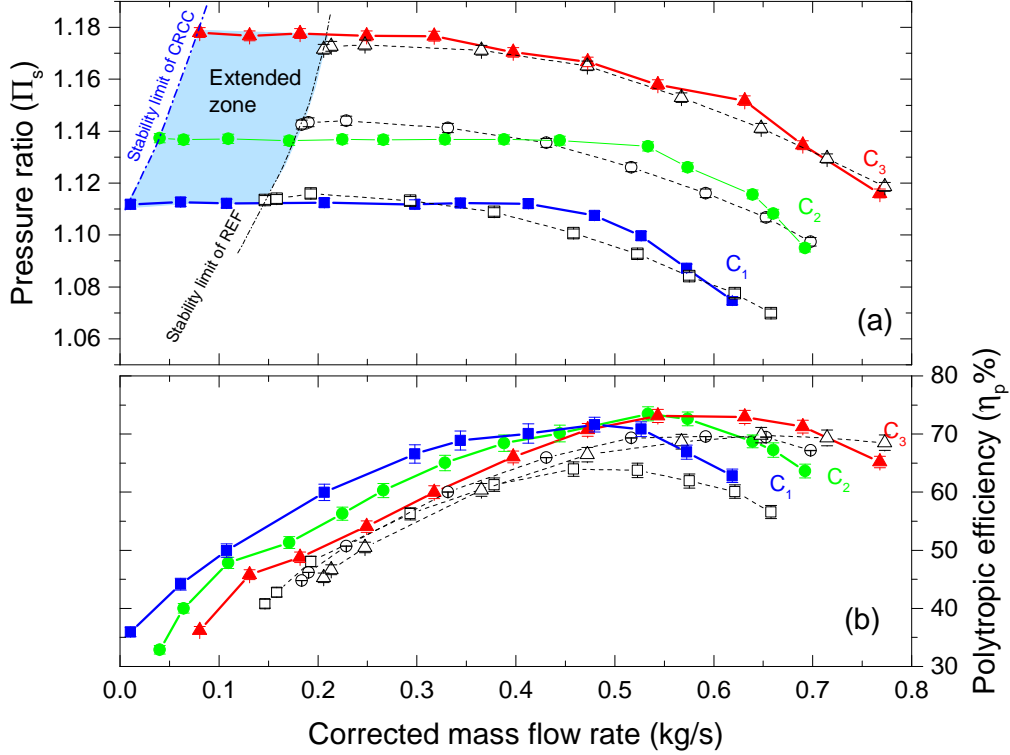


FIGURE 5.26 – Three performance curves C_1 (\blacksquare), C_2 (\bullet) and C_3 (\blacktriangle) of CRCC in comparison with those of SRCC at three rotation speeds of 9,000rpm (\square), 10,000rpm (\circ) and 11,000rpm (\triangle)

rate where the compressor still operates stably is 0.04kg/s with $\theta = \frac{6780\text{rpm}}{10560\text{rpm}} = 0.64$. The last one C_3 can achieve at mass flow rate of 0.081kg/s with $\theta = \frac{6240\text{rpm}}{12000\text{rpm}} = 0.52$. Comparing the limited mass flow rate of SRCC, it is found that CRCC operating range is extended significantly in the instability region of SRCC. Specifically, the limited point of SRCC at the speed of 9,000rpm is $\Pi_s = 1.113$ and mass flow rate of 0.146kg/s while this point of C_1 can achieve mass flow rate of 0.011kg/s with $\theta = 0.48$. That means the limited flow rate of CRCC is pushed toward the lower mass flow rate of 0.135kg/s . It can be remarked that the compressor operating range is expanded by 25% compared to the studied operating range. At the speed of 10,000rpm, the limited flow rate of SRCC and CRCC are respectively 0.184kg/s and 0.04kg/s with the $\theta = \frac{6,780\text{rpm}}{10,560\text{rpm}} = 0.64$. A decline of a mass flow rate of about 0.144kg/s , accounting for 28% of the operating range of the compressor. Finally, at the speed of 11,000rpm, SRCC can operate stably at the mass flow rate of 0.206kg/s , while CRCC can work stably at the mass flow rate of 0.081kg/s with $\theta = \frac{6,240\text{rpm}}{12,000\text{rpm}} = 0.52$. It can be mentioned that the limited flow rate of CRCC is shifted back about 0.125kg/s , which makes up 24% of the operating range. The set of limited points of CRCC generates a stability limit line. This line is moved to a lower mass flow rate and it seems to be paralleled to the limited line of SRCC.

Concerning the polytropic efficiency, figure 5.26b compares the polytropic efficiency between CRCC and SRCC at three main speed of SRCC. It is clear that the polytropic efficiency of CRCC is always higher than SRCC's one. The maximum efficiency values of SRCC at three speeds of 9,000rpm, 10,000rpm, and 11,000rpm are respectively $64\pm 2\%$, $70\pm 2\%$ and $70\pm 2\%$ while these values of the three curves C_1 , C_2 and C_3 are $72\pm 2\%$, $74\pm 2\%$, and 73.1% , respectively. It can be seen that the CRCC increases from

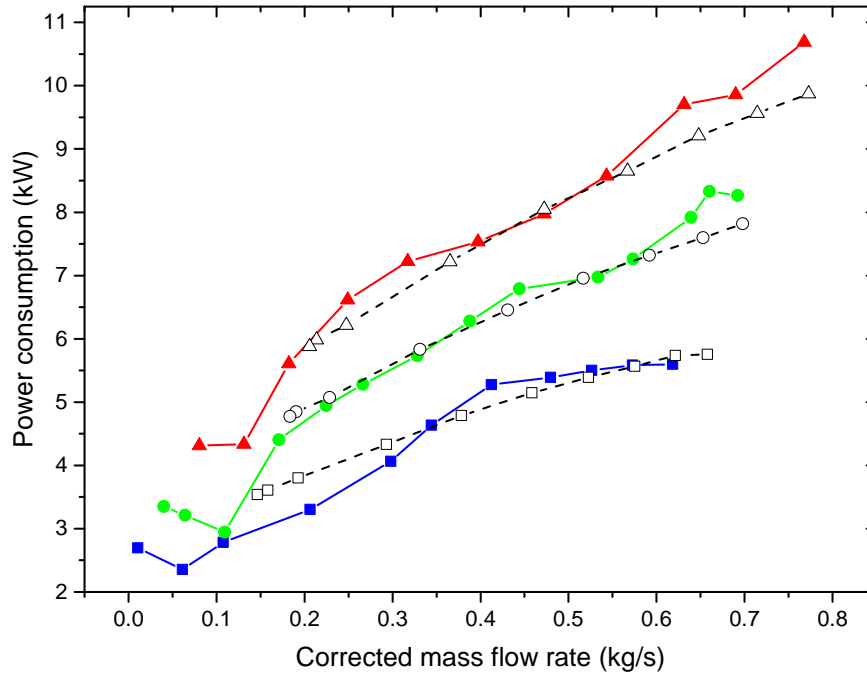


FIGURE 5.27 – Power consumptions of three characteristic curves C_1 (\blacksquare), C_2 (\bullet) and C_3 (\blacktriangle) of CRCC in comparison with those of SRCC at three rotation speeds of 9,000rpm (\square), 10,000rpm (\ominus) and 11,000rpm (\triangle)

3% to 8% efficiency and it depends on the rotor speed. In addition, the efficiency of CRCC improves about 5% (for the C_2 and C_3) and 10% (for the C_1) at the mass flow rate less than the maximum efficiency point. At the extended region, the efficiency drops rapidly due to the co-rotating effect.

Figure 5.27 depicts the comparison of power consumption between CRCC and SRCC at the three rotation speeds. It is clear that CRCC consumes slightly higher than SRCC at large flow rates. However, it spends a little smaller at the lower mass flow rate, especially in the expanded region. The power consumption of CRCC reaches a minimum value and then increases gradually. This could be explained that the first rotor rotates in the same direction as the second rotor to reduce the incidence angle of the fluid flow to maintain stability. Moreover, the speed of the second rotor increases to keep the pressure ratio value so that it needs more energy. In addition, the first rotor does not generate Euler's work, and it only directs the fluid flow into the second rotor with minimum loss to eliminate the instability phenomenon.

Figure 5.28 shows the relation between two rotors speed and pressure ratio of CRCC. It is obvious that the pressure ratio can be maintained constant if the speed of two rotors changes simultaneously in the opposite direction in counter-rotating mode or in the same direction in the co-rotating mode. Furthermore, CRCC gives better efficiency than SRCC in counter-rotating mode, but the efficiency descends rapidly in co-rotating mode. The desired operating point can be chosen in figure 5.28 according to the pressure ratio, efficiency, and mass flow rate. The coupled rotation speed of two rotors can be found easily. The extension region can be obtained when the compressor operates in co-rotating mode and the speed of the first rotor is equal to 48%-64% of second rotor speed. At this speed, the limited flow rate is shifted to an extremely low value and the working range of the compressor is significantly expanded toward the instability region.

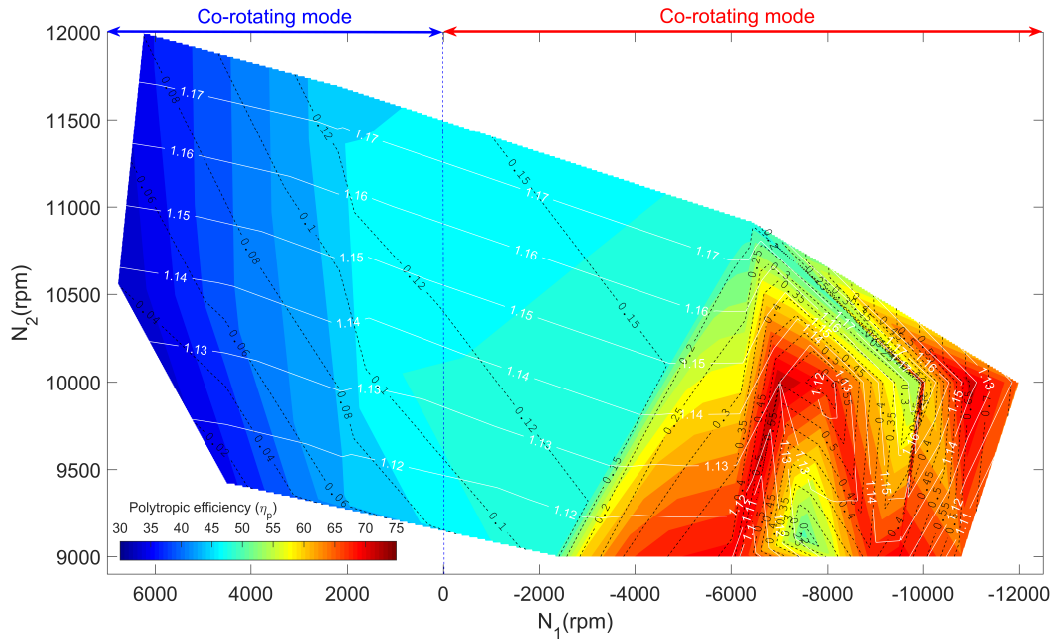


FIGURE 5.28 – The relation between coupled rotation speed of two rotors and corrected mass flow rate (black dashed line), pressure ratio (white solid line), polytropic efficiency (colored region) in case of expanding the operating range

5.4 CFD analysis in Co-rotating mode

A co-rotating mode is an effective solution to push back the instability appearance of the compressor as described in section 5.1. Changing the rotation speed of each rotor independently with the same direction improves the incidence angle at the leading edge of the rotor thereby reducing the instability phenomenon of the compressor for low mass flow. As illustrated in figure 5.26, in order to maintain the pressure ratio $\Pi_s = 1.177$ and to expand the working range toward the lowest flow rate $\dot{m}_{cr} = 0.08 \text{ kg/s}$, the speed of the first rotor can reach $N_1 = 6,240 \text{ rpm}$ and that of the second rotor $N_2 = 12,000 \text{ rpm}$. This point is called **Extended Stability Limit Point (ESLP)**. The instability region is pushed back to the lowest flow by about 0.125 kg/s . CFD simulations are conducted to better understand the pressure, temperature, and velocity fields as well as fluid flow streamlines inside the CRCC at this point. Figure 5.29 depicts the pressure field inside the compressor on three equipotential surfaces located at 0.25, 0.5, and 0.75span. It is clear that the pressure distribution inside the first rotor is quite uniform. The pressure increases gradually from the inlet to the outlet of the second rotor and goes up rapidly from the tongue of the volute to the exit cone. The high-pressure gradient has developed towards the inside of the volute and prevent the circulation of the fluid flow inside the blade passages close to the volute tongue. Consequently, four blade passages of the second rotor appear a small area of high pressure on the pressure side.

This can be explained by observing the streamline of the relative velocity of fluid flow at 0.5span, as shown in figure 5.30. It is observed that in the blade passages from (1) to (4), there are large vortices that completely block the fluid flow. In the blade passage number (5), this vortex is slightly smaller (occupying about 80 % of the area). Because the blade passages are completely blocked, at the trailing edge region of the

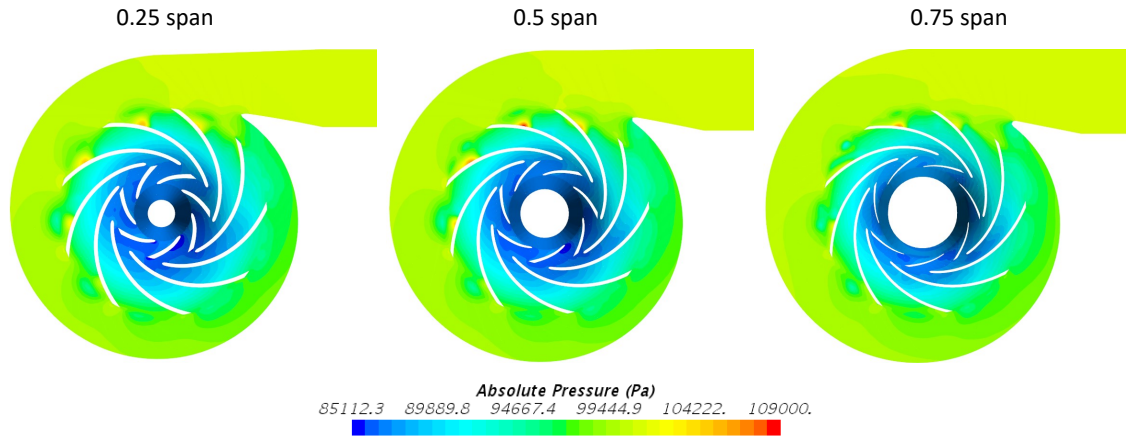


FIGURE 5.29 – Pressure distribution at ESLP with $N_1 = 6,420rpm$, $N_2 = 12,000rpm$ and $\dot{m}_{cr} = 0.08kg/s$ on three equipotential surfaces located at 0.25, 0.5 and 0.75span

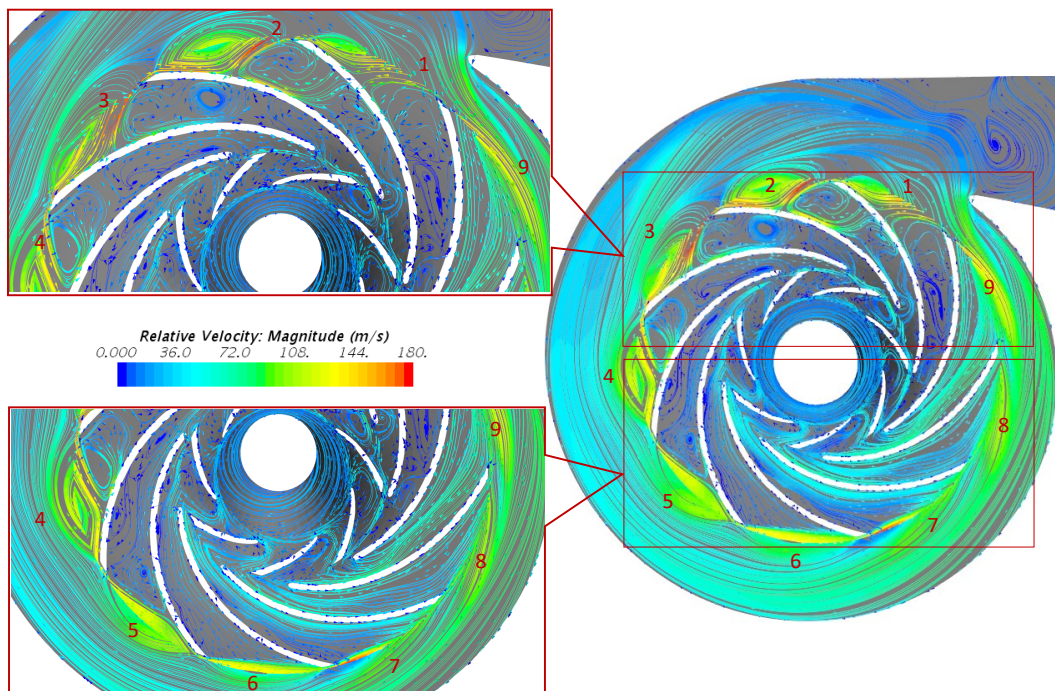


FIGURE 5.30 – Flow structure at ESLP with $N_1 = 6,420rpm$, $N_2 = 12,000rpm$ and $\dot{m}_{cr} = 0.08kg/s$

second rotor appears a local vortex perpendicular to the pressure side of the blade. Consequently, a small high-pressure area occurs on this surface. In the remaining four blade passages (numbered from 6 to 9) no vortex areas appear and the fluid flows through normally. This can be interpreted that at low flow, because of the high-pressure gradient at the exit cone, the secondary backflow is generated inside the blade passages to compensate for the lack of flow due to the continuity of the fluid. In combination with the increase of incidence angle at the leading edge, the stall cell is formed inside the blade passage. These stall cells appear in the blade passages next to the tongue of the volute and grow gradually in the adjacent one in the inverse rotational direction of the second rotor (the size of the vortex decreases from (1) to (5)). The propagation of these stall cells depends on the decrease of the flow of the compressor and appears

in most blade passages causing instability when the flow is too small. However, due to the co-rotation effect of the first rotor, the incidence angle at the leading edge of the second rotor is improved, hence reducing the vortex area in blade passages from (6) to (9). Although the stall phenomenon is still happened in some passage but does not develop in the whole rotor so that the compressor can still operate stably and does not enter in a state of rotating stall or surge.

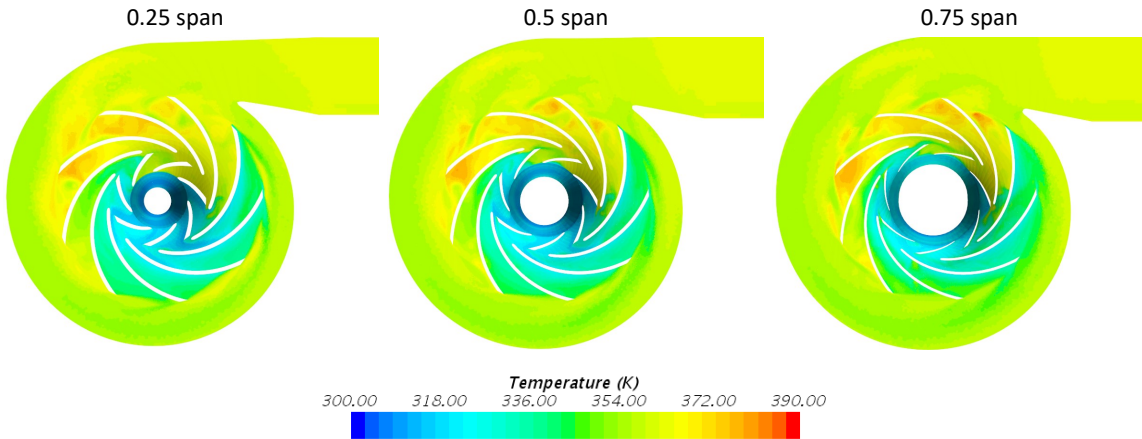


FIGURE 5.31 – Temperature distribution at [ESLP](#) with $N_1 = 6,420rpm$, $N_2 = 12,000rpm$ and $\dot{m}_{cr} = 0.08kg/s$ on three equipotential surfaces located at 0.25, 0.5 and 0.75span

Figure 5.31 illustrates the temperature field on the equipotential surfaces of the 0.5 span. It can be seen that in the five blocked blade passages the temperature field is very high due to the vortices, where the fluid flow moved at high velocities and interacts with nearby vortex regions. Because of the friction force, the temperature of this zone raises. In addition, the increase in temperature leads to a loss of power and a decrease in performance. Otherwise, the temperature field remains stable in the remaining blade passages because of the standard fluid flow.

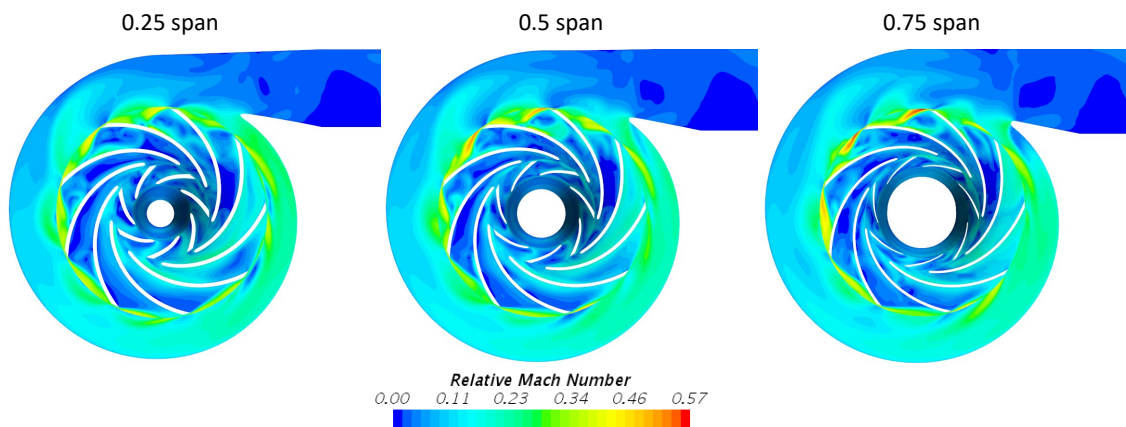


FIGURE 5.32 – Relative Mach number distribution at [ESLP](#) with $N_1 = 6,420rpm$, $N_2 = 12,000rpm$ and $\dot{m}_{cr} = 0.08kg/s$ on three equipotential surfaces located at 0.25, 0.5 and 0.75span

Figure 5.32 shows the distribution of relative Mach number on the equipotential surface at 0.5span. It can be identified that the relative Mach number inside rotors

is small due to the absence of the recirculation of fluid flow except for a few blade passages of the second rotor. It should be noticed that the maximum value reaches 0.57 can be observed at the trailing edge of the second rotor because the local vortex rotates in the opposite direction to the rotation of the second rotor, resulting in fluid flow at high velocity.

5.5 Conclusions

The instability phenomenon of CRCC is pushed back to a lower flow rate and the operating range is extended by using the first rotor speed controlled method. In counter-rotating mode, the reduction of the first rotor speed makes the compressor able to operate at a smaller flow rate, but the pressure ratio decreases rapidly. To maintain a constant pressure ratio, measurements with simultaneously changes in speeds of both rotors are conducted. In addition, the co-rotating mode is adopted to push back the compressor instability appearance region at a very low flow rate. Experimental results indicate that this operating mode can push back the limited flow rate about 0.135kg/s for the C_1 and 0.125kg/s for C_3 compared to the SRCC one. That means the operating range is extended about 24%-28% towards the low flow rate. This can be obtained when the first rotor speed ranges from 48% to 64% of the second rotor speed in co-rotating mode. Obviously, the instability region of the compressor is significantly reduced toward a lower flow rate. In addition, a CFD simulation of Extended Stability Limit Point (ESLP) in co-rotating mode is conducted to understand the fluid flow inside the compressor. The result shows that more than half of the blade passages are blocked by the vortices. However, the fluid flow is still circulating normally through the rest of the rotor passage. This shows that the compressor still maintains the ability to work stably at an extremely low flow rate thanks to the co-rotating effect.

Chapter 6

Conclusions and perspectives

6.1 Summary

The purpose of the study is to achieve two main objectives. The first is to assess the possibility of improving the centrifugal compressor performances when using the counter-rotating system. The second is to suspend the instability phenomenon and expand the operating range towards the instability region. Two counter-rotating rotors are designed based on the single rotor of a [Single Rotor Centrifugal Compressor \(SRCC\)](#). These rotors then replace the single rotor of [SRCC](#) to build a new compressor generation called [Counter-Rotating Centrifugal Compressor \(CRCC\)](#). A [Rotor - rotor Aerodynamic Interaction of a COunter-Rotating centrifugal compressor \(RAICOR\)](#) test bench is developed for an experimental study based on an existing centrifugal compressor test bench of [Laboratoire d'Ingénierie des Fluides et des Systèmes Énergétiques \(LIFSE\)](#).

6.2 Design of counter-rotating rotors

The counter-rotating rotors are designed according to the principle of conserving the geometric size of the reference rotor. Firstly, the dimensions of the first rotor are determined by the [Length Ratio \(LR\)](#) parameter, which is calculated by $LR = L_{1st}/L_m$ parameter. Four [CRCC](#) configurations: [CF1](#), [CF2](#), [CF3](#), [CF4](#) are built based on four values of [LR](#) parameters of 0.3, 0.4, 0.5, and 0.6 respectively. The blade angles of the rotors are calculated based on the aerodynamic relation. An investigation is conducted to evaluate the effect of counter-rotating on the performance of the centrifugal compressor. The simulation results show that the [CF1](#) gives the highest performance and the least loss between four configurations. So the [CF1](#) configuration is chosen to build the test bench for experimental studies.

6.3 Design of RAICOR test bench

[RAICOR](#) test bench is designed to be compatible with the existing centrifugal compressor test bench developed at [LIFSE](#). Due to the structure of [CRCC](#) with two electric motors on two sides of the compressor so that the bent pipe with an angle of 90° was used for this case. Numerical simulation shows that the use of bent inlet pipe has a slight influence on the performance in the near instability region. In addition, the components of the test bench are also designed and analyzed. The test results show

that all tested values are within safe limits and are guaranteed to avoid resonance. Besides, uncertainty calculation and measurement methods are presented to determine the reliability of the measurement values.

6.4 Experimental results

The experimental measurement are performed at three different speeds of the $N_2 = 9,000rpm$, $N_2 = 10,000rpm$ and $N_2 = 11,000rpm$. The rotation speed of $16,000rpm$ at the design operating point is obtained by using a similarity method. The results show that **CRCC** can improve not only performance but also the operating range.

6.4.1 Global performance

The global performance of the **CRCC** is studied carried out and compared to the global performance of **SRCC**. Three operating cases of **CRCC** are tested: case 1-the first rotor rotated freely, case 2- the first rotor is fixed and case 3- counter-rotating mode. A comparison of the three cases results shows that:

- Case 1: The first rotor works like a turbine. Experimental results indicate that **CRCC** produces lower pressure ratio and higher efficiency than **SRCC**. At $9,000rpm$, the efficiency is increased by about 8%, however, it is improved by about 3% when the rotation speed increases to $10,000rpm$ and $11,000rpm$. Consequently, **CRCC** consumes less energy than **REF** and the operating range is a little bit expanded to lower flow rate.
- Case 2: The global performance of **CRCC** is significantly reduced due to the incompatibility of the fluid flow at the second rotor inlet and a great inlet loss is generated. As a result, this case is not interesting because it is inefficient, so it is not further studied in this work.
- Case 3: The pressure ratio of **CRCC** is slightly improved from 2.5% to 4.65% compared to that **SRCC** at the same speed. Moreover, the polytropic efficiency remains constant compared to case 1. However, the **CRCC** consumes more power due to the higher pressure ratio rise and its instability limit appears earlier.

6.4.2 Influence of rotation speed ratio (θ)

A study on the influence of speed ratios is conducted in counter-rotating mode. The results show that the speed ratio greatly affects the pressure ratio while the efficiency remains constant. The pressure ratio increases linearly with the increase of the speed ratio. The explanation is that the fluid flow brings more energy before entering the second rotor. Higher kinetic energy because of a higher rotation speed leads to a higher pressure ratio. The pressure ratio can be increased up to 6.6% at a speed of $N_2 = 11,000rpm$ and a speed ratio of $\theta = -1.3$. It is worth noting that the best efficiency point of **CRCC** changes according to the change of speed ratio. The set of best efficiency points gives an effective range of the **CRCC**. This region is expanded and moved towards a lower mass flow rate in comparison with the region of **SRCC**. So, it can be concluded that **CRCC** gives the wider effective range and more flexible than **SRCC**. Moreover, **CRCC** can work at a lower speed than $2000rpm$ in comparison with the speed of **SRCC** to obtain the same performance. However, the appearance of instability phenomena in this configuration is earlier. This can be explained by an increase in the pressure ratio

resulting in a change in inlet condition. The vortex cells in the blade passage are formed earlier due to the higher incident angle. This phenomenon can be solved by simultaneously adjusting the speed of the two rotors to reduce the incident angle.

6.4.3 Similarity method

The similarity method allows calculating and constructing the performance curve of a family of compressors based on the known operating parameters at a specific rotation speed. In this method, the characteristic of **CRCC** at $10,000rpm$ is chosen. The results are compared to the experimental results of $9,000rpm$ and $11,000rpm$ in order to evaluate the reliability of the method. The results showed that the similarity method correctly predicted the working parameters of the compressor at those speeds. Therefore, it is used to build the **CRCC** characteristic curves at the design speed of $16,000rpm$. These curves show that **CRCC** improves significantly pressure ratio while the efficiency remains constant and slightly reduces by about 1% compared to the performance of **SRCC**. The pressure ratio of **CRCC** is always greater and it can be increased up to 15.3% at the speed ratio of $\theta_7 = -1.3$ compared to the pressure ratio of **SRCC** at the speed of $16,000rpm$.

6.4.4 CFD analysis

Numerical simulation studies were conducted to further investigate the fluid flow characteristics inside the **CRCC**. The mesh sensitivity studies were conducted to make sure that the selected model is an independent mesh. A comparison with experimental results shows that the numerical model is quite close to the experimental measurements, especially at a low flow rate. The smallest deviation value of pressure ratio is about 0.7% at a low flow rate and gradually increases to about 4% at a high flow rate. Besides, the divergence of polytropic performance is quite close to the experimental results at a low flow rate. The smallest deviation at the best efficiency point is about 0.15%. Two special points, **Best Efficiency Point (BEP)** and **Near Instability Point (NIP)**, are studied in steady and unsteady simulations to analyze the characteristics of the internal fluid flow with $N_1 = 10,000rpm$ and $N_2 = 10,000rpm$. The distribution of pressure, velocity, and temperature is quite uniform in the rotor as well as in the volute at **BEP**. The fluid flow inside the rotor does not show the vortex region and the flow is quite compatible with the rotor. However, some blade passages present a large vortex representing the stall cell at **NIP**. These vortices blocked all or a part of the blade passage due to secondary back-flow generated by the downstream pressure gradient and fluid continuity to compensate for the flow deficit. Although vortex cells appear inside the second rotor in a few blade passages and they are not spread to the entire rotor so that the compressor remains stable. If the flow rate continues to decrease, these stall cells continue to grow and to spread to the entire rotor causing the instability phenomenon. The unsteady simulation is also conducted to study the relative position between blade rows of the two rotors and the changes of stall cells inside blade passages. The results indicate that stall cells appear near the volute tongue and grow gradually in the blade passages in the inverse direction of the rotation. When the blade passage passes the volute tongue region, its stall cells gradually decrease in size and disappear. The fluid flow can normally circulate. Furthermore, wall pressure fluctuations are also observed in this simulation. The FFT analysis results can identify the frequency of blade passing and its harmonic frequencies.

6.5 Instability control and extension of the operating range

Using the first rotor speed controlled method, the instability phenomenon of the CRCC compressor is pushed back to a lower flow rate. The results of the experiment show that the instability phenomenon is suspended if the first rotor speed is reduced. Thus, the compressor can operate at a smaller flow rate but the pressure ratio is decreased sharply. One solution to maintain a constant pressure ratio is to simultaneously change the rotation speed of both rotors. In addition, the co-rotating mode is then adopted to improve the compressor instability phenomenon at a very low mass flow rate. Experimental results indicate that this method can push back the limit flow rate about 0.135kg/s for $\Pi = 1.11$ and 0.125kg/s for $\Pi = 1.177$ compared to the limit flow rate of SRCC at the same pressure ratio. That means the operating range is expanded by about 25% towards the lower flow rate in comparison with the operating range of SRCC. This can be obtained when the first rotor speed ranges from 48% to 64% of the second rotor speed in co-rotating mode. Additionally, A CFD analysis at the Extended Stability Limit Point (ESLP) is conducted in the co-rotating mode in order to better understand the fluid flow structure inside the compressor. The result shows that more than half of the blade passages are blocked. However, the fluid flow still circulates normally through the rest of the blade passages. This indicates that the compressor maintains the ability to work stably at the extremely low flow rate, thanks to the co-rotating effect.

6.6 Recommendations for future work

The results of this thesis show the outstanding advantages of applying the counter-rotating system on a centrifugal compressor. To develop this type of compressor, several proposals are suggested as follows:

- The numerical results show that the pressure ratio increases with the increase of length ratio parameter but the efficiency reduces. However, the influence of this parameter on the instability region cannot be realized by simulation. Therefore, it is necessary to conduct experimental investigations of the rest three configurations (as shown in figure 6.1).



FIGURE 6.1 – Three configurations with three value of LR: 0.3, 0.4 and 0.5 need to experimental study in the future

- The first rotor outlet blade angle affects considerably the performance of the counter-rotating centrifugal compressor. Two rotors with the different outlet angles are manufactured to investigate.

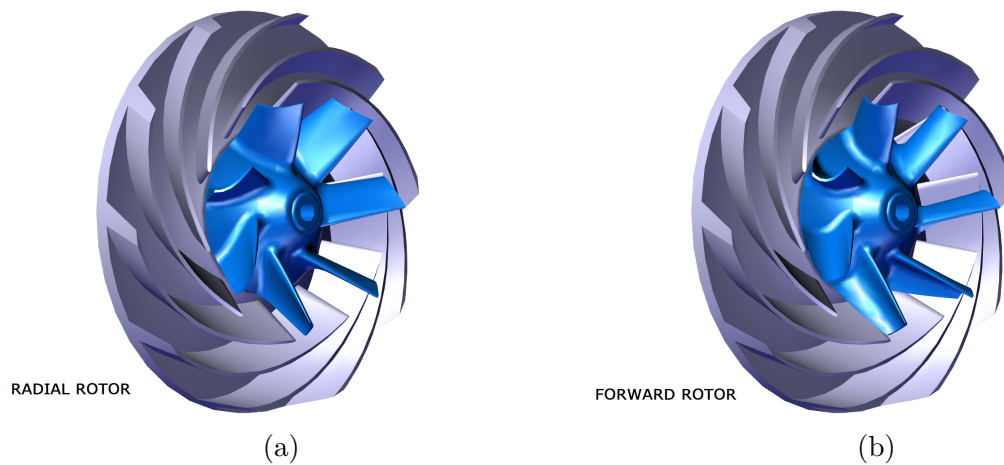


FIGURE 6.2 – The first rotor with the different outlet blade angles: (a) radial angle and (b) forward angle of the configuration 1

- The compressor generates noise during the operation due to the interaction between two blades rows. Thus, the investigations of a distance of two blades rows, the gap between the rotors and the casing, the number of blades of each rotor should be performed to analyze its impact on the aerodynamic as well as aeroacoustic performance.
- The suction application of the CRCC is conducted in this thesis. In addition, the behavior of the compressor in the compressed application needs to realize to develop this type of turbomachinery.
- This work presented the experimental investigation of a counter-rotating rotor based on the single rotor of a high specific speed compressor. The application of the counter-rotating system on a low specific speed centrifugal compressor should be performed to explore the behavior of the counter-rotating system.
- The most interesting thing about the counter-rotating system is that this type of compressor can improve the performance and work at a very low mass flow rate. Therefore, using an additional counter-rotating rotor placed upstream of a centrifugal rotor of a compressor would be a good idea to improve the performance, especially in the instability region. This rotor can rotate in counter-rotating mode in case of increasing performance or in the co-rotating mode in case of improving the instability region to extend the operating range.

References

- [1] A Busemann. The pump head ratio of radial centrifugal pumps with logarithmic spiral blades. *Z. Angew. Math. Mech*, 8(5):372–384, 1928. [vii](#), [6](#), [7](#)
- [2] J. Fukutomi, T. Shigemitsu, and T. Yasunobu. Performance and internal flow of sirocco fan using contra-rotating rotors. *Journal of Thermal Science*, 17(1):35, 2008. [vii](#), [14](#), [15](#)
- [3] Stefano Tosin, Jens Friedrichs, Rehan Farooqi, and Andreas Dreiss. New approach for multi-rotor mixed-flow pump design and optimization. In *ASME 2014 4th Joint US-European Fluids Engineering Division Summer Meeting collocated with the ASME 2014 12th International Conference on Nanochannels, Microchannels, and Minichannels*, pages V01AT02A007–V01AT02A007. American Society of Mechanical Engineers, 2014. [vii](#), [15](#), [16](#), [27](#), [92](#)
- [4] Stefano Tosin, Jens Friedrichs, and Andreas Dreiss. Pumping unit power-density improvement by application of counter-rotating impellers design. *Journal of Turbomachinery*, 138(11):111004, 2016. [vii](#), [16](#), [17](#)
- [5] Quentin Dejour and Huu Duc Vo. ASSESSMENT OF A NOVEL NON-AXIAL COUNTER-ROTATING COMPRESSOR CONCEPT FOR AERO-ENGINES. pages 1–9, 2018. [vii](#), [17](#), [18](#)
- [6] Lars Vicum. *Flow Structure and Stability of a Turbocharger Centrifugal Compressor*. PhD thesis, 2005. [xi](#), [102](#)
- [7] Abraham Engeda. Early Historical Development of the Centrifugal Impeller. *International Gas Turbine & Aeroengine Congress & Exhibition Stockholm, Sweden — June 2–June 5*, pages 1–2, 1998. [1](#)
- [8] Klaus H Ludtke. *Process Centrifugal Compressors*. Springer. [1](#)
- [9] S.L. Dixon and C.A. Hall. *Fluid mechanics and thermodynamics of turbomachinery*, volume 53. ELSEVIER, 2010. [5](#), [7](#)
- [10] A. (Aurel) Stodola. *Steam and gas turbines*. New York : P. Smith, 1945. [6](#)
- [11] JD Stanitz. Some theoretical aerodynamic investigations of impellers in radial-and mixed flow centrifugal compressors. ASME, 1951. [7](#)
- [12] C Pfeleiderer. *Die kreiselpumpen fur flussigkeiten und gase*, 1961. [8](#)
- [13] F. J. Wiesner. A Review of Slip Factors for Centrifugal Impellers. *Journal of Engineering for Gas Turbines and Power*, 89(4):558–566, 1967. [8](#), [23](#)

- [14] Xuwen Qiu, David Japikse, Jinhui Zhao, and Mark R Anderson. Analysis and validation of a unified slip factor model for impellers at design and off-design conditions. *Journal of Turbomachinery*, 133(4):041018, 2011. 8
- [15] J.L. Taylor. Counter rotating propellers. *Flight*, 39, 1941. 11, XXXIV
- [16] M. W. Bourdon. The influence of heat conduction on acoustic streaming. *Automotive and aviation industries*, 86(12), 1942. 11, XXXIV
- [17] R.H Young. Counter rotating fans. *JHIVE*, 18, 1952. 11, XXXIV
- [18] Ward W. Wilcox. An analysis of the potentialities of a two-stage counterrotating supersonic compressor. 1952. 11, XXXIV
- [19] P. B. Sharma, Y. P. Jain, N. K. Jha, and B. B. Khanna. Stalling behaviour of a contra-rotating axial compressor stage. In *International Symposium on Air Breathing Engines, 7th, Beijing, People's Republic of China*, pages 734–740, 1985. 11, XXXIV
- [20] P. B. Sharma and A. Adekoya. A review of recent research on contra-rotating axial flow compressor stage. In *ASME 1996 International Gas Turbine and Aeroengine Congress and Exhibition*, pages V001T01A073–V001T01A073. American Society of Mechanical Engineers, 1996. 11, XXXIV
- [21] Akinori Furukawa, Toru Shigemitsu, and Satoshi Watanabe. Performance test and flow measurement of contra-rotating axial flow pump. *Journal of Thermal Science*, 16(1):7–13, 2007. 12
- [22] J. L. Kerrebrock, a. H. Epstein, a. a. Merchant, G. R. Guenette, D. Parker, J.-F. Onnee, F. Neumayer, J. J. Adamczyk, and a. Shabbir. Design and Test of an Aspirated Counter-Rotating Fan. *Journal of Turbomachinery*, 130(April):021004, 2008. 12
- [23] Leonid Moroz, Petr Pagur, Yuri Govorushchenko, and Kirill Grebennik. Comparison of counter – rotating and traditional axial aircraft low-pressure turbines integral and detailed performances. In *Int. Symp. on Heat Transfer in Gas Turbine Systems*, number August, 2009. 12
- [24] CHO Lee-Sang, CHA Bong-Jun, and CHO Jin-Soo. Experimental study on the three-dimensional unsteady flow characteristics of the counter-rotating axial flow fan. *Journal of Fluid Science and Technology*, 4(1):200–209, 2009. 12
- [25] Akinori Furukawa, Satoshi Usami, Yusuke Tsunenari, Satoshi Watanabe, and Kusuo Okuma. Limiting streamlines measurement in contra-rotating axial flow pump. In *Fluid Machinery and Fluid Mechanics*, pages 161–166. Springer, 2009. 13
- [26] S Momosaki, S Usami, S Watanabe, and A Furukawa. Numerical simulation of internal flow in a contra-rotating axial flow pump. In *IOP conference series: Earth and environmental science*, volume 12, page 012046. IOP Publishing, 2010. 13
- [27] A. Alexiou, I. Roumeliotis, N. Aretakis, A. Tsalavoutas, and K. Mathioudakis. Modeling Contra-Rotating Turbomachinery Components for Engine Performance Simulations: The Geared Turbofan With Contra-Rotating Core Case. *Journal of Engineering for Gas Turbines and Power*, 134(November):111701, 2012. 13

- [28] Toru Shigemitsu, Junichiro Fukutomi, and Hiroki Shimizu. Influence of blade row distance on performance and flow condition of contra-rotating small-sized axial fan. *International Journal of Fluid Machinery and Systems*, 5(4):161–167, 2012. [13](#)
- [29] H. Nouri, A. Danlos, F. Ravelet, F. Bakir, and C. Sarraf. Experimental Study of the Instationary Flow Between Two Ducted Counter-Rotating Rotors. *Journal of Engineering for Gas Turbines and Power*, 135(2):022601, 2013. [14](#), [17](#), [70](#)
- [30] Madhur Tiwari. *Axial Compressor Design with Counter-Rotation and Variable RPM for Stall Mitigation Axial Compressor Design with Counter - Rotation and Variable RPM for Stall Mitigation*. Master thesis, Embry-Riddle Aeronautical University-Daytona Beach, 2014. [14](#)
- [31] Stefano Tosin, Jens Friedrichs, and Andreas Dreiss. Experimental and numerical investigation of a counter-rotating mixed-flow single stage pump. In *ASME Turbo Expo 2015: Turbine Technical Conference and Exposition*, pages V02CT42A006–V02CT42A006. American Society of Mechanical Engineers, 2015. [16](#), [70](#)
- [32] Juan Wang. *Experimental study of two counter rotating axial flow fans*. Phd thesis, ENSAM ParisTech, 2014. [17](#)
- [33] H. Pitkänen, H. Esa, P. Sallinen, and J. Larjola. CFD Analysis of a Centrifugal Compressor Impeller and Volute. *International Gas Turbine & Aeroengine Congress & Exhibition*, (1997):1–8, 1999. [31](#)
- [34] I. Ariga, N. Kasai, S. Masuda, Y. Watanabe, and I. Watanabe. The Effect of Inlet Distortion on the Performance Characteristics of a Centrifugal Compressor. *Journal of Engineering for Power*, 105(2):223, 1983. [39](#)
- [35] T. Wright, S. Madhavan, and J. DiRe. Centrifugal Fan Performance With Distorted Inflows. *Journal of Engineering for Gas Turbines and Power*, 106(4):895, 1984. [39](#)
- [36] Y. Kim, A. Engeda, R. Aungier, and G. Direnzi. The influence of inlet flow distortion on the performance of a centrifugal compressor and the development of an improved inlet using numerical simulations. *Proceedings of the Institution of Mechanical Engineers, Part A: Journal of Power and Energy*, 215(3):323–338, 2001. [39](#), [95](#)
- [37] Wang Yan, Dong Quanlin, and Xiaomeng Liu. Numerical investigation on the effect of inlet acceleration on inlet flow distortion in a centrifugal fan. 102(Icmmse):336–341, 2012. [39](#)
- [38] Du Li, Ce Yang, Mi Zhou, Zhifu Zhu, and Hang Wang. Numerical and experimental research on different inlet configurations of high speed centrifugal compressor. *Science China Technological Sciences*, 55(1):174–181, 2012. [40](#)
- [39] Ander Eza. Flow simulations with relevance to a centrifugal compressor and the effect of the inlet geometry. *Master thesis*, 2015. [40](#)
- [40] www.nde-ed.org/generalresources/uncertainty/gaussian.pdf.htm. [50](#)

- [41] www.infoclimat.fr/observations-meteo/temps-reel/paris-montsouris/07156.html. 52
- [42] Meherwan P. Boyce. Principles Of Operation And Performance Estimation Of Centrifugal Compressors. *Xxiii Turbo Machinery Symposium*, (Figure 2):18, 1993. 62, XLIII
- [43] P. B. Sharma, Y. P. Jain, and D. S. Pundhir. A study of some factors affecting the performance of a contra-rotating axial compressor stage. In *Proceedings of the Institution of Mechanical Engineers, Part A: Journal of Power and Energy*, volume 202, pages 15–21, 1988. 69
- [44] Akinori Furukawa, Toru Shigemitsu, and Satoshi Watanabe. Performance test and flow measurement of contra-rotating axial flow pump. *Journal of Thermal Science*, 16(1):7–13, 2007. 69
- [45] Y. Y. Chen, B. Liu, Y. Xuan, and X. R. Xiang. A study of speed ratio affecting the performance of a contra-rotating axial compressor. *Proceedings of the Institution of Mechanical Engineers, Part G: Journal of Aerospace Engineering*, 222(7):985–991, 2008. 69
- [46] G A O Limin, L I Xiaojun, Xie Jian, and L I U Bo. The Effect of Speed Ratio on the First Rotating Stall Stage in Contra-Rotating Compressor. In *Turbine Technical Conference and Exposition*, volume 8, pages 207–216, 2012. 69
- [47] Chetan Mistry and A. M. Pradeep. Effect of variation in axial spacing and rotor speed combinations on the performance of a high aspect ratio contra-rotating axial fan stage. *Proceedings of the Institution of Mechanical Engineers, Part A: Journal of Power and Energy*, 227(2):138–146, 2013. 69
- [48] Rayapati Subbarao and M. Govardhan. Effect of speed ratio on the performance and flow field of a counter rotating turbine. In *Energy Procedia*, volume 54, pages 580–592, 2014. 70
- [49] Arnold Whitfield and Nicholas C Baines. *Design of radial turbomachines*. New York, NY (USA); John Wiley and Sons Inc., 1990. 78, XXVIII
- [50] C. Xu and M. Müller. Development and Design of a Centrifugal Compressor Volute. *International Journal of Rotating Machinery*, (3):190–196, 2005. 93
- [51] E. M. Greitzer. The Stability of Pumping. *Journal of Fluids Engineering*, 103(June 1981), 1981. 94, 103
- [52] Jan van Helvoirt. *Centrifugal Compressor Surge: Modeling and Identification for Control*. Number 2007. 2007. 94, 102, 104
- [53] J. Paduano, L. Valavani, and A. H. Epstein. Parameter identification of compressor dynamics during closed-loop operation. *Journal of Dynamic Systems, Measurement and Control, Transactions of the ASME*, 115(4):694–703, 1993. 94, 103
- [54] Maurice Stewart. *Dynamic compressors*. 2019. 101

- [55] Bram de Jager. Rotating stall and surge control: a survey. *Proceedings of the IEEE Conference on Decision and Control*, 2(December):1857–1862, 1995. [101](#), [104](#)
- [56] Alex Stein, Saeid Niazi, and L. N. Sankar. *Computational analysis of stall and separation control in centrifugal compressors*. PhD thesis, 2000. [101](#)
- [57] D. A. Fink, N. A. Cumpsty, and E. M. Greitzer. Surge dynamics in a free-spool centrifugal compressor system. *Journal of Turbomachinery*, 114(2):321–332, 1992. [102](#)
- [58] JD Paduano, EM Greitzer, and AH Epstein. Compression System Stability and active Control. *Annual Review of Fluid Mechanics*, 33(1):491–517, 2001. [102](#)
- [59] K. K. Botros and J. F. Henderson. Developments in centrifugal compressor surge Control-A technology assessment. *Journal of Turbomachinery*, 116(2):240–249, 1994. [102](#)
- [60] N. Dukle and K. Narayanan. Rotating equipment: Validating anti-surge control systems. 8:87, 89–92, 94, 06 2003. [102](#)
- [61] H. Simon, T. Wallmann, and T. Mönk. Improvements in performance characteristics of single-stage and multistage centrifugal compressors by simultaneous adjustments of inlet guide vanes and diffuser vanes. *Journal of Turbomachinery*, 109(1):41–47, 1987. [103](#)
- [62] K. Jiao, H. Sun, X. Li, H. Wu, E. Krivitzky, T. Schram, and L. M. Larosiliere. Numerical investigation of the influence of variable diffuser vane angles on the performance of a centrifugal compressor. *Proceedings of the Institution of Mechanical Engineers, Part D: Journal of Automobile Engineering*, 223(8):1061–1070, 2009. [103](#)
- [63] V. V.N.K.Satish Koyyalamudi and Quamber H. Nagpurwala. Stall margin improvement in a centrifugal compressor through inducer casing treatment. *International Journal of Rotating Machinery*, 2016, 2016. [103](#)
- [64] P. A. Eynon, J. L. Whitfield, M. R. Firth, A. J. Perkes, and R. Sexton. A study of the flow characteristics in the inducer bleed slot of a centrifugal compressor. *ASME 1996 International Gas Turbine and Aeroengine Congress and Exhibition, GT 1996*, 1, 1996. [103](#)
- [65] Bahram Nikpour. Turbocharger compressor flow range improvement for future heavy duty diesel engines. In *THIESEL 2004 Conference on Thermo-and Fluid Dynamic Processes in Diesel Engines, Valencia, Spain, September*, pages 7–10, 2004. [103](#)
- [66] Franciscus Petrus Thomas Willems. *Modeling and Bounded Feedback Stabilization of Centrifugal Compressor Surge*. PhD thesis, 2000. [103](#)
- [67] I. J. Day. Active suppression of rotating stall and surge in axial compressors. *Journal of Turbomachinery*, 115(1):40–47, 1993. [103](#)

- [68] REY (R.);BAKIR (F.). *Machines centrifuges et helicocentrifuges,Cours UEE Ingénierie des fluides et des machines tournantes, Arts et Métiers ParisTech.* [I](#), [II](#)
- [69] Michel PLUVIOSE. Similitude des turbomachines à fluide compressible. *Techniques de l'ingénieur Machines hydrauliques et thermiques : fondamentaux et concepts innovants*, base documentaire : TIB171DUO.(ref. article : bm4680), 2005. [XI](#)
- [70] Cd-adapco (2016). star-ccm+ 11.0 user guide. melville, ny, usa: Cd-adapco inc. [XXIX](#), [XXXI](#)
- [71] J. E. Bardina, P. G. Huang, and T. J. Coakley. Turbulence Modeling Validation, Testing, and Development. *Nasa Technical Memorandum*, (110446):8 – 20, 1997. [XXIX](#)
- [72] F. R. Menter. Two-equation eddy-viscosity turbulence models for engineering applications. *AIAA Journal*, 32(8):1598–1605, 1994. [XXIX](#)
- [73] David C Wllcox and Alexander Bell Drive. Turbulence Modeling : An Overview. *American Institute of Aeronautics and Astronautics*, 2001. [XXIX](#)

Appendix A

APPENDIX

A.1 Dimensioning method of a centrifugal rotor

<This part is an extract of the dimensioning method presented in article [68]>

The size of a centrifugal rotor is primarily designed according to an empirical characteristic because it is still based on a large number of experiments and statistical rules. The reason is that a large number of quadratic parameters need to determine the complete shape of the rotor and its immediate environment. These multiple choices are often arbitrary and can be guided by various considerations such as regularity of flow, reduction of mass, optimization of performance (efficiency, pressure ratio, noise, and vibrations), the stability of characteristics, etc.

The design of machines takes place in various steps ranging from pre-dimensioning of the mechanic and hydraulic parameters, until the fine analysis of the flow structures. To simplify, the following steps can be defined:

1 - The specifications define the expected overall performance: pressure and flow generated, expected overall efficiency, and overall dimension. The nature of fluids and the environment of the machine are also defined.

2 - The know-how makes it possible to arbitrarily retain the rotation speed, the number of stages, the type of rotor, the type of blades...

3 - The calculation of preliminary design defines, thanks to a flow model, the fields of velocity, pressure, and temperature, etc. giving access to the principle efforts in presence.

4 - Mechanical pre-dimensioning: from this stage, the position and the type of bearings, the balancing devices, the thickness of the housings, the diameter of the shaft, and its different critical speeds, the sealing devices are determined...

In case of incompatibility of these results with the previous choices, step 2 or step 3 starts again with more and more fine models concerning the analysis of the flows (using CFD software). This approach is assumed to be successful when the performances calculated by various CFD software or others, confirm that the expected results are achieved.

A.1.1 Inlet velocity triangles

As described in the section [1.1.3](#), the fluid is assumed that it is not subjected to any pre-rotation at the entrance of the rotor. The property of the velocity triangles

makes it possible to write:

$$\tan \beta_1 = \frac{U_1}{C_1} \quad (\text{A.1})$$

The continuity equation at the nominal point allows writing the inlet angle of fluid flow equal to the blade angle:

$$\begin{aligned} \tan \beta_1 &= \tan \beta_{1b} \\ C_1 &= \frac{Q}{S_1} \end{aligned} \quad (\text{A.2})$$

Where S_1 is a blade inlet section and is defined by:

$$S_1 = 2\pi r_1 b_1 \quad (\text{A.3})$$

According to the basis of theoretical developments, the good capacity inlet section can be determined from an optimal radius:

$$r_{opt} = 2.25 \sqrt[3]{\frac{Q}{N}} \quad (\text{A.4})$$

From the equation A.3 and A.4, the optimized inlet area can be calculated by:

$$S_1 = S_{1opt} = \pi r_{opt}^2 \quad (\text{A.5})$$

Combining the equations A.1, A.2, A.4 and A.5, the geometry parameters at the inlet can be determined:

$$\begin{aligned} r_1 &= \frac{Q \tan \beta_{10}}{\pi \omega r_{opt}^2} \\ b_1 &= \frac{S_1}{2\pi r_1} \end{aligned} \quad (\text{A.6})$$

A.1.2 Outlet velocity triangles

Outlet diameter calculation

The choice of the outer radius is made from a common reference value used for the construction of compression machines. This standard value depending on the specific angular speed Ω is selected by Cordier diagram¹ [68]. It shows the relation between the specific angular velocities Ω and the specific radius Λ as presented in figure A.1. It reveals that at each specific speed of Ω , it can be found an optimal value of a specific radius Λ to obtain maximum efficiency. If selecting a larger or smaller optimal specific radius, the efficiency deteriorates.

The specific angular speed is defined:

$$\Omega = \frac{\omega \sqrt{Q}}{(gH)^{3/4}} \quad (\text{A.7})$$

The specific radius is determined by:

$$\Lambda = \frac{r_2 (gH)^{1/4}}{\sqrt{Q}} \quad (\text{A.8})$$

1. The Cordier diagram is a statistical diagram from experimental results

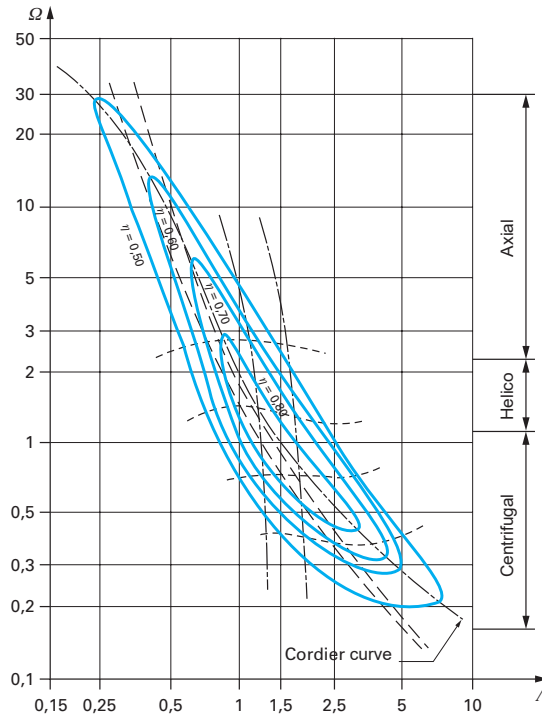


FIGURE A.1 – Cordier diagram

For a given operation point, the specific radius is chosen by selecting the high-efficiency region of the turbomachine. From the equation A.8 the outlet diameter of the rotor is calculated as:

$$r_2 = \frac{\Lambda \sqrt{Q}}{(gH)^{1/4}} \quad (\text{A.9})$$

Selection of outlet blade angle

When the fluid enters the rotor without pre-rotation, the theoretical and infinite head rise is given by the Euler equation:

$$\begin{aligned} H_{th} &= \frac{U_2 C_{u2}}{g} \\ H_{thb} &= \frac{U_2 C_{ub}}{g} \end{aligned} \quad (\text{A.10})$$

It can be seen from this relation that the theoretical head rise of a centrifugal machine only depends on the blade speed U_2 and the tangential velocity component C_{u2} . The ratio between U_2 and C_{u2} can be chosen in rather wide limits, it is closely related to the angle of exit β_{2b} , as shown in figure A.2. The value of β_{2b} is chosen between 60° and 70° (this value is chosen arbitrarily).

Determination of blade width b_2

To determine the blade width b_2 , firstly, the hydraulic efficiency η_H of the rotor is estimated from the empirical formula of Lomakine at the maximum efficiency point:

$$\eta_H = 1 - \frac{0.42}{[\lg d_\eta - 0.172]^2} \quad (\text{A.11})$$

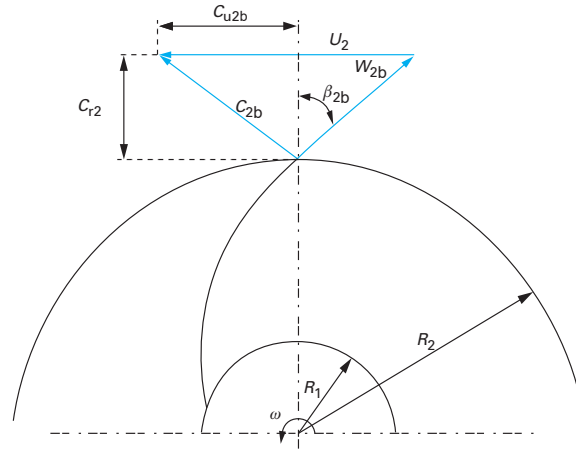


FIGURE A.2 – Velocity triangles at the outlet of a rotor

Where:

$$d_\eta = 4250 \sqrt[3]{\frac{Q}{N}} \quad (\text{A.12})$$

The theoretical and infinite head rise can be derived:

$$H_{th} = \frac{H}{\eta_H} \quad (\text{A.13})$$

$$H_{th_b} = \frac{H_{th}}{\mu}$$

The slip factor μ is determined by Pfleiderer formulation:

$$\mu = \frac{1}{1 + \frac{K_m \sin \phi}{Z} \frac{1 + \cos \beta_{2b}}{1 - \left[\frac{r_1}{r_2}\right]^2}} \quad (\text{A.14})$$

ϕ is the taper angle of the mean exit line as shown in figure A.3a

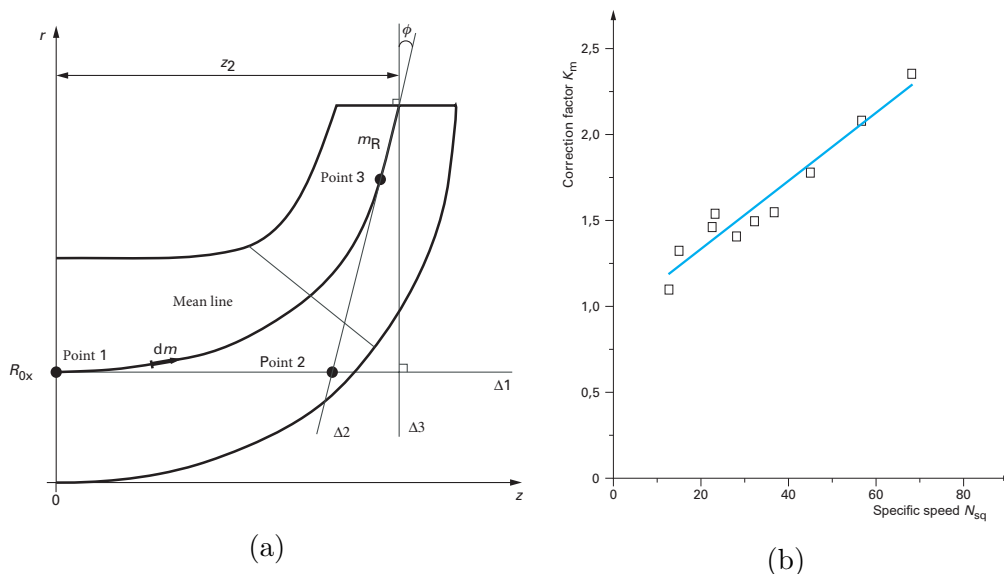


FIGURE A.3 – Definition of (a) mean line and (b) correction factor K_m

The proposed relation for the correction factor (K_m) is as follows:

$$\begin{aligned} K_m &= 0.02N_{sq} + 0.94 \\ 0 &\leq N_{sq} \leq 120 \\ 60^\circ &\leq \beta_{10} \text{ and } \beta_{2b} \leq 75^\circ \end{aligned} \quad (\text{A.15})$$

An angular difference $\Delta\beta$ shown in figure A.4 is associated with the slip factor μ . It represents a reduction of the head rise by a finite blade.

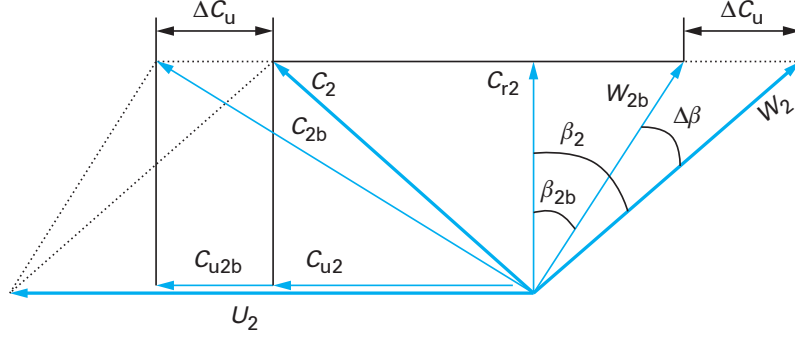


FIGURE A.4 – Influence of slip factor on the outlet velocity triangles

The tangential velocity component can be derived from the Euler equation of the infinite blade:

$$C_{u2b} = \frac{gH_{thb}}{U_2} \quad (\text{A.16})$$

From the velocity triangles as shown in figure A.2, the radial velocity component C_{r2} and the blade width b_2 can be calculated:

$$C_{r2} = \frac{U_2 - C_{u2b}}{\tan \beta_{2b}} \quad (\text{A.17})$$

$$b_2 = \frac{Q}{2\pi r_2 C_{r2}} \quad (\text{A.18})$$

If the ratio of b_2/r_2 is not compatible with the standards corresponding to the specific speed, the value of blade width b_2 , the number of blades Z and the radius at the outlet r_2 can be changed to find out the best ratio by iterative calculation.

A.1.3 Tracing blades in a meridional view

Definition of a mean line

The mean line of the rotor can be defined by the association of a Bezier curve with three poles and a straight portion at the output as shown in figure A.3a. The three poles are defined as:

+ The first pole has a coordinate $(0, r_{0x})$, with $r_{0x} = \frac{r_0}{2}$ (r_0 is the radius of a rotor entry) for a cantilever rotor and $r_{0x} = \frac{r_0 + r_a}{2}$ for a rotor with a radius of traversing shaft r_a ;

+ The second pole is defined by the intersection of two lines Δ_1 and Δ_2 : Δ_1 is a line parallel to the rotational axis and passing through the first pole $(0, r_{0x})$; Δ_2 is a line passing through the point (z_2, r_2) and forming an angle ϕ with a line Δ_3 ; Δ_3 is perpendicular to the trailing edge b_2 at the point of coordinates (z_2, r_2) .

+ The third pole is on the Δ_2 at a distance m_R from the point (z_2, r_2) .

In this definition, the value of m_R depends on the specific speed of the machine and diminishes with it. The angle ϕ called the taper angle is a free parameter. The correct choice of this parameter allows us to adjust the concavity of the two front and rear flanges. The distance z_2 is also a free parameter characterizing axial size. The retained value corresponds in most cases to a compromise between the losses and the size of the machine.

Surface law definition

The evolution of a meridian surface is explained according to a horizontal curvilinear measured on the mean line: $S = S(m)$ this curve is calculated from the following relation:

$$m(z) = \int_0^z \sqrt{1 + \left[\frac{dr}{dz} \right]^2} dz \quad (\text{A.19})$$

The analytic determination of this integral is often impossible for $r(z)$ functions which have a degree greater than one. To do that, a numerical integration method (Gauss method) is used. A series of simple equations can be used to describe and control the evolution of the flow surface or meridian surface. It is obtained by cutting the rotor in the plane through the symmetry axis or the rotating axis of the rotor.

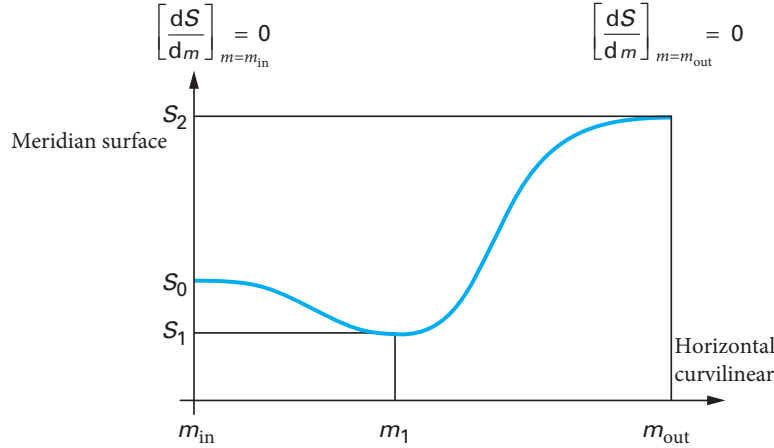


FIGURE A.5 – Evolution and regularity of the meridian surface according to the horizontal curvilinear

Considering the meridional view, there are two distinct parts:

- The upstream part: between a suction side and a leading edge;
- The blade part: between a leading edge and a trailing edge.

Then, an arbitrary surface law is defined by the most common boundary conditions given by different equations. It respects the regularity of the evolution of the meridian velocity (figure A.5):

$$S(m_{in}) = S_1 \quad \text{and} \quad S(m_{out}) = S_2 \quad (\text{A.20})$$

Determination of hub m_h and shroud m_{sh} contours

The mean line is discretized into a number of segments of equal curvilinear length, the coordinates $[r, z]$ of each discretization point are determined. From the imposed

surface law, the diameters of the osculating circles are easily calculated by:

$$b = \frac{S(m)}{2\pi r} \tag{A.21}$$

The determination of r, z, b as shown in figure A.6 allows to determine:

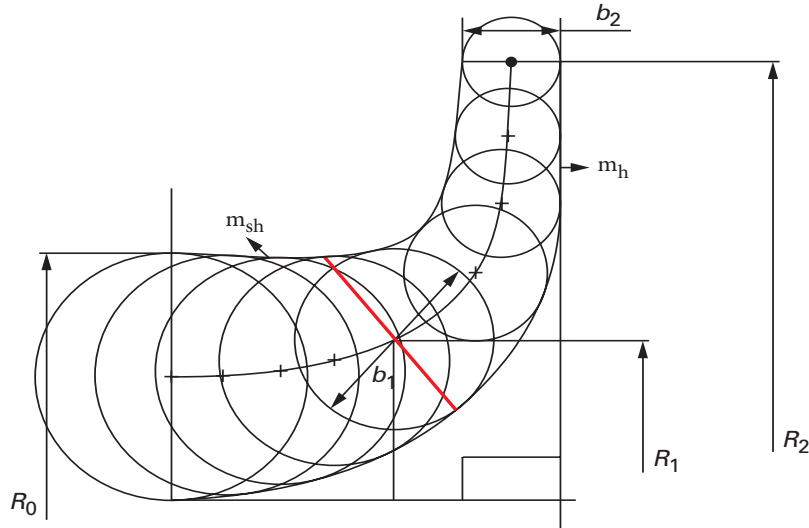


FIGURE A.6 – Tracing hub and shroud contours

- + The shroud contour of the circles m_{sh} ;
- + The hub contour of the circles m_h .

Inclination of the blade leading edge θ_i and blade inlet angles β_{1h}, β_{1sh}

For a low specific speed turbomachine, the leading edge in the meridional view is generally horizontal ($\theta_i = 0^\circ$). However, with a high specific speed machine, the tracing blades become three-dimensional (figure A.7) and it is no longer possible to limit the blade to a purely radial portion. In fact, the entrance of such a rotor is a centrifugal spiral and it makes sense that the leading edge of the blades is substantially coincident with a meridian equipotential of flow.

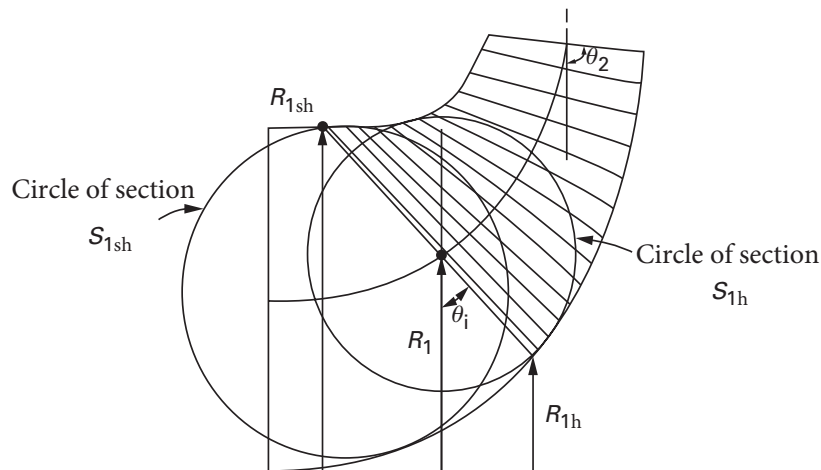


FIGURE A.7 – Definition of leading and trailing edge for a high specific speed rotor

In practice, this calculation is not reachable so that the inclination θ_i is fixed arbitrarily close to 45° . Then, the starting velocity is matched with those associated with their own oscillating circles. Consequently, two different values of the flow velocity are obtained:

$$C_{m1h} = \frac{Q}{S_{1h}} \quad \text{and} \quad C_{m1sh} = \frac{Q}{S_{1sh}} \quad (\text{A.22})$$

Starting from the velocity triangles, the inlet blade angle is calculated based on the meridional velocity by the following relation:

$$\tan \beta_{1h} = \frac{U_{1h}}{C_{m1}} = \frac{\omega r_{1h}}{C_{m1}} \quad \text{and} \quad \tan \beta_{1sh} = \frac{U_{1sh}}{C_{m1}} = \frac{\omega r_{1sh}}{C_{m1}} \quad (\text{A.23})$$

Inclination of trailing edge θ_2 and outlet blade angles β_{2h} , β_{2sh}

For the centrifugal machine, the trailing edge is parallel to the rotational axis $\theta_2 = 90^\circ$. Thus, the inclinations of the trailing edge rise gradually when the specific speed increases. This inclination is fixed considering the regularity and feasibility of flow. The choice of the inclination is closely related to the distribution of the tangential absolute velocity component C_{u2} , which is initiated by the designer. A free vortex distribution is proposed:

$$C_{u2b} = \frac{K_3}{r} \quad (\text{A.24})$$

Where:

The factor K_3 is calculated on the mean line.

The vortex is fixed. The velocity triangle permits to calculate the blade angles at the hub (β_{2h}) and the shroud (β_{2sh}):

$$\tan \beta_{2h} = \frac{U_{2h} - C_{u2h}}{C_{r2h}} \quad \text{and} \quad \tan \beta_{2sh} = \frac{U_{2sh} - C_{u2sh}}{C_{r2sh}} \quad (\text{A.25})$$

Where:

$$U_{2h} = \omega R_{2h} \quad \text{and} \quad U_{2sh} = \omega R_{2sh} \quad (\text{A.26})$$

$$C_{u2h} = f(K_i, R_{2h}) \quad \text{and} \quad C_{u2sh} = f(K_i, R_{2sh}) \quad (\text{A.27})$$

The value of C_{r2} is determined following the same method for the blade inlet.

A.1.4 Tracing blades in two views

A mean line of the meridional channel is generated by the imprint of the blade on a revolution surface as shown in figure A.8b. One element of the blade is cut by two planes perpendicular to the axis of rotation passing through points 1 and 2. The element can be constituted in two projections:

- The element lengths dm , dr and dz in meridional view (figure A.8a);
- The values $r d\theta$ and dr in front view (figure A.8c).

In a planar Cartesian coordinate system, dm is taken on the x-axis and $r d\theta$ on the y-axis. When the number of elements is sufficient, this representation reproduces the true magnitude and the blade angles in every point. In this case, this line is called a developed blade angle (figure A.8d).

The distribution of blade angle can be constructed if the blade inlet angle β_1 and the outlet angle β_2 are known by the following method:

Considering an element dm with an arbitrary small relative to the total length at the mean line from the input radius r_1 to the output radius r_2 in meridional view

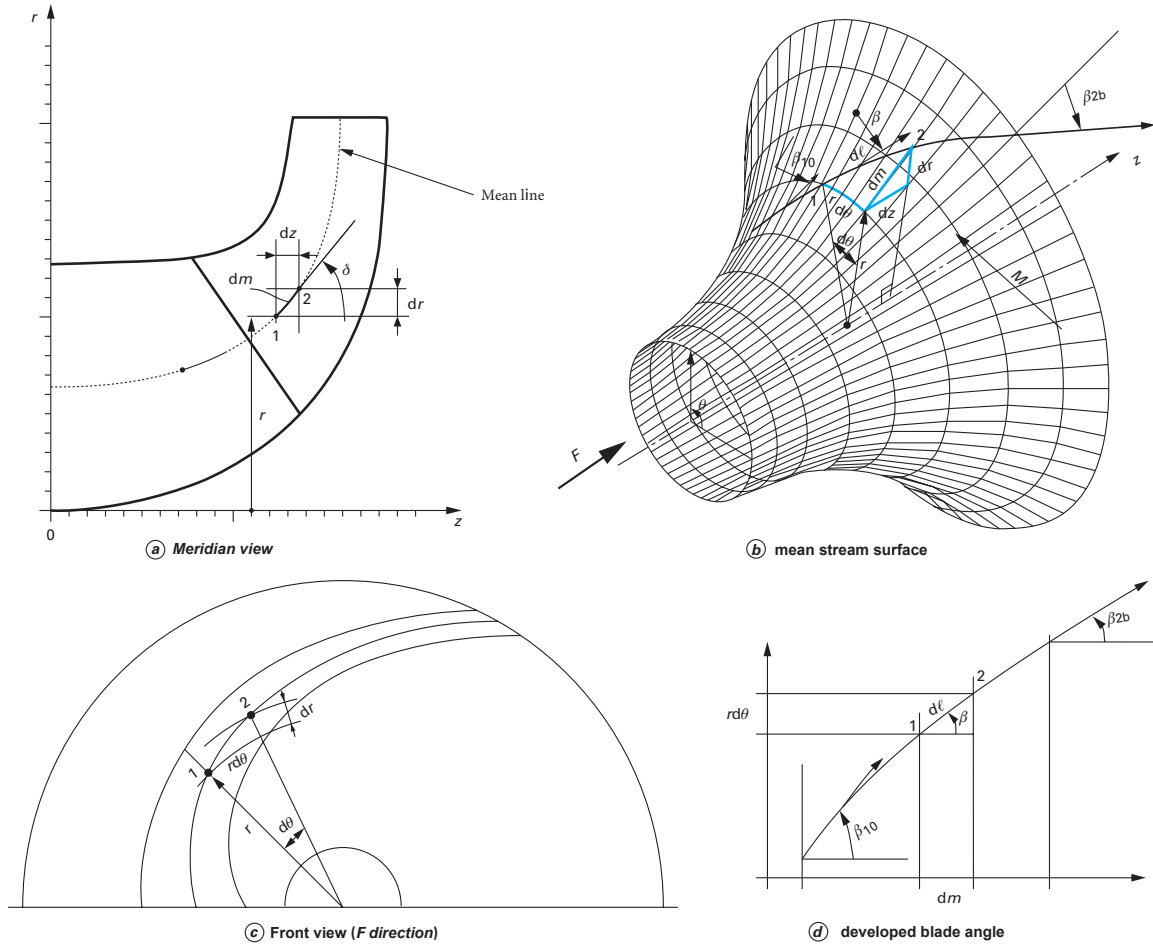


FIGURE A.8 – Set of geometries elements used to draw the blade: (a) meridian view, (b) mean stream surface, (c) front view and (d) developed blade angle

(figure A.8a). This element is defined by dr in meridional view (figure A.8a) and $r d\theta$ in front view (figure A.8c). The curve of the developed angle can be deduced by combining with parameters $r d\theta$ and dr in the front view from inlet to outlet or vice versa.

Variations of the developed blade angle

For reasons of uniformity with the camber laws of the majority of the aerodynamic profiles. The development is defined by a line in the double arc of a circle (figure A.9). The length of the blade has a certain influence on the performances of the machine. It can be modified to meet the requirement in case of optimization. There are two adjustable parameters:

- The angle β_3 is defined in the case of a single circular arc by increasing or reducing this angle. It allows to increase or reduce the length of the blade;
- The form factor (FF) is a ratio that defines the position of β_3 on the horizontal axis. When changing this factor, the length of the blade also changes. In design, the limitation in the interval of $[0.25; 0.75]$ to allow a suitable evolution between the angles β_1 and β_3 on the left-hand side and between β_3 and β_{2b} on the other side. This theory is integral in the 3D turbo software; the design of a centrifugal compressor present in figure 2.1.

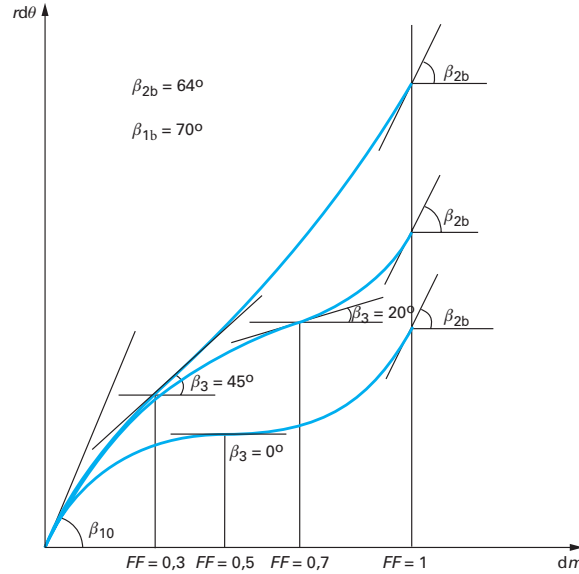


FIGURE A.9 – Definition of the developed blade angle

A.2 Theory of similarity method

The similarity laws of compressible fluids lead to simple relations with the assumption that the gas is ideal perfect. Under these conditions, the operation of a compressible turbomachinery is defined by the following various variables:

- The geometric dimensions of the compressor which are characterized by a reference length r . It is often the outside radius of the rotor;
- The nature characteristic of the fluid which is characterized by the gas constant R which fixes the mechanical characteristics of the fluid ($R = 287 Jkg^{-1}K^{-1}$), the ratio of specific heats $\gamma = c_p/c_v$, which is sufficient to define the thermal properties of the fluid; $C_p = R \frac{\gamma}{\gamma-1}$; the dynamic viscosity μ ;
- The angular speed ω or the rotation speed N ;
- The mass flow rate of the fluid equal to the internal flow rate;
- The isentropic stagnation pressures P_{1i} and P_{2i} at the inlet and outlet of the turbomachinery;
- The isentropic stagnation temperature T_{1i} of the fluid at the inlet of the turbomachinery;
- The isentropic efficiency $\eta_{i,s}$, sometimes called adiabatic efficiency. In addition, the internal polytropic efficiency $\eta_{i,p}$ can be used;
- The variation of stagnation enthalpy: $\Delta h_i = h_{2i} - h_{1i}$
- The internal power: $P_{o_i} = \dot{m} C_p \Delta T$.

The similarity properties applied to geometrically similar compressors make it possible to reduce the number of independent operating variables by defining dimensionless groupings of variables or reduced variables. The independent variables are selected as presented in the following table A.1:

There are eight independent variables, can be measured by four fundamental dimensions (M, L, T and Θ). According to the π theorem², the number of dimensionless

2. Which is often called the Buckingham theorem. In fact, various forms of the theorem are independently discovered by Vaschy (1892), Federmann (1911), and Riabouchinsky (1911)

TABLE A.1 – Independent variables

Symbol	Definition	Dimension
P_{1i}	Isentropic stagnation pressure at the inlet	$ML^{-1}T^{-2}$
T_{1i}	Isentropic stagnation temperature at the inlet	Θ
r	Reference dimension (outside radius of the second rotor)	L
\dot{m}	Mass flow rate	MT^{-1}
N	Rotational speed	T^{-1}
γ	Specific heat ratio	Dimensionless
μ	Dynamic viscosity of the gas	$ML^{-1}T^{-1}$
R	Gas constant	$L^2T^{-2}\Theta^{-1}$

independent variables can be reduce to 4 ($= 8 - 4$). So that four groups of dimensionless independent variables can be made: $\pi_1 = \frac{\dot{m}\sqrt{RT_{1i}}}{r^2T_{1i}}$ (dimensionless mass flow); $\pi_2 = \frac{Nr}{\sqrt{RT_{1i}}}$ (dimensionless rotational speed); $\pi_3 = \frac{\dot{m}}{\mu R}$ (dimensionless Reynolds number); $\pi_4 = \gamma$.

Besides the above independent variables, the remaining variables are dependent. They are listed in the table [A.2](#)

TABLE A.2 – Dependent variables

Symbol	Definition	Dimension
P_{2i}	Isentropic stagnation pressure at the outlet	$ML^{-1}T^{-2}$
$\eta_{i,S}$	Isentropic efficiency	Dimensionless
Δh_i	Variation of stagnation enthalpy	L^2T^{-2}
P_i	Power	ML^2T^{-3}

By applying the π theorem, the following four dimensionless groups are obtained: $\pi_5 = \frac{P_{2i}}{P_{1i}}$ (Pressure ratio); $\pi_6 = \eta$ (efficiency); $\pi_7 = \frac{\Delta T_i}{T_{1i}}$ (dimensionless enthalpy); $\pi_8 = \frac{P_{o_i}}{r^2 P_{1i} \sqrt{RT_{1i}}}$ (dimensionless power).

Two turbomachines are geometrically similar when it can get one from the other by multiplying all the linear dimensions by a same factor k called geometric similarity coefficient. All similar turbomachines form a family characterized by consistency:

- All the linear dimension ratios to a reference length that it chose equal to the outside radius of the rotor r ;
- Homologous angles, in particular angles defining the position of the blades, both fixed and mobile.

Consequently, the turbomachinery of a given family is entirely determined if only one linear dimension is identified. Let us take two compressors of the same type (i.e. geometrically similar) α and β . They deliver a compressible fluid of the same γ . Let us take two operating points where they have a similar velocity triangle (figure [A.10\[69\]](#)). Generally, the positions of these points are indifferent to the characteristic curves of the compressors. Clearly, these can be points far from the nominal point. Either:

- The geometric similarity coefficient k : $(r)_{\beta} = k \cdot (r)_{\alpha}$;
- The ratio of two velocity c : $(U_2)_{\beta} = c \cdot (U_2)_{\alpha}$.

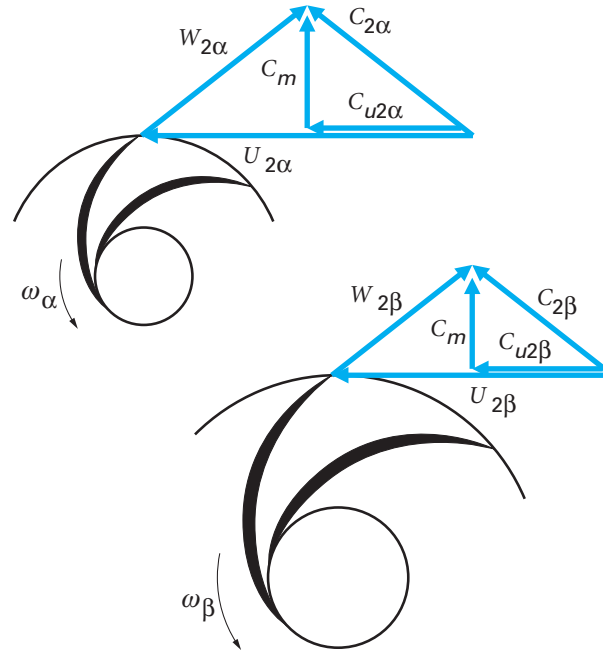


FIGURE A.10 – Similar velocity triangles of two turbomachines of the same family

Pressure coefficient

According to the velocity relation of two turbomachines:

$$(U_2)_\beta = c \cdot (U_2)_\alpha \quad \text{and} \quad (C_{u2})_\beta = c \cdot (C_{u2})_\alpha \quad (\text{A.28})$$

So that:

$$(U_2)_\beta (C_{u2})_\beta = c^2 \cdot (U_2)_\alpha (C_{u2})_\alpha \quad (\text{A.29})$$

On the other hand, the following relation is given:

$$(U_2)_\beta = c^2 \cdot (U_2)_\alpha \quad (\text{A.30})$$

The pressure coefficient is calculated by:

$$\left\{ \frac{U_2 C_{u2}}{(U_2)^2} \right\}_\beta = \left\{ \frac{U_2 C_{u2}}{(U_2)^2} \right\}_\alpha \quad (\text{A.31})$$

Variation of non-dimensional enthalpy

According to the first thermodynamics law in adiabatic turbomachinery:

$$\Delta h_i = U_2 C_{u2} \quad (\text{A.32})$$

From the relation of equation (A.31), the following equation is got:

$$\left\{ \frac{\Delta h_i}{(U_2)^2} \right\}_\beta = \left\{ \frac{\Delta h_i}{(U_2)^2} \right\}_\alpha \quad (\text{A.33})$$

$$\frac{(\Delta h_i)_\beta}{(\Delta h_i)_\alpha} = \frac{(U_1)_\beta}{(U_1)_\alpha} = c^2$$

In all homologous points, and therefore especially at the aspiration, the Mach numbers must be equal. The velocity triangles being similar, as a result between the blade having

the speeds U and speed of sound a at two similarities, the following equation can be got:

$$\left\{ \frac{U_1}{a_1} \right\}_\beta = \left\{ \frac{U_1}{a_1} \right\}_\alpha \quad (\text{A.34})$$

therefore:

$$\left\{ \frac{U_1}{\sqrt{RT_1}} \right\}_\beta = \left\{ \frac{U_1}{\sqrt{RT_1}} \right\}_\alpha \quad (\text{A.35})$$

With $(T_1)_\beta$ and $(T_1)_\alpha$ the static temperatures.

It knows that between static temperatures and isentropic stagnation temperatures. A general relationship can be obtained:

$$\frac{T_i}{T} = 1 + \frac{\gamma - 1}{2} M^2 \quad (\text{A.36})$$

Moreover, γ and M are constant during the similarity, so:

$$\left\{ \frac{T_{1i}}{T_1} \right\}_\beta = \left\{ \frac{T_{1i}}{T_1} \right\}_\alpha \quad (\text{A.37})$$

From the relation of the equation (A.35), the following relation can get:

$$\frac{(RT_1)_\beta}{(RT_1)_\alpha} = \frac{(U_1^2)_\beta}{(U_1^2)_\alpha} = c^2 \quad (\text{A.38})$$

By Combining equation (A.33) and equation (A.38) the following relation is obtained:

$$\frac{(\Delta h_i)_\beta}{(\Delta h_i)_\alpha} = c^2 = \frac{(RT_{1i})_\beta}{(RT_{1i})_\alpha} \quad (\text{A.39})$$

So that, the dimensionless enthalpy variation can be obtained:

$$\left\{ \frac{\Delta h_i}{RT_1} \right\}_\beta = \left\{ \frac{\Delta h_i}{RT_1} \right\}_\alpha \quad (\text{A.40})$$

The equation (A.40) can be written into:

$$\left\{ \frac{\Delta T_i}{T_{1i}} \right\}_\beta = \left\{ \frac{\Delta T_i}{T_{1i}} \right\}_\alpha \quad (\text{A.41})$$

Non-dimensional rotation speed

Due to the similarity of the velocity of the two compressors, the following relation can be obtained:

$$\frac{(U_1)_\beta}{(U_1)_\alpha} = \frac{(\sqrt{RT_{1i}})_\beta}{\sqrt{RT_{1i\alpha}}} = c = \frac{(U_2)_\beta}{(U_2)_\alpha} \quad (\text{A.42})$$

Besides that:

$$\frac{(U_2)_\beta}{(U_2)_\alpha} = \frac{(rN)_\beta}{(rN)_\alpha} = c \quad (\text{A.43})$$

From equations (A.42) and (A.43) the non-dimensional rotation speed can be written as:

$$\left\{ \frac{rN}{\sqrt{RT_{1i}}} \right\}_\beta = \left\{ \frac{rN}{\sqrt{RT_{1i}}} \right\}_\alpha \quad (\text{A.44})$$

Efficiency

The Reynolds number and the Mach number are equal, and the velocity triangle is similar. In addition, the shaft power is proportional to U^2 so both compressors have the same efficiency. So:

$$(\eta_{i,S})_{\beta} = (\eta_{i,S})_{\alpha} \quad (\text{A.45})$$

Similar to polytropic efficiency:

$$(\eta_{i,P})_{\beta} = (\eta_{i,P})_{\alpha} \quad (\text{A.46})$$

Pressure ratio

A relationship between the inlet and outlet pressures can be obtained as:

$$\frac{P_{2i}}{P_{1i}} = \left(1 + \eta_{i,P} \frac{\Delta T_i}{T_{1i}}\right)^{\frac{\gamma}{\gamma-1}} \quad (\text{A.47})$$

Because γ is constant and from equation (A.45), equation (A.41) the expression of equation (A.47) can be written:

$$\left\{ \left(1 + \eta_{i,P} \frac{\Delta T_i}{T_{1i}}\right)^{\frac{\gamma}{\gamma-1}} \right\}_{\beta} = \left\{ \left(1 + \eta_{i,P} \frac{\Delta T_i}{T_{1i}}\right)^{\frac{\gamma}{\gamma-1}} \right\}_{\alpha} \quad (\text{A.48})$$

In addition, $\frac{P_{2i}}{P_{1i}}$ is constant so that two turbomachines have the same pressure ratio during similarity.

Non-dimensional mass flow rate

The mass flow rate \dot{m} is equal to the product of ρSC . It can be considered two homologous points:

$$\left\{ \begin{array}{l} (\dot{m})_{\beta} \\ (\dot{m})_{\alpha} \end{array} \right\} = \left\{ \begin{array}{l} (\rho_1 S_1 C_1)_{\beta} \\ (\rho_1 S_1 C_1)_{\alpha} \end{array} \right\} \quad (\text{A.49})$$

Because of perfect gas, $\frac{P}{\rho} = RT$, so:

$$\left\{ \begin{array}{l} (\dot{m}RT_1) \\ (\rho_1 S_1 C_1) \end{array} \right\}_{\beta} = \left\{ \begin{array}{l} (\dot{m}RT_1)_{\beta} \\ (\rho_1 S_1 C_1)_{\alpha} \end{array} \right\}_{\alpha} \quad (\text{A.50})$$

The geometry similarity gives:

$$\frac{(S_1)_{\beta}}{(S_1)_{\alpha}} = k^2 = \frac{(r^2)_{\beta}}{(r^2)_{\alpha}} \quad (\text{A.51})$$

The equality of the Mach numbers gives:

$$\frac{(C_1)_{\beta}}{(C_1)_{\alpha}} = \frac{(a_1)_{\beta}}{(a_1)_{\alpha}} = \frac{(\sqrt{RT_1})_{\beta}}{(\sqrt{RT_1})_{\alpha}} \quad (\text{A.52})$$

Therefore, the two properties translate to equality:

$$\left\{ \frac{\dot{m}\sqrt{RT_1}}{P_1 r^2} \right\}_{\beta} = \left\{ \frac{\dot{m}\sqrt{RT_1}}{P_1 r^2} \right\}_{\alpha} \quad (\text{A.53})$$

From equation (A.37), the equation (A.53) becomes:

$$\left\{ \frac{\dot{m}\sqrt{RT_{1i}}}{P_{1i} r^2} \right\}_{\beta} = \left\{ \frac{\dot{m}\sqrt{RT_{1i}}}{P_{1i} r^2} \right\}_{\alpha} \quad (\text{A.54})$$

Non-dimensional characteristics

It can be written the expression of general operation of a turbomachinery as:

$$\frac{P_{2i}}{P_{1i}}, \quad \frac{\Delta T_i}{T_{1i}}, \quad \eta, \quad \frac{P_{0i}}{r^2 P_{1i} \sqrt{RT_{1i}}} = f_{1,2\dots} \left(\frac{\dot{m} \sqrt{RT_{1i}}}{P_{1i} r^2}; \quad \frac{Nr}{\sqrt{RT_{1i}}}; \quad \frac{\dot{m}}{\mu r}; \quad \gamma \right) \quad (\text{A.55})$$

In most cases, the similarity is used for a constant γ gas from the characteristics of given turbomachinery (homothetic ratio $k = 1$). In this case, it can be removed some variables such as the size of the compressor as well as the characteristics of the fluid to form non-dimensional variables:

$$\frac{P_{2i}}{P_{1i}}, \quad \frac{\Delta T_i}{T_{1i}}, \quad \eta, \quad \frac{P_{0i}}{P_{1i} \sqrt{T_{1i}}} = f_{1,2\dots} \left(\frac{\dot{m} \sqrt{T_{1i}}}{P_{1i}}; \quad \frac{N}{\sqrt{T_{1i}}}; \quad Re \right) \quad (\text{A.56})$$

A.3 Instability control method

A.3.1 Instability control at the speed of $N_2 = 10,000rpm$

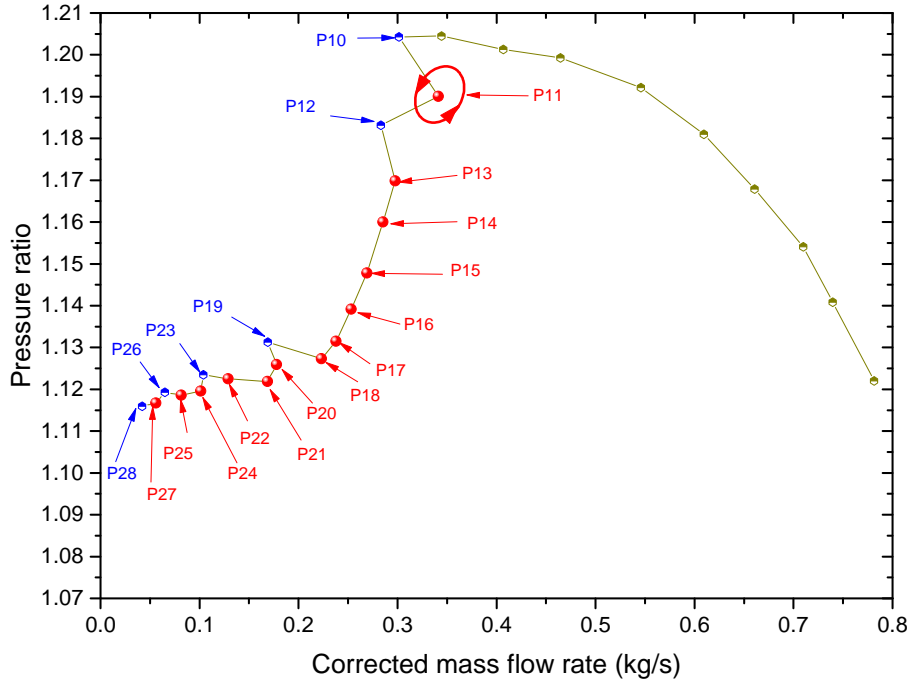


FIGURE A.11 – Controlling the stability limit points to enlarge the operating range of CRCC with $N_2 = 10,000rpm$ by varying the first rotor speed (N_1)

Fig. A.11 shows the characteristic curves of CRCC for $N_2 = 10,000rpm$ with a speed ratio of $\theta_7 = -1.3$. The blue points indicate that the compressor works stably, while the red points represent instability state. The pressure fluctuations in the system at unstable points (the red points) show that its amplitude depends on the pressure rise. The FFT transforms of the pressure signals (as shown in fig. A.12 - fig. A.30) illustrate that the pressure fluctuation frequency is always maintained at $2Hz$. The harmonic frequencies are also clearly observed as at the speed of $N_2 = 9,000rpm$. Fig. A.31 depicts the characteristic curves of CRCC with different speed ratios in comparison with the SRCC. The variable speed of the first rotor for suppressing the instability phenomenon is also shown in fig. A.32.

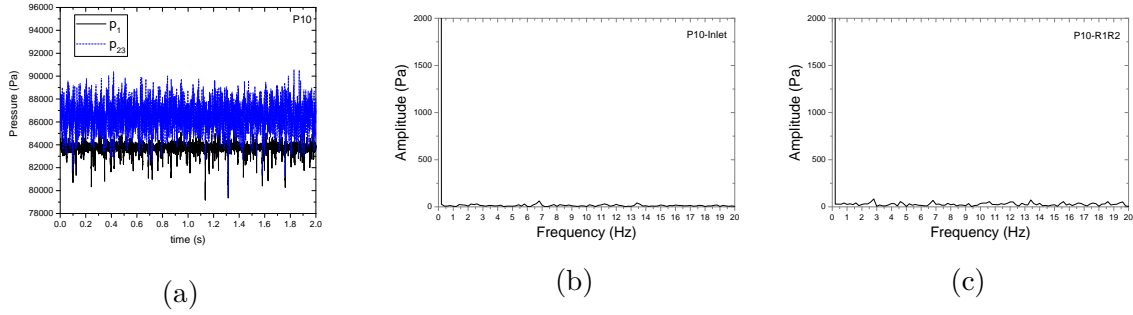


FIGURE A.12 – The pressure signals (a) and its FFT analysis at the inlet (b) and between two rotors (c) of the point **P10** with $N_1 = -13,000rpm$ and $N_2 = 10,000rpm$

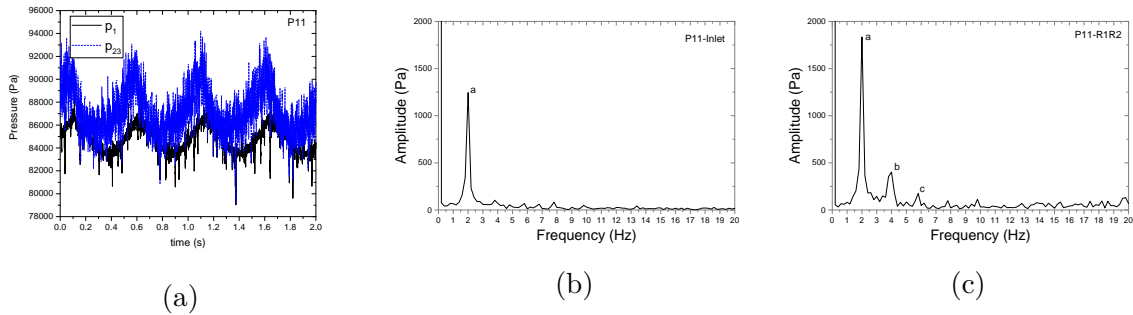


FIGURE A.13 – The pressure signals (a) and its FFT analysis at the inlet (b) and between two rotors (c) of the point **P11** with $N_1 = -13,000rpm$ and $N_2 = 10,000rpm$

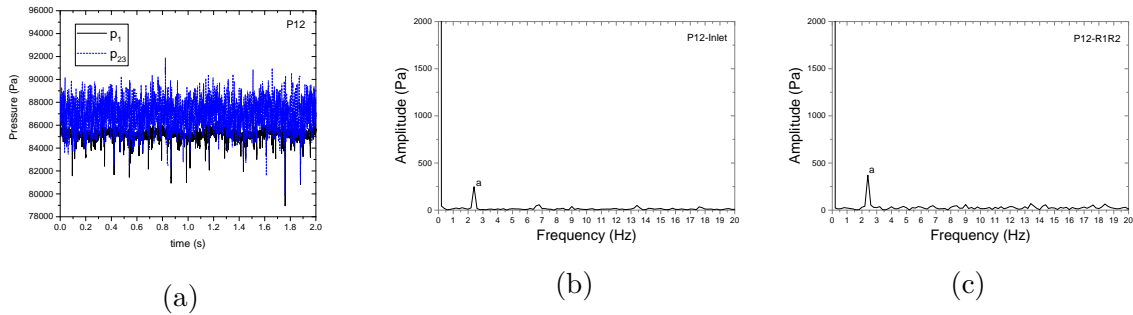


FIGURE A.14 – The pressure signals (a) and its FFT analysis at the inlet (b) and between two rotors (c) of the point **P12** with $N_1 = -11,200rpm$ and $N_2 = 10,000rpm$

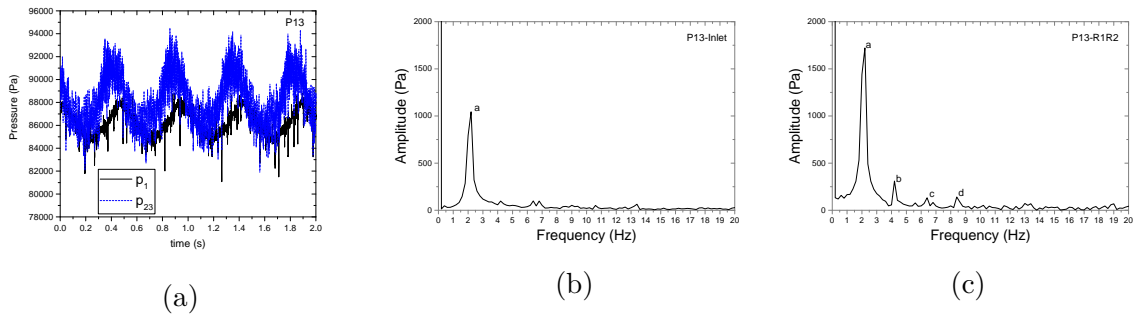


FIGURE A.15 – The pressure signals (a) and its FFT analysis at the inlet (b) and between two rotors (c) of the point **P13** with $N_1 = -11,200rpm$ and $N_2 = 10,000rpm$

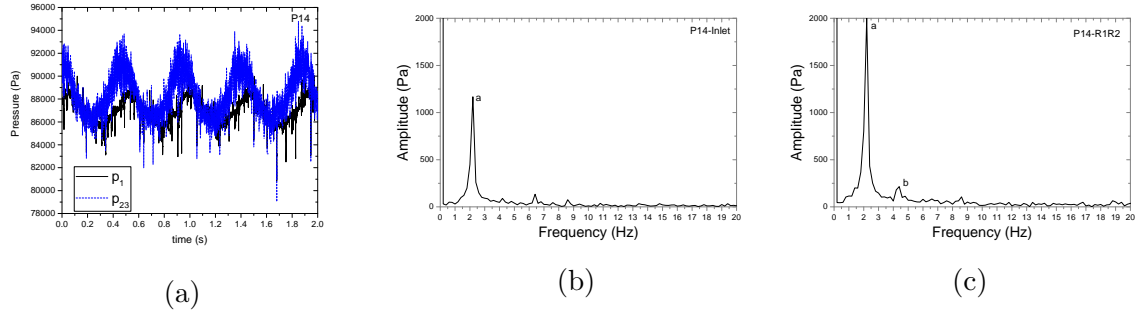


FIGURE A.16 – The pressure signals (a) and its FFT analysis at the inlet (b) and between two rotors (c) of the point **P14** with $N_1 = -10,000rpm$ and $N_2 = 10,000rpm$

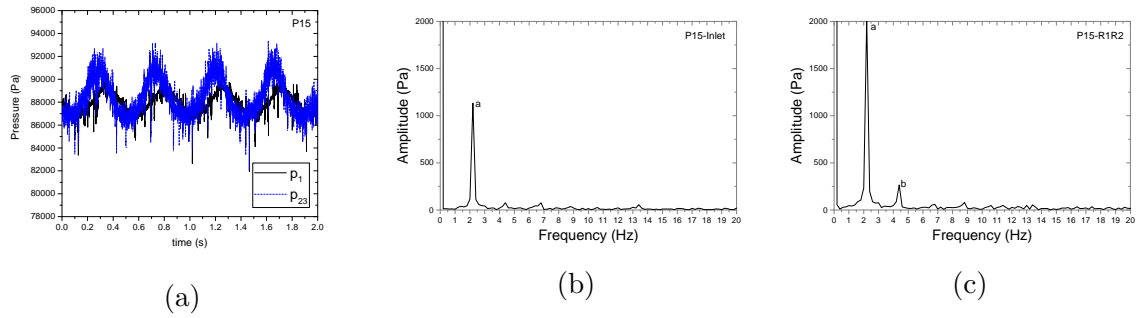


FIGURE A.17 – The pressure signals (a) and its FFT analysis at the inlet (b) and between two rotors (c) of the point **P15** with $N_1 = -8,200rpm$ and $N_2 = 10,000rpm$

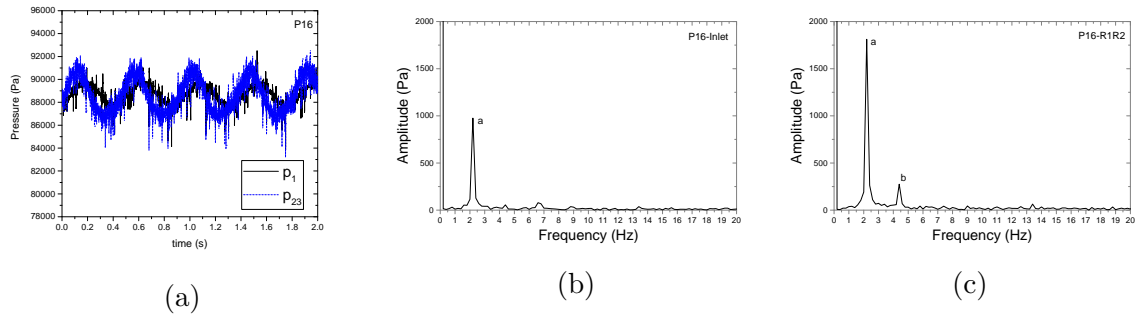


FIGURE A.18 – The pressure signals (a) and its FFT analysis at the inlet (b) and between two rotors (c) of the point **P16** with $N_1 = -6,400rpm$ and $N_2 = 10,000rpm$

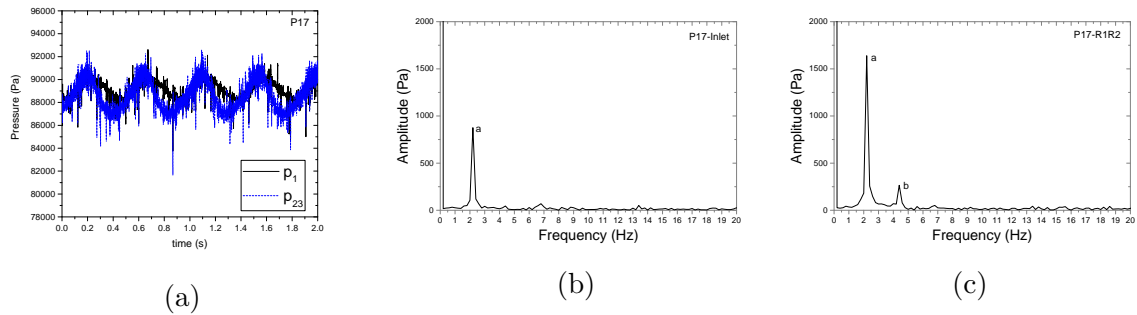


FIGURE A.19 – The pressure signals (a) and its FFT analysis at the inlet (b) and between two rotors (c) of the point **P17** with $N_1 = -4,600rpm$ and $N_2 = 10,000rpm$

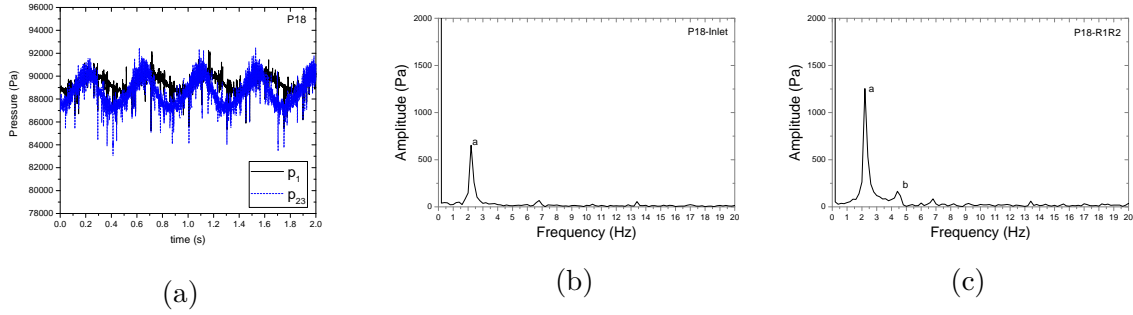


FIGURE A.20 – The pressure signals (a) and its FFT analysis at the inlet (b) and between two rotors (c) of the point **P18** with $N_1 = -2,800rpm$ and $N_2 = 10,000rpm$

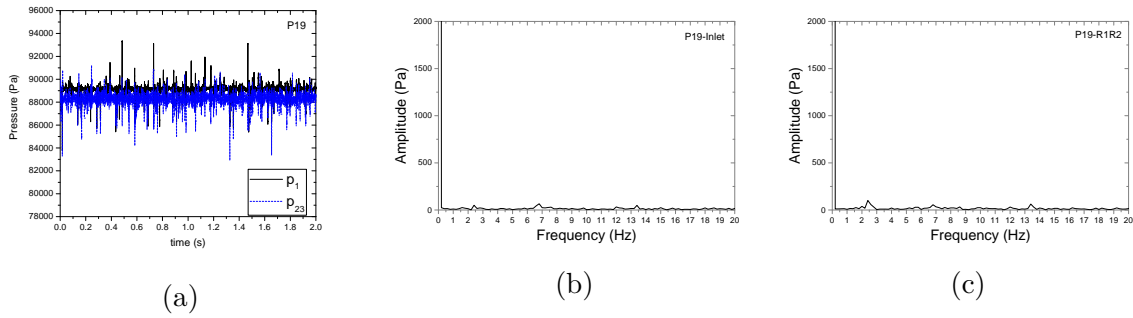


FIGURE A.21 – The pressure signals (a) and its FFT analysis at the inlet (b) and between two rotors (c) of the point **P19** with $N_1 = -2,200rpm$ and $N_2 = 10,000rpm$

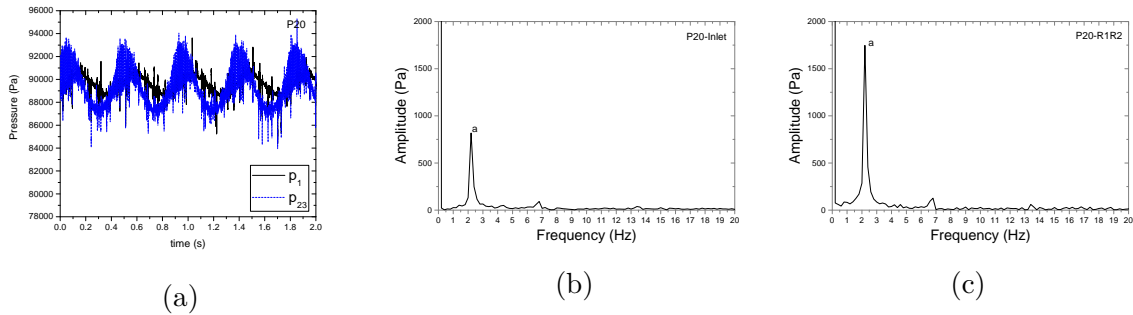


FIGURE A.22 – The pressure signals (a) and its FFT analysis at the inlet (b) and between two rotors (c) of the point **P20** with $N_1 = -2,200rpm$ and $N_2 = 10,000rpm$

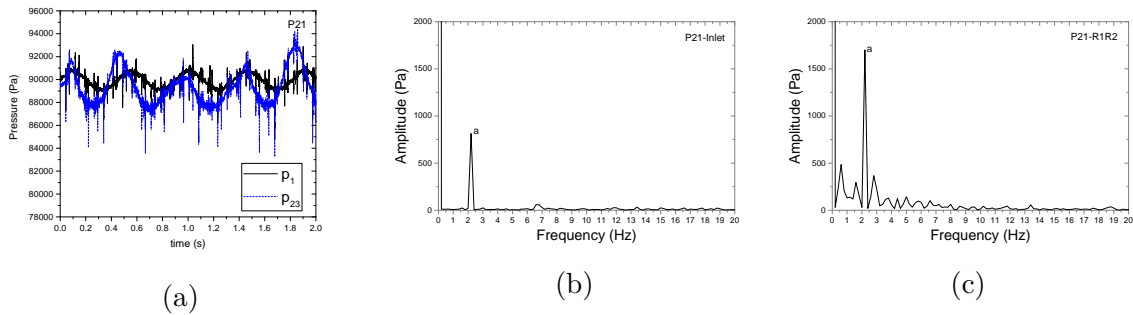


FIGURE A.23 – The pressure signals (a) and its FFT analysis at the inlet (b) and between two rotors (c) of the point **P21** with $N_1 = 0rpm$ and $N_2 = 10,000rpm$

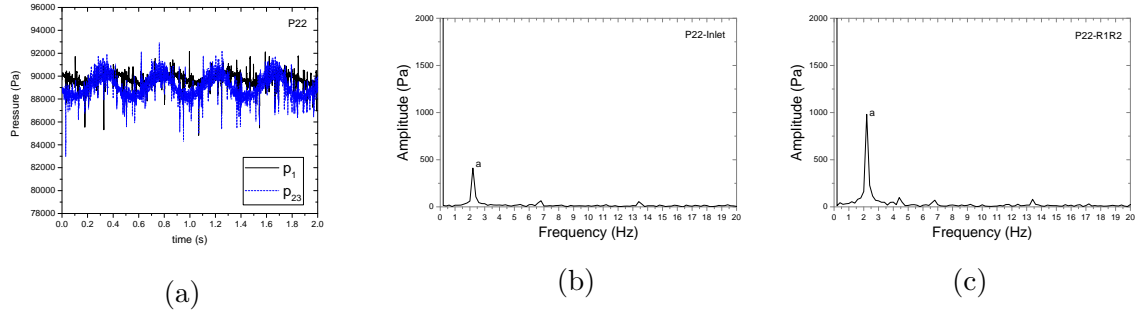


FIGURE A.24 – The pressure signals (a) and its FFT analysis at the inlet (b) and between two rotors (c) of the point **P22** with $N_1 = 1,400rpm$ and $N_2 = 10,000rpm$

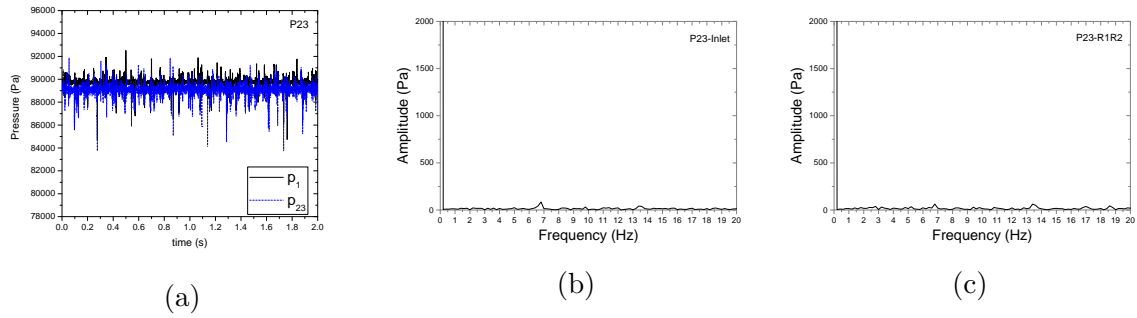


FIGURE A.25 – The pressure signals (a) and its FFT analysis at the inlet (b) and between two rotors (c) of the point **P23** with $N_1 = 2,660rpm$ and $N_2 = 10,000rpm$

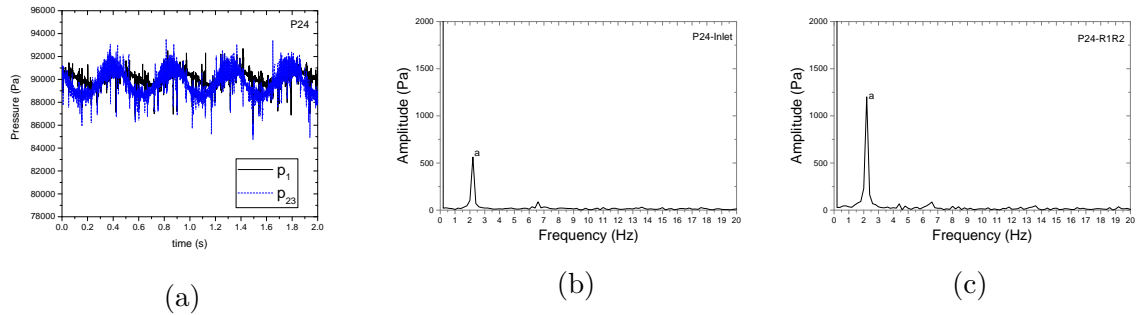


FIGURE A.26 – The pressure signals (a) and its FFT analysis at the inlet (b) and between two rotors (c) of the point **P24** with $N_1 = 2,660rpm$ and $N_2 = 10,000rpm$

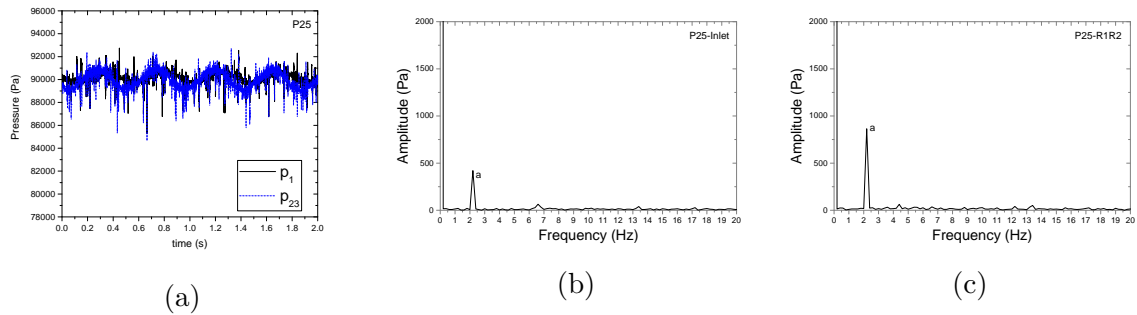


FIGURE A.27 – The pressure signals (a) and its FFT analysis at the inlet (b) and between two rotors (c) of the point **P25** with $N_1 = 4,460rpm$ and $N_2 = 10,000rpm$

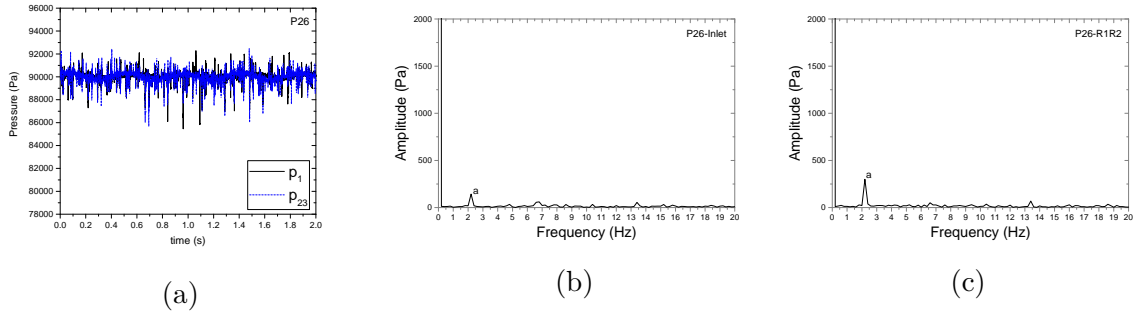


FIGURE A.28 – The pressure signals (a) and its FFT analysis at the inlet (b) and between two rotors (c) of the point **P26** with $N_1 = 5,240rpm$ and $N_2 = 10,000rpm$

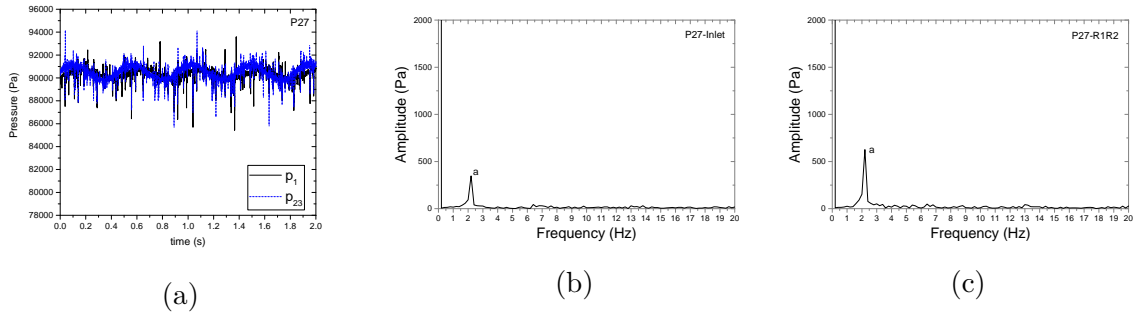


FIGURE A.29 – The pressure signals (a) and its FFT analysis at the inlet (b) and between two rotors (c) of the point **P27** with $N_1 = 5,240rpm$ and $N_2 = 10,000rpm$

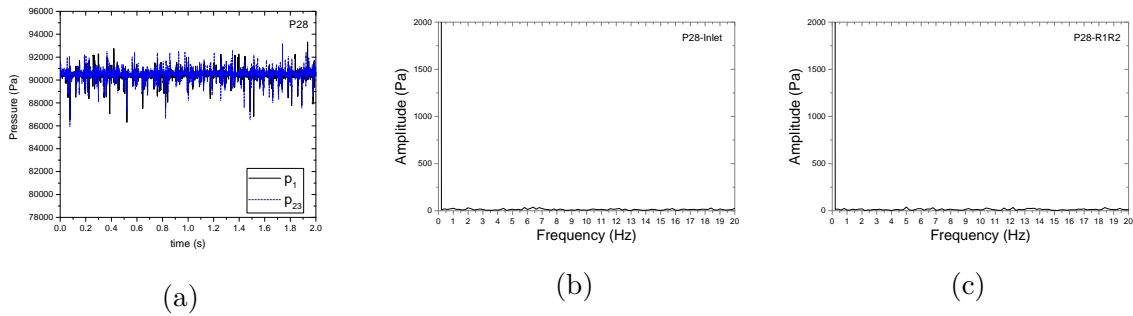


FIGURE A.30 – The pressure signals (a) and its FFT analysis at the inlet (b) and between two rotors (c) of the point **P28** with $N_1 = 6,260rpm$ and $N_2 = 10,000rpm$

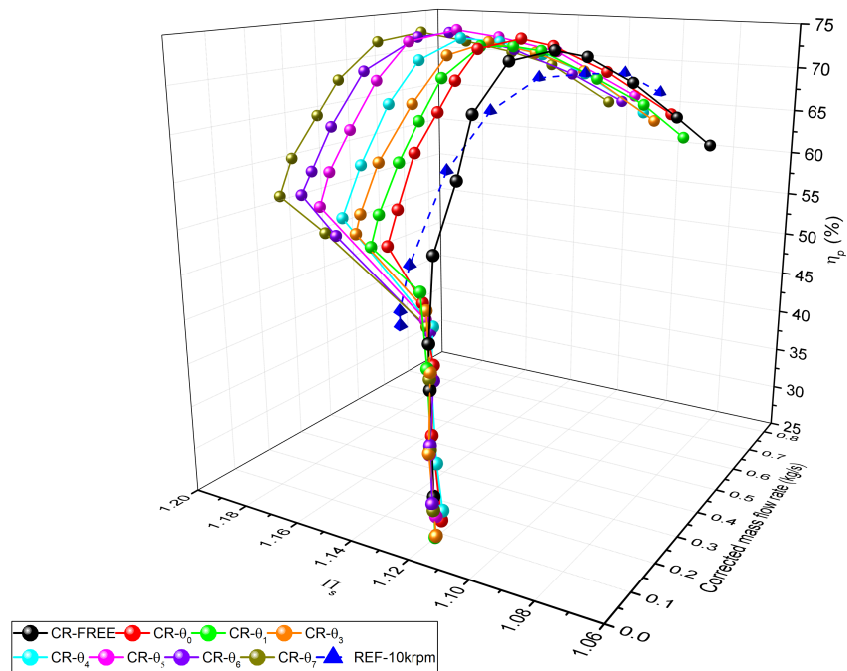


FIGURE A.31 – Characteristic curves of CRCC at different speed ratios without the unstable working points by reducing the rotation speed of the first rotor while the second rotor speed is fixed at $N_2 = 10,000rpm$ compared to the characteristic curve of SRCC at $10,000rpm$ (REF-10krpm)

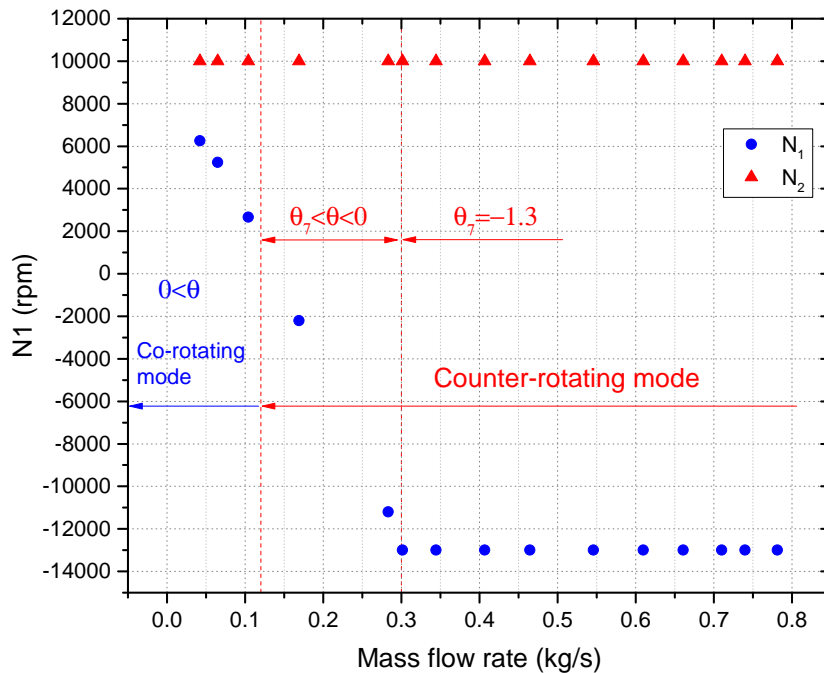


FIGURE A.32 – The variation of the first rotor speed for suppressing the instability phenomenon at the speed of $N_2 = 10,000rpm$

A.3.2 Instability control at the speed of $N_2 = 11,000rpm$

Fig. A.33 shows the characteristic curves of CRCC for $N_2 = 11,000rpm$ with a speed ratio of $\theta_7 = -1.3$. The blue points indicate that the compressor works stably, while the red points represent instability state. Like other speeds, the FFT transform of the pressure signals at the unstable points (the red points) shows that the frequency of the pressure signal always remains at 2Hz. To eliminate the instability phenomenon, the reduction of the rotation speed of the first rotor is carried out and is shown in fig. A.50. The characteristics of the compressor with different speed ratios after eliminating instability are also shown in fig. A.49. It is easy to see that all curves are the same at the improved region because of the same speed as the second rotor at $11,000rpm$.

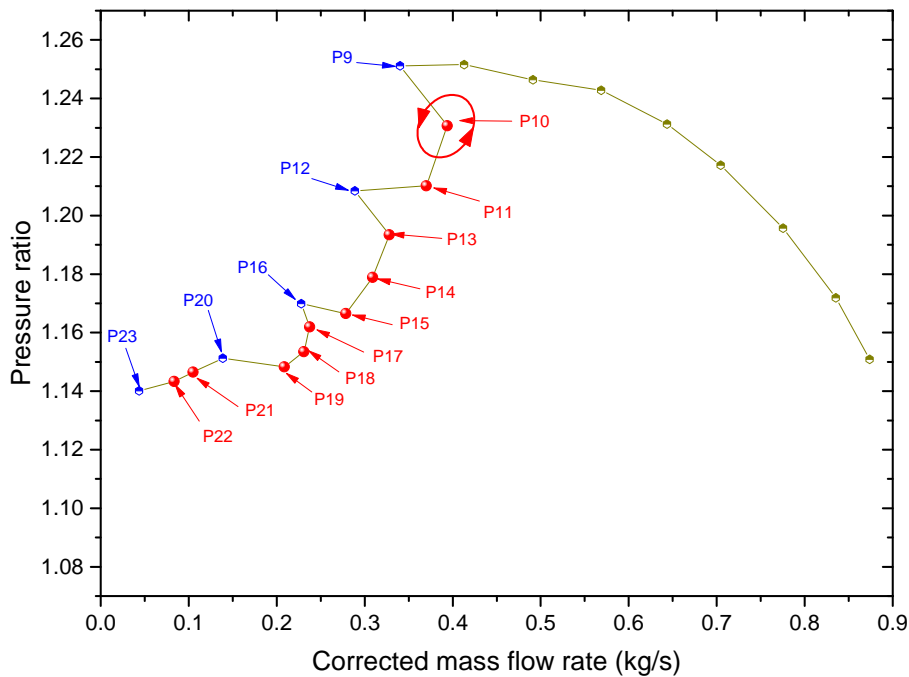


FIGURE A.33 – Controlling the instability limit points to enlarge the operating range of CRCC with $N_2 = 11,000rpm$ by varying the first rotor speed (N_1)

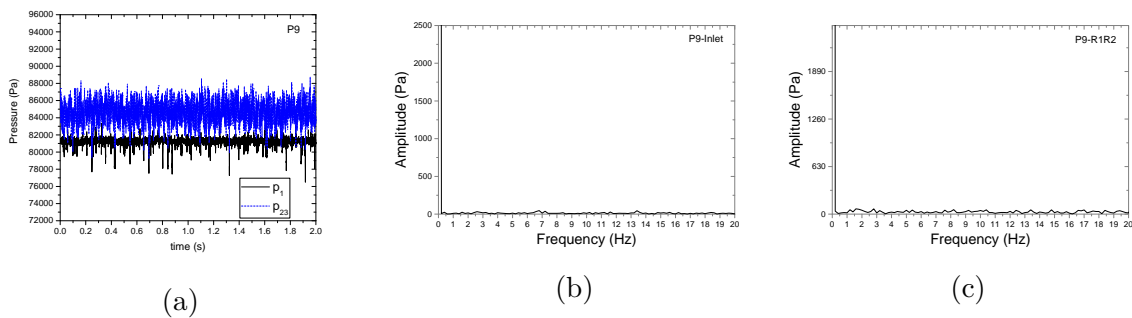


FIGURE A.34 – The pressure signals (a) and its FFT analysis at the inlet (b) and between two rotors (c) of the point **P9** with $N_1 = -14,300rpm$ and $N_2 = 11,000rpm$

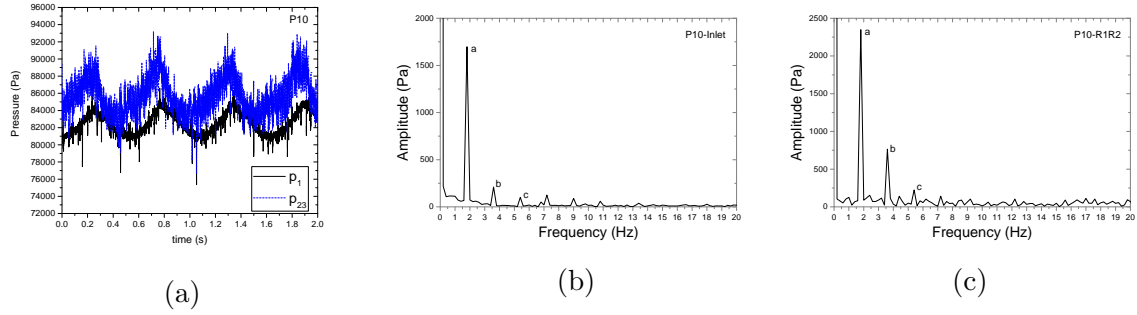


FIGURE A.35 – The pressure signals (a) and its FFT analysis at the inlet (b) and between two rotors (c) of the point **P10** with $N_1 = -14,300rpm$ and $N_2 = 11,000rpm$

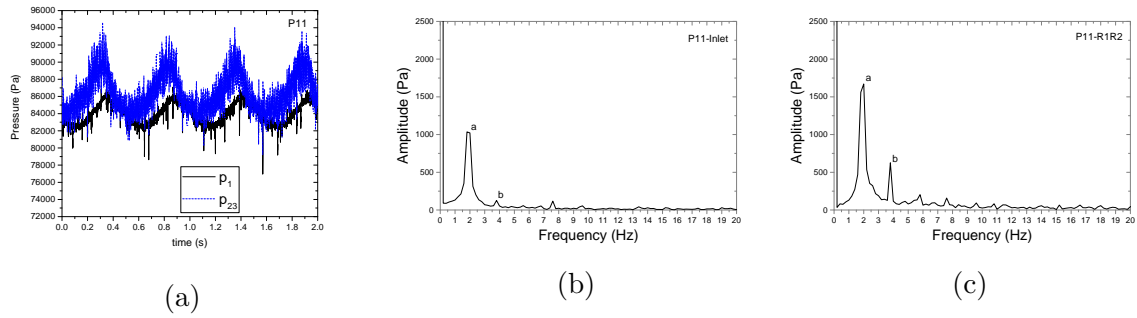


FIGURE A.36 – The pressure signals (a) and its FFT analysis at the inlet (b) and between two rotors (c) of the point **P11** with $N_1 = -12,500rpm$ and $N_2 = 11,000rpm$

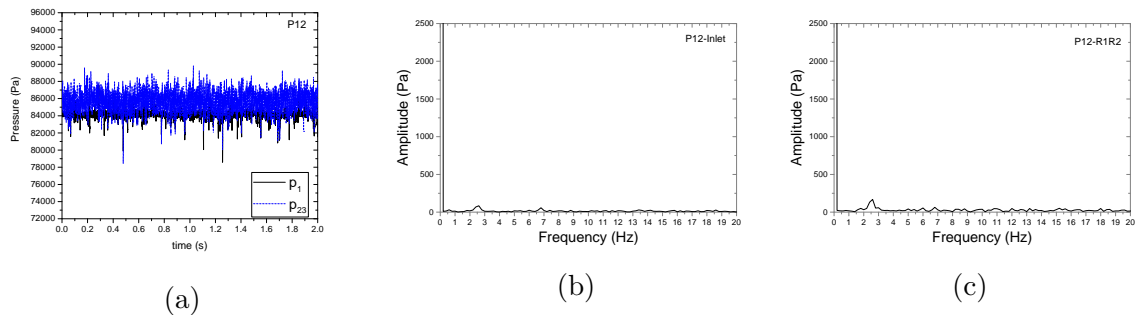


FIGURE A.37 – The pressure signals (a) and its FFT analysis at the inlet (b) and between two rotors (c) of the point **P12** with $N_1 = -10,640rpm$ and $N_2 = 11,000rpm$

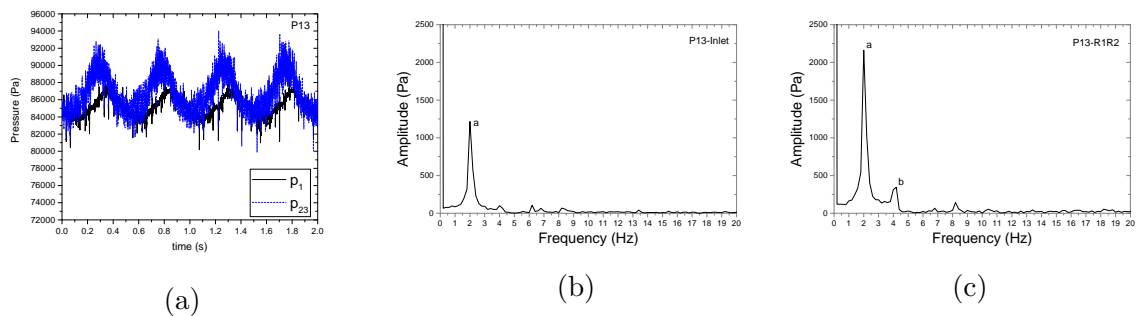


FIGURE A.38 – The pressure signals (a) and its FFT analysis at the inlet (b) and between two rotors (c) of the point **P13** with $N_1 = -10,640rpm$ and $N_2 = 11,000rpm$

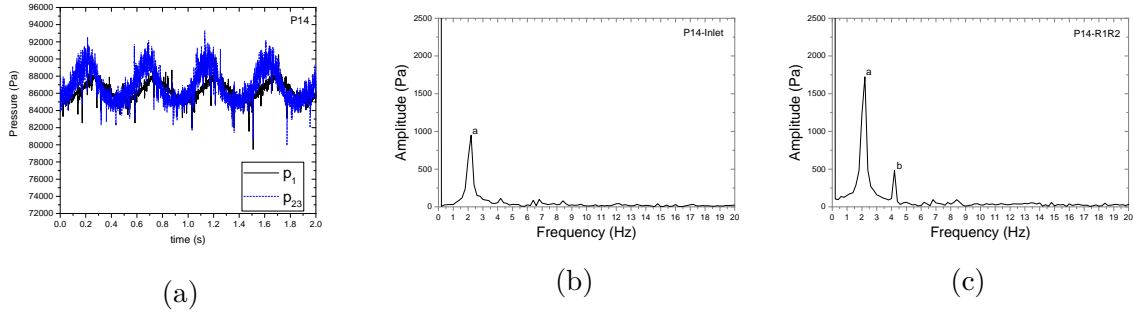


FIGURE A.39 – The pressure signals (a) and its FFT analysis at the inlet (b) and between two rotors (c) of the point **P14** with $N_1 = -8,660rpm$ and $N_2 = 11,000rpm$

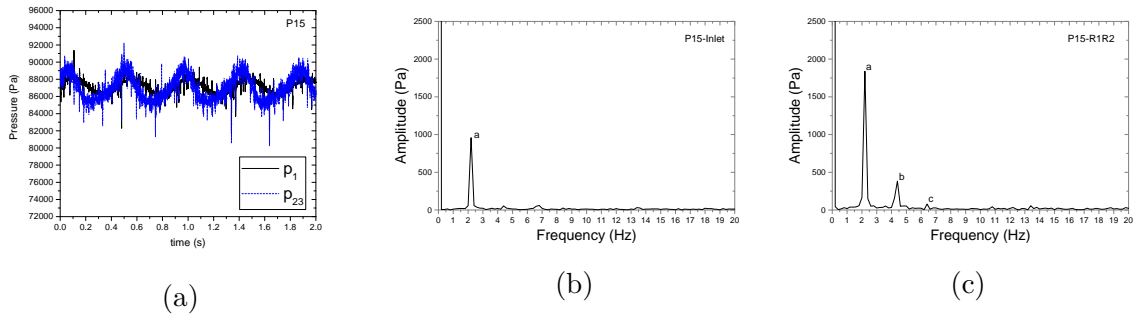


FIGURE A.40 – The pressure signals (a) and its FFT analysis at the inlet (b) and between two rotors (c) of the point **P15** with $N_1 = -6,140rpm$ and $N_2 = 11,000rpm$

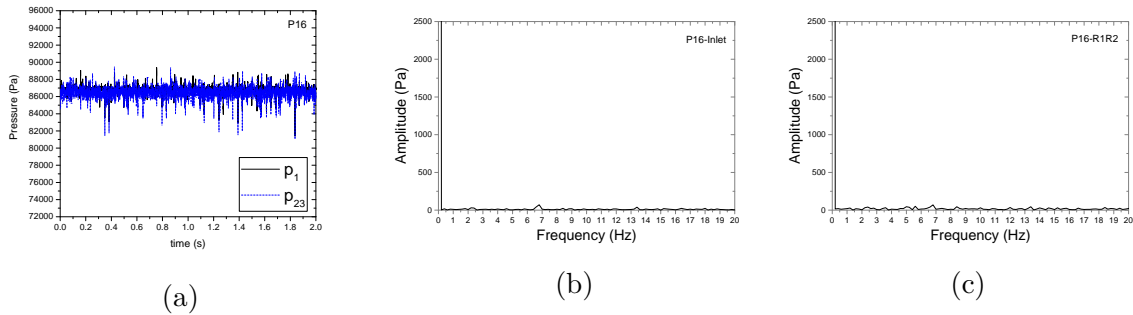


FIGURE A.41 – The pressure signals (a) and its FFT analysis at the inlet (b) and between two rotors (c) of the point **P16** with $N_1 = -5,120rpm$ and $N_2 = 11,000rpm$

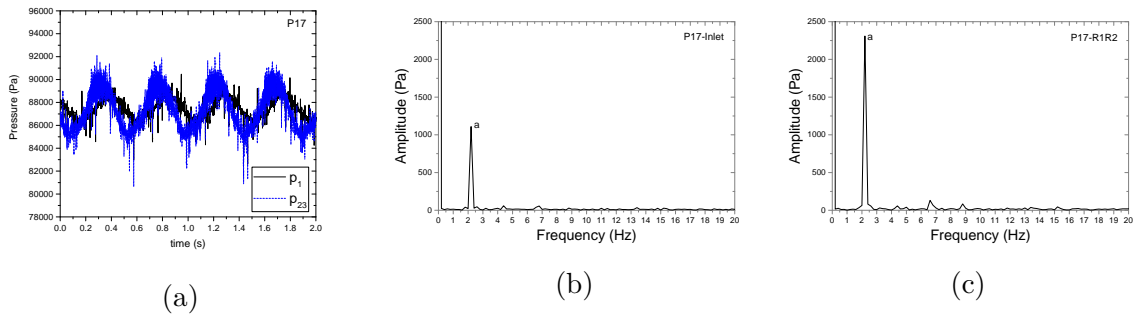


FIGURE A.42 – The pressure signals (a) and its FFT analysis at the inlet (b) and between two rotors (c) of the point **P17** with $N_1 = -5,120rpm$ and $N_2 = 11,000rpm$

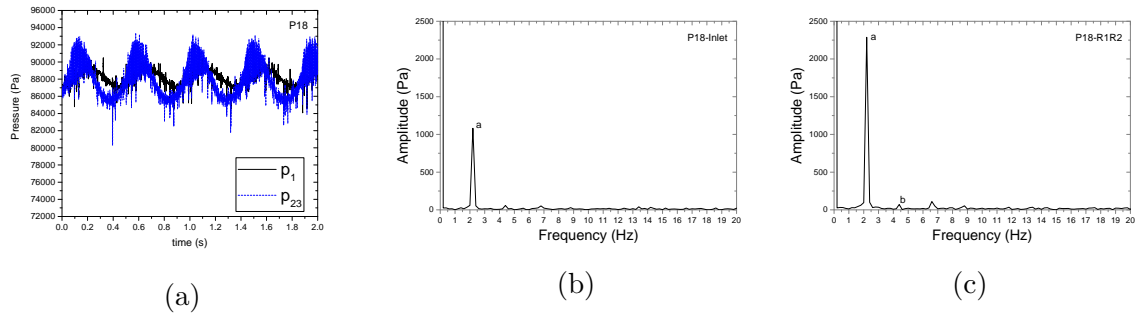


FIGURE A.43 – The pressure signals (a) and its FFT analysis at the inlet (b) and between two rotors (c) of the point **P18** with $N_1 = -2,720rpm$ and $N_2 = 11,000rpm$

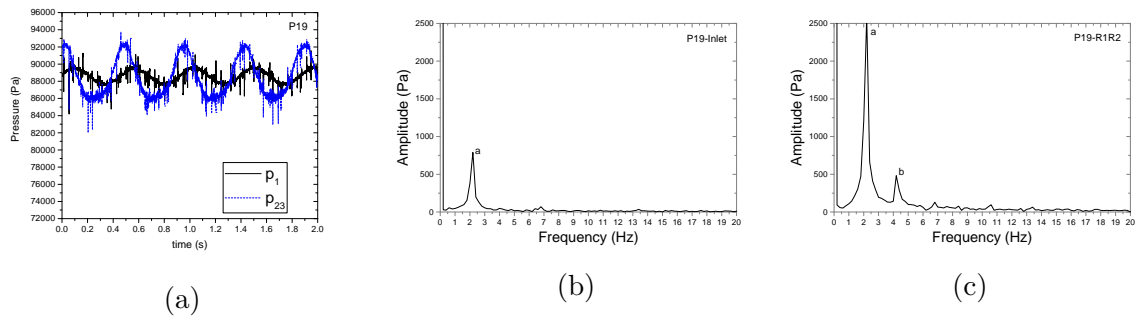


FIGURE A.44 – The pressure signals (a) and its FFT analysis at the inlet (b) and between two rotors (c) of the point **P19** with $N_1 = 0rpm$ and $N_2 = 11,000rpm$

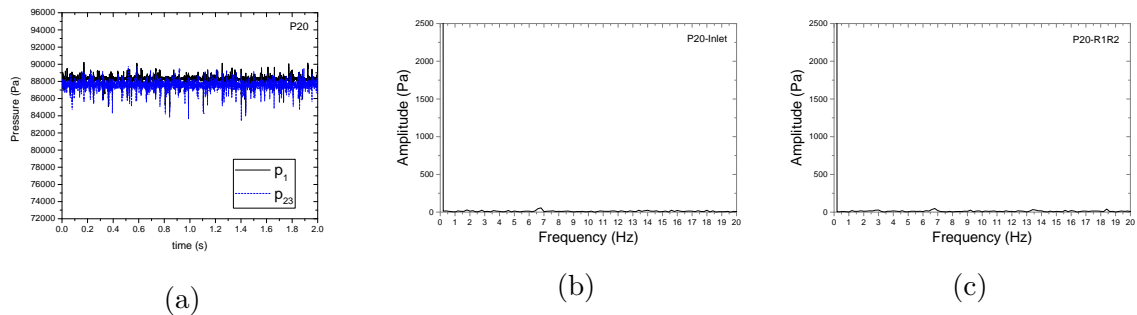


FIGURE A.45 – The pressure signals (a) and its FFT analysis at the inlet (b) and between two rotors (c) of the point **P20** with $N_1 = 2,700rpm$ and $N_2 = 11,000rpm$

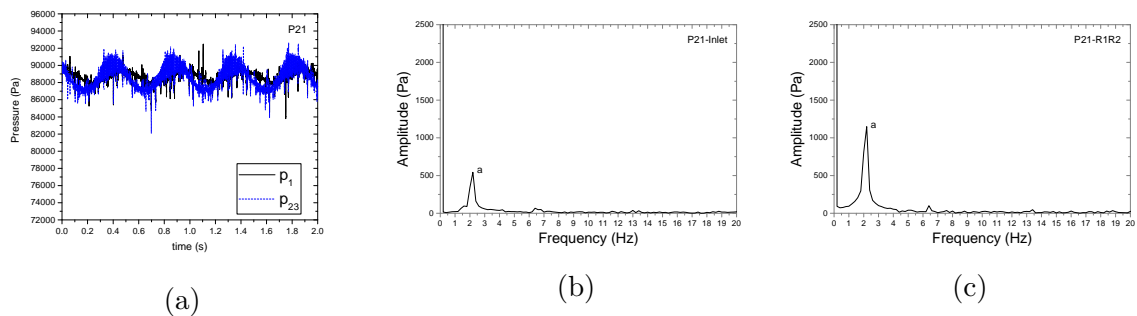


FIGURE A.46 – The pressure signals (a) and its FFT analysis at the inlet (b) and between two rotors (c) of the point **P21** with $N_1 = 2,700rpm$ and $N_2 = 11,000rpm$

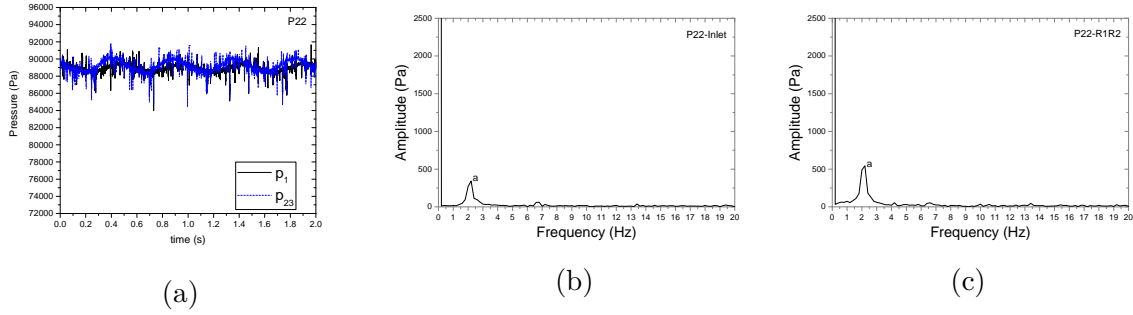


FIGURE A.47 – The pressure signals (a) and its FFT analysis at the inlet (b) and between two rotors (c) of the point **P22** with $N_1 = 6,420rpm$ and $N_2 = 11,000rpm$

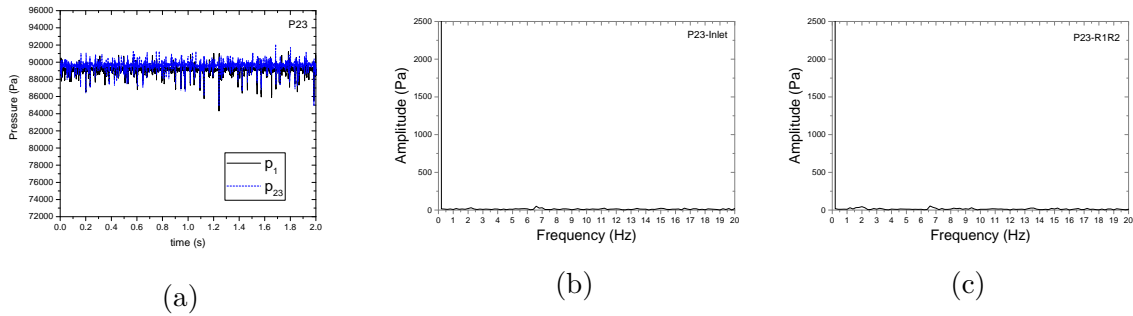


FIGURE A.48 – The pressure signals (a) and its FFT analysis at the inlet (b) and between two rotors (c) of the point **P23** with $N_1 = 7,080rpm$ and $N_2 = 11,000rpm$

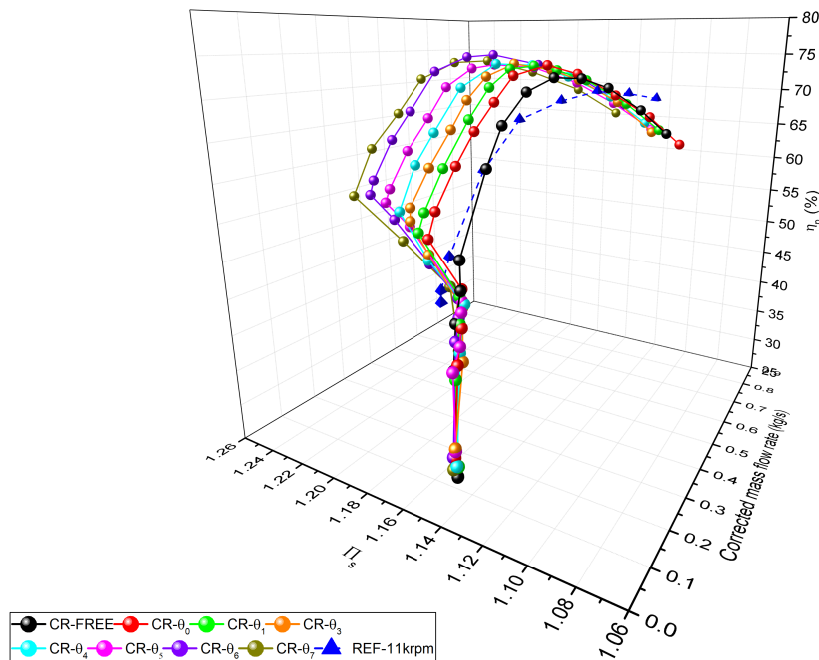


FIGURE A.49 – Characteristic curves of **CRCC** at different speed ratios without the unstable working points by reducing the rotation speed of the first rotor while the second rotor speed is fixed at $N_2 = 11,000rpm$ compared to the characteristic curve of **SRCC** at $11,000rpm$ (REF-11krpm)

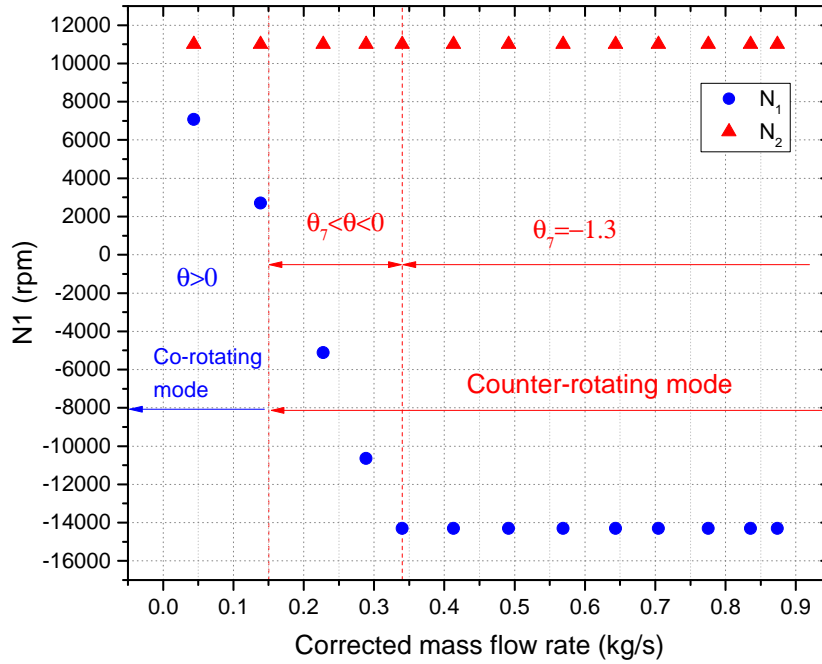


FIGURE A.50 – The variation of the first rotor speed for suppressing the instability phenomenon at the speed of $N_2 = 11,000rpm$

A.4 Numerical simulation

A.4.1 Governing equations

The fluid flow is governed fundamentally by the conservation of mass, momentum, and energy, together with the second law equation if the flow is non-isentropic.

Conservation of mass equation

This equation gives the rate of change of mass contained within a defined region of space, equal to the sum of the mass fluxes in and out of the region.

$$\frac{\partial \rho}{\partial t} + \nabla \cdot (\rho \mathbf{C}) = 0 \quad (\text{A.57})$$

where, in Cartesian coordinates, $\mathbf{C} = C_x \mathbf{i}_x + C_y \mathbf{i}_y + C_z \mathbf{i}_z$ is the velocity vector, \mathbf{i} is a unit vector and:

$$\nabla = \left(\frac{\partial}{\partial x} \right) \mathbf{i}_x + \left(\frac{\partial}{\partial y} \right) \mathbf{i}_y + \left(\frac{\partial}{\partial z} \right) \mathbf{i}_z \quad (\text{A.58})$$

In cylindrical polar coordinates, $\mathbf{C} = C_r \mathbf{i}_r + C_\theta \mathbf{i}_\theta + C_z \mathbf{i}_z$ and

$$\nabla = \left(\frac{\partial}{\partial r} \right) \mathbf{i}_r + \left(\frac{\partial}{\partial \theta} \right) \mathbf{i}_\theta + \left(\frac{\partial}{\partial z} \right) \mathbf{i}_z \quad (\text{A.59})$$

Momentum equation

The momentum equates the net flux of fluid momentum through a volume of space with the force acting on this volume. These may be body forces, caused by solid surfaces

next to the volume, pressure forces caused by the action of viscosity in the working fluid [49].

$$\frac{\partial}{\partial t}(\rho \mathbf{C}) + \rho \mathbf{C} \cdot \nabla \mathbf{C} = \rho \mathbf{B} - \nabla \mathbf{P} + \rho \mathbf{f} \quad (\text{A.60})$$

The left-hand side of the equation represents the rate of change of fluid momentum in the volume and the total momentum of fluid crossing the boundaries of the volume respectively. On the right-hand side, \mathbf{B} and \mathbf{f} are respectively the net body force and shear force per unit mass. $\nabla \mathbf{P}$ represents the pressure force. This equation is known as the Navier-Stokes equation.

The shear force term \mathbf{f} in equation A.60 can be expressed in terms of the fluid viscosity μ for laminar flow of a Newtonian fluid:

$$\rho \mathbf{f} = 2\mu \left[\nabla^2 \mathbf{C} + \frac{1}{3} \nabla (\nabla \cdot \mathbf{C}) \right] \quad (\text{A.61})$$

In principle, the Navier-stokes equation is applied to turbulent eddies as well as to laminar flows. In fact, the computational effort required tracking, even the largest eddies encountered, is far beyond present capabilities. It is necessary to resort to simplified means of application for the turbulent flows which are in practice far more commonly encountered in compressible flow turbomachines than laminar flows. In this case, the Navier-Stokes equation is averaged in time over the turbulent fluctuations, and the influence of turbulence appears as an additional shear stress term:

$$(\tau_{ij})_{turb} = -\rho \overline{c_i c_j} \quad (\text{A.62})$$

where c_i is the component of turbulent fluctuation superimposed on the mean velocity component C_i , and i, j are the two coordinate directions. The stress terms in equation (A.62) are known as the Reynolds stress. When they are added to the viscous stresses it gives:

$$\tau_{total} = \tau_{viscous} + \tau_{turb} \quad (\text{A.63})$$

This equation is known as the Reynolds averaged Navier-Stokes equation. For viscous turbomachinery flow calculations, this is the form usually used.

Energy equation

The energy of a fluid per unit mass is the sum of the specific internal energy u and the specific kinetic energy $\mathbf{C}^2/2$. The rate of change of this quantity is equal to the sum of the energy fluxes crossing the boundaries of the volume (enthalpy h to include work done on the boundary of the volume). The net transfer of heat \mathbf{Q} and the external work done on the volume by body shear force:

$$\frac{\partial}{\partial t} \left[\rho \left(u + \frac{1}{2} \mathbf{C}^2 \right) \right] + \nabla \cdot \left[\rho \left(h + \frac{1}{2} \mathbf{C}^2 \right) \mathbf{C} \right] = -\rho \mathbf{B} \cdot \mathbf{C} - \mathbf{Q} + \rho \mathbf{f} \cdot \mathbf{C} \quad (\text{A.64})$$

In practice, it is rarely necessary to use the energy equation in its full form. The flow can often be regarded as adiabatic so that the heat transfer term is eliminated. In this case, the stagnation enthalpy is constant along the streamline in the case of a stator passage, and either the relative stagnation enthalpy or enthalpy is constant along a streamline in a rotor passage. In many techniques to obtain a solution, the energy equation is reduced to a simple statement of this nature. If it can further be assumed that the stagnation or relative stagnation enthalpy is constant across the inlet to the passage, the energy equation is even simpler, and merely states that the relevant property is everywhere constant.

A.4.2 Turbulence model

Two relevant models of turbulence are commonly applied in the numerical simulation of a compressor: $k - \epsilon$ and $k - \omega$ models. Both of these models combine the turbulent kinetic energy k with a dissipation term in order to determine the turbulence eddy viscosity [70]. The $k - \epsilon$ model is developed to improve the mixing-length model and to avoid the algebraic prescription of the turbulent length scale in complex flows. The transport equations are solved for two turbulent components: the k -equation is a model of the transport equation for the turbulent kinetic energy and the ϵ -equation is a model for the dissipation rate of turbulent kinetic energy. This model gives a good result for free-shear-layer flows with relatively small pressure gradients. For all bounded flows it gives good agreement with the experimental results for zero and small mean pressure gradient, but it is less accurate for a large adverse pressure gradient. The $k - \omega$ model is developed in parallel with the $k - \epsilon$ model as an alternative to defining the eddy viscosity function. Convective transport equations are solved for the turbulent kinetic energy and its specific dissipation rate, k and ω , respectively [71]. This model is more stable than the $k - \epsilon$ model in the viscous sub-layer near the wall. In addition, it does not require explicit wall-damping functions as the $k - \epsilon$ and the other two-equation models do because of the large values of ω in the wall region. In the logarithmic region, it gives good agreement with experimental results for mild adverse pressure gradient flows and sensitive to small free-stream values of ω . Because of the problem of sensitivity to free-stream condition, Menter [72] recognized that the ϵ transport equation from standard $k - \epsilon$ model could be transformed into a ω transport equation by variable substitution. His developed model called $k - \omega$ SST combines several desirable elements of existing two-equation models and using the blending function (a function of wall distance). The standard $k - \omega$ model (Wilcox's model) is applied near the solid walls and the standard $k - \epsilon$ model is used near the boundary edges and in the free-shear layer. The switching is achieved with the blending function. The shear stress transport modeling also modifies the eddy viscosity by forcing the turbulent shear stress to be bounded by a constant time the turbulence kinetic energy inside boundary layers (a realizability constraint). This modification improves the prediction of flow with strong adverse pressure gradients and separation. Wilcox [73] conducted an overview to compare the curacy between the turbulence models and found that the $k - \omega$ model and $k - \omega$ SST model give a good agreement with the test results. Consequently, the $k - \omega$ SST model is used to predict the performance of the CRCC.

A.4.3 Motion

There are different ways to simulate the rotational movement in CFD. The two most important techniques are the sliding mesh and the moving reference frames. In the moving reference frames approach, a new rotating coordinate system is applied to an entire region, simulating motion but the mesh is actually not moving. Instead, the Coriolis and centrifugal forces are added to the momentum equations (A.60) so even though the positions of the cell vertices do not change the modeled rotation. The moving reference frame technique is normally used in steady-state simulations. In a centrifugal compressor geometry, the moving reference frame is usually applied to the rotor region whereas the rest of the compressor remains static. Some parts such as the shroud, however, are not rotating so the source terms are actually activated only in the regions where rotation exists. An important drawback of this method is that the flow field which is seen by the stationary elements depends on the relative position of these

elements. It is actually a very limited technique because it is very unrealistic that the rotor remains stationary. However, the computational cost is very affordable, and it is the only way to succeed in running and calculating several points on the compressor map.

The sliding mesh, on the other hand, allows the adjacent cells to another one. The sliding interface is updated every time step and the cells do not have a correspondent on the other side of the interface but the connectivity changes every time. In spite of being far more realistic than the moving reference frames technique, it is much more expensive and it is generally used when running transient simulations. In this thesis, the Moving Reference Frames method and sliding mesh are used to handle the rotation of the wheel and capture the interaction between the two rotors.

A.4.4 Interface

Interfaces can be divided into direct and indirect interfaces. Direct interfaces directly join the two boundaries that compose the interface by creating an explicit connection between cells. The two boundaries are merged during the meshing process to guarantee a conformal mesh across the interface. An example would be the in-place interface that is used for interfaces in this thesis. In this interface, there is no physical separation between the boundaries that conforms the interface and mass, momentum and energy are transferred directly from cell to cell.

Indirect interfaces, however, make an association between the faces of the boundaries. The mixing plane interface, for example, tries to mitigate the disadvantage of the influence of the relative position that the moving reference frame brings. This interface averages circumferentially the flow conditions on both sides making the flow circumferentially uniform and thus giving rise to a single radial profile. The effect of this approach is similar to the idea of increasing the number of blades which would lead to much more uniform flow. If we take a look at a fast-rotating rotor outlet, we see a circumferential homogeneous flow and this is what the mixing plane is basically trying to imitate. However, we have to be careful when using the mixing plane interface because, for instance, wake effects cannot be predicted given the circumferential averaging that is done.

A.4.5 Boundary condition

Boundary conditions play an important role in [CFD](#) calculations. Having good control over our boundary conditions makes it possible to obtain a good solution to our problem. Star-CCM+ provides the possibility to set different boundary conditions for the inlet and the outlet of the set-up.

Inlet boundary condition

Typically for the inlet, a velocity inlet, stagnation inlet, mass flow inlet, or free stream boundary conditions can be applied. The free stream is a none re-effective boundary condition frequently used when studying acoustics. For the stagnation inlet boundary condition, a total pressure needs to be specified. A mass flow inlet is chosen in this thesis since the mass flow is the known variable - from the specifications - that is imposed to calculate every case. The total temperature is set at $300K$, while the turbulence intensity and turbulent viscosity ratio remain as default.

Outlet boundary condition

For the outlet boundary condition, a pressure outlet is often specified. In this thesis, the outlet static pressure is imposed (atmospheric pressure at 101,325 Pa).

The Wall boundary condition

Together with the inlet and outlet boundary conditions, the wall closes the computational domain. The whole compressor casing including the inlet, outlet pipe, shroud, and the volute is set as wall boundary conditions. The walls are treated adiabatically since we are not interested in the heat transfer phenomenon. A non-slip wall condition is specified, this is, the velocity of the fluid is zero on the walls.

A.4.6 Solving strategies

Star-CCM+ provides two different solving strategies. The segregated flow model which solves sequentially the equations and a predictor-corrector approach is used to link the momentum and continuity equations. It is based on a collocated variable arrangement (as opposed to staggered) and a Rhie-and-Chow-type pressure-velocity coupling combined with a SIMPLE-type algorithm [70]. In addition, it is normally used in constant-density, for example, the mildly compressible flows and low Rayleigh number natural convection. So, it is not applicable to a high Mach number, shock waves, and high Rayleigh-number applications.

The Coupled Flow model solves the conservation equations for mass, momentum, and energy simultaneously using a pseudo-time-marching approach. The advantage of this model is its robustness for solving flows with dominant source terms, such as rotation and the CPU time scales linearly with the number of cells; in other words, the convergence is usually slower and harder to achieve if the mesh is refined [70]. Besides, this model needs a higher resource, so it is quite expensive to simulate. In this thesis, the flow is mildly compressible and the Mach number is not high, so model segregated flow is applied to save the resource and to converge faster.

Appendix B

Résumé de thèse

Étude expérimentale de l'interaction aérodynamique rotor-rotor pour un compresseur centrifuge contrarotatif

B.1 Introduction

L'histoire du système contrarotatif commence au début du XXe siècle avec l'apparition d'un concept de turbine à gaz contrarotatif appliqué à l'hélice d'un avion par Taylor [15] et Bourdon [16]. Les auteurs ont constaté que l'utilisation d'un système contrarotatif améliore non seulement le débit, mais également la poussée. De même, Young [17] et Wilcox [18] ont rapporté qu'une machine contrarotative avec la même vitesse de rotation fournit une augmentation de pression plus élevée et, par conséquent, une meilleure capacité d'écoulement. Selon Sharma et al. [19, 20] les performances d'un contra-étage sont affectées de manière significative par de nombreux paramètres tels que le rapport de vitesses des deux rotors, l'écart axial entre eux, le rapport moyeu-tête d'aube et le rapport corde-pas. L'augmentation du rapport de vitesses peut améliorer les performances, mais elle diminue aussi progressivement les performances aéroacoustiques. Étant donné les multiples avantages du système contrarotatif, beaucoup d'études dans ce domaine ont été menées. Elles visent à améliorer les performances des applications dans de nombreux types des turbomachines. Cependant, aucune étude semble avoir été menée sur le système contrarotatif appliqué aux compresseur centrifuges. Au Laboratoire d'Ingénierie des Fluides et Systèmes Energétiques (LIFSE), Arts et Métiers, un compresseur centrifuge contrarotatif innovant a été conçu à partir d'un compresseur conventionnel. Le rotor du compresseur conventionnel est remplacé par deux rotors contrarotatifs. Un banc d'essai a été développé afin de comparer les performances d'un système contrarotatif par rapport à un compresseur centrifuge conventionnel. La thèse se compose de 5 chapitres principaux :

- Le chapitre 1 présente les connaissances de base des compresseurs centrifuges et l'état de l'art du système contrarotatif.
- Le chapitre 2 présente la méthode de conception d'un rotor seul et des rotors contrarotatifs basée sur le rapport de la longueur méridienne LR du premier rotor. Les quatre configurations de type contrarotatif ont été conçues sur la base de quatre coefficients LR : 0.3, 0.4, 0.5 et 0.6. Une étude numérique a été effectuée sur ces quatre configurations. La configuration " $LR = 0.3$ " obtient de meilleures performances avec moins de pertes locales que les autres configurations. Cette configuration a donc été choisie afin d'être étudiée expérimentalement.
- Le chapitre 3 présente le banc d'essai et la méthode de mesure utilisée. Le calcul des incertitudes sur la mesure est également présenté dans cette partie.
- Le chapitre 4 présente les résultats expérimentaux obtenus avec le compresseur contrarotatif. Trois modes de fonctionnement du compresseur ont été étudiés : le premier rotor en rotation libre, le premier rotor fixe et en mode contrarotatif (le premier rotor tourne dans le sens opposé au second). La méthode des similitudes est également appliquée dans cette partie pour estimer les résultats pour une configuration à une vitesse de rotation de 16 000 tr/min . Des rapports de vitesses entre les rotors ont également été étudiés pour évaluer les performances de la machine. Une étude numérique des compresseurs contrarotatifs fonctionnant à une vitesse de 10 000 tr/min a menée. Le travail se focalise sur deux points principaux: le point de rendement maximal (BEP) et près de la limite de pompage (NIP). Des simulations en régime instationnaire sont également menées pour étudier l'écoulement du fluide à l'intérieur du compresseur.
- Le chapitre 5 présente des travaux ont menées pour repousser le limite de pompage. Les résultats obtenus montrent une réduction de cette zone de pompage

grâce au compresseur contrarotatif utilisé dans une configuration de co-rotation. De plus, le résultat numérique du point élargi (ESLP) vers la zone de pompage a été effectué pour comprendre l'écoulement à l'intérieur du compresseur.

Les résultats expérimentaux montrent que l'utilisation d'un système contrarotatif améliore non seulement le taux de compression, mais aussi les rendements de la machine à des vitesses inférieures à la vitesse de conception par rapport au compresseur conventionnel. L'étude par similitude ramenée à la vitesse de conception montrent que le système contrarotatif améliore le taux de compression de 15.13% avec un rendement reste presque identique à 72%. Avec une vitesse adéquate des deux rotors, le système contrarotatif étend significativement la plage de fonctionnement vers la zone de pompage.

B.2 Conceptions des rotors contrarotatif

Dans cette thèse, le rotor seul du compresseur centrifuge conventionnel est remplacé par deux rotors successifs. Ils sont entraînés indépendamment l'un de l'autre par deux moteurs électriques. La figure B.1 représente les deux rotors de la configuration contrarotatif. Sur cette figure, le premier rotor tourne avec à une vitesse angulaire ω_1 et le deuxième tourne dans la direction opposée avec une vitesse angulaire ω_2 . Le premier rotor a une taille plus petite et est situé en amont du deuxième rotor. Celui-ci reçoit donc directement le flux de fluide du premier et apporte plus d'énergie pour le comprimer afin d'augmenter la pression. Pour simplifier la conception, les paramètres du rotor basés sur la vue méridienne du rotor seul sont conservés. De plus, pour minimiser la perte entre le deuxième rotor et la volute, l'angle des aubes à la sortie du deuxième rotor reste le même que celui du rotor seul. Les rotors contrarotatifs ont été conçus de la manière suivante :

- Le taux de compression de chaque rotor et le taux de compression total du **compresseur centrifuge contrarotatif (CRCC)** sont imposés pour calculer la pression à l'entrée et à la sortie de chaque rotor ;
- Les paramètres géométriques des rotors sont déterminés en calculant les angles des aubes en fonction des relations aérodynamiques.

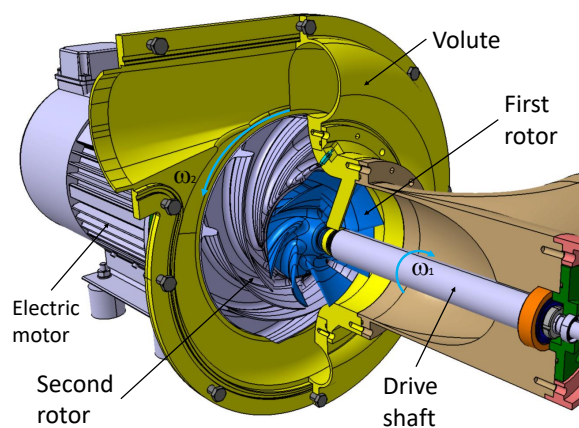


FIGURE B.1 – La structure du **compresseur centrifuge contrarotatif (CRCC)**

B.2.1 Conception du premier rotor

Le premier rotor est dessiné en fonction du diamètre de sortie. Il peut être déterminé par le **rapport de la longueur (LR)** qui est défini de la manière suivante :

$$LR = \frac{L_{1st}}{L_m} \quad (B.1)$$

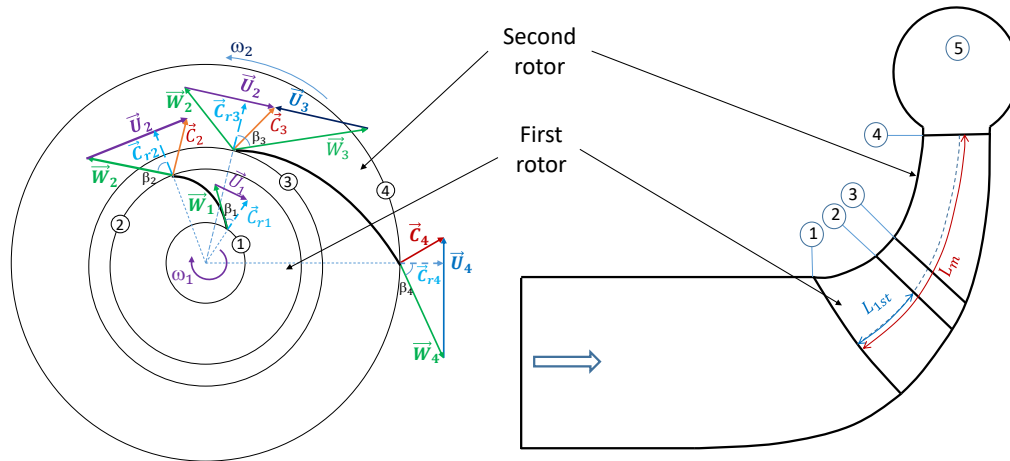


FIGURE B.2 – Schéma du triangle des vitesses du CRCC: (a) vue de face et (b) vue méridien

Ce paramètre est libre et est choisi arbitrairement. Dans cette étude, quatre valeurs de **LR** : 0.3, 0.4, 0.5, 0.6 ont été testé afin de construire respectivement quatre configurations **CF1**, **CF2**, **CF3** et **CF4**. Pour chaque configuration, les paramètres géométriques des aubes (angle à l'entrée et angle à la sortie) sont calculés selon les équations aérodynamiques. Les composantes de la vitesse à l'entrée et à la sortie sont identifiées par le triangle des vitesses comme montré sur la figure B.2.

Le premier rotor est conçu par BladeGen d'ANSYS15 en déterminant l'angle de l'aube à l'entrée et à la sortie du rotor. Quatre configurations du premier rotor sont représentées sur la figure B.3. Les spécifications géométriques des premiers rotors sont présentées dans le tableau B.1.

B.2.2 Conception du deuxième rotor

Les conditions aérodynamiques à la sortie du premier rotor sont utilisées comme conditions d'entrée pour le deuxième rotor. Pour simplifier le calcul, certaines hypothèses sont faites :

- La pression à la sortie du premier rotor est la même que celle à l'entrée du deuxième rotor, $P_3 = P_2$;
- La direction de l'écoulement du fluide reste la même de la sortie du premier rotor à l'entrée du deuxième rotor, $\alpha_2 = \alpha_3$;
- La température entre le premier et le deuxième rotor est constante, $T_2 = T_3$;
- La vitesse est constante de la sortie du premier rotor à l'entrée du deuxième rotor, $C_2 = C_3$.

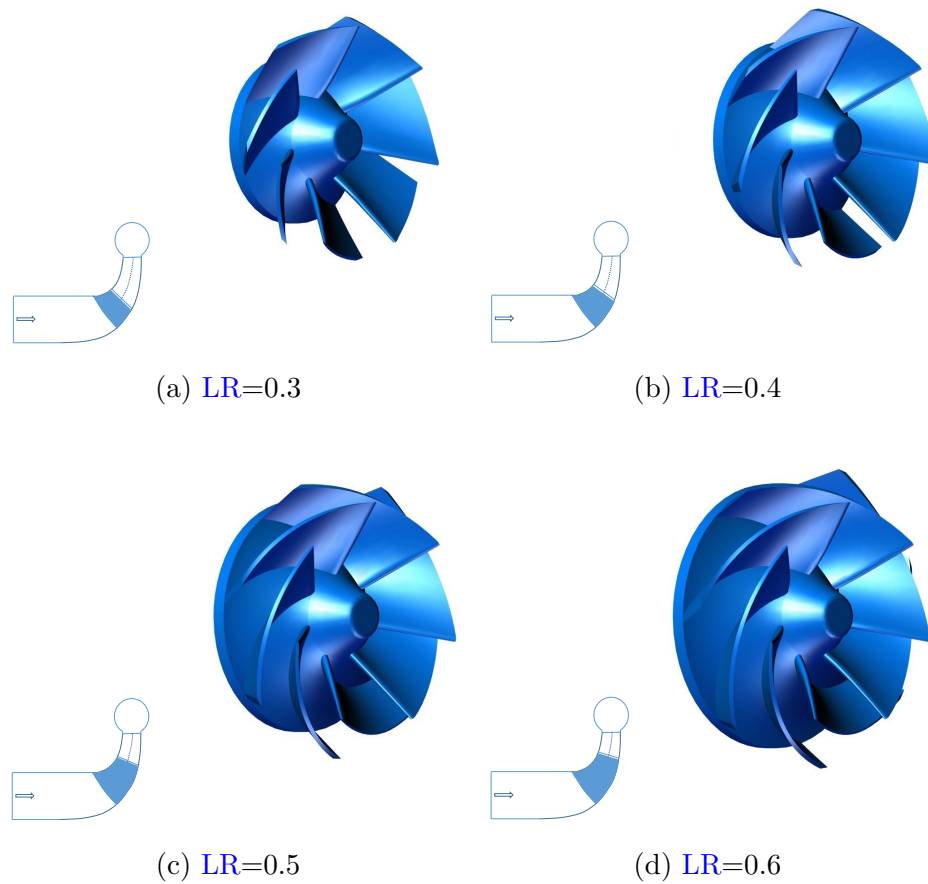


FIGURE B.3 – Schéma des quatre géométries de premier rotor étudiés pour les autres configurations de **CRCC** : (a) CF1, (b) CF2, (c) CF3 et (d) CF4

TABLE B.1 – Paramètres géométriques du premier rotor des quatre configurations de **CRCC**: CF1, CF2, CF3 et CF4

Paramètres	CF1	CF2	CF3	CF4
LR	0.3	0.4	0.5	0.6
d_{1h}	59.5mm	59.5mm	59.5mm	59.5mm
d_{1sh}	161mm	161mm	161mm	161mm
d_{2h}	118mm	140mm	163mm	186mm
d_{2sh}	176mm	186mm	200.8mm	216mm
Π_1	1.03	1.05	1.08	1.11
η_{1i}	90	90	90	90
β_{1h}	46°	46°	46°	46°
β_{1sh}	70.4°	70.4°	70.4°	70.4°
β_{2h}	51°	57.4°	56°	60°
β_{2sh}	68°	69.4°	68°	66.4°
N_1	-16000rpm	-16000rpm	-16000rpm	-16000rpm
Z_1	7	7	7	7

Par la même méthode, les angles des aubes à l'entrée et à la sortie du deuxième rotor sont déterminés par la relation aérodynamique. Les différentes conceptions du deuxième rotor sont réalisées dans BladeGen d'ANSYS15 comme indiqué sur la figure

B.4. Quatre configurations du **CRCC** sont obtenues. Ces paramètres de configuration

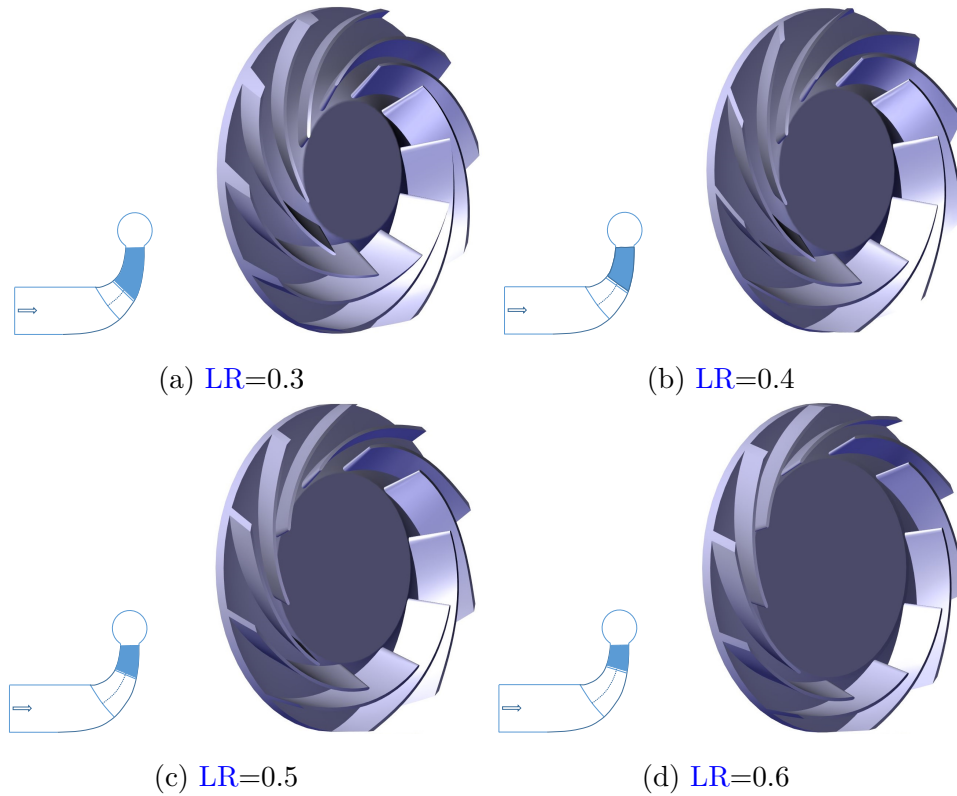


FIGURE B.4 – Schéma des quatre géométries de deuxième rotor étudiés pour les autres configurations de **CRCC** : (a) CF1,(b) CF2, (c) CF3 et (d) CF4

TABLE B.2 – Paramètres géométriques du deuxième rotor des quatre configurations de **CRCC**: CF1, CF2, CF3 et CF4

Paramètres	CF1	CF2	CF3	CF4
LR	0.3	0.4	0.5	0.6
d_{3h}	128.5mm	150mm	172mm	198mm
d_{3sh}	183mm	198mm	210mm	228mm
d_4	286mm	286mm	286mm	286mm
Π_2	1.27	1.25	1.22	1.20
η_{2i}	90	90	90	90
β_{3h}	73.9°	76.4°	79.6°	81.3°
β_{3sh}	77.7°	79°	80.9°	82.1°
β_4	64°	64°	64°	64°
N_2	16000rpm	16000rpm	16000rpm	16000rpm
Z_2	10	10	10	10

CRCC sont présentés dans le tableau B.2. Une étude numérique a été menée pour évaluer l'effet du LR sur les performances du compresseur. Les résultats obtenus ont permis de choisir la meilleure configuration de **CRCC** sur cette machine.

B.2.3 Évaluation des performances

Des simulations numériques ont été menée pour comparer l'effet du système contrarotatif par rapport à une compresseur conventionnel. Les simulations sont réalisées à

l'aide d'un modèle compressible tridimensionnel en régime permanent avec le logiciel commercial Star CCM+. Le modèle de turbulence choisi est le modèle $k-\epsilon$ réalisable à deux couches, ainsi la méthode de discrétisation du second ordre. Pour faciliter la comparaison des résultats, un même modèle de calcul est défini pour le **compresseur centrifuge mono roue (SRCC)** et pour les quatre configurations **CRCC**, dans les mêmes conditions de fonctionnement. Il est à noter que dans ce modèle de calcul, il n'est pas fait mention du jeu entre le rotor et le carter. Les conditions aux limites sont fixées avec les paramètres de fonctionnement du compresseur suivants : le débit massique au point nominal est fixé à $0,73 \text{ kg/s}$, la pression de sortie est la pression atmosphérique égale à $101\,325 \text{ Pa}$, la vitesse de rotation des rotors est de $16\,000 \text{ tr/min}$.

La convergence du maillage est vérifiée. Afin d'avoir des résultats indépendants du nombre de cellules, le maillage doit être constitué de plus de 5.26 millions mailles. La figure B.5 présente le taux de compression statique du **CRCC** en fonction de la variation du débit massique. Le taux de compression du **CRCC** semble être amélioré à un débit inférieur à celui du point de fonctionnement nominal (**DP**). Les configurations **CF1**, **CF3** et **CF4** permettent d'augmenter significativement le taux de compression. Le taux de compression de **CF2** est assez proche de celui de **SRCC**. Dans la zone proche du pompage, les taux de compression de **CF1**, **CF3**, **CF4** conservent des valeurs similaires. Tandis que la configuration **CF2** fournit une valeur similaire à celle de **SRCC**. **CF1** permet d'obtenir un taux de compression plus stable que les autres configurations.

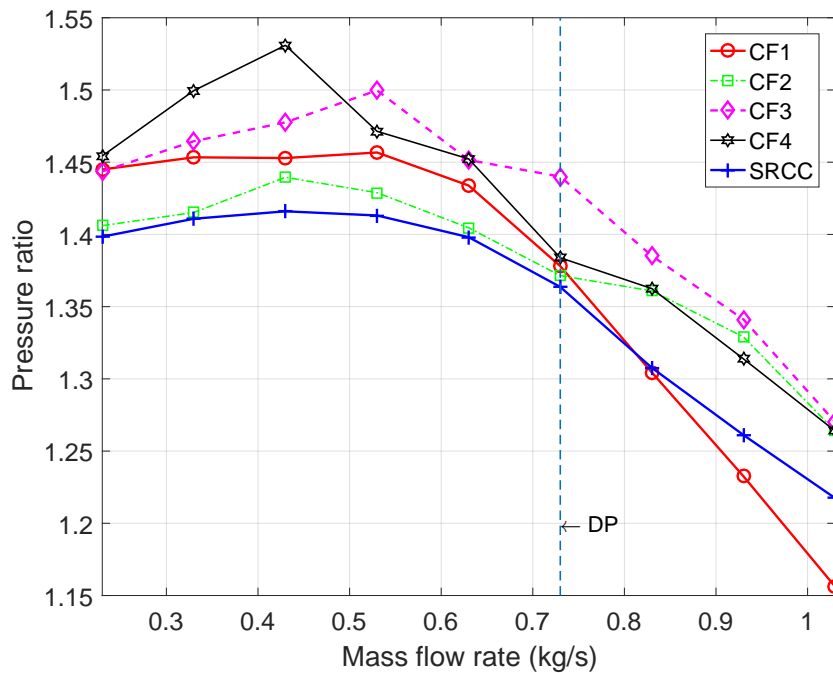


FIGURE B.5 – Comparaison des taux de compression des quatre configurations de **CRCC**

La figure B.6 montre les évolutions des rendements polytropiques en fonction du débit massique pour chaque configuration. **CF1** permet d'obtenir le meilleur rendement polytropique d'environ 80 % au **DP**. Par conséquent, la configuration **CF1** a été sélectionnée pour la suite de l'étude et notamment pour l'étude expérimentale.

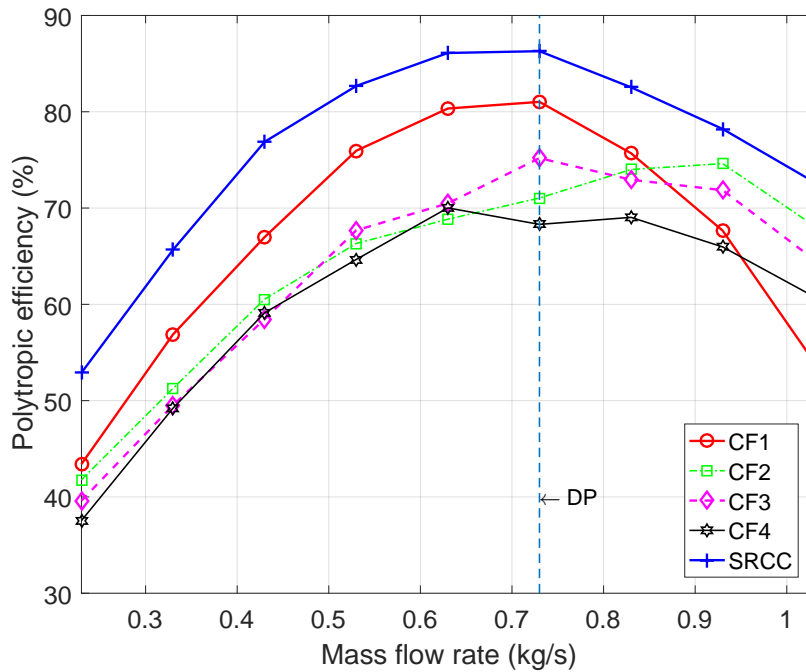


FIGURE B.6 – Comparaison des rendements polytropiques des quatre configurations de **CRCC**

B.3 Banc d'essai RAICOR

B.3.1 Adaptation avec le banc d'essai du compresseur conventionnel

Le banc d'essai RAICOR est développé à partir du banc d'essai du compresseur centrifuge conventionnel du LIFSE. Pour le dispositif CRCC, il est nécessaire d'adapter le banc pour contrôler l'entraînement des deux roues indépendamment l'une de l'autre. CRCC a deux rotors indépendants qui sont entraînés par deux moteurs électriques et disposés de chaque côté du compresseur. Pour ces raisons, le banc d'essai doit être modifié pour être compatible avec la nouvelle structure du CRCC. Le tuyau d'aspiration doit être adapté pour répondre au changement de structure de la nouvelle machine. Pour ce faire, un tuyau coudé est utilisé. Afin d'éviter le phénomène de résonance sur l'arbre d'entraînement, il est nécessaire de réduire la distance entre le rotor et le moteur d'entraînement. Pour cela, un tuyau courbé avec un angle de 90° est alors utilisé. L'impact du tuyau coudé sur les performances du CRCC a été évalué. Le résultat montre que le tuyau coudé affecte légèrement les performances du CRCC en raison de la vitesse asymétrique à l'entrée, en particulier, dans la région à faible débit. Pour ces travaux, l'impact du tuyau coudé est considéré comme acceptable.

B.3.2 Banc d'essai RAICOR

Le CRCC se compose de deux rotors, d'un arbre de transmission et de quelques composants supplémentaires tels que le bloc de carter, le bloc d'entrée, et le support de moteur électrique, etc. Le banc d'essai RAICOR est présenté sur la figure B.7.

Le banc d'essai fonctionne de la manière suivante : l'air entre dans le réservoir (1) à travers une plaque percée de 120 trous de 8mm de diamètre. L'obstruction d'un certain nombre de trous permet d'ajuster le débit d'entrée dans le compresseur. L'air

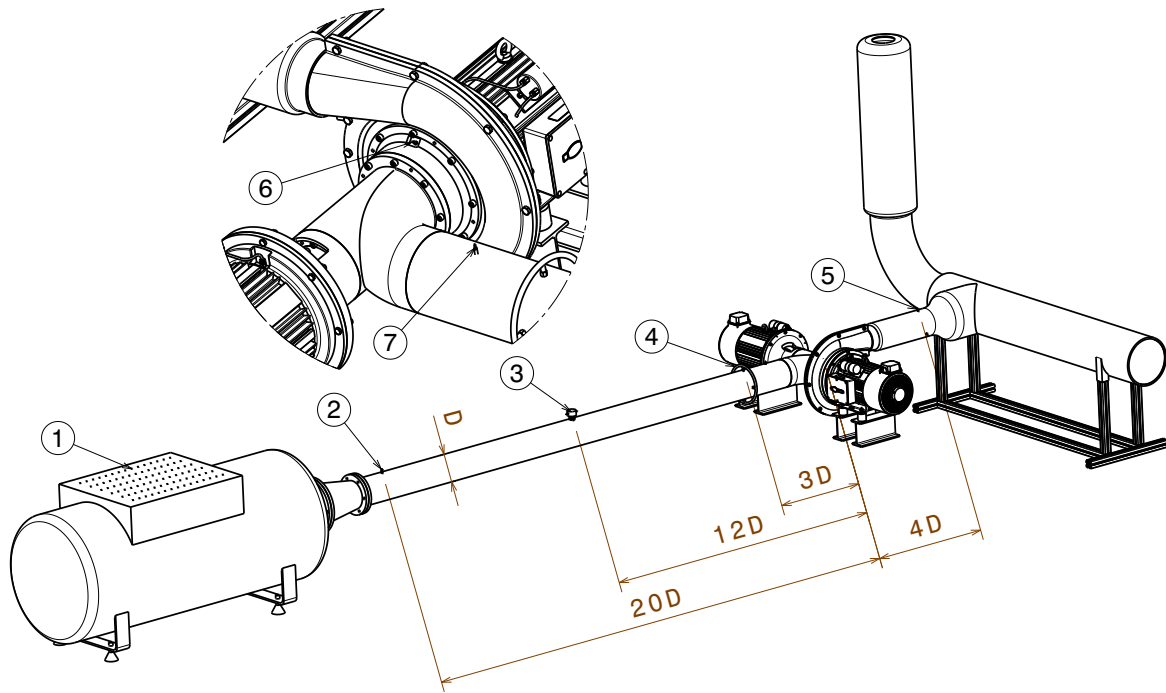


FIGURE B.7 – Schéma du banc d'essai RAICOR utilisé pour l'étude des compresseurs CRCC

passe ensuite à travers une conduite d'un diamètre de $D = 158,5\text{mm}$ de $3,5\text{m}$ de long. Un nid d'abeilles est placé en amont de la conduite afin de rendre le profil de vitesse uniforme à l'entrée. L'air entre ensuite dans le compresseur puis passe à travers un silencieux pour enfin ressortir dans l'air environnant à la pression atmosphérique. Les deux rotors de CRCC sont entraînés par deux moteurs électriques de vitesses maximales $17\,000\text{ tr/min}$. Deux variateurs sont utilisés pour régler indépendamment la vitesse de chaque rotor et pour mesurer les consommations énergétiques. Les capteurs utilisés sont présentés à la figure B.7. Un capteur de température Pt100 (2) situé à une distance de $20D$ en amont du compresseur permet de mesurer la température d'entrée. Le tube de Pitot-Platon (3) est fixé à $12D$ en amont du compresseur pour déterminer le débit massique. Quatre prises de pression réparties sur la circonférence de la conduite en entrée (4), situées à une distance de $3D$ en amont du compresseur permettent de mesurer la pression d'entrée par le biais d'un manomètre FC322. Trois capteurs de température Pt100 (5) sont situés au niveau de la conduite, en sortie, à une distance $4D$ en aval du compresseur. Deux capteurs de pression dynamique Kistler (6), (7) sont installés à l'entrée et entre les deux rotors afin de mesurer la pression instantanée et d'identifier la fréquence du pompage.

B.4 Résultats expérimentaux

B.4.1 Les limites des expérimentations

Toutes les limites de vitesse de rotation mentionnées dans cette section sont celles du deuxième rotor. Le banc d'essai est conçu pour fonctionner à une vitesse maximale de $16\,000\text{ tr/min}$. Cependant, le compresseur doit fonctionner jusqu'à une vitesse maximale de 75% de la vitesse de conception pour des raisons de sécurité. Ainsi, la vitesse de rotation maximale du deuxième rotor est limitée à $12\,000\text{ tr/min}$.

B.4.2 Performances globales du CRCC

Dans cette étude, l'évaluation des performances globales est réalisée dans trois cas :

- Cas 1 : le premier rotor tourne librement - le deuxième rotor est entraîné;
- Cas 2 : le premier rotor est fixe - le deuxième rotor est entraîné;
- Cas 3 : mode contrarotatif (les deux rotors sont entraînés et tournent en sens inverse l'un par rapport à l'autre)

Le premier rotor tourne librement - le deuxième rotor est entraîné (cas 1)

Dans cette configuration, le premier rotor se comporte comme une turbine et sa vitesse dépend du débit massique du compresseur. Sur la figure B.8 les performances globales du CRCC sont comparé à celles de SRCC pour trois vitesse de rotation 9 000 tr/min , 10 000 tr/min et 11 000 tr/min . Les résultats expérimentaux indiquent que CRCC produit de meilleures performances que SRCC. Cependant, le point de rendement maximal (PEP) du compresseur est déplacé vers un débit plus petit. À 9 000 tr/min , le taux de compression est inférieur à celui de SRCC mais le rendement augmente d'environ 8 %. Pour des vitesses supérieures à 10 000 tr/min et 11 000 tr/min , le taux de compression est amélioré mais il est toujours inférieur à celui de SRCC. En outre, le rendement de CRCC augmente de 3 % par rapport au SRCC. En conséquence, CRCC consomme moins d'énergie et sa plage de fonctionnement est plus étendue.

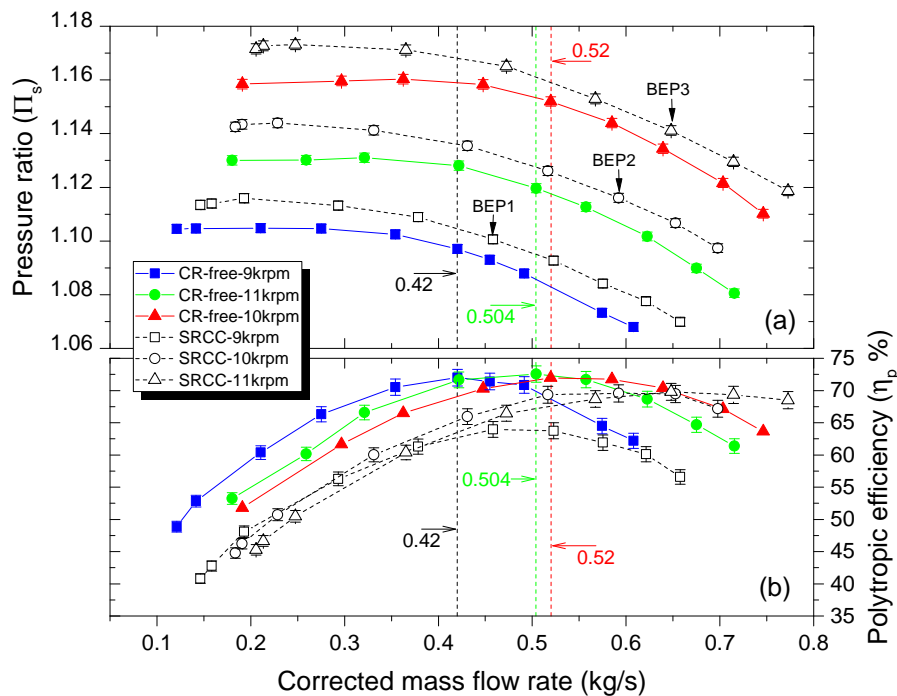


FIGURE B.8 – Comparaison des performances globales de CRCC dans le cas 1 (premier rotor en rotation libre et deuxième rotor entraîné) et SRCC (en noir et lignes pointillées) aux vitesses de rotation 9 000 tr/min , 10 000 tr/min et 11 000 tr/min

Le premier rotor fixe - le deuxième rotor est entraîné (cas 2)

Dans cette configuration, le premier rotor agit comme un système de pré-rotation. Cela diminue donc le nombre de Mach relatif à l'entrée du deuxième rotor [42]. Le triangle des vitesses pour cette configuration est représenté sur la figure B.9. L'enthalpie du deuxième rotor est calculée par l'équation B.2. De toute évidence, le travail diminue car la composante de vitesse C_{u3} a une valeur positive.

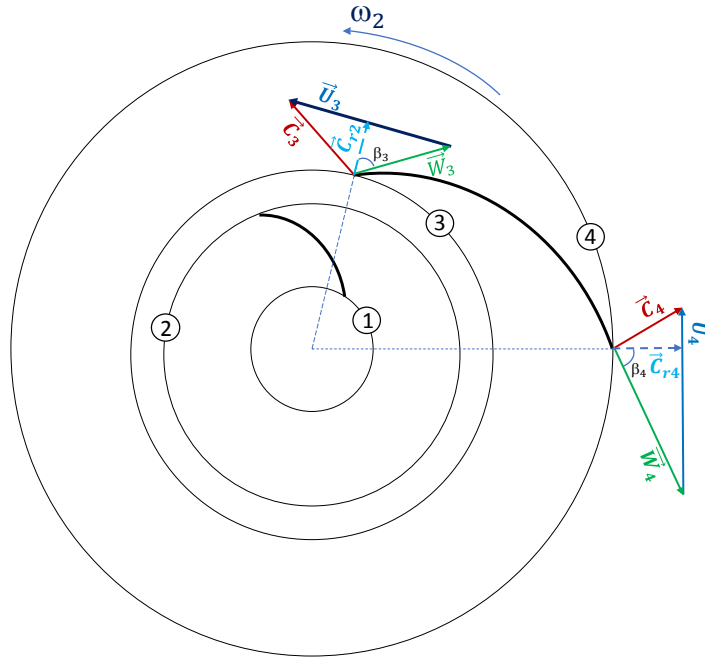


FIGURE B.9 – Schéma du triangle des vitesses de CRCC avec le premier rotor fixe (cas 2)

$$\Delta h_2 = U_4 C_{u4} - U_3 C_{u3} \quad (\text{B.2})$$

Les résultats expérimentaux montrent que les performances globales de CRCC sont considérablement réduites. Sur la figure B.10 les performances globales des cas 1 et 2 sont comparées pour les trois vitesses principales du deuxième rotor 9 000 *tr/min*, 10 000 *tr/min* et 11 000 *tr/min*. Pour les grands débits les performances globales du cas 2 sont bien inférieures à celles du cas 1. L'écoulement du fluide à la sortie du premier rotor semble ne pas être compatible avec l'angle des aubes à l'entrée du deuxième rotor. Cette perte par désadaptation réduit les performances. À faible débit, les deux configurations montrent les mêmes performances lorsque le premier rotor ne tourne plus. Cependant, ce cas n'est pas intéressant car il n'est pas efficace et il ne sera donc pas davantage étudiée.

Mode contrarotatif (cas 3)

Dans cette configuration, les deux rotors sont entraînés simultanément avec la même vitesse de rotation par les moteurs électriques. Sur la figure B.11 les performances globales de CRCC sont comparées à celles de SRCC en mode contrarotatif. À la vitesse de rotation de 9 000 *tr/min* (la ligne bleu), le taux de compression de CRCC est toujours supérieur à celui de SRCC. Au point de rendement maximal, le taux de compression

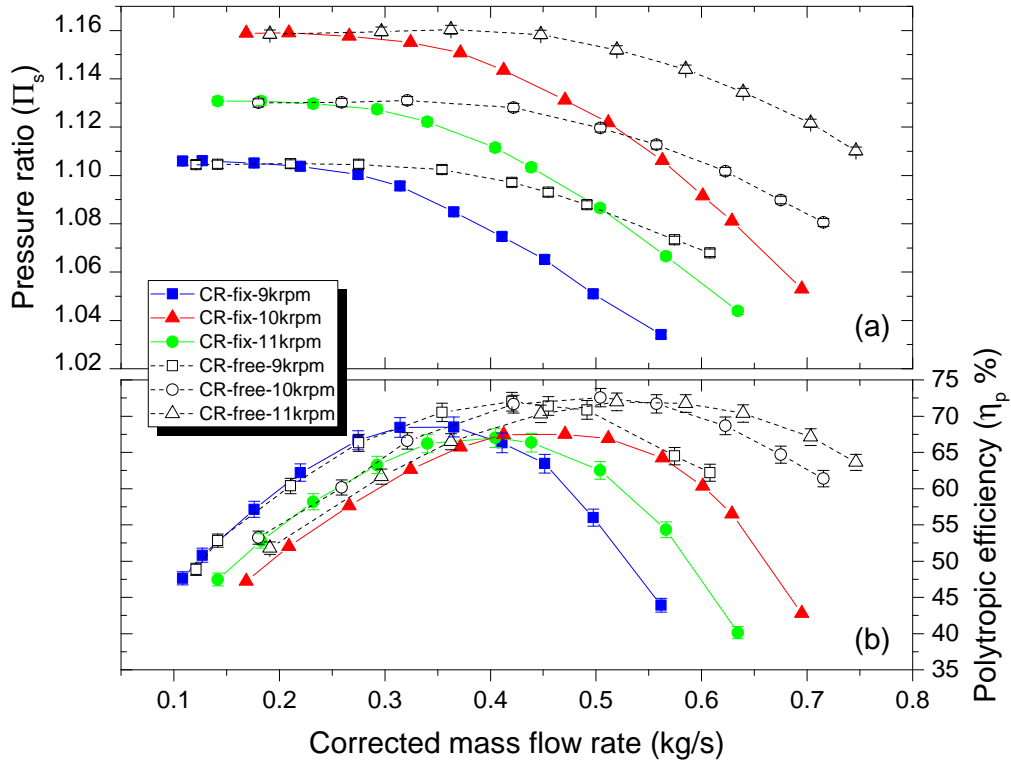


FIGURE B.10 – Comparaison des performances entre le premier rotor en rotation libre (CR-free: cas 1, en noir et lignes pointillées) et fixe (CR-Fix: cas 2, en couleur et lignes continues) avec le deuxième rotor tournant aux vitesses de rotation 9 000 tr/min , 10 000 tr/min et 11 000 tr/min

de CRCC est de $1,128 \pm 0.002$ tandis que celui de SRCC est de $1,100 \pm 0.002$. Ainsi, le taux de compression de CRCC augmente d'environ 2,5 % par rapport à celui de SRCC. De plus, le rendement polytropique de CRCC est également beaucoup plus élevé que celui de SRCC. Au point de fonctionnement, les rendements polytropiques de CRCC et SRCC sont respectivement de $72 \pm 2\%$ et $64 \pm 2\%$.

À la vitesse de rotation de 10 000 tr/mn (ligne verte), une comparaison au point de rendement maximal montre que le taux de compression de CRCC est toujours supérieur à SRCC. Il peut atteindre $1,158 \pm 0.002$, il augmente donc de 3,76 % par rapport à la valeur de SRCC qui est de $1,116 \pm 0.002$. De plus, le rendement polytropique varie également de manière significative. Le rendement de CRCC peut atteindre $72.6 \pm 2\%$ tandis que la valeur de SRCC est de $69.6 \pm 2\%$. Par conséquent, il y a une augmentation d'environ 3 % par rapport à SRCC.

À la vitesse de rotation de 11 000 tr/mn (la ligne rouge), le taux de compression de CRCC est toujours supérieur à celui de SRCC. Au point de rendement maximal, le taux de compression de CRCC atteint $1,194 \pm 0.002$ alors qu'il atteint $1,141 \pm 0.002$ pour SRCC. Cela signifie qu'en mode contrarotatif, CRCC a un taux de compression supérieur de 4,65 % à celui SRCC. De plus, le rendement polytropique de CRCC atteint $73.4 \pm 2\%$, ce qui est 3 % supérieur à $69.8 \pm 2\%$ pour SRCC. En conclusion, CRCC augmente le taux de compression de 2,5 % à 4,65 % par rapport à SRCC. En outre, le rendement polytropique est également amélioré de plus de 3%.

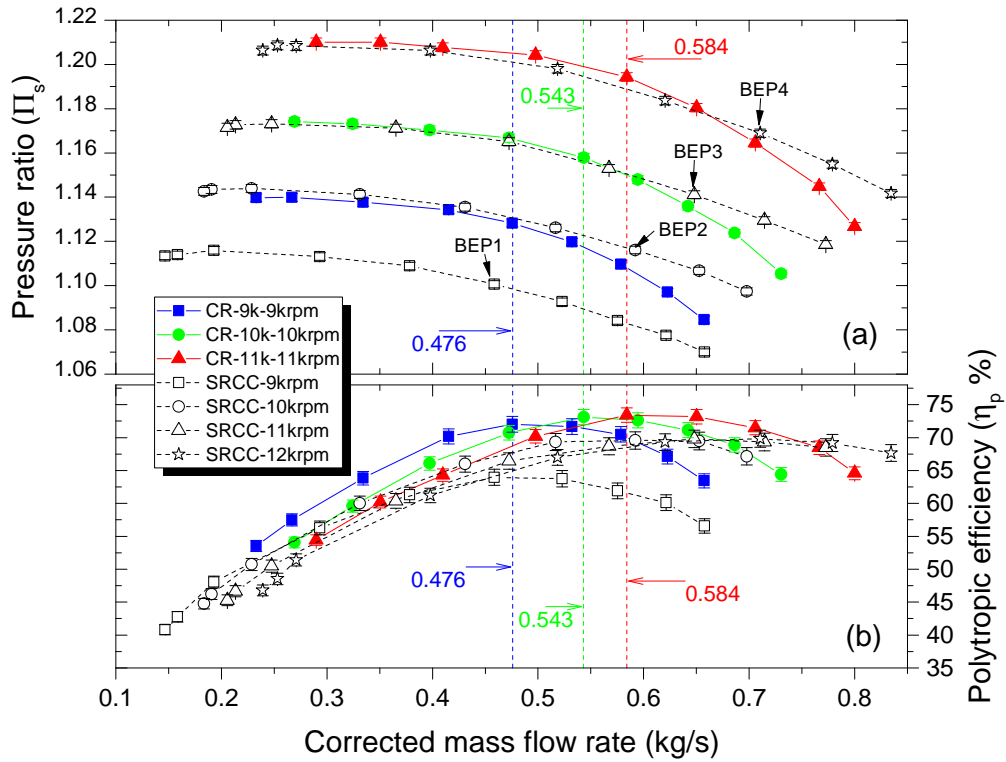
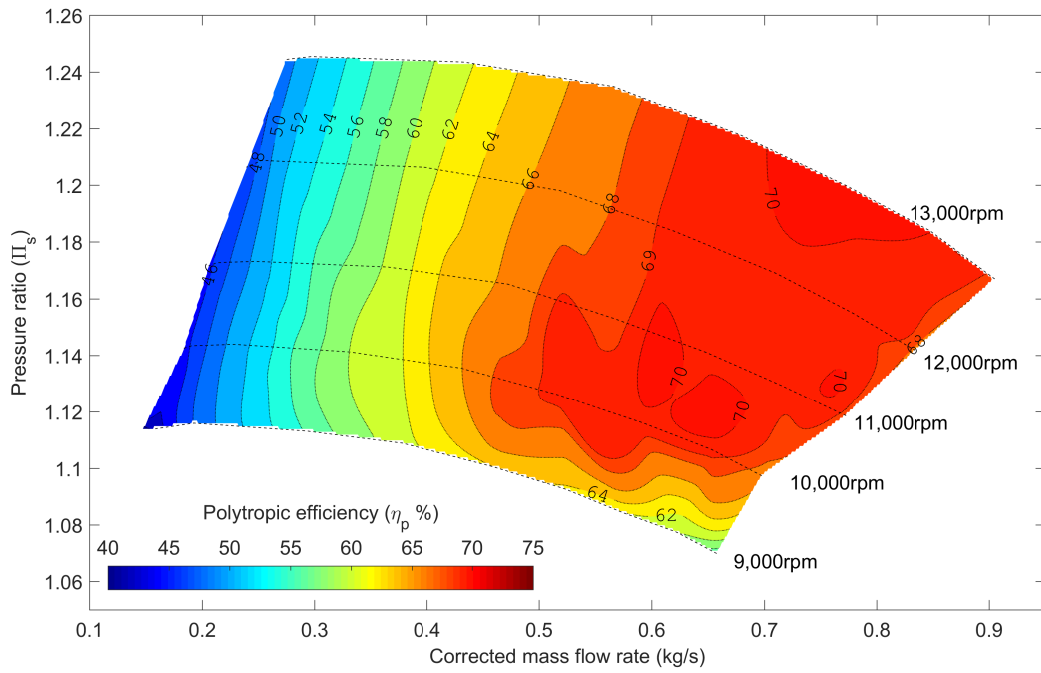


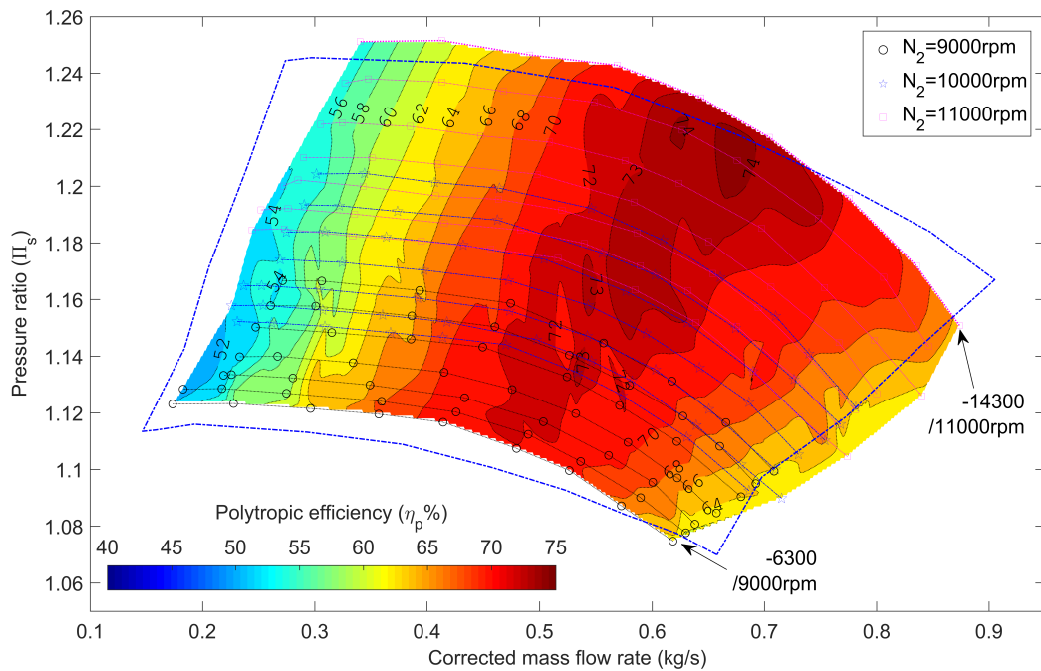
FIGURE B.11 – Comparaison des performances globales de CRCC et SRCC dans le cas 3

B.4.3 Influence du rapport de vitesses du rotor (θ)

L'utilisation du compresseur contrarotatif afin d'améliorer les performances énergétiques ou d'étendre la plage de fonctionnement nécessite de connaître l'effet du rapport de vitesses sur les caractéristiques du compresseur. C'est pour cela que, dans cette étude, des essais expérimentaux sont menés sur l'effet du rapport de vitesses sur les caractéristiques de CRCC sur les limites de la plage de fonctionnement. Les mesures sont effectuées avec trois vitesses de rotation principales du deuxième rotor (N_2): 9 000 tr/min , 10 000 tr/min et 11 000 tr/min . Pour à chaque vitesse de deuxième rotor, la vitesse du premier rotor (N_1) est adaptée pour obtenir un rapport de vitesses de $\theta = N_1/N_2$ dans la plage comprise entre $[-0,7 -1,3]$. Sept rapports de vitesses sont choisis pour l'étude expérimentale : $\theta_1 = -0,7$, $\theta_2 = -0,8$, $\theta_3 = -0,9$, $\theta_4 = -1$, $\theta_5 = -1,1$, $\theta_6 = -1,2$ et $\theta_7 = -1,3$ (le signe moins représente deux rotors tournant en sens inverse).



(a)



(b)

FIGURE B.12 – Comparaison des performances et des plages de fonctionnement entre (a) SRCC avec $9\,000\text{ tr/min} \leq N \leq 13\,000\text{ tr/min}$ et (b) CRCC avec différents rapports de vitesse tandis que $9\,000\text{ tr/min} \leq N_2 \leq 11\,000\text{ tr/min}$

Les résultats expérimentaux montrent que le rapport de vitesses a une grande influence sur les performances de **CRCC**. La figure B.12 montre la carte des performances de **CRCC** (figure B.12b) avec différents rapports de vitesses en comparaison avec celle de **SRCC** (figure B.12a) à la vitesse variant entre 9 000 *tr/min* et 13 000 *tr/min*. Il est clair que le taux de compression augmente linéairement avec le rapport de vitesse alors que le rendement maximal semble stable. Le taux de compression peut être augmenté de 6,6 % pour un rapport de vitesse égal à $-1,3$. Le rendement polytropique est amélioré de plus de 3%. Il convient de noter que les points de rendement maximal de **CRCC** changent à chaque rapport de vitesses de rotation. L'ensemble des points du rendement maximal à différents rapports de vitesses constitue la plage de fonctionnement efficace de **CRCC**. Cette zone est déplacée vers les débits plus petite et étendue à des taux de compressions plus élevés par rapport à **SRCC**. Ainsi, **CRCC** donne une plage de fonctionnement plus large, égale à celle de **SRCC** tournant à une vitesse plus élevée. Cela signifie que **CRCC** peut fonctionner à une vitesse périphérique inférieure à celle de **SRCC** (environ 2000 *tr/min*) pour obtenir les mêmes performances et la même plage de fonctionnement. Cependant, la limite de pompage de **CRCC** est déplacée vers un débit plus élevé. Le phénomène d'instabilité apparaît donc plus tôt dans le cas de **SRCC**.

B.4.4 Étude de la similitude

Les performances d'une turbomachine peuvent être définies par les courbes de pression tracées en fonction du débit volumique pour différentes valeurs de la vitesse de rotation. Une tentative pour étudier les variations de toutes les quantités impliquées nécessiterait un nombre trop important d'essai. Afin de réduire le nombre d'essais à réaliser, il est possible, par exemple, d'utiliser l'analyse dimensionnelle, qui permet de combiner les variables pour former un nombre plus petit et plus gérable de groupements sans dimension. Les caractéristiques peuvent alors être représentées raisonnablement par une seule courbe. À partir de cela, les performances à différentes vitesses peuvent être construites. Dans cette étude, les caractéristiques de **CRCC** à la vitesse de 16 000 *tr/min* sont construites par similitude sur la base des résultats empiriques obtenus à 10 000 *tr/min*. La figure B.13 montre que les courbes caractéristiques adimensionnées de **CRCC** à 10 000 *tr/min* sont obtenues par mesures expérimental. Les courbes de performances de **CRCC** à la vitesse de rotation de 9 000 *tr/min* et 11 000 *tr/min* sont tracées afin de comparer avec les courbes expérimentales aux mêmes vitesses. Les résultats montrent que les similitudes permettent de prédire les caractéristiques à différentes vitesses de manière assez précise et fiable. Les courbes des performances de **CRCC** à la vitesse de 16 000 *tr/min* sont prédites par cette méthode comme le montre la figure B.14.

Ces courbes montrent que le taux de compression de **CRCC** est toujours supérieur à celui de **SRCC**. Au point de rendement maximal, le taux de compression atteint 1,44, ce qui constitue une augmentation d'environ 10,3% par rapport à **SRCC**. De plus, pour le $\theta_7 = -1,3$, le taux de compression du **CRCC** peut atteindre une valeur de 1,514, soit une augmentation de 15,3 % par rapport à **SRCC**. En outre, **CRCC** donne un rendement polytropique maximal proche de celui de **SRCC** de 73%. Ces valeurs sont obtenues à différents débits massiques, c'est-à-dire qu'elles dépendent du rapport de vitesses de rotation des rotors.

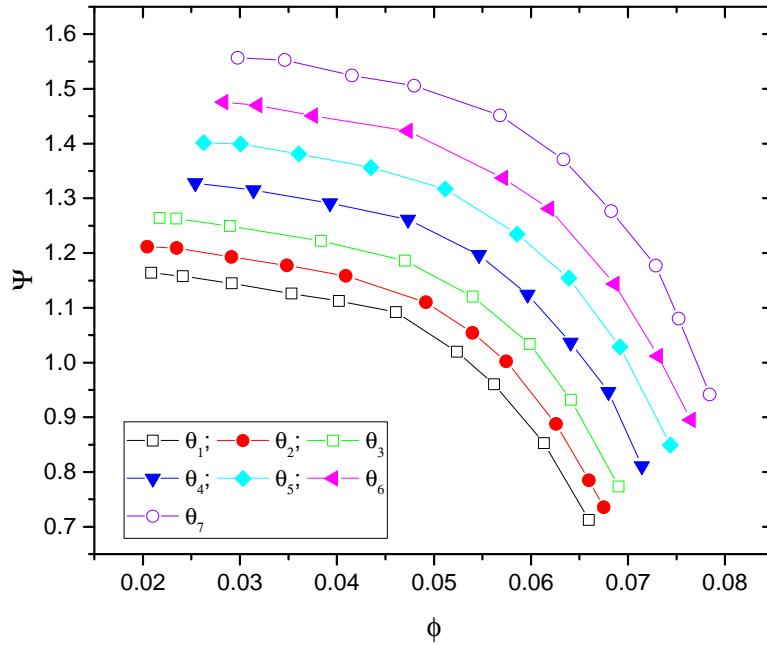


FIGURE B.13 – Caractéristiques adimensionnées de CRCC avec différents rapports de vitesses obtenues expérimentalement avec une vitesse de deuxième rotor fixée à 10 000 tr/min

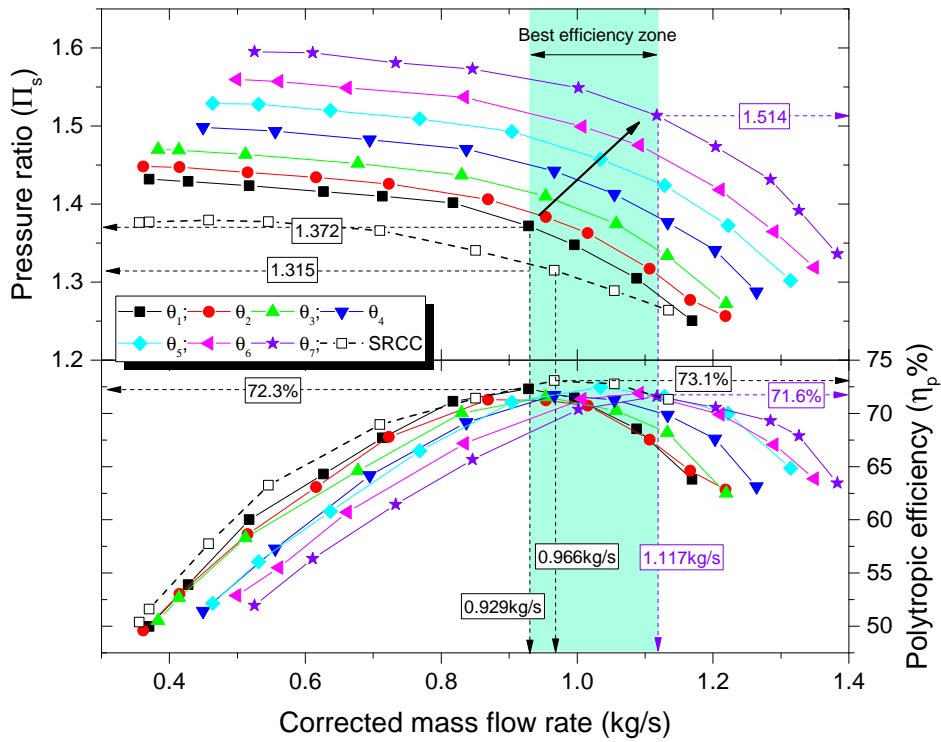


FIGURE B.14 – Caractéristiques de CRCC calculées par la méthode de similitude à la vitesse de 16 000 tr/min avec différents rapports de vitesses

B.4.5 Analyse CFD

Des simulations numériques ont été menées pour étudier trois points de fonctionnement intéressant: un point de rendement maximal (**BEP**), un point situé près de la limite d'apparition du pompage (**NIP**) en mode contra-rotatif et un point limite étendue (**ESLP**) en mode co-rotatif. De plus, une simulation instationnaire est également réalisée pour observer l'écoulement du fluide aux points ci-dessus. Cette étude permet d'observer le flux à l'intérieur de la machine dans le temps, qui dépend de la position relative de passages des aubes. Les caractéristiques de l'écoulement des fluides peuvent être analysées pour chaque point de fonctionnement, offrant ainsi des solutions pour ajuster les paramètres de géométrie et optimiser les performances de la machine. Les figures B.15 et figure B.16 présentent les blocs de maillage et les caractéristiques détaillées des rotors utilisés lors de la simulation. Le modèle comprend sept blocs principaux, notamment les domaines d'entrée, de coude d'entrée, de premier rotor, de deuxième rotor, de carter, de volute et de sortie. Le modèle utilise un maillage de base de 30 mm et est affiné dans les domaines du rotor avec des mailles dont la taille peut varier entre 1,5 mm et 0,3 mm. Pour garantir la conformité de deux domaines adjacents lors d'une simulation instationnaire, le maillage de zones juxtaposées est imposé à la même taille de 0,9 mm. L'épaisseur totale à la limite est fixée à 0,3 mm avec six couches pour garantir une valeur $Y+$ proche de 1. L'étude de la sensibilité du maillage montre que le modèle présentant $5,3 \cdot 10^6$ mailles est le maillage le plus adapté puisqu'il est indépendant du type de maillage et qu'il permet d'économiser du temps de calcul.

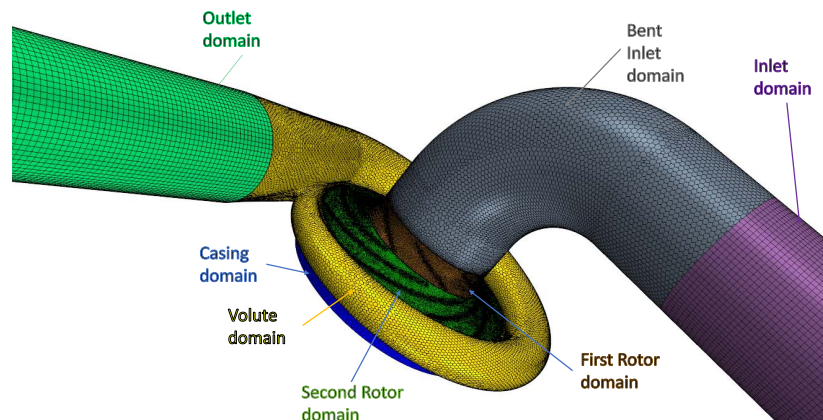


FIGURE B.15 – Domaines de maillages des différents blocs de CRCC utilisés pour les simulations numériques

Simulations numériques en régime stationnaire

Une comparaison avec les résultats expérimentaux montre que le modèle numérique est assez proche des mesures, notamment à faible débit. La plus petite valeur de déviation du taux de compression est d'environ 0,7 % à faible débit et augmente progressivement jusqu'à environ 4 % pour des débits élevés. Par ailleurs, la divergence des rendements polytropiques est assez proche des résultats expérimentaux à faible débit. La plus petite déviation au point proche du rendement maximal est d'environ 0,15 %. Deux points particuliers, **BEP** et **NIP**, sont étudiés dans des simulations de fonctionnement stable et instable pour étudier les caractéristiques d'écoulement de fluide interne pour $\theta = -1$ avec une vitesse de rotation constante de 10 000 tr/min . Au point **BEP**,

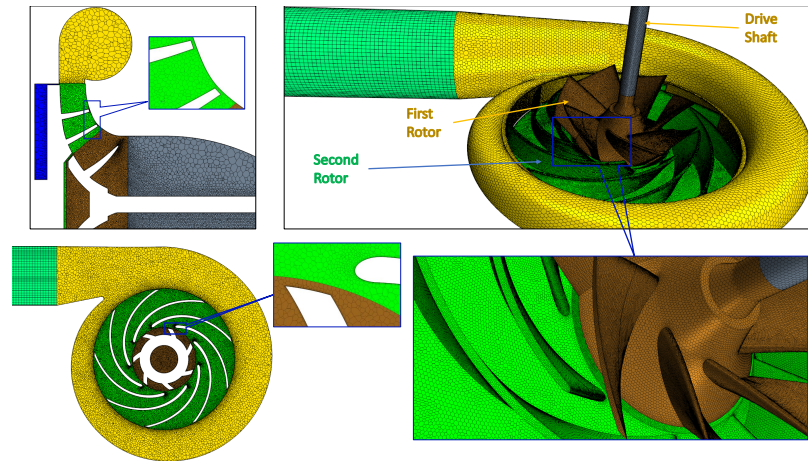
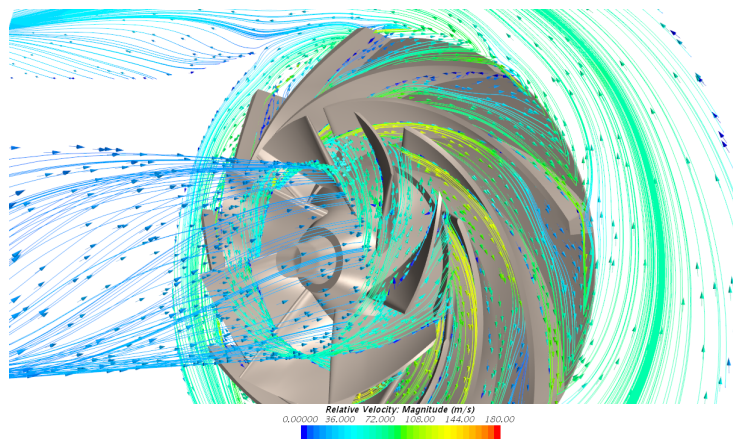


FIGURE B.16 – Détails des maillages du rotor dans différentes vues

les champs de pression, de vitesse et de température sont assez uniformes dans les rotors ainsi que dans la volute. L'écoulement de fluide à l'intérieur du rotor ne montre pas de zones de tourbillon, donc l'écoulement de fluide est tout à fait compatible avec le rotor pendant le fonctionnement (figure B.17). Cependant, au point NIP, un grand tourbillon se forme dans certains passages inter-aubes. Ces tourbillons bloquent tout ou une partie du passage inter-aubes en raison d'un reflux secondaire généré par le gradient de pression aval et la continuité du fluide pour compenser le déficit de débit (figure B.18). Bien que des cellules de tourbillon apparaissent à l'intérieur du deuxième rotor, elles ne se forment que dans quelques passages inter-aubes et ne se propagent pas à l'ensemble du rotor, de sorte que le compresseur reste stable. Si le débit continue de diminuer, ces cellules de tourbillon continuent de croître et de se propager à l'ensemble du rotor, provoquant l'instabilité du compresseur.

FIGURE B.17 – Visualisation 3D des lignes de courant au point BEP du compresseur CRCC avec $N_1 = -10\,000\text{ tr/min}$, $N_2 = 10\,000\text{ tr/min}$ et $\dot{m}_{cr} = 0.543\text{ kg/s}$

Simulations numériques en régime instationnaire

Une simulation instationnaire est réalisée pour étudier la position relative entre les rangées des aubes de rotors et les changements de cellules de tourbillon à l'intérieur des

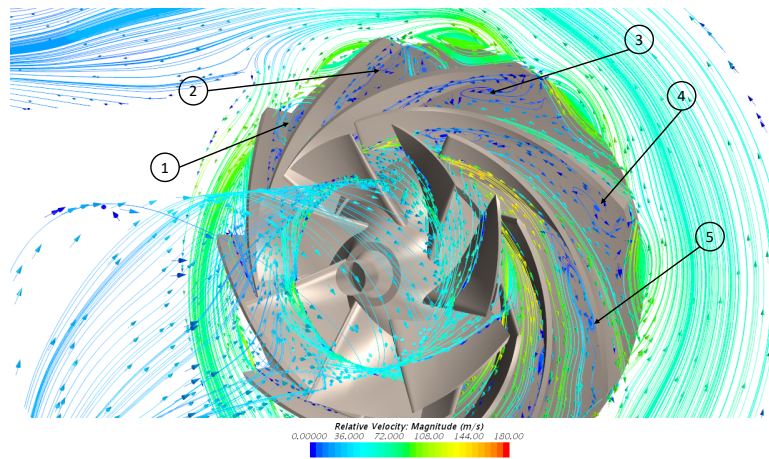


FIGURE B.18 – Visualisation 3D des lignes de courant au point NIP du compresseur CRCC avec $N_1=-10\ 000\ tr/min$, $N_2=10\ 000\ tr/min$ et $\dot{m}_{cr}=0.27\ kg/s$

passages des aubes. Les résultats indiquent que les cellules de tourbillon apparaissent près du bec de la volute et se développent progressivement dans les passages inter-aubes dans le sens inverse de la rotation, comme indiqué sur la figure B.19. Lorsque le passage inter-aubes traverse la région du bec, ses cellules de tourbillon diminuent progressivement de taille et disparaissent. Le flux de fluide circule normalement. De plus, des fluctuations de pression sont également observées en paroi dans cette simulation. Les résultats de l'analyse FFT (Transformée de Fourier Rapide) permettent d'observer la fréquence de passage des aubes et ses fréquences harmoniques.

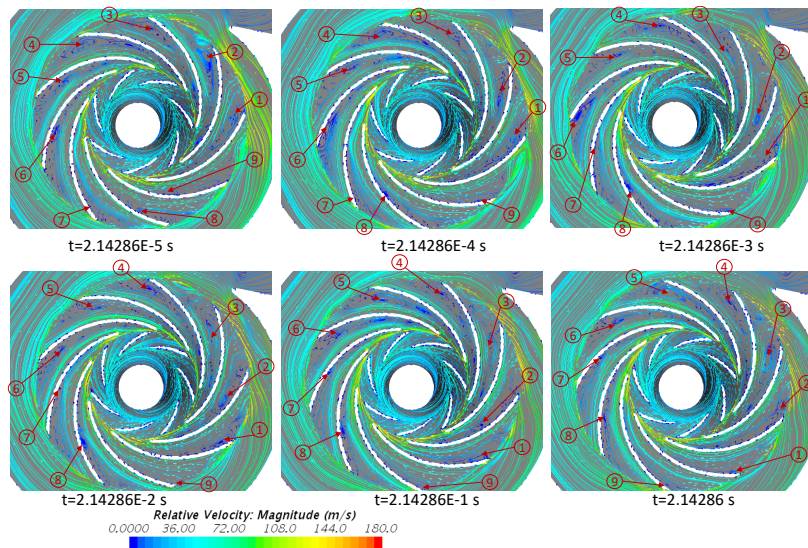


FIGURE B.19 – Visualisation séquentielle des lignes de courant au point NIP avec $N_1=-10\ 000\ tr/min$, $N_2=10\ 000\ tr/min$ et $\dot{m}_{cr}=0.27\ kg/s$. Les nombres représentent l'ordre des tourbillons dans les passages inter-aubes et ils se déplacent dans le sens de rotation dans le temps.

B.5 Contrôle d'instabilités

B.5.1 Méthode de contrôle d'instabilité

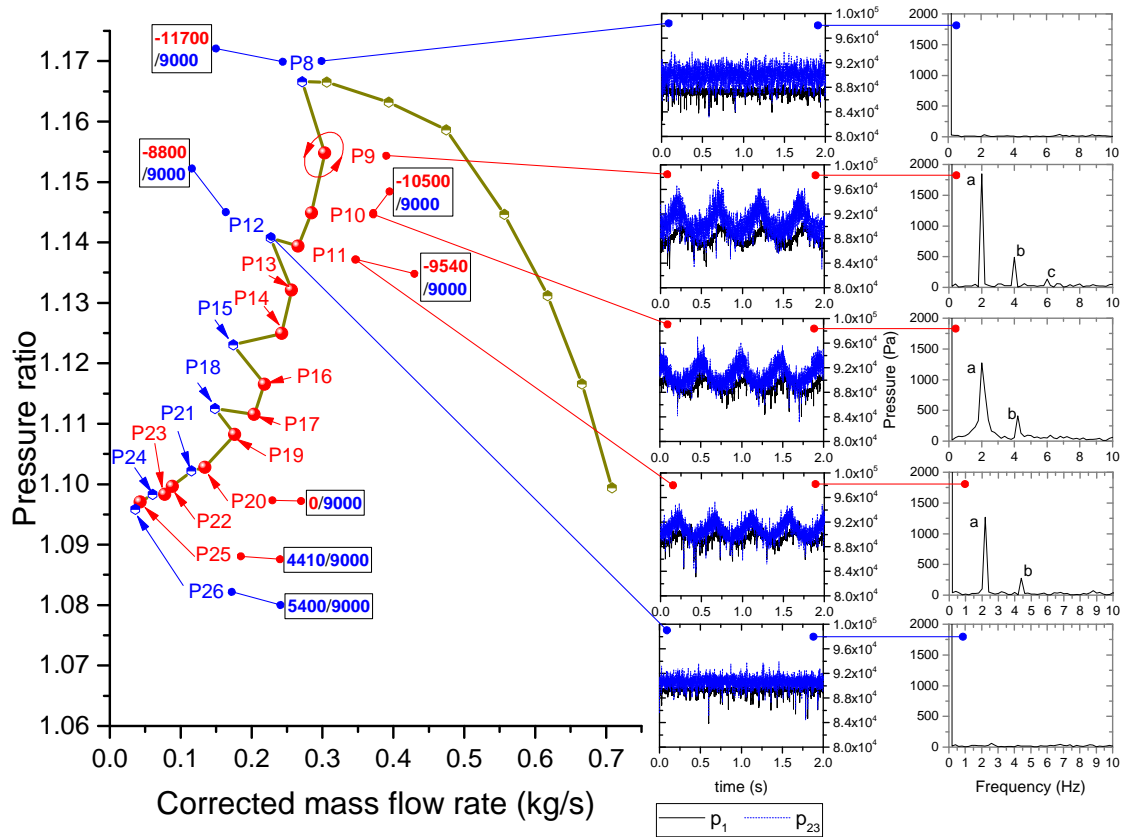


FIGURE B.20 – Étude du contrôle de la vitesse du premier rotor pour une vitesse du deuxième rotor fixée à 9 000 tr/min pour repousser l'apparition du phénomène d'instabilités de CRCC

Chaque compresseur a une limite basse de fonctionnement correspondant à la valeur minimale du débit massique à laquelle le compresseur peut fonctionner de manière stable. Si cette valeur est dépassée, le compresseur fonctionne de manière instable. Dans cette partie une solution pour réduire la limite basse de fonctionnement d'un compresseur centrifuge est proposée. Cette limite peut être réduite en contrôlant les vitesses des deux rotors de CRCC. La région d'instabilités de CRCC est améliorée (la limite d'apparition des instabilités est repoussée vers de plus faibles débits) en réduisant la vitesse de rotation du premier rotor. Cependant, si la vitesse du premier rotor diminue jusqu'à atteindre 0, le phénomène d'instabilités du compresseur existe toujours. Une solution consiste alors à le faire tourner dans le même sens que le deuxième rotor. Dans ce cas, le taux de compression sera diminué, mais cela améliorera également la région d'instabilité en augmentant la plage de fonctionnement. La figure B.20 montre les améliorations de la zone d'instabilité du CRCC obtenues en modifiant la vitesse du premier rotor. Du point P8 au point P20, les instabilités sont éliminées en réduisant progressivement la vitesse de rotation du premier rotor jusqu'à 0. Du point P21 au point P26, la région d'instabilités est encore étendue vers les faibles débits grâce à l'effet co-rotatif des deux rotors. La figure B.21 présente la variation de la vitesse du premier rotor de CRCC pour repousser l'apparition du phénomène d'instabilités en fixant un rapport

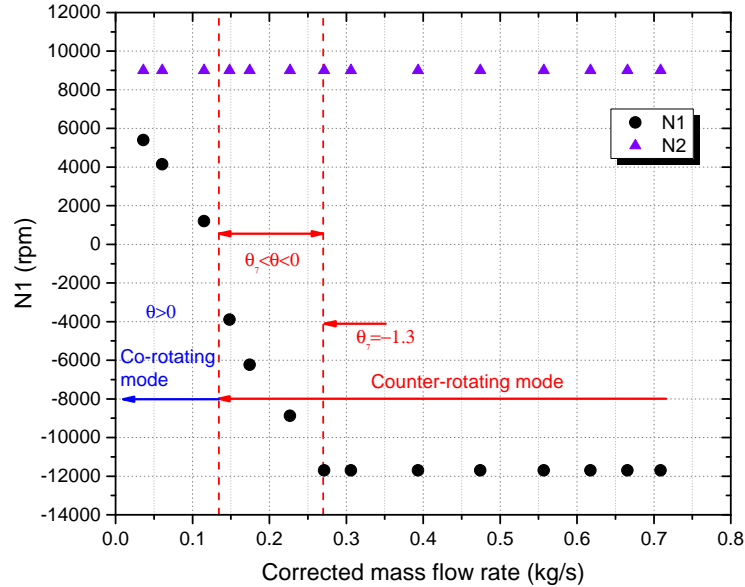


FIGURE B.21 – Variation de la vitesse du premier rotor pour repousser la limite d'apparition des instabilités à faibles débit de CRCC pour un rapport de vitesse θ_7 et $N_2 = 9,000rpm$

de vitesse θ_7 . Le phénomène d'instabilités semble suspendu en réduisant la vitesse du premier rotor entraînant ainsi une diminution du taux de compression. Si la vitesse de rotation du deuxième rotor ne change pas, toutes les caractéristiques présentent la même tendance lorsque le premier rotor change de sens de rotation. En conséquence, la plage de fonctionnement de CRCC est étendue vers les débits plus faibles.

B.5.2 Extension de la plage de fonctionnement

Afin d'évaluer l'augmentation de la plage de fonctionnement de CRCC dans la région d'instabilités, trois courbes caractéristiques expérimentales¹ sont construites et comparées à celles de SRCC à trois vitesses de rotation : $9\,000\ tr/min$, $10\,000\ tr/min$ et $11\,000\ tr/min$. L'extension de la plage de fonctionnement est plus évidente lorsque le taux de compression est maintenu constant dans la région à faibles débits. Un taux de compression constant peut être obtenu de diverses manières. Par exemple, en augmentant ou en diminuant la vitesse de rotation des deux rotors de CRCC, indépendamment, en modifiant la vitesse de rotation des deux rotors simultanément lorsque le débit massique diminue. La courbe caractéristique C_1 de CRCC est obtenue en fixant la vitesse de rotation initiale du deuxième rotor $N_2 = 9\,000\ tr/min$. La vitesse du premier rotor N_1 est ensuite modifiée en mode contrarotatif pour atteindre un taux de compression proche de la valeur de SRCC au même débit massique. Cette courbe caractéristique est donc contrôlée pour être proche de celle de SRCC à la vitesse de $9\,000\ tr/min$. Lorsque le taux de compression atteint $\Pi_s = 1,112$, valeur proche du taux de compression de SRCC au point d'apparition des instabilités (pour un débit massique égal à $0,146\ kg/s$), le compresseur est contrôlé pour maintenir un taux de compression constant en modifiant simultanément la vitesse des deux rotors. À un débit massique inférieur à la valeur limite de SRCC (région d'apparition des instabilité de SRCC), le mode de co-rotation est appliqué pour repousser le phénomène d'instabilités. Cette méthode permet une

1. Ces caractéristiques sont obtenues en modifiant simultanément la vitesse de rotation des deux rotors.

observation claire de l'élargissement de la plage de fonctionnement. Les courbes C_2 et C_3 sont proches des courbes de SRCC avec les vitesses 10 000 tr/min et 11 000 tr/min , en utilisant la même méthode que celle présentée précédemment pour C_1 . Ces courbes des performances sont comparées à celles de SRCC et sont illustrées à la figure B.22.

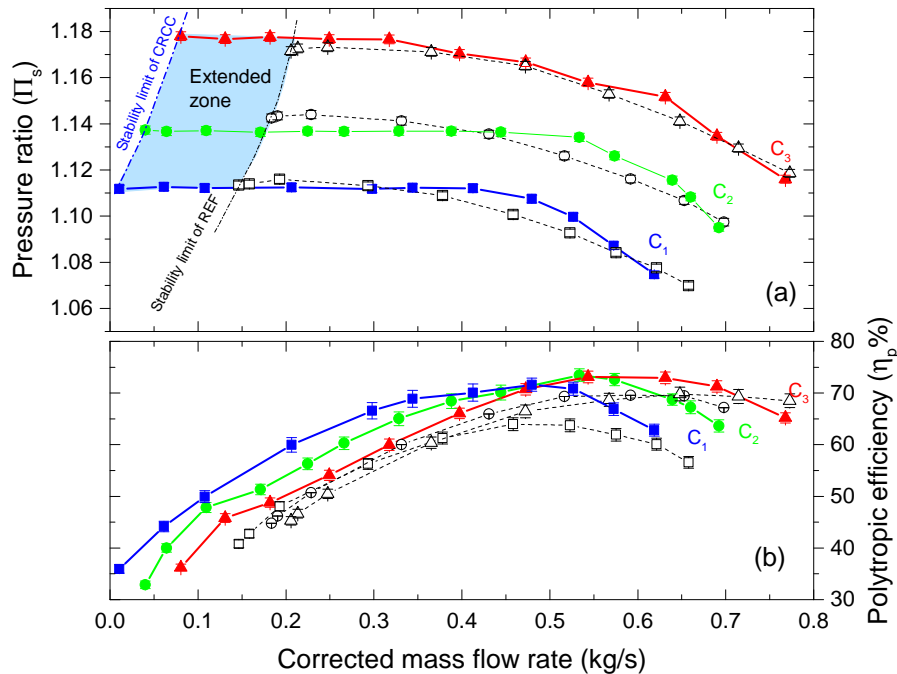


FIGURE B.22 – Comparaison des courbes de performances C_1 (\blacksquare), C_2 (\bullet) et C_3 (\blacktriangle) de CRCC par rapport aux courbes de performance de SRCC pour les trois vitesses 9 000 tr/min (\square), 10 000 tr/min (\circ) et 11 000 tr/min (\triangle)

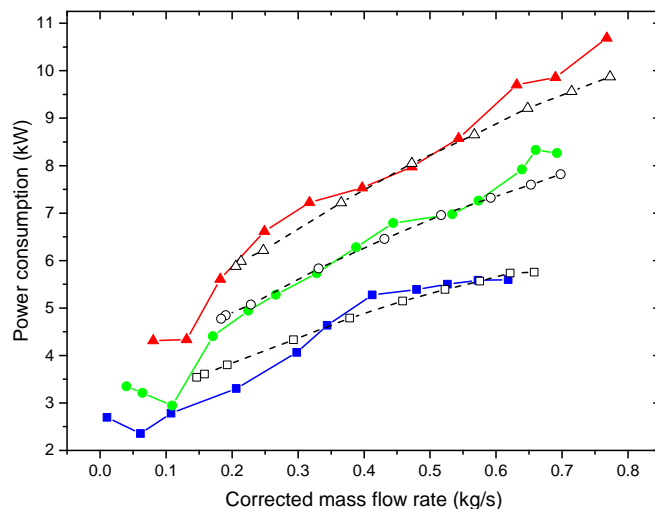


FIGURE B.23 – Consommation électrique des courbes de performances C_1 (\blacksquare), C_2 (\bullet) et C_3 (\blacktriangle) de CRCC et de SRCC pour les vitesses 9 000 tr/min (\square), 10 000 tr/min (\circ) et 11 000 tr/min (\triangle)

Pour la courbe C_1 , la configuration CRCC peut diminuer la zone d'instabilités de 0.135 kg/s par rapport au débit limité de SRCC à la vitesse 9 000 tr/min . De plus, à

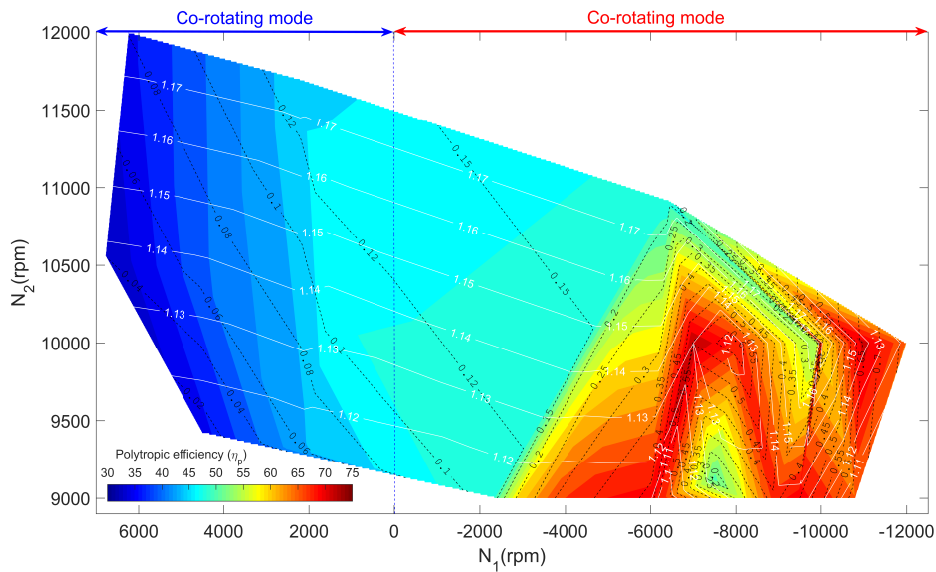


FIGURE B.24 – Les relations entre les vitesses des deux rotors et le rendement polytropique (la couleur), le débit massique corrigé (la ligne pointillée), et le taux de pression (la ligne continue) en cas d’extension de la plage de fonctionnement

la courbe C_3 , la configuration CRCC permet un déplacement d’environ 0.125 kg/s vers des débits plus faibles par rapport à la configuration de SRCC pour une vitesse de $11\,000 \text{ tr/min}$. Ainsi, en modifiant la vitesse des deux rotors, la plage de fonctionnement de CRCC a été étendue d’environ 25% vers des débits plus faibles par rapport à SRCC, pour le même taux de compression. En outre, les rendements de CRCC sont également considérablement améliorés par rapport à ceux de SRCC dans la zone des faibles débits. Cela peut également être observé en analysant la consommation d’énergie de CRCC par rapport à celle de SRCC (figure B.23). On peut voir clairement qu’à faible débit, la consommation d’énergie de CRCC pour C_1 est inférieure à celle de SRCC au même taux de compression. La figure B.24 montre les relations entre les vitesses des deux rotors et le rendement polytropique (en couleur), le débit massique corrigé (lignes pointillées), et le taux de compression (lignes continues) en cas d’extension de la plage de fonctionnement. Il est évident que le taux de compression peut être maintenu constant si la vitesse des deux rotors change simultanément dans le sens opposé, en mode contrarotatif, ou dans le même sens, en mode co-rotatif. De plus, CRCC donne un meilleur rendement que SRCC en mode contrarotatif, mais celui-ci diminue rapidement en mode co-rotatif. On peut facilement choisir un point de fonctionnement souhaité en recherchant la valeur du débit massique, du taux de compression et du rendement pour connaître le couplée de vitesses de rotation des deux rotors. La plage de fonctionnement peut être augmentée lorsque le compresseur fonctionne en mode co-rotatif et que la vitesse du premier rotor comprise entre 48 % et 64 % de la vitesse du deuxième rotor. À cette vitesse, le débit de la limite d’instabilités est déplacé vers une valeur extrêmement faible et la plage de fonctionnement du compresseur est considérablement étendue.

B.5.3 Analyse CFD en mode corotation

Un autre point intéressant est le cas de la co-rotation pour améliorer la plage de fonctionnement du compresseur dans la zone du pompage. Le compresseur peut fonctionner de manière stable au débit le plus bas de $\dot{m}_{cr} = 0,08 \text{ kg/s}$ comme il a été montré précédemment la figure B.22 à un taux de compression constant de $\Pi_s = 1.177$. Observer l'écoulement du fluide à l'intérieur du compresseur comme présenté sur la figure B.25. Cela montre que plus de la moitié des passages inter-aube sont bloqués, cependant, le flux de fluide circule toujours normalement à travers le reste des passages du rotor. Cela montre qu'à un débit extrêmement faible, le compresseur conserve la capacité de fonctionner de manière stable grâce à l'effet co-rotatif du premier rotor.

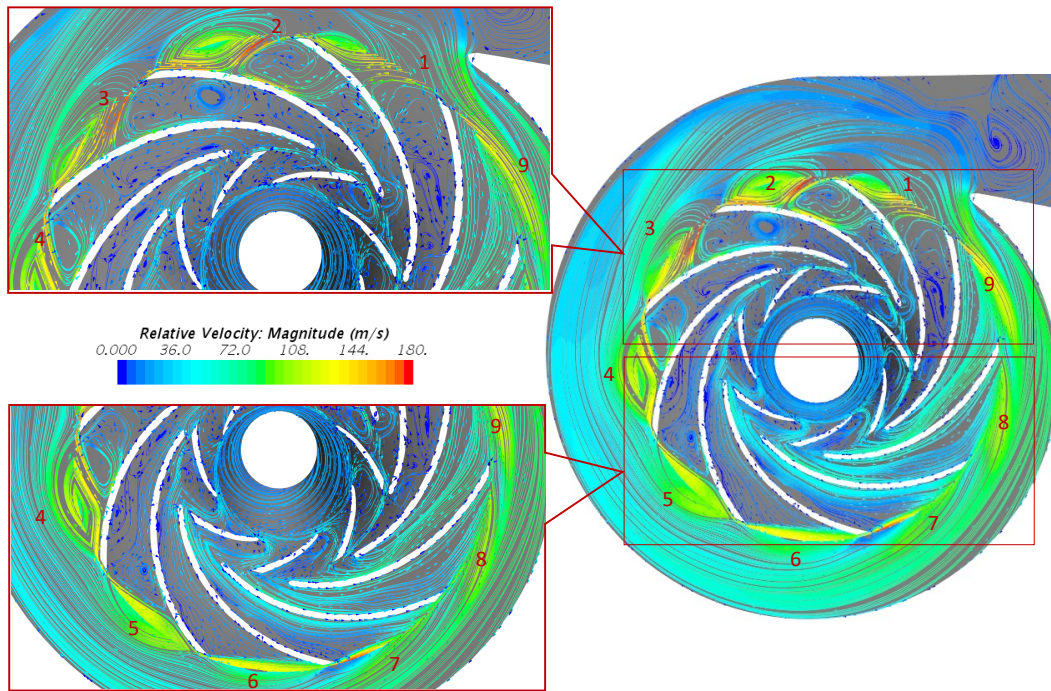


FIGURE B.25 – Structure d'écoulement au point **ESLP** en mode co-rotatif avec $N_1=6240 \text{ tr/min}$, $N_2=12\ 000 \text{ tr/min}$ et $\dot{m}_{cr}= 0,08 \text{ kg/s}$

B.6 Conclusions

Le but de l'étude était d'atteindre deux objectifs principaux. Le premier consistait à évaluer la possibilité d'améliorer les performances des compresseurs centrifuges lors de l'utilisation du système contrarotatif. Le seconde consistait à améliorer la zone d'instabilité pour étendre la plage de fonctionnement du compresseur. Une paire de rotors contrarotatifs (**CRCC**) est conçue pour remplacer un rotor seul (**SRCC**) en gardant la même géométrie et la même volute. Un banc d'essai appelé RAICOR a été développé pour réaliser une étude expérimentale des ces deux compresseurs (**CRCC** et **SRCC**).

Les résultats expérimentaux ont montré que **CRCC** pouvait présenter des performances supérieures à celles du compresseur conventionnel à des vitesses inférieures à la vitesse de conception en mode contra-rotatif. De plus, l'étude du rapport de vitesses des deux rotors montre également que **CRCC** peut s'améliorer le taux de compression jusqu'à 6,6 % à $\theta = -1,3$ avec une vitesse du deuxième rotor de 11 000 tr/min . Le rendement peut être amélioré jusqu'à 8 % pour une vitesse du deuxième rotor de 9 000

tr/min. On peut noter que le meilleur point de fonctionnement du compresseur change lorsque le rapport de vitesses varie. On peut donc obtenir une plage de fonctionnement plus grande pour **CRCC** que pour **SRCC**.

Pour des raisons de sécurité, **CRCC** ne peut pas fonctionner à la vitesse de rotation pour laquelle il a été dessiné (à 16 000 *tr/min*), la méthode des similitudes a donc été utilisée pour prédire les performances du système à cette vitesse. Les résultats des calculs montrent que **CRCC** peut améliorer le taux de compression jusqu'à 15,3 % à $\theta = -1, 3$. En outre, les rendements à cette vitesse fluctuent autour de la valeur de rendement maximal de **SRCC** de 73 % environ. Cependant, on voit clairement que **CRCC** permet de bien améliorer le taux de compression, mais dans ce cas instabilités à faible débit peuvent apparaître plus tôt que pour **SRCC**. Heureusement, **CRCC** peut ajuster la vitesse des deux rotors indépendamment. L'apparition des instabilités peut donc être repoussé et ainsi la limite de pompage peut-être considérablement reculée pour augmenter la plage de fonctionnement du compresseur. Les résultats du changement simultané de la vitesses des rotors montrent que le débit limite de **CRCC** peut se déplacer de 0.135 kg/s par rapport au débit limite de **SRCC** à 9 000 *tr/min*. A des vitesses supérieures à 12 000 *tr/min*, il est possible de réduire d'environ 0.125 kg/s le débit par rapport à **SRCC** à 11 000 *tr/min*. Par conséquent, la plage de fonctionnement a été étendue de 24 % à 28 % vers la zone de pompage. Pour ce faire, les deux rotors doivent tourner dans le même sens avec une vitesse du premier rotor variant de 48 % à 64 % de la vitesse du deuxième rotor.

Une étude par simulation numérique a été menée pour surveiller davantage la structure de l'écoulement des fluides à l'intérieur de la machine en trois points de fonctionnement particuliers : le point de rendement maximal (**BEP**), un point de la limite de pompage (**NIP**) en mode contra-rotatif et un point étendue (**ESLP**) en mode co-rotatif. Les résultats de la simulation montrent qu'à **BEP**, l'écoulement dans la machine est assez uniforme. Cependant, au point **NIP**, des zones de tourbillons apparaissent à l'intérieur des passages d'aubes. La taille de ces tourbillons dépend de la position relative du rotor avec la volute. Ils peuvent bloquer tout ou une partie du passage inter-aubes. Une étude instationnaire est également menée pour observer l'évolution des zones de tourbillon au point **NIP** dans le mode contrarotatif du **CRCC**. Les résultats montrent que l'air s'écoule toujours normalement dans la moitié des passages inter-aubes du deuxième rotor à un débit extrêmement faible.

Ainsi, l'utilisation d'un système contrarotatif dans un compresseur centrifuge montre qu'il améliore non seulement les performances mais permet également d'élargir la plage de fonctionnement vers un faible débit.

Appendix C

List of acronyms

- BEP** Best Efficiency Point. [x](#), [xi](#), [xvi](#), [91–98](#), [123](#), [XLIV](#), [LVII](#), [LX](#), [LXVII](#)
- CF** counter-rotating ConFiguRation. [vii](#), [viii](#), [xix](#), [21](#), [24](#), [26–28](#), [30–32](#), [34](#), [35](#), [121](#), [XLVI](#), [XLIX](#)
- CFD** Computational Fluid Dynamic. [viii](#), [xi](#), [16](#), [17](#), [19](#), [26](#), [39](#), [55](#), [83](#), [96–98](#), [116](#), [XXIX](#), [XXX](#)
- CR** Counter-Rotating mode. [ix](#), [65–68](#)
- CRCC** Counter-Rotating Centrifugal Compressor. [iii](#), [iv](#), [vii–xvi](#), [xix](#), [20](#), [26–35](#), [37](#), [39–49](#), [55](#), [57–84](#), [86](#), [88–93](#), [95](#), [96](#), [98](#), [103–105](#), [107](#), [113–116](#), [119](#), [121–124](#), [XV](#), [XXI](#), [XXII](#), [XXVI](#), [XXIX](#), [XLV](#), [XLVII–LXV](#), [LXVII](#)
- DP** Design Point. [27](#), [28](#), [31–35](#), [XLIX](#)
- ESLP** Extended Stability Limit Point. [xii](#), [xiii](#), [xvii](#), [116–119](#), [124](#), [XLV](#), [LVII](#), [LXVI](#), [LXVII](#)
- LIFSE** Laboratoire d’Ingénierie des Fluides et des Systèmes Énergétiques. [19](#), [37](#), [55](#), [121](#), [XLIV](#), [L](#)
- LR** Length Ratio. [xiii](#), [21](#), [23](#), [24](#), [26](#), [28](#), [35](#), [121](#), [124](#), [XLIV](#), [XLVI–XLVIII](#)
- NIP** Near Instability Point. [x](#), [xi](#), [xvi](#), [91–98](#), [123](#), [XLIV](#), [LVII](#), [LX](#), [LXI](#), [LXVII](#)
- RAICOR** Rotor - rotor Aerodynamic Interaction of a COunter-Rotating centrifugal compressor. [iii–v](#), [ix](#), [xvi](#), [37](#), [48–55](#), [121](#), [L](#), [LI](#)
- SRCC** Single Rotor Centrifugal Compressor. [iii](#), [vii–xii](#), [xiv–xvi](#), [xix](#), [19](#), [20](#), [27–35](#), [37–39](#), [48](#), [55](#), [57–61](#), [64–77](#), [82](#), [83](#), [104](#), [107](#), [113–115](#), [119](#), [121–124](#), [XV](#), [XXI](#), [XXVI](#), [XLIX](#), [LII–LVII](#), [LXIII–LXV](#), [LXVII](#)

Appendix D

List of Symbols

- α Absolute flow angle, *rad.* 3, 23, XLVI
- C** Absolute velocity, *m/s.* 2–5, 8, 10, 22, 23, 106, II, XIV, XLVI
- ω Angular speed of rotor, *rads⁻¹.* 4, 9, 20, II, VIII, X
- z** Axial distance, *m.* V–VII
- C_x Axial velocity component, *m/s.* 3
- C_a Axial velocity component, *m/s.* 22
- β_b Blade angle, *rad.* vii, 6, 7, 23
- s** Pitch of blade, $s = 2\pi r/Z$. 7, 9
- S** Blade section area, *m².* 22, 25, II, VI, VIII, XIV
- t** Thickness of blade, *m.* 9, 22, 25
- b** Blade passage width, *m.* 8, 9, 22, 25, II, III, V, VII
- U** Blade velocity $U = r\omega$, *m/s.* 2–9, 22–25, 62, 78, 106, II, III, V, VIII, XII, XIII, LIII
- L_{1st} Contour length at hub/shroud of the first rotor, *m.* 21, XLVI
- ρ Density, [*kg/m³*]. 8, 9, 22, 25, 54, 78, XIV
- δ Deviation. 9
- η Efficiency. 10, 22, 25, 54, X, XIV
- h** Specific enthalpy, *Jkg⁻¹.* 4, 5, 23, 25, 62, 78, X, XII, XIII, LIII
- \dot{W} Euler work rate, *J/s.* 4
- k** Expansion factor. 50
- ψ' Experience number. 8
- β Relative flow angle, *rad.* 3, 5–9, 19, 22–25, II–V, VII–IX
- \dot{m} Mass flow rate, *kg/s.* 4, 9, 22, 25, 54, 78, X, XIV
- ϕ Flow coefficient. 6–9, 78
- Q** Volume Flow rate, *m³/s.* II–V, VIII
- R** Gas constant, $R = 287\text{Jkg}^{-1}\text{K}^{-1}$. 9, 22, 23, 25, 54, X, XIII, XIV
- g** Gravity of earth, *ms⁻².* 4, 14, II, III, V

- H** Head rise, m . II–V
- y** head rise of rotor, J . 9
- \dot{Q} Heat transfer rate, J/s . 4
- Ψ Head coefficient. 9, 78
- η_H Hydraulic efficiency. III
- D** Diameter of inlet pipe, m . 49, 54, 86, LI
- U_A Measurement error of K repeated measurement of type A. 50
- U_B Measurement error of K repeated measurement of type B. 51
- ω_{loss} Loss coefficient. 31, 32
- M** Mach number. 9, 23
- C_m Meridian velocity component, m/s . 22, 23, 25, VIII
- τ Torque at rotating shaft, Nm . 4
- K** Number of mesurement. 50
- Z** Number of blade. 6–8, 23, 25, IV, V
- p** Output coefficient. 8
- μ Pfeleiderer slip factor. IV
- Π Pressure ratio. 22, 23, 25, 54, 55
- P** Pressure, Pa . 9, 10, 22, 23, 25, 31, 54, X, XIV, XLVI
- C_{pr} Pressure recovery coefficient. 31
- r** Radius, m . 4, 6–9, 22, 25, II–XI, XIII, XIV
- C_r Radial velocity component, m/s . 3, 5, 6, 22–25, V
- u_A Random measurement error of type A. 50
- u_B Random measurement error of type B. 51
- W** Relative velocity, m/s . 2, 3, 5, 22, 25, 106
- W_u Relative tangential velocity component, m/s . 5, 23, 25
- N** Rotational speed, rpm . IV, XIII
- σ Slip factor. 6–8, 23, 25
- C_{us} Slip velocity, m/s . 6–8
- a** Speed of sound, ms^{-1} . 9, XIII
- Ω Specific angular speed, $rads^{-1}$. II
- γ Specific heat ratio. 9, 10, 22, 23, 25, 54, X, XIII, XIV
- Λ Specific radius. II
- C_p Specific heat at constant pressure, $Jkg^{-1}K^{-1}$. 10, 23, 25, X
- C_v Specific heat at constant volume, $Jkg^{-1}K^{-1}$. X
- δ Surface stream angle. 22
- C_u Tangential velocity component, m/s . 3–6, 8, 14, 23–25, 62, 106, III, V, XII, LIII
- T** Temperature, K . 9, 10, 22, 23, 25, 54, 55, X, XIII, XIV, XLVI
- L_m Total contour length at hub/shroud of the reference rotor, m . 21, XLVI
- u** Uncertainty value. 51

Résumé : L'objectif de la thèse est d'étudier d'une part l'effet du système contrarotatif sur les performances du compresseur centrifuge et d'autre part l'influence de le système sur la zone de pompage lorsque le débit massique est très faible. Le mono rotor du compresseur centrifuge conventionnel est remplacé par deux rotors qui tournent en sens inverse et ayant la même taille. Les autres composants du compresseur sont préservés. L'étude expérimentale montre que l'utilisation d'un système contrarotatif améliore non seulement les performances du compresseur à des vitesses de rotation inférieures à la vitesse de conception, mais diminue aussi la zone de pompage. Le compresseur fonctionnant en mode contrarotatif offre un meilleur taux de compression ainsi qu'un meilleur rendement que le compresseur conventionnel. Pour améliorer la zone de pompage, un mode de co-rotation est adopté pour permettre au compresseur de fonctionner à un débit inférieur à celui du compresseur de référence. La limite du pompage est alors repoussée jusqu'à 24%-28% de la plage de fonctionnement du compresseur, vers les débits plus faibles. Le point limite est atteint lorsque la vitesse de rotation du rotor en amont est comprise entre 48% et 64% de celle du rotor en aval. Les résultats de cette étude jouent un rôle important dans le développement d'une nouvelle génération de compresseur centrifuge pouvant fonctionner sous un très faible débit massique.

Mots clés : Contrarotatif, co-rotatif , interaction rotor-rotor, compresseur centrifuge, améliorer du pompage

Abstract : The objective of the thesis is to study the effect of the counter-rotating system on the performance of centrifugal compressors and the ability to improve a surge region when the flow is very low flow rate. The single rotor of the conventional centrifugal compressor is replaced by two counter-rotating rotors, which have the same size. The remaining components of the compressor are preserved. Experimental results show that the use of a counter-rotating system not only improves the performance of the compressor at rotational speeds lower than the design speed but also decreases the instability region. The compressor operating in counter-rotating mode gives a better pressure ratio as well as a better efficiency than the conventional compressor. A co-rotation mode is adopted to allow the compressor to operate at a lower flow rate. The instability limit of the compressor is then pushed back from 24% to 28% of the operating range towards the lower flow rates. The limit point is reached when the upstream rotor speed is between 48% and 64% of the downstream rotor speed. The results of this study play an important role in the development of a new generation of centrifugal compressor that can operate at a very low mass flow rate.

Keywords : Counter-rotating, co-rotating, centrifugal compressor, rotor-rotor interaction, improved surge